Electrical Activation Studies of Ion Implanted Gallium Nitride

Dissertation

James A. Fellows, Major, USAF

AFIT/DS/ENP/02-2

DEPARTMENT OF THE AIR FORCE
AIR UNIVERSITY

AIR FORCE INSTITUTE OF TECHNOLOGY

Wright-Patterson Air Force Base, Ohio

APPROVED FOR PUBLIC RELEASE; DISTRIBUTION UNLIMITED.

Report Documentation Page

Report Date	Report Type	Dates Covered (from... to)
20 Nov 2001	Final	Aug 1998 - Nov 2001

Title and Subtitle Electrical Avtivation Studies of Ion Implanted Gallium Nitride	**Contract Number**
	Grant Number
	Program Element Number
Author(s) Major James A. Fellows, USAF	**Project Number**
	Task Number
	Work Unit Number
Performing Organization Name(s) and Address(es) Air Force Institute of Technology Graduate School of Engineering & Management (AFIT/EN) 2950 P Street, Bldg 640 WPAFB OH 45433-7765	**Performing Organization Report Number** AFIT/DS/ENP/02-2
Sponsoring/Monitoring Agency Name(s) and Address(es) Major Daniel K. Johnstone AFOSR/NE 801 North Randolph St. Arlington, VA 22203-1977 Dr. William C. Mitchel AFRL/MLPS 3005 P St., Ste 6 WPAFB OH 45433-7707	**Sponsor/Monitor's Acronym(s)**
	Sponsor/Monitor's Report Number(s)
Distribution/Availability Statement Approved for public release, distribution unlimited	
Supplementary Notes	

Abstract
A comprehensive and systematic electrical activation study of Si-implanted GaN was performed as a function of ion implantation dose, anneal temperature, and implantation temperature. Additionally, Mg-implanted GaN was also investigated. Temperature-dependent Hall effect measurements and photoluminescence (PL) spectra were used to characterize the samples. GaN wafers capped with AlN were implanted with Si ions at doses ranging from 1x1013 to 5x1015 cm-2 and annealed from 1050 to 1350 oC. The optimum anneal temperature for samples implanted with the higher Si doses is around 1350 oC, exhibiting nearly 100% electrical activation efficiency. Exceptional mobilities and carrier concentrations were obtained on all Si-implanted samples. PL spectra revealed nearly complete implantation damage recovery as well as the nature of the yellow luminescence plaguing nearly all Si-doped GaN. Additionally, GaN wafers were implanted with Mg and various coimplants and annealed from 1100 to 1350 oC. All of the Mg-implanted and most of the Mg-coimplanted GaN samples became extremely resistive, and did not show definite p-type conductivity even after annealing at 1350 oC, remaining highly resistive even at a sample temperature as high as 800 K. A dominant 2.36 eV green luminescence band observed in the PL spectra of all Mg-implanted samples is attributed to a Mg-related deep complex DAP transition. The inefficient electrical activation of Mg acceptors implanted into GaN is attributed to these Mg-related deep complexes.

Subject Terms
Wide Bandgap Semiconductor, Gallium Nitride (GaN), Ion Implanation, Silicon, Activation Efficiency, Hall Effect, Photoluminescence

Report Classification	**Classification of this page**
unclassified	unclassified
Classification of Abstract	**Limitation of Abstract**
unclassified	UU

Number of Pages
221

“The views expressed in this dissertation are those of the author and do not reflect the official policy or position of the Department of Defense or the U.S. Government”

AFIT/DS/ENP/02-2

ELECTRICAL ACTIVATION STUDIES OF ION IMPLANTED GALLIUM NITRIDE

DISSERTATION

Presented to the Faculty

Graduate School of Engineering and Management

Air Force Institute of Technology

Air University

Air Education and Training Command

In Partial Fulfillment of the Requirements for the

Degree of Doctor of Philosophy

in Materials Science and Engineering

James A. Fellows, B.S., M.S.

Major, USAF

November 2001

Approved for public release; distribution unlimited

AFIT/DS/ENP/02-2

ELECTRICAL ACTIVATION STUDIES OF ION IMPLANTED GALLIUM NITRIDE

James A. Fellows, B.S., M.S.
Major, USAF

Approved:

Yung Kee Yeo — 5 Nov. 2001
Yung Kee Yeo, PhD
Professor of Physics
Chairman, Advisory Committee

Date

Robert L. Hengehold — 5 Nov 2001
Robert L. Hengehold, PhD
Professor and Head, Department of Engineering Physics
Member, Advisory Committee

05 NOVEMBER 2001
James A. Lott, Lt Col, USAF
Professor and Deputy Head
Department of Electrical and Computer Engineering
Member, Advisory Committee

William C. Mitchel — 7 Nov 2001
William C. Mitchel, PhD
Senior Scientist, Air Force Research Laboratory
Member, Advisory Committee

Anthony N. Palazotto — 7 Nov 2001
Anthony N. Palazotto, PhD
Professor, Department of Aero & Astronautics
Dean's Representative

Accepted:

Robert A. Calico, Jr.
Dean, Graduate School of Engineering and Management

Acknowledgments

Any significant milestone in one's life is made successful by the contributions of many others along the way. The successful completion of this research is no different for me. I am extremely appreciative and thankful for my advisor Dr. Yung Kee Yeo. He provided the guidance, motivation, and instruction to press on through the many frustrating times common in experimental research. As a mentor, his desire and ability to support me in whatever I needed were crucial to finishing this task. Mr. Greg Smith provided invaluable technical support throughout my research. I am very thankful for his instruction on experimental procedures, his masterful ability to fix problems, and his encouraging discussions. I would like to thank Dr. Mohamed Ahoujja for our many discussions on experimental measurements and doctoral research. I must also thank Mr. Rick Patton for his support in AFIT's new cleanroom, Dr. William Mitchel for use of his annealing furnace, Dr. Joseph Van Nostrand and Dr. Brendan Gaffey for their AlN growth, Dr. Leonid Krasnobaev for his ion implantation, and Major Mike Scott for his encouragement that I would eventually succeed. I am thankful for Mr. Bill Gorman who always had an ear to listen to my frustrations and my joys. I have much gratitude for my mother, who instilled within me, by her own example, the importance of hard work and a good education. My deepest appreciation goes to my wife and children. I cannot thank them enough for their patience, support, encouragement, understanding, sacrifice, and love throughout this journey. Of course, I am also indebted to the many who supported me with their prayers; and I thank God for answering our prayers.

James A. Fellows

Table of Contents

Page

Acknowledgments iv

List of Figures vii

List of Tables xiii

Abstract xiv

I. Introduction 1

High-temperature, High-power, High-frequency, and High-radiation Electronics 1
Wide Bandgap Semiconductors 5
Gallium Nitride 7

II. Semiconductors, Energy Bands, and Impurities 11

Historical Perspectives 11
Crystal Structure 12
Crystal Growth 13
Energy Bands 15
Semiconductor Statistics 21
Impurities 23

III. Ion Implantation, Defects, and Annealing Theory 29

Introduction 29
Ion Implantation Theory 31
Radiation Damage: Crystal Defects 34
Annealing 38
Coimplantation 42

IV. Characterization Techniques 45

Introduction 45
Hall Effect Measurements 45
Photoluminescence 50

V. Experimental Procedures 58

Sample Growth, Ion Implantation, and Annealing 58
Initial Annealing and AlN Encapsulation After Implantation. 59
The Search for a Better AlN Encapsulant. 60
AlN Encapsulation During GaN Growth. 63
Optimized Annealing and AlN Removal. 64
Ohmic Contact Deposition. 65
Hall Effect Measurements 67

Photoluminescence and Cathodoluminescence Measurements 68

VI. Results and Discussion 70

Mg-Implanted and Mg-Coimplanted GaN 70
Low-temperature Photoluminescence. 74
Temperature-dependent Photoluminescence. 86
Electrical Characterization of Acceptor-implanted GaN. 96
Silicon Implanted into GaN at Room Temperature 112
Room-Temperature Hall Effect Measurements. 114
Temperature-Dependent Hall Effect Measurements. 124
Low-Temperature Photoluminescence. 135
Temperature-Dependent Photoluminescence. 146
Silicon Implanted into GaN at 800 ^{o}C 150
Room-Temperature Hall Effect Measurements. 151
Temperature-Dependent Hall Effect Measurements. 159
Low-Temperature Photoluminescence. 167
Temperature-Dependent Photoluminescence. 170
Comparison of GaN Implanted with Si at Room Temperature and 800 ^{o}C 173

VII. Conclusions and Recommendations 178

Appendix A: Publications Summary 185

Appendix B: Sample Processing Procedures 186

Sample Cutting and Cleaning Procedures 186
Oxy-Gon Sample Preparation Procedures 187
Oxy-Gon AlN/GaN Anneal Procedures 188
Post-Anneal Contact Preparation Procedures 190
Edwards Auto 306 Evaporator Procedures 191
Photoluminescence Procedures 193
Cathodoluminescence Procedures 195

Appendix C: GaN Energy Bandgap versus T 198

Bibliography 199

List of Figures

Figure Page

1. Intrinsic carrier concentration for Si, GaAs, and GaN as a function of temperature..... 3

2. Semiconductor crystal unit cells: (a) cubic symmetry represented by zincblende GaAs with lattice constant *a*, and (b) hexagonal symmetry represented by wurtzite CdS with lattice constants *a* and *c* (Sze, 1981:8,9)..... 14

3. Energy band structure of wurtzite GaN in k-space showing various points of crystal symmetry and a direct bandgap at the Γ point (Madelung, 1996:87)..... 18

4. Hexagonal crystal structure showing points and directions of high-symmetry..... 19

5. Bandgap energy and bandgap wavelength versus lattice constant for several direct and indirect semiconductors that crystallize in either the cubic or hexagonal structures..... 21

6. Empirical ionization energies in eV for several donor and acceptor species and deep levels in GaAs (Sze, 1985:23). 26

7. Gaussian implantation depth profiles showing the effects of ion energy and mass for various Si and Ar implants each at a dose of $1x10^{14}$ cm^{-2}. 33

8. Damage tracks of implanted ions: light ion (M_1) and heavy ion (M_2) relative to host semiconductor atoms. 37

9. van der Pauw technique for Hall effect measurements showing forced current, **I**, applied magnetic field, **B**, induced Hall voltage, V_H, and electron accumulation for an *n*-type semiconductor sample..... 47

10. Schematic diagram of an automated Hall effect system used for high resistivity and temperature-dependent Hall effect measurements..... 49

11. Schematic diagram of a photoluminescence system used to collect temperature- and power-dependent luminescence spectra..... 51

12. Radiative transitions observed in semiconductor luminescence spectra. 52

13. Morphology of AlN/GaN test samples annealed at 1250 ^{o}C for 3 min in minimally flowing N_2: (a) 500 Å and (b) 1000 Å thick hot-growth AlN (750 ^{o}C), (c) 500 Å and (d) 1000 Å thick cold-growth AlN (100 ^{o}C) arranged (i) open-face, (ii) open-face in Ta foil, and (iii) face-to-face in Ta foil. 62

14. Anneal temperature profiles for representative 1350 ^{o}C for17 sec and 1250 ^{o}C for 21 sec anneals showing obtainable ramp rates in the Oxy-Gon furnace. 66

15. PL spectra taken at 3 K for GaN implanted with Mg and annealed at various temperatures from 1100-1300 ^{o}C. Also shown are the spectra from two unimplanted samples and an *in-situ* Mg-doped sample. 75

16. PL spectra taken at 3K for GaN implanted with Mg and various coimplants annealed at 1250 ^{o}C for 18 s. 77

17. PL spectra taken at 3K for GaN implanted with Mg+C, Mg+O, and Mg+P at various doses and anneal temperatures. 79

18. CL spectra taken at 10 K for GaN implanted with 200 keV Mg at either 25 or 500 ^{o}C and annealed at various temperatures from 1100-1200 ^{o}C for 20 minutes. 81

19. CL spectra taken at 10 K for GaN implanted at 25 ^{o}C with Mg, Si, and Mg+Si at a dose of $1x10^{15}$ cm^{-2} for Si and $2x10^{15}$ cm^{-2} for Mg, and annealed at 1100 ^{o}C for 20 minutes. 82

20. CL spectra taken at 10 K for GaN coimplanted at either 25 or 500 ^{o}C with Mg+Si at a dose of $2x10^{15}$ cm^{-2} for Mg and $1x10^{15}$ cm^{-2} for Si. Samples were annealed at either 1150 or 1100 ^{o}C for 20 min. 84

21. PL spectra for GaN coimplanted at either 25 or 500 ^{o}C with Mg+Si at doses of $2x10^{14}$ cm^{-2} for Mg and $1x10^{14}$ cm^{-2} for Si and annealed at various temperatures from 1150-1300 ^{o}C and times from 15 sec to 20 min. 85

22. Temperature-dependent PL spectra for GaN implanted at 800 ^{o}C with 200 keV Mg at a dose of $5x10^{15}$ cm^{-2} and annealed at 1300 ^{o}C for 23 sec. 87

23. Temperature-dependent PL spectra for GaN implanted at 800 ^{o}C with Mg+O at doses of $5x10^{15}$ cm^{-2} for Mg and $2x10^{15}$ cm^{-2} for O and annealed at 1250 ^{o}C for 18 s. 91

24. Temperature-dependent PL spectra for GaN coimplanted at 500 ^{o}C with Mg+Si at doses of $2x10^{14}$ cm^{-2} for Mg and $1x10^{14}$ cm^{-2} for Si and annealed at 1300 ^{o}C for 23 sec. 93

25. PL spectra taken at 3K for GaN implanted at 800 ^{o}C with Li, Li+P, and C annealed at various temperatures from 1200-1300 ^{o}C and times from 9 sec to 5 min. Also shown are the PL spectra for unimplanted GaN annealed at 1250 ^{o}C and *in-situ* Mg-doped GaN. 95

26. Arrhenius plot of resistivity data from GaN implanted at 25 ^{o}C with Mg at a dose of $2x10^{14}$ cm^{-2} and annealed at 1150 ^{o}C for 15 sec. 111

27. Room-temperature sheet electron concentrations for GaN implanted at room temperature with 200 keV Si ions at doses ranging from $1x10^{13}$ to $5x10^{15}$ cm^{-2} and annealed at 1050 to 1350 ^{o}C from 5 min to 17 sec in a flowing nitrogen environment. 115

28. Electrical activation efficiency for GaN implanted at room temperature with 200 keV Si ions at doses ranging from $1x10^{13}$ to $5x10^{15}$ cm^{-2} and annealed at 1050 to 1350 ^{o}C from 5 min to 17 sec in a flowing nitrogen environment. 117

29. Sheet carrier concentration versus actual implanted dose for GaN implanted at 25 ^{o}C with 200 keV Si ions at doses ranging from $1x10^{13}$ to $5x10^{15}$ cm^{-2} and annealed at 1050 to 1350 ^{o}C from 5 min to 17 sec in a flowing nitrogen environment. 119

30. Room-temperature Hall mobility for GaN implanted at room temperature with 200 keV Si ions at doses ranging from $1x10^{13}$ to $5x10^{15}$ cm^{-2} and annealed at 1050 to 1350 ^{o}C from 5 min to 17 sec in a flowing nitrogen environment. 121

31. Temperature-dependent sheet electron concentrations taken from 10-800 K for GaN implanted at room temperature with 200 keV Si ions at doses ranging from $1x10^{13}$ to $5x10^{15}$ cm^{-2} and annealed at 1350 ^{o}C for 17 sec in a flowing nitrogen environment. 125

32. Calculated implantation profiles for 200 keV Si ions through a 500 Å AlN cap into GaN at doses of $5x10^{13}$ and $1x10^{14}$ cm^{-2}. 126

33. Measured ionization energies for GaN implanted at room temperature with 200 keV Si ions at doses ranging from $1x10^{13}$ to $5x10^{15}$ cm^{-2} and annealed at 1350 ^{o}C for 17 sec in a flowing nitrogen environment. 129

34. Measured ionization energies for GaN implanted at room temperature with 200 keV Si ions at a dose of $1x10^{13}$ cm^{-2} and annealed at 1350 ^{o}C for 17 sec along with unimplanted GaN annealed at 1300 ^{o}C for 9 sec in a flowing nitrogen environment. 131

35. Temperature-dependent Hall mobility taken from 10-800 K for GaN implanted at room temperature with 200 keV Si ions at doses ranging from $1x10^{13}$ to $5x10^{15}$ cm^{-2} and annealed at 1350 ^{o}C for 17 sec in a flowing nitrogen environment. 132

36. Temperature-dependent sheet resistivity taken from 10-800 K for GaN implanted at room temperature with 200 keV Si ions at doses ranging from $1x10^{13}$ to $5x10^{15}$ cm^{-2} and annealed at 1350 ^{o}C for 17 sec in a flowing nitrogen environment. 134

37. Measured ionization energies for GaN implanted at room temperature with 200 keV Si ions at a dose of $5x10^{14}$ cm^{-2} and annealed from 1100 to1350 ^{o}C for 5 min to 17 sec in a flowing nitrogen environment. 136

38. Temperature-dependent Hall mobility taken from 10-800 K for GaN implanted at room temperature with 200 keV Si ions at a dose of $5x10^{14}$ cm^{-2} and annealed from 1100 to1350 ^{o}C for 5 min to 17 sec in a flowing nitrogen environment..... 137

39. PL spectra taken at 3 K for unimplanted GaN as-grown and annealed at 1250, 1300, and 1350 ^{o}C from 9 to 17 sec in a flowing nitrogen environment. 139

40. PL spectra taken at 3 K for GaN implanted at room temperature with 200 keV Si ions at doses ranging from $1x10^{13}$ to $5x10^{15}$ cm^{-2} and annealed at 1350 ^{o}C for 17 sec in a flowing nitrogen environment..... 140

41. PL spectra taken at 3 K for GaN implanted at room temperature with 200 keV Ar ions at doses ranging from $1x10^{13}$ to $5x10^{15}$ cm^{-2} and annealed at 1350 ^{o}C for 22 sec in a flowing nitrogen environment..... 144

42. PL spectra taken at 3 K for GaN implanted at room temperature with 200 keV Si ions at a dose of $1x10^{13}$ cm^{-2} and annealed at 1250, 1300, and 1350 ^{o}C for approximately 20 sec in a flowing nitrogen environment. 145

43. Temperature-dependent PL spectra (3-300 K) from GaN implanted at room temperature with 200 keV Si ions at a dose of $5x10^{13}$ cm^{-2} and annealed at 1350 ^{o}C for 17 sec in a flowing nitrogen environment. 147

44. Room-temperature sheet electron concentrations for GaN implanted at 800 ^{o}C with 200 keV Si ions at doses ranging from $1x10^{13}$ to $5x10^{15}$ cm^{-2} and annealed at 1050 to 1350 ^{o}C from 5 min to 17 sec in a flowing nitrogen environment. 153

45. Electrical activation efficiency for GaN implanted at 800 ^{o}C with 200 keV Si ions at doses ranging from $1x10^{13}$ to $5x10^{15}$ cm^{-2} and annealed from 1050 to 1350 ^{o}C for 5 min to 17 sec in a flowing nitrogen environment..... 155

46. Sheet carrier concentration versus actual implanted dose for GaN implanted at 800 ^{o}C with 200 keV Si ions at doses ranging from $1x10^{13}$ to $5x10^{15}$ cm^{-2} and annealed at 1050 to 1350 ^{o}C from 5 min to 17 sec in a flowing nitrogen environment. 157

47. Room-temperature Hall mobility for GaN implanted at 800 ^{o}C with 200 keV Si ions at doses ranging from $1x10^{13}$ to $5x10^{15}$ cm^{-2} and annealed at 1050 to 1350 ^{o}C from 5 min to 17 sec in a flowing nitrogen environment. 158

48. Temperature-dependent sheet electron concentrations from 10-800 K for GaN implanted at 800 ^{o}C with 200 keV Si ions at doses ranging from $1x10^{13}$ to $5x10^{15}$ cm^{-2} and annealed at 1350 ^{o}C for 17 sec in a flowing nitrogen environment. 161

49. Measured ionization energies for GaN implanted at 800 ^{o}C with 200 keV Si ions at doses ranging from $1x10^{13}$ to $5x10^{15}$ cm^{-2} and annealed at 1350 ^{o}C for 17 sec in a flowing nitrogen environment..... 163

50. Temperature-dependent Hall mobility from 10-800 K for GaN implanted at 800 ^{o}C with 200 keV Si ions at doses ranging from $1x10^{13}$ to $5x10^{15}$ cm^{-2} and annealed at 1350 ^{o}C for 17 sec in a flowing nitrogen environment..... 164

51. Temperature-dependent sheet resistivity from 10-800 K for GaN implanted at 800 ^{o}C with 200 keV Si ions at doses ranging from $1x10^{13}$ to $5x10^{15}$ cm^{-2} and annealed at 1350 ^{o}C for 17 sec in a flowing nitrogen environment..... 166

52. PL spectra taken at 3 K for GaN implanted at 800 ^{o}C with 200 keV Si ions at doses ranging from $1x10^{13}$ to $5x10^{15}$ cm^{-2} and annealed at 1350 ^{o}C for 17 sec in a flowing nitrogen environment..... 168

53. PL spectra taken at 3 K for GaN implanted at 800 ^{o}C with 200 keV Ar ions at doses ranging from $1x10^{13}$ to $5x10^{15}$ cm^{-2} and annealed at 1350 ^{o}C for 22 sec in a flowing nitrogen environment..... 171

54. Temperature-dependent PL spectra (3-300 K) from GaN implanted at 800 ^{o}C with 200 keV Si at a dose of $5x10^{13}$ cm^{-2} and annealed at 1350 ^{o}C for 17 sec in a flowing nitrogen environment..... 172

55. Room-temperature sheet electron concentrations for GaN implanted at 25 and 800 ^{o}C with 200 keV Si ions at doses ranging from $5x10^{14}$ to $5x10^{15}$ cm^{-2} and annealed at 1050 to 1350 ^{o}C from 5 min to 17 sec in a flowing nitrogen environment. 174

56. Room-temperature Hall mobility for GaN implanted at 25 and 800 ^{o}C with 200 keV Si ions at doses ranging from $5x10^{14}$ to $5x10^{15}$ cm^{-2} and annealed at 1050 to 1350 ^{o}C from 5 min to 17 sec in a flowing nitrogen environment. 176

57. PL spectra taken at 3 K for GaN implanted at 25 and 800 ^{o}C with 200 keV Si ions at doses ranging from $1x10^{13}$ to $1x10^{14}$ cm^{-2} and annealed at 1350 ^{o}C for 17 sec in a flowing nitrogen environment..... 177

58. An empirical expression for the bandgap energy of GaN as a function of absolute temperature along with the associated graph of E_g versus T (Monemar, 1974). 198

List of Tables

Table Page

1. Comparison of Semiconductor Material Properties..... 2

2. Figures of merit for several semiconductor materials normalized to silicon..... 5

3. Acceptor Implantation and Anneal Conditions..... 97

4. Range of currents on acceptor implanted and annealed samples..... 100

5. Hall Effect Data for Mg+P-, Mg+Si-, Li-, Li+P-, and C-implanted GaN at 300 K..... 101

6. Room-Temperature Hall Effect Data for Si implanted into GaN at 25°C 123

7. Hall Effect Data for Si-implanted GaN at 25, 800, and 800 ^{o}C Corrected..... 156

8. Room-Temperature Hall Effect Data for Si implanted into GaN at 800 ^{o}C 160

Abstract

A comprehensive and systematic electrical activation study of Si-implanted gallium nitride (GaN) was performed as a function of ion implantation dose, anneal temperature, and implantation temperature. Additionally, acceptor-implanted GaN was also investigated. Temperature-dependent Hall effect measurements from 10-800 K and photoluminescence (PL) spectra taken from 3-300 K were used to characterize the samples. GaN wafers capped with 500 Å AlN were implanted at room temperature and at 800 ^{o}C with 200 keV Si ions at doses ranging from $1x10^{13}$ to $5x10^{15}$ cm^{-2} and annealed from 1050 to 1350 ^{o}C for 5 min to 17 sec in a flowing nitrogen environment.

Generally, the higher the Si dose, the greater the activation efficiency at any given anneal temperature. The optimum anneal temperature for samples implanted with higher doses ($\geq 1x10^{15}$ cm^{-2}) is around 1350 ^{o}C, exhibiting nearly 100% electrical activation efficiency. Even the sample implanted with the lowest dose of $1x10^{13}$ cm^{-2} shows an electrical activation of 40% after annealing at 1350 ^{o}C. The mobilities and carrier concentrations increase with anneal temperature for every dose in spite of the increased ionized impurity scattering from an increased number of active donors. The highest room-temperature mobility is 250 $cm^2/V{\cdot}s$ on the sample implanted at room temperature with a dose of $1x10^{13}$ cm^{-2} after annealing at 1350 ^{o}C. Even the sample implanted at 800 ^{o}C with the highest dose of $5x10^{15}$ cm^{-2} had a room-temperature mobility of 105 $cm^2/V{\cdot}s$ after annealing at 1300 ^{o}C. The data show that Si implantation at 800 ^{o}C did not offer decisive advantages over implantation at room temperature.

PL spectra measured as a function of anneal temperature showed that Si implantation damage was almost completely recovered after annealing at 1350 ^{o}C. Also,

temperature-dependent PL spectra revealed that the yellow luminescence (YL) plaguing nearly all Si-doped GaN is not caused by a shallow Si donor, but rather a much deeper level. Samples implanted with Si at both room temperature and 800 ^{o}C show that the 3.29 eV donor-to-acceptor pair (DAP) peak, which is widely believed to involve a shallow donor, thermally quenches much more rapidly than the 2.2 eV YL band.

Additionally, GaN wafers capped with 500 Å AlN were implanted at 25, 500, and at 800 ^{o}C with Mg, Mg+Si, Mg+C, Mg+P, Mg+O, C, Li, and Li+P at doses ranging from $1x10^{14}$ to $5x10^{15}$ cm^{-2} and annealed from 1100 to 1350 ^{o}C. All of the Mg-implanted and most of the Mg-coimplanted GaN samples became extremely resistive, and did not show definite *p*-type conductivity even after annealing at 1350 ^{o}C. Furthermore, the samples did not show any *p*-type conductivity and remained highly resistive even at a sample temperature as high as 800 K. A dominant 2.36 eV green luminescence (GL) band observed in the PL spectra of all Mg implanted samples is attributed to a deep DAP transition with at least one level caused by a Mg-related complex. These Mg-related deep complexes, which form independent of the various coimplants or the implantation temperature, remain thermally stable even at anneal temperatures as high as 1350 ^{o}C, and are mainly responsible for the inefficient electrical activation of Mg acceptors implanted into GaN.

ELECTRICAL ACTIVATION STUDIES OF ION IMPLANTED GALLIUM NITRIDE

I. Introduction

High-temperature, High-power, High-frequency, and High-radiation Electronics

Electronic devices find applications seemingly everywhere. Where they are used and how well they perform depend not only on their design (e.g., geometry and fabrication process), but primarily on the fundamental material properties of the semiconductors from which they are fabricated. The material workhorse of the electronics industry is unquestionably silicon. The preeminence of silicon is due to its abundance (i.e., the raw material is inexpensive), excellent general-purpose material properties, and processing maturity. Since the early 1950s, researchers and manufacturers have been growing and fabricating devices with silicon so that virtually all aspects of material physics and device processing are fully understood and exploited. Currently, ultra pure silicon ingots (impurity concentrations < 10^{12} cm^{-3}) are grown 300 mm (12") in diameter with ultra low defects ~ 1 cm^{-2} (Dreike *et. al.*, 1994). Although the ground floor of the electronics industry was forged with silicon, in many key applications silicon has fundamental limitations imposed by its material properties. Silicon is unable to meet the ever-increasing demands of high-temperature, high-power, high-frequency, and high-radiation electronics. The material properties of several common semiconductors are shown in Table 1.

Table 1. Comparison of Semiconductor Material Properties

Property	Si	GaAs	InP	4H-SiC	GaN	Diamond
Bandgap at 300 K (eV)	1.12 (I)	1.424 (D)	1.344 (D)	3.26 (I)	3.44 (D)	5.47 (I)
Dielectric constant	11.7 (dc)	13.2 (dc) 10.9 (∞)	12.4 (dc) 9.66 (∞)	9.6 (dc) 6.7 (∞)	8.9 (dc) 5.35 (∞)	5.57 (dc)
Thermal expansion ($x10^{-6}$ K·Δa/a)	2.56	6.86	4.5	4.2	5.59	0.08
Lattice constant (Å)	5.431	5.653	5.869	3.073 (a) 10.05 (c)	3.189 (a) 5.185 (c)	3.567
m_c^*/m_o	1.18	0.063	0.077	-	0.22	0.2
m_v^*/m_o	0.81	0.53	0.64	-	0.8	0.25
Bulk Mobility Electron Hole	 1450 500	 8500 400	 4600 150	 1140 50	 900 150	 2200 1600
Saturation velocity ($x10^7$ cm/sec)	1.0	1.0	-	2.0	2.5	2.7
Breakdown field (MV/cm)	0.3	0.4	-	3	5	10
Thermal conductivity (W/cm·K)	1.5	0.46	0.68	4.9	1.3	22
Melting Point (^oC)	1412	1238	1070	Sublimes T > 1827	Sublimes T > 1300	3826

An electronic device operating in a high-temperature regime fails when it no longer functions as designed. There are several likely failure mechanisms: electromigration of conductors, interdiffusion of contacts, corrosion, thermally induced stress, and extrinsic to intrinsic conversion. The latter occurs when the intrinsic carrier concentration becomes comparable to or exceeds the extrinsic concentration, resulting in excessive reverse-biased *p-n* junction leakage currents, threshold voltage shifts, or latchup. Leakage currents limit Si device operation to under 300 ^oC, and to under 200 ^oC in some device designs. Although silicon-on-insulator (SOI) technology greatly reduces

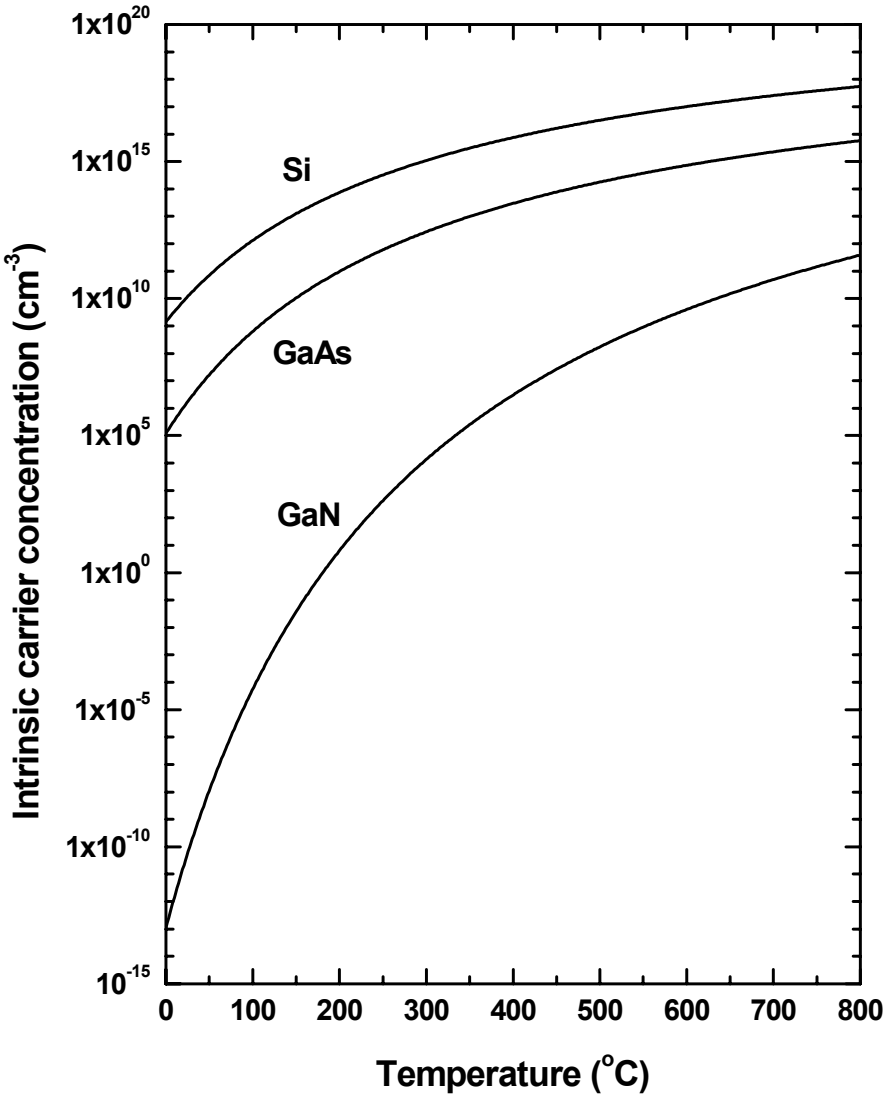

Figure 1. Intrinsic carrier concentration for Si, GaAs, and GaN as a function of temperature.

junction leakage, SOI devices are still limited to 300 ^{o}C operation. Figure 1 shows the intrinsic carrier concentration for Si, GaAs, and GaN as a function of temperature. Even at 800 ^{o}C, the intrinsic carrier concentration of GaN remains several orders of magnitude below that of either Si or GaAs as well as far below the typical doping concentrations of *n*- and *p*-regions in semiconductor devices.

The ambient temperature range over which many electronic devices are rated to operate is –55 to 125 ^{o}C. This range originated from an obsolete MIL-STD that attempted to encompass the temperature range that a generic electronic component would likely see in worldwide combat. However, many potential military as well as non-military applications call for electronic components to operate reliably at temperatures exceeding 125 ^{o}C. Such applications involve placing sensors and controlling electronics within harsh or caustic environments not only to improve the accuracy of the data collected, but to make the system lighter and the control process faster and more accurate. The control process would include signal amplification, conditioning, processing, and actuating. The following are applications requiring high-temperature electronics: drilling heads for oil, gas, and geothermal exploration, automotive and aerospace engines, heavy equipment, heavy vehicle anti-lock brakes, nuclear and space environments, distributed control systems, power systems, phased array radars, and conformal electronics on aircraft skins.

To meet these demands device designers are always searching for the optimum material. Fifteen years ago, GaAs and InP were considered immature and novel material technologies. But GaAs and InP have several material properties that give them an advantage over silicon in some applications, and today both of these materials are mature with widespread commercial devices satisfying high-performance military and commercial requirements. To assist in the selection of the best material for a given application, device designers have derived certain figures of merit (FOM). These FOM are calculated from the semiconductor material properties that have the largest impact on device performance.

There are four common FOM stressing performance in different applications; however, in each case the larger the FOM value, the greater the expected device performance. The Johnson FOM (JFOM) provides an indication of which materials are best for power amplifiers. The Keyes FOM (KFOM) emphasizes materials for high-speed digital integrated circuits. The Baliga FOM (BFOM) identifies which materials are best in minimizing conduction power losses in lower-frequency, high-power switching systems, whereas the Baliga high-frequency FOM (BHFFOM) indicates the best material for high-frequency power systems where switching losses due to the charging and discharging of input capacitance dominates. These FOM reveal that the critical field (i.e., dielectric strength), saturation velocity, mobility, energy bandgap, thermal conductivity, and dielectric constant are the best predictors of device performance in extreme applications. Table 2 compares these FOM normalized to silicon for several conventional and wide bandgap semiconductors (Chow and Tyagi, 1994).

Table 2. Figures of merit for several semiconductor materials normalized to silicon

	Si	InP	GaP	GaAs	GaN	6H-SiC	4H-SiC
JFOM	1.0	13	37	11	790	260	410
KFOM	1.0	0.72	0.73	0.45	1.8	5.1	5.1
BFOM	1.0	10	16	28	910	90	290
BHFFOM	1.0	6.6	3.8	16	100	13	34

Wide Bandgap Semiconductors

Wide bandgap semiconductors (WBG) possess several material properties that allow them to outperform conventional semiconductors in many extreme applications. Many of the attractive intrinsic material properties of WBG are physically related to the wide bandgap. The most obvious is their ability to operate at much higher temperatures

before becoming intrinsic or suffering from thermally generated leakage current. Generally, WBG have higher thermal conductivities that allow them to quickly dissipate junction heat and thus function more efficiently and reliably in high-temperature, high-power density device applications. The ambient temperature in which any electrical device works is generally much cooler than the actual temperature of the device due to internal power losses and current density induced self-heating. This concept is universally evident in the importance of heat sinks and adequate cooling air for silicon CMOS digital processors operating at 500 MHz to 1.5 GHz even in air-conditioned offices. As a result of their wider bandgaps, WBG have higher breakdown fields ($V_{br} \propto E_g^{3/2}$), i.e., the maximum internal electric field strength before the onset of junction breakdown. This allows WBG to operate as high-power amplifiers, switches, or diodes. The high breakdown field also allows further device miniturization beyond what is possible with conventional semiconductors, because the internal fields increase linearly as device dimensions become smaller. Another intrinsic material property that can be related to the bandgap is the dielectric constant. The dielectric constant of a non-metallic crystal is a measure of how well the material's internal charge distribution can be displaced or polarized in the presence of a macroscopic electric field. The lower high-frequency dielectric constant of WBG reduces device parasitic capacitance allowing more efficient operation as RF and millimeter-wave amplifiers. The higher saturation velocities of WBG also allow them to operate at higher-frequencies than their conventional cousins. Due to the larger cohesion energies of their constituent atoms, WBG are chemically robust materials, less vulnerable to attack in caustic environments, and more resistant to radiation damage. The inert nature of WBG makes them less

susceptible to unwanted impurity in-diffusion, as well as dopant out-diffusion and redistribution that would otherwise degrade device reliability and performance.

Gallium Nitride

Currently, GaN is one of the most widely studied semiconductors for advanced electrical and optical device applications due to its outstanding material properties as seen in Table 1. Though still in their infancy, the group III-nitrides, particularly GaN, have experienced rapid progress in material growth, processing, and device technology over the past decade. As experienced with most semiconductors however, initial progress was slow. In 1932, GaN was synthesized in powder form, and in 1938 small needles of GaN were synthesized. Not until 1969 was GaN first grown on a sapphire substrate using hydride vapor phase epitaxy (HVPE). Two years later GaN was grown epitaxially via metal-organic chemical vapor deposition (MOCVD), and in 1974 by molecular beam epitaxy (MBE). Epitaxial layer quality through the 1970s and much of the 1980s was rather poor due to the lack of a lattice-matched substrate. These early epilayers were always unintentionally doped *n*-type ($n \geq 1\text{x}10^{17}$ cm^{-3}), resulting from growth defects or impurities inadvertently introduced during growth (Monemar, 1998; Pearton *et. al.*, 1999; Jain *et. al.*, 2000). Epilayer quality began to improve through the use of a two-step growth method developed by Yoshida *et. al*. in 1983 (Yoshida *et. al*.,1983). By first growing a thin AlN buffer layer on the sapphire substrate, most of the mismatch-induced dislocations are confined to a thin AlN/GaN interfacial region rather than throughout the GaN epilayer. Despite the progress in GaN epilayer quality, material doped with acceptors remained at best highly resistive until 1989 when Amano *et. al*. produced *p*-

type GaN via low energy electron beam irradiation (LEEBI) of Mg-doped GaN (Amano *et. al*., 1989). The energy provided by the electron beam depassivated the Mg acceptors by breaking the Mg—H bonds formed during MOCVD growth. Presently, the same effect is more commonly achieved via thermal annealing around 800 ^{o}C.

Today, GaN epilayers are almost entirely grown on either 2" sapphire (β-Al_2O_3) or 6H-SiC substrates. Sapphire wafers are much less expensive and are insulating. SiC, however, has a much better lattice match to GaN (3.5% mismatch versus 13% mismatch for sapphire) and is about ten times more thermally conductive than sapphire, which is important for high-power device applications. Currently, the largest difference between GaN grown on sapphire or SiC substrates is the threading dislocation concentration of either ~$2x10^9$ cm^{-2} or ~$5x10^8$ cm^{-2} s, respectively, due primarily to lattice mismatch (Eastman *et. al.* 2001). Although intense research efforts are underway to develop a practical technique for bulk growth of GaN, MOCVD and MBE are the main techniques for most GaN layers. Due to it's slight advantage in maturity, MOCVD is more popular for group III-nitride growth with an optimum growth temperature for GaN around 1050 ^{o}C and typical growth rate of about 2 μm/hour. The best MBE processes typically use NH_3 as the nitrogen source at a growth temperature of 900-1000 ^{o}C and a growth rate of 1 μm/hour. Two techniques receiving increased attention are HVPE and epitaxial lateral overgrowth (ELOG). The growth rate of HVPE is typically 10 μm/hour allowing for not only thick epilayers, but lower dislocation density free-standing thick GaN layers after the substrate has been removed. During ELOG of GaN, thin strips of SiO_2 are patterned on a GaN buffer layer. GaN growth continues selectively on the GaN buffer layer then laterally over the SiO_2 strips. When the SiO_2 mask has been overgrown, the GaN over

the SiO_2 has a much lower dislocation density (Monemar, 1999). The ELOG technique was used to demonstrate Nichia's 10,000 hour blue laser diode in 1997.

Despite commercially available blue LEDs and laser diodes, GaN material and device technology lags several years behind its main WBG competitor, SiC. Recently, CREE announced commercially available 3" *n*-type 4H- and 6H-SiC substrates (2001). However, GaN can offer a much greater potential than SiC for some advanced high-performance electrical devices as seen in the FOM comparisons of Table 2. Additionally, the group III-nitride family possessing direct bandgaps from 1.9-6.2 eV presents an abundance of ternary heterostructures for novel electrical and optical devices. In addition to laser and light-emitting diodes, a wide variety of electronic devices have already been fabricated using GaN: heterojunction field effect transistors (HFETs), heterojunction bipolar transistors (HBTs), and high electron mobility transistors (HEMTs) (Ohno and Kuzuhara, 2001; McCarthy *et. al.*, 2001; Wu *et. al.*, 2001).

Many such devices fabricated with the more mature GaAs material system enjoy widespread use throughout the military and commercial sectors. The success of GaAs is due largely to a coordinated research and development effort called the GaAs microwave and millimeter-wave monolithic integrated circuit (MIMIC) program begun in 1987. Although there exists an enormous GaAs manufacturing infrastructure, GaAs integrated circuits can no longer meet the advancing requirements of tomorrow's weapon systems (Dixon, 2001). Clearly, electronics is a dominant force multiplier in these weapon systems, whose requirements are driven by affordability and operational superiority. The Department of Defense 2001 Basic Research Plan stresses the need for wide-bandgap semiconductor research to satisfy critical requirements in communications, ultraviolet

detectors, high-temperature engine controls, as well as high-power/high-frequency radars for target tracking, acquisition, and fire-control.

In spite of GaN's many advantages, the fabrication of successful devices must still overcome some important problems such as efficient doping and selected area doping. Since the group-III nitrides are very chemically inert, thermal diffusion doping in these materials is impractical due to the extremely low diffusivity of impurity species. In addition to *in-situ* doping of GaN during crystal growth, an alternative method of doping GaN is by ion implantation. Although this doping technique has many advantages including independent control of the doping level, selective area doping, and the ability of fabricating planar devices and self-aligned structures, one of the major problems associated with this technique is the need to anneal out the implantation damage-related crystalline defects, and electrically activate the implanted ions. Although ion implantation has become a mature technology for Si and GaAs doping, the technique is less well developed for GaN. This research effort has performed a comprehensive and systematic electrical activation study of Si-implanted GaN as a function of ion implantation dose, anneal temperature, and implantation temperature. Additionally, acceptor-implanted GaN was investigated. Both objectives were pursued with a goal to increase understanding of the implant activation process, and the defect levels associated with this process so that ion-implanted GaN can be exploited in advanced electrical and optical device applications.

II. Semiconductors, Energy Bands, and Impurities

Historical Perspectives

In 2001, the world has become virtually dependent on personal computers, the Internet, cellular phones, compact disks (CDs), personal digital assistants (PDAs), laptops, notebooks, digital versatile disks (DVDs), and MP3 players for information, business, and recreation. None of these seemingly indispensable items would exist if it were not, in part, for the underlying fundamental research in solid-state physics, and specifically semiconductor materials.

Research in semiconductors was evident as early as 1833 when Michael Faraday discovered the semiconducting properties of silver sulfide (Ag_2S). Although Ferdinand Braun's invention of the solid-state rectifier using a point contact to lead sulfide (PbS) occurred 30 years before John Fleming's invention of the vacuum tube diode, early complex electrical machines were made using vacuum tube technology. Vacuum tube technology dominated electronics largely due to a lack of understanding of solids. In the 1920s, the theory of quantum mechanics was developed, which lead to a more comprehensive understanding of the electronic band structure of metals, insulators, and semiconductors. Driven by the insights afforded by quantum mechanics, research in semiconductors lead to the historic invention of the point-contact bipolar junction transistor in 1947 by the Bell Lab team of William Shockley, Walter Brattain, and John Bardeen. The implications of a solid-state transistor were so enormous to communications and radar technology that the military considered classifying the Bell Lab discovery as top secret (Brinkman *et. al.*, 1997; Barbour).

In the quest to control electrical information at higher frequencies, solid-state transistors gradually supplanted vacuum tubes. Since 1947, continual research has been critical to understanding the structural, electrical and optical properties of various semiconductor materials and in exploiting these properties in a host of novel electronic devices. Currently, electronic devices are found in everything from a simple toaster, to worldwide communication systems, to cutting edge military weapon systems. What accounts for the prevalence of semiconductor materials in our world today is our ability to accurately and reliably control their electrical and optical properties. The remainder of this chapter provides a brief background on the theory of semiconductors including periodic potentials, energy bands, and carrier concentrations.

Crystal Structure

In 1913, the science of X-ray crystallography was founded by a father and son, both named William Bragg. Their work on X-ray diffraction provided the first empirical evidence on how atoms are arranged in solids. A Bravais lattice is an infinite array of discrete points that appears the same when viewed from any of these points. There are 14 unique Bravais lattices and 7 crystal symmetry groups that fully describe the 3-dimensional geometry of the periodic arrays of all crystalline solids. Nearly all semiconductors crystallize in either the cubic or hexagonal symmetry groups. The zincblende structure is comprised of two interpenetrating face-centered cubic Bravais lattices as found in many III-V semiconductor compounds containing Ga or In, along with P, As, or Sb. The wurtzite structure is comprised of two interpenetrating hexagonal Bravais lattices common in many II-VI semiconductor compounds containing Zn or Cd,

along with S, Se, or Te. The zincblende and wurtzite structures are shown in Figure 2. Interestingly, both structures are based on tetrahedral bonding; the only difference is that in wurtzite structures alternating planes of tetrahedra are mirror images of each other, while in zincblende structures alternating planes of tetrahedra are rotated 60°. In addition to their structure, crystalline solids are further characterized by their lattice constants that define the size of their unit cell. When the unit cell is repeated in real space, the macroscopic crystal is generated. A unit cell possessing cubic symmetry, such as that shown in Figure 2 (a), has a single lattice constant, *a*, whereas a hexagonal unit cell is described by two orthogonal lattice constants, *a* and *c*. Closely matching the lattice constants in the growth plane of two semiconductors is important when one semiconductor is heteroepitaxially grown on another.

Crystal Growth

Most bulk semiconductor single crystals are grown under strict thermodynamic equilibrium conditions where high purity sources of the constituent atoms are made to crystallize by bringing them together at a certain temperature and pressure, then allowing them to cool at a precise rate. The resulting bulk crystals are then cut into thin wafers and polished for further processing. Generally, semiconductor devices are fabricated from thin layers, on the order of microns, of single crystal semiconductors that are epitaxially grown on these bulk substrate wafers. The surface of the substrate wafer serves as a crystal template when growing the epitaxial layers. Although epitaxial layers nearly always possess the same crystal structure as the substrate, their lattice constants can differ significantly, (i.e., greater than 10%). During growth, the epitaxial layer will

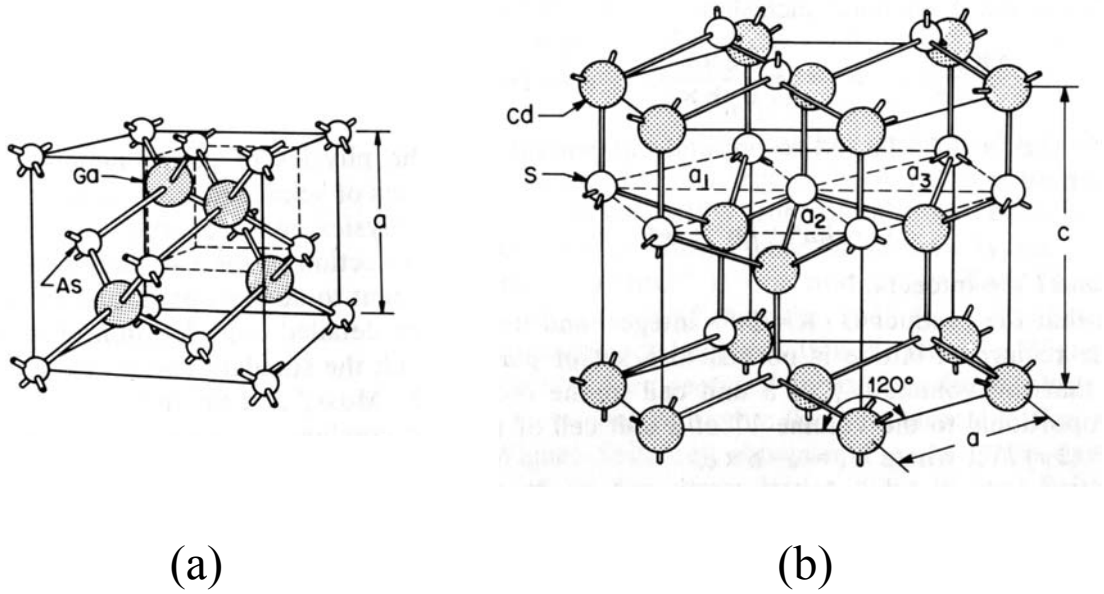

Figure 2. Semiconductor crystal unit cells: (a) cubic symmetry represented by zincblende GaAs with lattice constant *a*, and (b) hexagonal symmetry represented by wurtzite CdS with lattice constants *a* and *c* (Sze, 1981:8,9).

experience biaxial compressive or tensile strain proportional to the extent of lattice mismatch. As the growth continues, there exists a critical thickness dependent on both the lattice mismatch and the material, below which the minimum energy state of the heteroepitaxial system is achieved by strain. Such an epitaxial layer is called pseudomorphic as it assumes the lattice constant of the substrate. Above this critical thickness, energy is minimized by the formation of dislocation lines that can act as free carrier recombination centers or electrically active levels within the bandgap of the epitaxial device layer (Bhattacharya, 1994:21-25). Exploiting semiconductor material properties to optimize electrical and optical device performance requires an understanding of energy band structure.

Energy Bands

All crystalline solids can be classified by their conductivity as metals, insulators, or semiconductors. The conductivity of all such materials is fundamentally dependent on the interrelationships and occupancy of their electronic energy levels or bands. The electronic energy levels of individual atoms quantify how tightly each of the atom's electrons is held in position around the nucleus. The inner or core electrons are very tightly bound and thus have large binding energies, whereas the outer or valence electrons, due to the screening effects of the core electrons, are held less tightly. When atoms bond to form crystalline solids, the discrete electronic energy levels of the individual atoms spread out into bands of levels. Because electrons are fermions, no two electrons can occupy the same exact energy level, thus a band of energies is needed to hold all the electrons from a particular atomic orbital when a macroscopic solid is formed.

In addition to responding to the multitude of other electrons in a solid by forming energy bands, the electrons also respond to the periodic potential resulting from each atom in the solid residing at a crystal lattice position. Each individual electron in the crystal senses the coulombic attractive force exerted on it by each of the positively charged ion cores. The interaction of the electrons with this periodic potential determines the set of energy levels that the electrons can occupy. Due to the difficulties in solving a problem involving so many electrons and ion cores, the energy levels of a macroscopic solid cannot be analytically determined; however, quantum mechanics allows us to approximate these energy bands to a reasonable degree of accuracy.

The simplest and perhaps most important case to consider is that of a free electron which experiences no potential either from other electrons or ion cores. The energy levels that a single free electron can occupy are exactly determined by solving Shrödinger's wave equation

$$H\psi(\mathbf{r}) = \left[-\frac{\hbar}{2m_o} \nabla^2 + U(\mathbf{r}) \right] \psi(\mathbf{r}) = E\psi(\mathbf{r}) \tag{1}$$

with the periodic potential, $U(\mathbf{r})$, identically zero. H is the Hamiltonian operator, $\psi(\mathbf{r})$ is the single electron wave function, $\hbar$ is the reduced Plank constant, m_o is the electron's mass, and E is the energy of the electron. The solutions to this equation are plane waves of the form

$$\psi_k(\mathbf{r}) = e^{i\mathbf{k}\cdot\mathbf{r}}, \tag{2}$$

where $\mathbf{k}$ is the electron's wave vector and $\mathbf{r}$ is the positional vector. The eigenvalues corresponding to the eigenstates of equation (2) are then

$$E = \frac{\hbar^2 k^2}{2m_o}. \tag{3}$$

Clearly, the dispersion relation describing the free electron's energy in one-dimensional k-space is a parabola, and in 3-D k-space is spherical. In an actual crystalline solid, none of the electrons is truly free; however, due to the screening effect of the core electrons on each nucleus, the valence electrons can be considered nearly free, or under the influence of only a weak periodic potential. The allowed values of k are thus dependent on the periodicity of the crystal lattice. Considering many nearly free electrons in a crystal, there are multiple reciprocal lattice vectors, $\mathbf{K}$, in 3-D k-space at which point the corresponding energies of multiple bands are equivalent and therefore

degenerate. In the presence of a weak periodic potential, the actual allowed electron energy values, E, will differ from the free electron values as a function of the periodic potential, U. In an actual crystal, a range of energies surrounding the degenerate values will be shifted by an amount on the order of U from the free electron energy values. This shifting of the energy bands in k-space occurs near Bragg planes, or planes of crystal symmetry. As one approaches a Bragg plane in k-space, the higher energies are shifted up and the lower energies are shifted down. This shifting produces an energy bandgap, or forbidden region, whose magnitude is determined by the periodic potential of the crystal lattice (Ashcroft and Mermin, 1976:155). Figure 3 shows the energy band structure of GaN in k-space. The letter ordinates in Fig. 3 represent points of symmetry within the first Brillouin zone of the hexagonal symmetry group. The $E(k)$ dispersion relation for GaN is mapped for directions of high-symmetry is this band diagram. The Brillouin zone center is always the Γ point as shown in Figure 4.

The classification of crystalline solids as metals, insulators, or semiconductors is universally based on the magnitude of this energy bandgap. In metals, the metallic bonding results in an appreciable density of electrons in the regions between the ion cores. This density is likely to cause broad energy bands and appreciable band overlap in k-space. When an energy band fully populated with electrons overlaps with an empty or partially full band, conduction readily occurs because there are many unoccupied states to which an electron can move. In I-VII ionic solids, a full and stable ns^2np^6 shell configuration is achieved; there are no loosely held valence electrons, and there is a large periodic potential due to the highly ionic nature of the crystal. Consequently, there is a large energy bandgap between the highest occupied band and lowest unoccupied band so

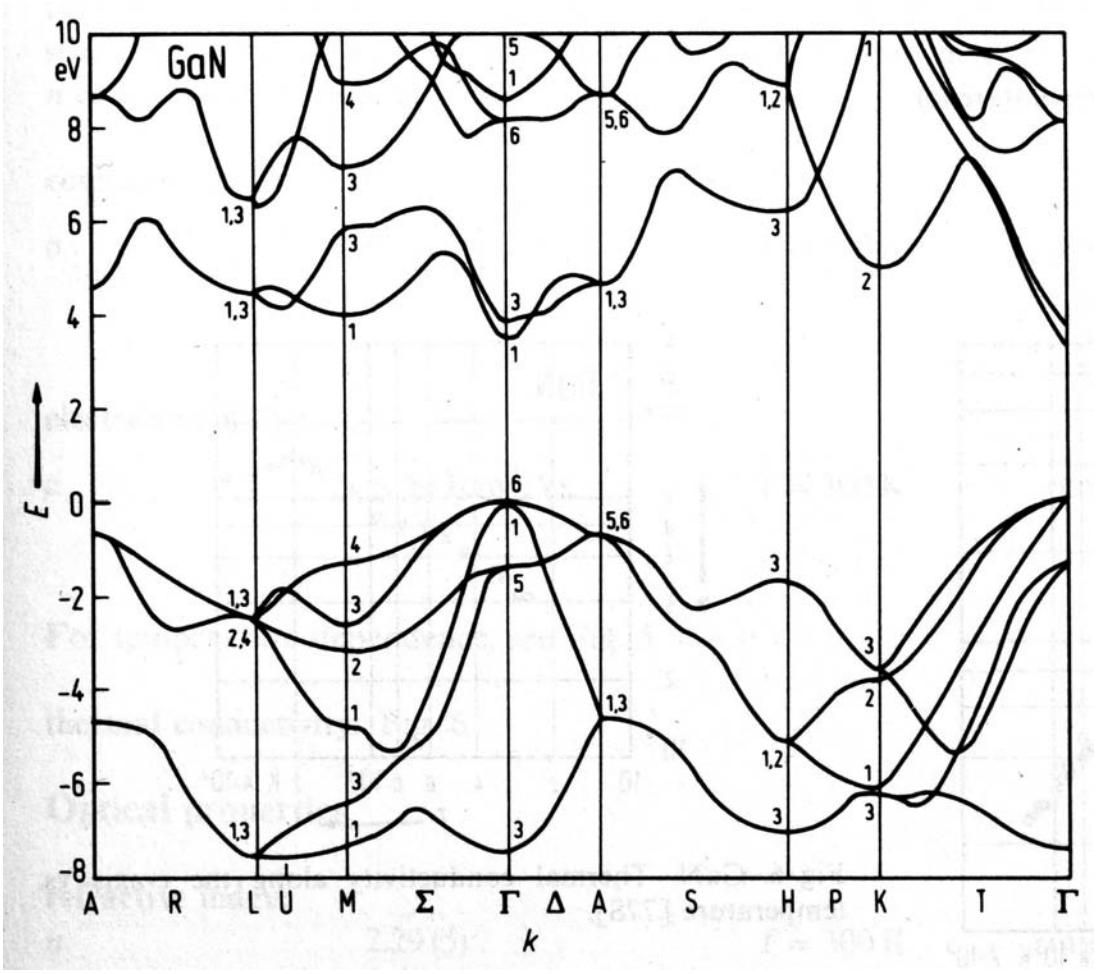

Figure 3. Energy band structure of wurtzite GaN in k-space showing various points of crystal symmetry and a direct bandgap at the Γ point (Madelung, 1996:87).

that a large amount of energy must be provided for conduction to occur. Insulators are solids in which the bandgap is on the order of 6 eV or greater.

Semiconductors are solids in which the bandgap ranges from the order of few meV to greater than 3 eV. Such solids include crystals of II-VI (e.g., ZnS, CdTe), III-V (e.g., $Al_xGa_{1-x}As$, InP), and IV-IV (SiC, $Si_{1-x}Ge_x$) compounds that have an increasingly covalent nature, with group IV elemental crystals being perfectly covalent. In each case,

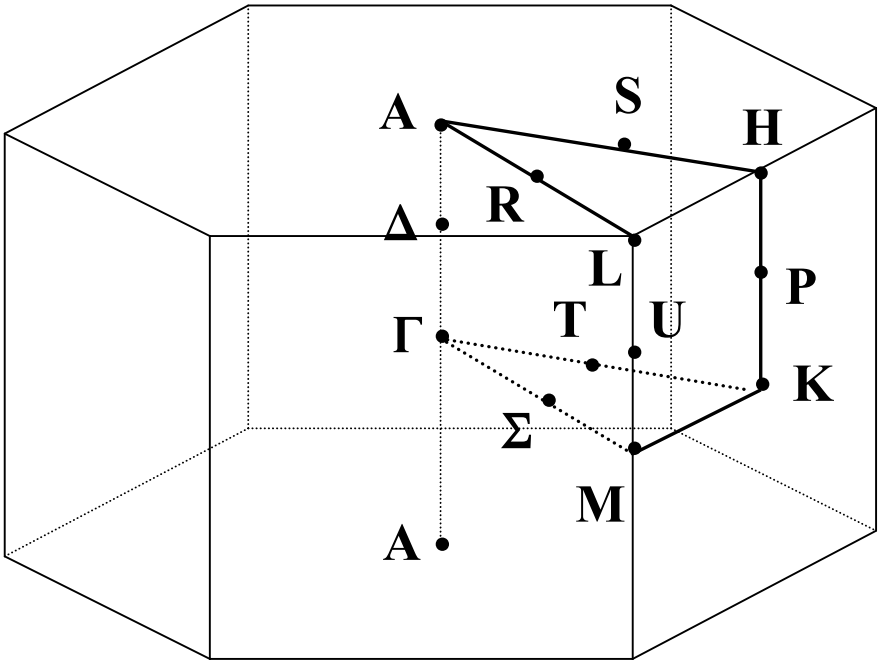

Figure 4. Hexagonal crystal structure showing points and directions of high-symmetry.

a full and stable ns^2np^6 shell configuration is achieved, but only via an increased electron density along covalent bond directions. In II-VI and III-V compounds the difference in electronegativities between the anion and cation is a general measure of the ionicity of the bonding with the more ionic compounds having larger energy bandgaps. Because there exists such a wide range of energy bandgaps in semiconductors, this classification is often further broken down into narrow bandgap and wide bandgap semiconductors. Narrow bandgap semiconductors (e.g., $Hg_{1-x}Cd_xTe$, InSb) have energy gaps less than 1 eV and have received widespread use as infrared detectors. Wide bandgap semiconductors (e.g., GaN, SiC) are those with bandgaps larger than about 2.2 eV, and are advantageous as blue-ultraviolet LEDs/lasers or ultraviolet detectors.

Regardless of the magnitude of their bandgaps, all pure semiconductors are insulators at absolute zero temperature. The highest occupied band (valence band) is full and the band just above the bandgap (conduction band) is completely empty. In addition to the magnitude of their bandgaps, another important characteristic of all semiconductors is whether their bandgap is direct or indirect. A direct bandgap semiconductor is one in which the valence band maxima and the conduction band minima occur at the same point in k-space, $k = 0$. In an indirect bandgap, the conduction band minima occur at $k \neq 0$. In these semiconductors, all energy transitions across the bandgap must be accompanied by a quanta of lattice vibration (i.e., a phonon) due to the requirement for conservation of crystal momentum, $\hbar\mathbf{k}$. One of the more significant implications is that lasers cannot be fabricated from indirect semiconductors. Figure 5 shows the relationship between bandgap energy and lattice constant for several direct and indirect semiconductors that crystallize in either the cubic or hexagonal structures. Also identified in this figure is the wavelength of the minimum energy photon required to excite an electron across the bandgap. The majority of semiconductors can absorb photons from the visible portion of the electromagnetic spectrum, while the wide bandgaps are transparent to visible light.

Due to the periodic potential of the semiconductor lattice, electrons (or holes) are not truly free and their real momentum is not a constant of motion, as is the crystal momentum. Knowing that the time rate of change of crystal momentum equals the force on the electron, $-e\mathbf{E}$, where e is the elementary charge, and $\mathbf{E}$ is the electric field vector, one can easily derive an expression for the effective mass of an electron (or hole) in the conduction (or valence) band (McKelvey, 1966:218):

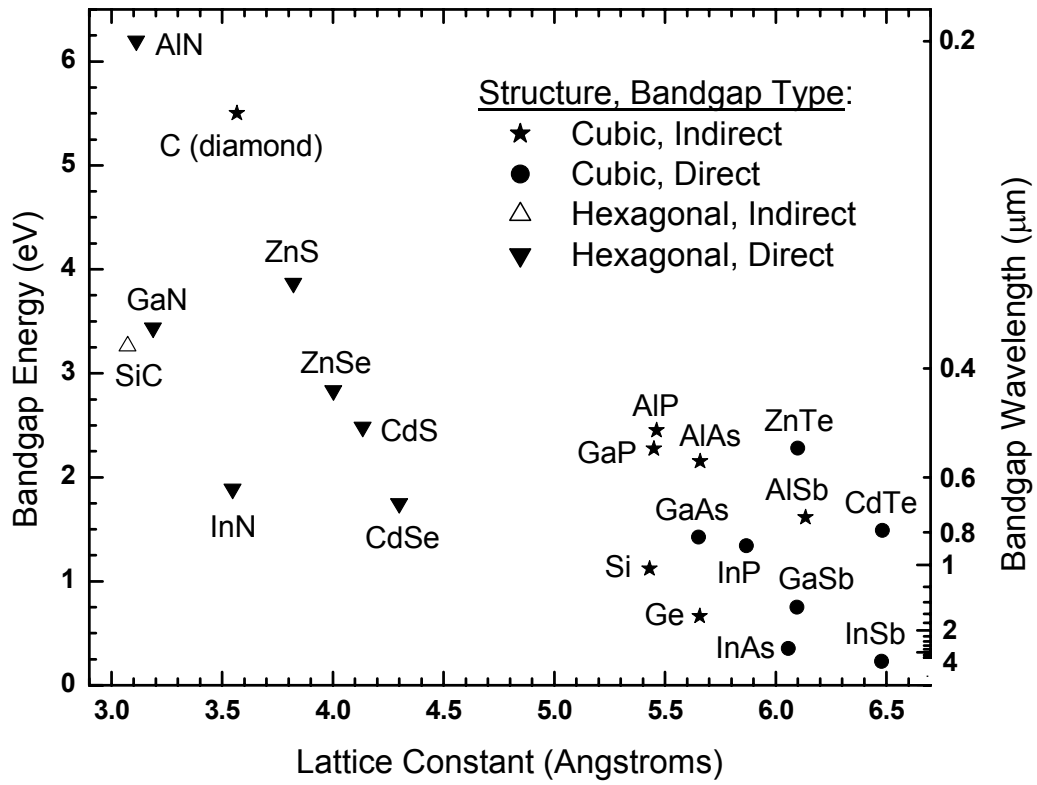

Figure 5. Bandgap energy and bandgap wavelength versus lattice constant for several direct and indirect semiconductors that crystallize in either the cubic or hexagonal structures.

$$m_{c,v}^{*} = \hbar^2 \left[\frac{d^2 E_{c,v}}{dk^2} \right]^{-1} . \tag{4}$$

The effective mass of an electron, seen here to be proportional to the inverse curvature of the conduction band dispersion relation, is generally less than the rest mass of an electron.

Semiconductor Statistics

An important expression in semiconductor statistics is the density of energy states per unit energy and unit volume of *k*-space. Due to the Heisenberg uncertainty principle,

$\Delta x \Delta p \geq h$, where x is position, p is momentum, and h is Plank's constant, the smallest volume of phase space (i.e., $(\Delta x \Delta k)^3$) is $8\pi^3$. Within this volume only one discrete value of wave vector exists, and therefore only one energy level; however, accounting for spin degeneracy, the volume of a single electron energy level is $4\pi^3$. (Schubert, p81, 1993) Qualitatively, the greatest density of energy states per unit energy will be inversely proportional to the slope of the $E(k)$ dispersion relation. Because the constant energy surfaces for $k \approx 0$ are spherical, one can use the dispersion relation of equation (3). An expression for the density of energy states in the conduction or valence band is given by

$$g_{c,v}(E) = \frac{1}{4\pi^3} \int_{Surface} \frac{ds}{\nabla_k E(k)} = \frac{\sqrt{2\left|E - E_{c,v}\right|}}{\pi^2 \hbar^3} (m_{c,v}{}^*)^{3/2} , \tag{5}$$

where the integral is performed over a constant energy surface in k-space, and $E_{c,v}$ are the energies of the conduction band minima and valence band maxima, respectively.

The number of electrons occupying energy states in the conduction band is then given by

$$n(T) = \int_{E_c}^{\infty} g(E) f(E) dE , \tag{6}$$

where $f(E)$ is the Fermi-Dirac distribution function given by

$$f(E) = \frac{1}{\exp\left[\dfrac{E - E_F}{k_B T}\right] + 1} . \tag{7}$$

Here E_F is the Fermi energy, k_B is Boltzmann's constant, and T is absolute temperature. When E_F is generally $3k_BT$ or more lower than E_c (i.e., non-degenerate), the Fermi-Dirac distribution may be adequately approximated by the much simpler Maxwell-Boltzmann

distribution: $f_{MB} = \exp[-(E - E_F)/k_B T]$. Using the Maxwell-Boltzmann approximation to solve the integral of equation (6), one obtains

$$n(T) = \frac{1}{\sqrt{2}}\left[\frac{m_c^* k_B T}{\pi\hbar^2}\right]^{\frac{3}{2}} \exp\left[\frac{-(E_c - E_F)}{k_B T}\right]. \tag{8}$$

The pre-exponential factor in equation (8) is known as the effective density of states in the conduction band and represents an upper limit on the volume concentration of conduction electrons in a non-degenerate semiconductor. (McKelvey, 1966:265; Schubert, 1993:81; Ashcroft and Mermin, 1976:574). A similar derivation provides the concentration of holes in the valence band,

$$p(T) = \frac{1}{\sqrt{2}}\left[\frac{m_v^* k_B T}{\pi\hbar^2}\right]^{\frac{3}{2}} \exp\left[\frac{-(E_F - E_v)}{k_B T}\right], \tag{9}$$

which can then be used to calculate the intrinsic carrier concentration given by

$$n_i(T) = \sqrt{n(T)p(T)} = \frac{1}{\sqrt{2}}\left(m_c^* m_v^*\right)^{\frac{3}{4}}\left[\frac{k_B T}{\pi\hbar^2}\right]^{\frac{3}{2}} \exp\left[\frac{-E_g}{2k_B T}\right], \tag{10}$$

where E_g is the bandgap energy. At any given temperature, n_i is a unique material parameter depending only on the carrier effective masses and the bandgap. In a pure semiconductor crystal free of defects and impurities, at every temperature $n_i = n = p$.

Impurities

Due to the different curvatures of conduction band and valence band, generally $m_c^* \neq m_v^*$, but more importantly, a semiconductor is rarely free of impurities. Impurities are the essence of semiconductor material and device physics. As mentioned previously, the prevalence of semiconductor materials in our world today results from our ability to

accurately and reliably control their electrical properties. The three primary electrical properties of a semiconductor that can be controlled, and therefore exploited, are its conductivity, carrier concentration, and mobility. These three properties are not independent, but rather interrelated as shown in the expression for conductivity

$$\sigma = e(n\mu_n + p\mu_p)\,, \tag{11}$$

where e is the elementary charge, n and p are, as before, the equilibrium concentrations of electrons in the conduction band and holes in the valence band, respectively, and μ_n and μ_p are the mobilities of those electrons and holes, respectively. Although, as will be reviewed shortly, n and p can be controlled, there is a fundamental law of statistical physics that governs their relationship: the law of mass action, $n_i^2 = np$. Because the intrinsic carrier concentration, n_i, is a constant material property at any given temperature, a change in the equilibrium concentration of one carrier type forces a change in the other. The conductivity of any semiconductor is thus greatest when the material has a large concentration of conduction electrons (n-type) or valence holes (p-type). A semiconductor can be made either n-type or p-type by the careful and intentional introduction of impurities called dopants.

Because of the well-structured nature of the covalent bonding in (e.g., III-V) semiconductors, a complete ns^2np^6 shell configuration is achieved. When an impurity from a different group substitutes on either the cation (III) or anion (V) sublattice, the result will be an extra valence electron (donor) or a vacant electron level (acceptor) with respect to a complete ns^2np^6 shell configuration. Qualitatively, the donor or acceptor impurities can be ionized to "donate" an electron to the conduction band or "accept" an electron from the valence band (thus leaving behind a hole), respectively. Quantitatively,

the resulting equilibrium concentrations of electrons and holes in a semiconductor depend on the ionization energy of the impurity species. The ionization energies of most impurities can be approximated using a hydrogen atom model in which an electron (-*e*) is coulombically bound to a proton (+*e*). The well-known solution to this simple system is

$$E = -\frac{m_o e^4}{2\hbar^2 \kappa^2} = -13.06 \text{ eV}, \tag{12}$$

where $\kappa = 4\pi\epsilon$, and ϵ is the permittivity of a vacuum. When applying this hydrogenic model to semiconductors, two important modifications must be made. Firstly, because of the influence of the periodic lattice potential, the electron (hole) has an effective mass, m_c^* (m_v^*). Secondly, the relative dielectric constant, ϵ_r, of semiconductors is several times larger than that of a vacuum. For these reasons, the ionization energy of effective mass dopants or hydrogenic dopants in semiconductors empirically follows the hydrogenic ionization energy modified by the factors $m_{c,v}^*/m_o$ and ϵ_r^{-2}. Considering GaAs, which has $m_c^* = 0.063m_o$, $m_v^* = 0.53m_o$, and $\epsilon_r = 13.2$, one estimates the nominal ionization energy to be 5 meV for effective mass donors and 41 meV for effective mass acceptors. Using the data from Table 1, the analogous values for donors and acceptors in GaN are 36 and 132 meV, respectively. The empirical ionization energies for several donor and acceptor species in GaAs are shown in Figure 6. Virtually all impurities and defects introduce energy levels within the bandgap of semiconductors. Shallow donor levels are just beneath the conduction band minima, while shallow acceptor levels are just above the valence band maxima. Deep levels resulting from localized impurities are often 140 meV or greater from the nearest band-edge. When a donor (acceptor) is

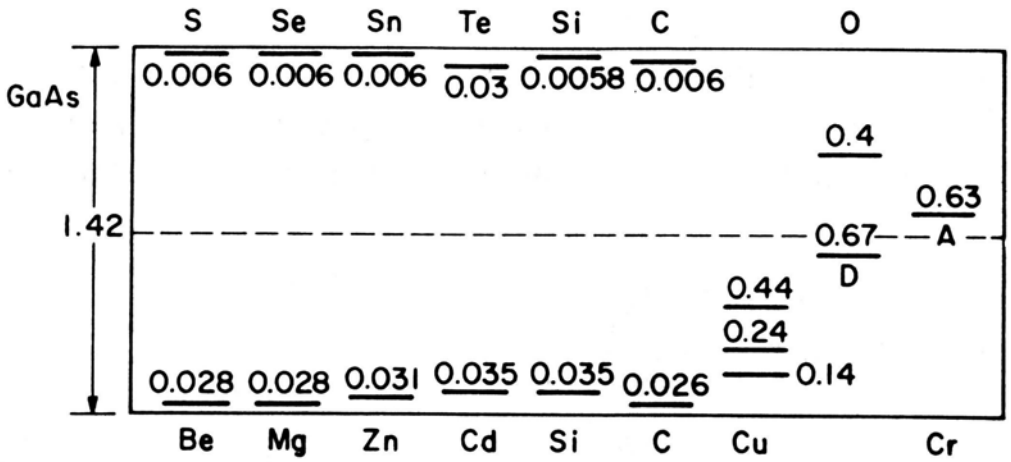

Figure 6. Empirical ionization energies in eV for several donor and acceptor species and deep levels in GaAs (Sze, 1985:23).

ionized, a free electron (hole) is introduced into the conduction (valence) band of the semiconductor, thus increasing the conductivity proportional to the dopant concentration.

In the absence of other external excitation, shallow donors and acceptors are generally thermally ionized. Statistical physics allows us to calculate the concentration of free carriers in either the conduction or valence bands by solving the charge balance equation given by

$$n + (N_a - p_a) = p + (N_d - n_d), \tag{13}$$

where N_a and N_d are the total concentrations of acceptor and donor impurities, respectively; p_a and n_d are the concentration of unionized acceptor and donor impurities, respectively. Under thermal equilibrium, the expressions for p_a and n_d are given by

$$p_a = \frac{N_a}{1 + \frac{1}{g_v} \exp\left[\frac{E_F - E_a}{k_B T}\right]} \tag{14}$$

and

$$n_d = \frac{N_d}{1 + \frac{1}{g_c}\exp\left[\frac{E_d - E_F}{k_B T}\right]}, \tag{15}$$

where $g_{v,c}$ are the degeneracies of the energy levels in the valence and conduction bands, respectively, and $E_{a,d}$ are the ionization energies of acceptors and donors, respectively (McKelvey, 1966:271). Depending on the relative doping concentrations (N_a versus N_d), and the temperature regime considered, certain terms in equation (13) can be assumed negligible, thus simplifying the calculation. Often one must fit the measured carrier concentrations as a function of temperature, *n(T)* or *p(T)*, to equation (13) to extract values for N_a and N_d, and the appropriate ionization energy.

The thermal ionization energy extracted from a fit to measured data (e.g. an Arrhenius plot) can be lower than the actual ionization energy of an isolated impurity on a substitutional lattice site due to impurity screening. When the concentration of impurities becomes so large that the average separation is on the order of the effective Bohr radius, the semiconductor can undergo a Mott transition to a metal. This critical doping density is given by

$$N_{crit} = \left[(\frac{\kappa_r}{3}\frac{m_o}{m_{c,v}*})5.29 \text{ x } 10^{-9} \text{ cm} \right]^{-3}, \tag{16}$$

where $\kappa_r = 4\pi\epsilon_r$, and ϵ_r is the relative dielectric constant of the semiconductor. The actual donor ionization energy, E_{d0}, will be reduced to the effective donor ionization energy, E_d, due to the effects of impurity screening per (Schubert, 1993:36)

$$E_d = E_{d0}\left[1-\left(\frac{N_d}{N_{crit}}\right)^{1/3}\right]. \tag{17}$$

In addition to effective ionization energy reduction, other high doping effects are the formation of an impurity band, band tailing, and band filling. Under the condition $N << N_{crit}$, impurities can be considered isolated and non-interacting with discrete energy levels within the bandgap. However, as the doping concentration increases and $N \leq N_{crit}$, the overlap of donor electron wavefunctions increases, and an impurity band forms. When $N \geq N_{crit}$, this impurity band merges with the conduction band. Because impurities have a random spatial distribution, there are random fluctuations in the band edges that result in band tailing. Free carriers no longer occupy states only at the bottom of the conduction band, and band filling is observed for heavily doped, highly degenerate semiconductors.

III. Ion Implantation, Defects, and Annealing Theory

Introduction

There are three primary methods of introducing impurities into a semiconductor crystal for the purpose of controlling its electrical and optical properties: via epitaxial growth, via diffusion, and via ion implantation. Ion implantation is a well-established technique with widespread use in fabricating integrated circuits from the more mature material systems such as Si, GaAs, and InP. The method involves ionizing the dopant source, accelerating these ions at a given energy, forming a beam with a given fluence, then rastering this beam across the target surface to produce a desired dose. Standard acceleration energies range from 10 to 500 keV. Common doses of impurity atoms implanted in semiconductors range from 10^{11} to 10^{16} cm^{-2}. Doping during growth is typically the most expensive option and provides limited flexibility. Due to the chemically robust nature of wide bandgap materials, the diffusivities of nearly all dopant impurities into these materials are very low. Thus, doping wide bandgap materials via diffusion is impractical due to the temperature and duration that would be required.

Alternatively, ion implantation offers many technological advantages that are important in the fabrication of electronic and optical devices:

1. Excellent reproducibility, uniformity, and speed of the doping process.
2. Precise control of the amount of dopant introduced (≤ 1% over the typical dose range, which is especially important for low concentrations) even with impurity concentrations above their equilibrium solid solubility limits.

3. Less stringent requirements on dopant source purity because mass separation is used.
4. Avoidance of high temperatures during the implantation process itself (room-temperature implantation is typical though implantation has been performed from 77 K-800 ^{o}C).
5. Ability to provide selective area doping by using simple masking methods (e.g., oxides, nitrides, photoresists), as well as the ability to implant through similar thin passivating layers (e.g., AlN thermal encapsulants).
6. Ability to dope shallow layers with very high impurity concentrations with relatively small lateral straggle of the implanted ions (e.g., small geometry devices, IMPATT diodes, microwave transistors).
7. Ability to create unique doping profiles by performing multiple implantations modifying the accelerating voltage, dose, or ion species.

Ion implantation also has certain disadvantages which must be considered:

1. Radiation damage is produced during implantation causing undesirable electrical and optical properties. Thus, high temperature annealing is required to restore the crystal lattice and move the implanted ions onto electrically active lattice positions; in some cases, a significant amount of damage remains even after annealing.
2. Implanted layers are generally limited to the surface ($\leq 1\ \mu$m). Greater penetration depths can be achieved with greater accelerating voltages, but at the expense of greater radiation damage which can be prohibitive.

3. Secondary effects either during implantation or the subsequent annealing (e.g., channeling, diffusion) tend to reduce peak concentrations and deepen the implanted profile beyond the theoretical predictions (Pearton, 1988; Ryssel and Ruge, 1986:1,2).

Ion Implantation Theory

Predicting the depth profile of the implanted ions is critical for device applications. The depth at which a typical ion will come to rest within the host semiconductor lattice is dependent upon the energy of the ion, the mass of the ion, the mass of the host atoms, and the density of the host. The two primary stopping methods for ions within a solid are electronic and nuclear stopping. Electronic stopping occurs when the incident ion collides inelastically with bound electrons of the host producing heat and host atom excitation or ionization. Nuclear stopping occurs when the incident ion undergoes an elastic collision with a host nucleus. Depending on the ion's energy, this can cause the host atom to be displaced from its equilibrium lattice position, which itself can cause a cascade of further displacements.

The energy of the incident ion determines which stopping effect will be dominant. At lower energies, nuclear stopping will dominate while at higher energies electronic stopping dominates, because at higher energies the ion is moving too fast to sufficiently transfer energy to any host atom nuclei. Electronic stopping power remains proportional to $\sqrt{E}$ (i.e., the velocity of the ions) within the range of typical implantation energies used to dope semiconductors, whereas nuclear stopping power peaks at low energy and then drops below the electronic stopping power as energy increases. Summing both

stopping effects, the projected range of most ions is roughly proportional to the ion's incident energy.

The projected range of implanted ions was first theoretically investigated by Lindhard, Scharff and Schiøtt (1963) and their results are generally referred to as the LSS theory. They showed that the statistical range of implanted ions will follow a Gaussian distribution about an average range called the projected range, R_p, with a standard deviation called the projected straggle, ΔR_p. If the ion beam is scanned uniformly across the wafer surface the distribution of implanted ions varies only in the projected direction; there is no lateral straggle. The volume concentration of implanted ions is then given by

$$N(x) = \frac{\phi}{\sqrt{2\pi}\Delta R_p} \exp\left[-\left(\frac{x - R_p}{\sqrt{2}\Delta R_p} \right)^2 \right], \tag{18}$$

where ϕ is the implantation dose (cm^{-2}). Clearly, the peak concentration will occur at a depth of R_p beneath the sample's surface given by

$$N_{peak} = \frac{\phi}{\sqrt{2\pi}\Delta R_p}. \tag{19}$$

The projected range and projected straggle (or the peak concentration from which the projected straggle may be calculated for the given dose) are the two parameters which uniquely define the Gaussian depth profile given the ion's mass, the ion's energy, and the atomic mass and molecular density of the host. The profiles are best estimated using a program which considers these values and then performs the necessary calculations to determine the projected range and projected straggle. Figure 7 shows the Gaussian profiles of Si-implanted GaN for a variety of energies as well as the profile of an Ar-implant in GaN to demonstrate the effects of differing acceleration voltages and ion

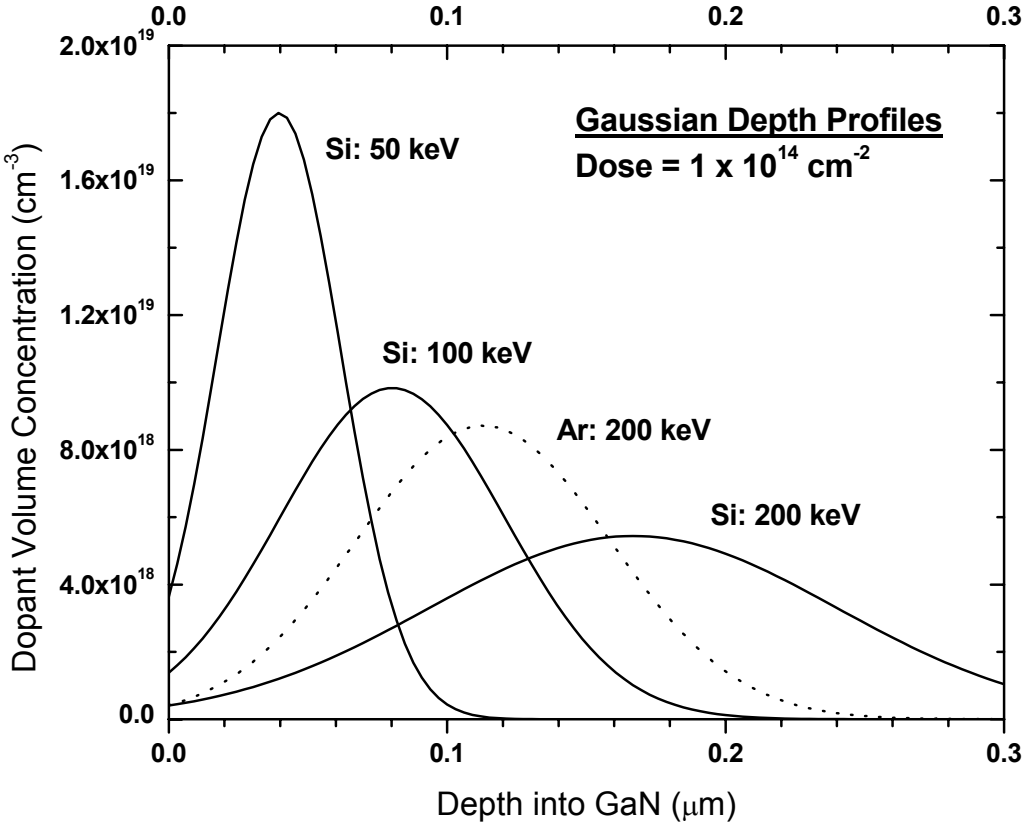

Figure 7. Gaussian implantation depth profiles showing the effects of ion energy and mass for various Si and Ar implants each at a dose of $1x10^{14}$ cm^{-2}.

masses on the position of the profile. These profiles were calculated using a commercial software package developed by Implant Sciences Corporation called Profile Code, version 2.1.

The Gaussian distribution is a very good first-order approximation to the actual depth profile of implanted ions in semiconductors despite the fact that the LSS theory assumes an amorphous solid. Although semiconductors are crystalline and highly symmetrical, they can be made to appear essentially amorphous by tilting the host lattice (typically 7°) so that the incident ion beam is slightly off a host axis of symmetry. This procedure will

minimize any ion channeling, which occurs when an ion moves through the host along a crystal axis in between planes of symmetry, practically unimpeded by any nuclear collisions. Considering moments of higher order in the range calculation will result in more complicated distributions which are theoretically more accurate. However, due to other difficult to model non-idealities (e.g., channeling, diffusion) associated with all ion implantations, the more complicated distributions offer little improvement over the basic Gaussian profile which remains a sufficient prediction for nearly all ion implantations into semiconductors.

Radiation Damage: Crystal Defects

An inevitable consequence of ion implantation in semiconductors is radiation damage. This damage, which manifests as various defects to the semiconductor's crystal structure, can have serious detrimental effects on the electrical and optical properties of the semiconductor. As discussed previously, nuclear collisions between an ion and a host atom can displace the host atom that can then cause a cascade of further displacements. After an ion has come to rest at random within the host lattice, it has left behind a network of simple, complex, and extended defects.

Simple or point defects are those involving only a single host atom, and involve vacancies, interstitials, and antisites. Considering GaN, for example, one could have either a gallium or nitrogen vacancy (V_{Ga} or V_N), a gallium or nitrogen interstitial (Ga_i or N_i), as well as a gallium or nitrogen antisite (Ga_N or N_{Ga}) in which a host atom has been displaced and has come to rest on the opposite sublattice. A Frenkel pair is a vacancy with the displaced atom as a neighboring interstitial. Because each of these point defects

represents a host atom removed from its equilibrium position within the crystal lattice, there will be unpaired valence electrons that when ionized will make these defects either singly or multiply charged. A nitrogen vacancy leaves behind a center consisting of four Ga atoms and three unpaired electrons, two of which will pair making V_N a single donor. Similarly, a gallium vacancy removes three electrons from a center consisting of four N atoms making V_{Ga} a triple acceptor. A Ga_i has three valence electrons that can be ionized making it a triple donor whereas N_i is a triple acceptor. Because Ga_N is two electrons short of that needed to properly bond with it's four Ga neighbors, it can be a double acceptor. Similarly, N_{Ga} can be a double donor.

When two or more point defects combine, a complex is formed. Additionally, divacancies and trivacancies can be formed directly from a collision. The introduction of an impurity atom into the host lattice allows for an even greater variety of complexes. Group IV ions are unique because they are amphoteric and, when implanted into a III-V semiconductor, can occupy either the cation or anion sublattice. Silicon, when implanted into GaN for example, can be either a single donor (Si_{Ga}) or a single acceptor (Si_N). As-implanted however, many of the implanted ions are interstitial. Nonetheless, an ionized single donor can be coulombically attracted to a singly ionized triple acceptor to form a double acceptor complex (e.g., V_{Ga}^{-}-Si_{Ga}^{+}). A myriad of other potential complexes are possible. Some are much more probable than others based on the energy gained when the complex is formed. Simple and complex defects can cluster to form dislocation loops or lines, which are classified as extended defects. It is important to note that due to the lattice mismatch between GaN epilayers and the substrates upon which they are grown (e.g., 12% for sapphire), there will be simple, complex, and extended defects in the as-

grown GaN even before implantation. Although implantation will increase the concentration of these defects by orders of magnitude, it is important to both electrically and optically characterize the as-grown epilayers to establish a baseline and more clearly identify the effects of the implantation itself.

Several factors influence the chemical nature and concentrations of the implant-induced defects: mass of the ion, implanted ion energy, implanted ion dose, temperature of substrate during implantation, and the electronic structure of the ion relative to (in the case of III-V compounds) the electronic structure of the host cations and anions (e.g. band structure, atomic orbitals, electronegativities, as well as ionic and covalent radii). Understandably, radiation damage tends to increase as the implantation dose, the ion's energy, or the ion's mass is increased. Light ions (relative to the host atoms) generally leave tracks with small amounts of damage. Initially, they are slowed by electronic stopping with little displacement damage. Then, as their energy decreases, nuclear stopping becomes dominant at the end of their range where displacements are more likely. The tracks of heavy ions are more characterized by displacements throughout their range. These effects are shown in Figure 8. Because a certain amount of energy is required to displace a host atom, an implanted ion will typically travel somewhat beyond its last displacement before coming to rest. The result is a damage concentration profile that peaks slightly closer to the surface of the host lattice than the ion concentration does. The number of displaced host atoms per ion (including cascades) depends on the ion's mass and energy as well as the atomic mass of the host, but can be several hundred to several thousand within the range of typical implantations into semiconductors. When

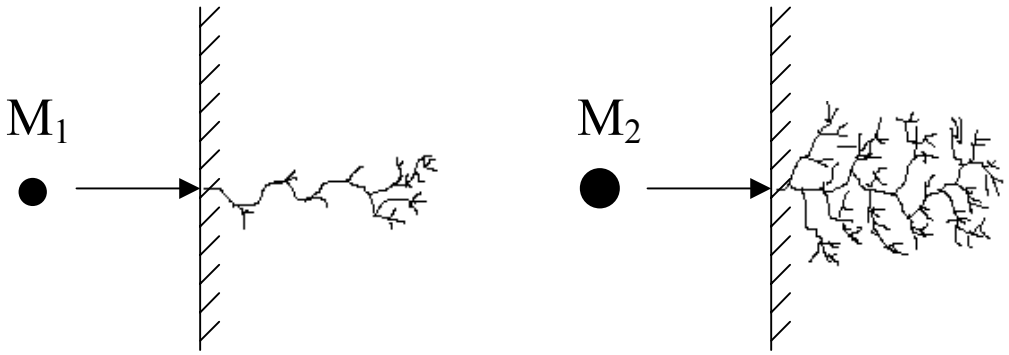

Figure 8. Damage tracks of implanted ions: light ion (M_1) and heavy ion (M_2) relative to host semiconductor atoms.

the damage becomes so great that the concentration of displacements approaches the host atomic density, amorphization begins.

Generally, the more ionic the semiconductor the more difficult it is to amorphize. GaN is a fairly ionic semiconductor and is reported to resist amorphization resulting from 90 keV Si ion implantation at 77 K for doses less than $1x10^{16}$ cm^{-2}, at which point amorphization begins at the surface and extends into the bulk as the dose is increased. Residual implantation damage resulting from doses less than $1x10^{16}$ cm^{-2} consists of a dense network of clusters and loops. (Tan *et. al*., 1996) In the case of GaN, amorphization is suppressed by a natural dynamic annealing in which damage is repaired during the implantation process. In other semiconductors, dynamic annealing is often accomplished by performing implants into heated substrates. The additional lattice vibrations caused by the heat assist the implanted and host ions in reaching equilibrium lattice positions. Even when amorphization is fully suppressed, there is still a rather extensive array of simple, complex, and extended defects that must be removed in order to fully exploit the desired electrical and optical properties that originally motivated the

implantation. Therefore, whenever semiconductors are implanted with donor or acceptor ions, a post-implantation anneal must be performed.

Annealing

There are two reasons for annealing semiconductors after implantation doping: to repair the radiation damage to the crystal lattice, and to activate the implanted species onto the appropriate sublattice position. Many defects within the implanted region form localized deep levels that act as traps for free carriers and compensate shallow donors or acceptors. These deep levels can also reduce the efficiency of optical devices by offering preferential non-radiative recombination routes. The crystalline disorder provides a high concentration of scattering centers that greatly decreases the mobility, a measure of how efficiently free carriers move through the semiconductor under the influence of an applied voltage. When an implanted sample is annealed, several thermodynamic processes occur. Not only are implanted atoms electrically activated by substitution on the appropriate host sublattice and radiation damage being repaired, but also anneal-induced defects may simultaneously be formed. Because annealing is a thermodynamic process, temperature and time can theoretically be traded off to produce similar results.

Despite the technological maturity of the implantation-annealing process in doping elemental semiconductors (e.g., Si) as well as various III-V semiconductors (e.g., GaAs), there are several important differences between the two:

1. Avoiding amorphization in III-V semiconductors is more critical than in elemental semiconductors due to the greater difficulty in restoring order to both the cation and anion sublattices.

2. A more thorough understanding of the dopant activation process is required in III-V semiconductors to ensure the implanted ion substitutes on the desired sublattice, whereas stoichiometry is always maintained in elemental semiconductors.
3. The different masses of the cation and anion in III-V materials will cause unequal recoil during implantation collisions as the lighter host mass will recoil further upsetting local stoichiometry.
4. Due to the higher vapor pressures of all group V anions, steps must be taken to prevent dissociation of the III-V compound and subsequent loss of the group V atoms during high-temperature annealing.

Typically, the lower the dose, energy, or mass of the ion, the less damage created and thus, the lower the anneal temperature required to repair the damage and activate the implanted dopants. However, even the lowest concentrations of radiation damage in III-V materials still require a high enough anneal temperature that dissociation is a significant concern. There are three common procedures practiced in post-implantation annealing of III-V materials to prevent or minimize the evaporation of the group V atoms: 1) an epitaxially-grown or deposited encapsulant (e.g., SiO_2, Si_3N_4, AlN), 2) group V overpressure in the annealing chamber, and 3) a proximity cap placed face-to-face with the sample to be annealed. An encapsulant is often the most effective method, but there are certain requirements the encapsulant must satisfy:

1. Prevent dissociation of the III-V material during the anneal, which necessarily means that the encapsulant must possess sufficient thermal integrity itself to survive the anneal.

2. Prevent out diffusion of the implanted species.
3. Not react chemically with the implanted layer.
4. Be easily removed after annealing.
5. Possess excellent uniformity across the implanted wafer if the implantation is performed through the encapsulant.
6. Have thermal expansion coefficient reasonably close to the implanted layer to minimize any stress or strain that may be induced. Thinner encapsulants better withstand mismatches and are less likely to peel or crack.
7. Allow for low-temperature deposition if applied after implantation to minimize any potential dopant diffusion (Pearton, 1988:262).

Often the type of anneal performed will influence the selection of the thermal encapsulant or other method to prevent dissociation. There are three general types of implant anneals: rapid thermal anneal (RTA), conventional furnace anneal (CFA), and beam anneal (e.g., pulsed laser anneal (PLA), electron-beam anneal). RTAs are typically characterized by fast temperature ramp rates (> 50 ^{o}C/sec) and short dwell times at the anneal temperature (≤ 1 min). CFAs are usually much longer (10-30 min) though anneals as long as 90 min are not uncommon. Because beam anneals are designed to very rapidly melt then resolidify the implanted layer, they have not received widespread use in annealing implanted III-V materials due to the unique difficulties involved in preventing group V evaporation under such conditions.

When systematic ion implantation and annealing studies are performed, generally the answers to the following questions are sought:

1. At each dose, how do the carrier concentration and mobility vary with anneal temperature?
2. At a given anneal temperature, how do the implant activation efficiency and mobility vary with dose?
3. What are the ionization energies of the activated implants?
4. How does the implantation temperature affect the carrier concentration and mobility?

Usually, the driving goal for device applications is to determine an optimum anneal temperature at which the maximum activation is obtained, or to determine the maximum activation at a certain temperature with a certain anneal time. These two goals are met by isochronal and isothermal annealing studies, respectively. The anneal time is kept constant as the anneal temperature is varied in isochronal annealing, which can be performed as either an RTA or CFA. The anneal time is varied as the anneal temperature is held constant in isothermal annealing, which is best performed in CFAs.

Although CFAs have received the most use in annealing implanted semiconductors, RTAs, frequently employing a heat source comprised of banks of high power quartz halogen lights, have grown in popularity for two reasons. Firstly, the shorter time of an RTA is more desirable for production line usage. Secondly, many common dopants diffuse rather quickly in some III-V semiconductors, thus broadening the as-implanted profile; this concern can be minimized by the short duration of an RTA. However, there are reasons to consider a CFA of implanted samples. The CFA furnaces can reach higher anneal temperatures than many commercially available RTA ovens, and they can also physically maintain those temperatures longer without reliability concerns.

Depending on the particular dopant and semiconductor host to be annealed, dopant diffusion is not always a major concern. Additionally, the various implantation defects recover at different temperatures. Such recovery may occur before or after substitutional dopant activation. In some materials (e.g., GaAs), some radiation damage is eliminated after annealing at 500 ^{o}C; however, temperatures of more than 700 ^{o}C are required for electrical activation of the implanted ions. (Ryssel and Ruge, 1986:52). In other materials (e.g., GaN), implanted Si ions occupy substitutional lattice positions between 1050 and 1100 ^{o}C but remain compensated (electrically inactive) until point defects are repaired at higher temperatures. (Zolper, 1997:379). Thus, substitution is a necessary but insufficient condition for acceptable electrical activation.

Some wide bandgap semiconductors that have high melting points (e.g., GaN, SiC) require annealing temperatures exceeding 1300 ^{o}C to fully remove defects. Pearton (1999) reported that temperatures above 1300 ^{o}C are required to completely remove implantation damage in GaN and that peak activation for implanted Si is achieved at 1400 ^{o}C for AlN-encapsulated samples. These results provide evidence for an empirical rule of thumb which states that anneal temperatures approaching 2/3 of a semiconductor's melting point (T_m = 2518 ^{o}C for GaN) are needed for removal of defects caused by implantation.

Coimplantation

The concept of dual implantation was first proposed by Heckingbottom and Ambridge (1973), who theorized that the activation of an implanted dopant into a III-V semiconductor would be increased if stoichiometry was maintained via an equal dose

coimplantation of the opposite sublattice host atom. Under thermodynamic equilibrium, the product of group III and group V vacancy concentrations is a constant. Thus, when a dopant occupies a particular sublattice vacancy, the vacancy concentration of the opposite sublattice increases which tends to limit dopant activation by the formation of compensating dopant-vacancy complexes. The coimplant maintains stoichiometry and increases dopant activation by preferentially occupying the opposite sublattice. Further, if the dopant species is amphoteric, the coimplant increases the probability that the dopant will substitute on the desired sublattice thereby avoiding self-compensation. Many experiments involving a variety of implants and semiconductor materials have validated this theory.

There are two other rationales in addition to stoichiometry maintenance that support the practice of coimplantation to enhance dopant activation or to otherwise improve electrical properties of the implanted material. The first is to coimplant a heavier ion to create additional vacancies into which the dopant implant may more easily substitute. This technique has been used in GaAs to improve carbon activation. Being a relatively light ion, carbon is unable to produce sufficient lattice damage, i.e., arsenic vacancies, to assist in activation. Coimplantation of Ga, Zn, or Cd significantly improves the electrical activation of the implanted C (Morton *et. al.*, 1998). The second is a technique in which both acceptors and donors are implanted to improve *p*-type conductivity and the concentration of holes. This method was first reported for *in-situ* doping at about the same time by Brandt *et. al*. (1996) and Yamamoto and Katayama-Yoshida (1997). Brandt *et. al*. refer to the technique as “reactive codoping” because the

donors are believed to react with the acceptors forming donor-acceptor complexes having the following results:

1. The solubility of both species is enhanced, preventing self-compensation. (Due to the non-equilibrium nature of ion implantation, solubility limits are not a concern as they are during growth when acceptor nitride precipitates are likely to form at high doping concentrations.)
2. Donor-acceptor ion pairs are predicted to form, reducing the energy levels of both species (i.e., closer to their respective band edge), thus reducing activation energy. For example, in GaN, Be_{Ga}^{-}-O_{N}^{+} nearest neighbor pairs could be formed. (Because the ion pair complex is energetically favored, there is a reduction in the Be acceptor energy level which serves to increase the concentration of ionized Be acceptors, and thus the hole concentration. Obviously, doping with both donors and acceptors results in compensation, which is overcome by doping Be at a slightly higher concentration than O.)
3. The formation of donor-acceptor ion pairs transforms two long-range coulombic scattering centers resulting from each isolated species into a single short-range dipole scattering center, thus enhancing the mobility and indirectly the conductivity of the implanted layer (Ploog and Brandt, 1998).

IV. Characterization Techniques

Introduction

There are a wide variety of characterization techniques that can be used to discover the numerous semiconductor material properties. Virtually all techniques involve probing the material and then measuring the material's response to the probe, or the material's effect on the probe. These responses or effects are usually recorded as a function of time, temperature, dimension, or some probe attribute such as energy, wavelength, or intensity. The type of probe used determines the material property examined. Nearly all material properties fall into one of the following categories: electrical, optical, magnetic, physical, structural, or chemical. Most research characterizing semiconductor materials has focused on their electrical, optical or structural properties. All three of these properties are closely related to each other because energy states within the bandgap are influenced by defects in the crystalline structure. Because of the vast application of semiconductors in electrical and optical devices, naturally, the electrical and optical properties are the most important. Among those properties that can be engineered, carrier concentration, carrier mobility, and radiative centers within the bandgap are the most meaningful in determining device performance.

Hall Effect Measurements

The Hall effect (Hall, 1879) is used to determine the conductivity type and carrier concentration of semiconductors by forcing a current (induced by an electric field, **E**)

through a sample within a magnetic field, **B**. Under such conditions, the free charge carriers will experience a Lorentz force, $\mathbf{F}_L$ given by:

$$\mathbf{F}_L = e(\mathbf{v} \times \mathbf{B}), \tag{20}$$

where **v** is the velocity of the carriers moving under the influence of the **E** field. In Hall effect measurements, the sample surface through which the current is forced is positioned orthogonal to the **B** field. The resulting Lorentz force on the carriers is then directed orthogonally to both the applied **B** and **E** fields. Because electrons and holes have opposite charge ($-e$ and $+e$) and flow in opposite directions ($-v_x$ and $+v_x$), the magnetic field, B_z, causes both particles to move in the y-direction. If either carrier type is dominant, the accumulation of internal charge induces a steady state Hall voltage, V_H, in the y-direction whose sign determines the carrier type, and whose magnitude is inversely proportional to the net sheet carrier concentration, n_s. The net accumulation of electrons on one side of an n-type semiconductor resulting from a fixed current in a magnetic field is shown in Figure 9. When the electrostatic force caused by the induced Hall field, $e{\cdot}E_H$, balances the oppositely directed Lorentz force, internal charge accumulation stops and an equilibrium Hall voltage is measured as described by the following expression:

$$V_H = \frac{I_x B_z r_H}{e n_s} = R_{Hs} I_x B_z r_H , \tag{21}$$

where I_x is the magnitude of the forced current, r_H is the Hall factor which accounts for the effect of different scattering mechanisms on the carrier velocity distribution, and R_{Hs} is the sheet Hall coefficient. The carrier concentration, n, and the Hall coefficient, R_H are given by the expressions $n = n_s / t$, and $R_H = t \cdot R_{Hs}$, where t is the thickness of the semiconductor layer. For simplicity r_H is generally assumed to be unity, although

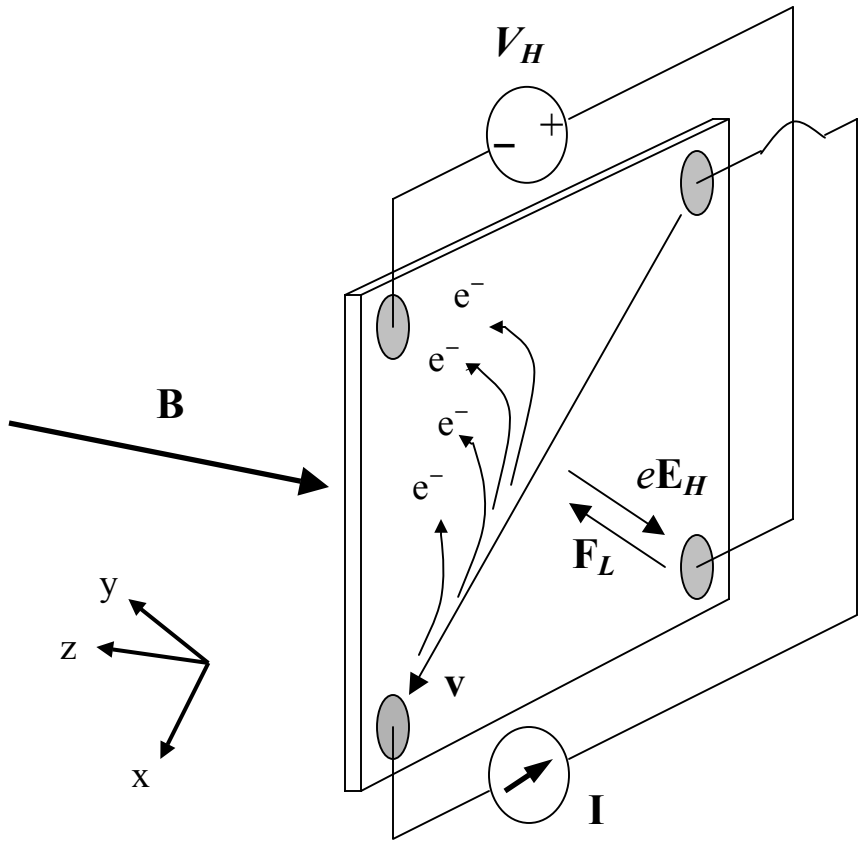

Figure 9. van der Pauw technique for Hall effect measurements showing forced current, **I**, applied magnetic field, **B**, induced Hall voltage, V_H, and electron accumulation for an *n*-type semiconductor sample.

because $1 \leq r_H < 2$, Hall measurements tend to underestimate the actual sheet carrier concentration.

The contact geometry shown in Figure 9 represents the van der Pauw technique (van der Pauw, 1958), which is used to measure the Hall effect and determine the sample sheet resistivity while minimizing the effect of the contact resistivities. Although van der Pauw's theory states that all contacts must lay on the sample periphery and ideally be point contacts, it is most important that all contacts be highly ohmic to obtain meaningfully reliable measurements. A total of eight different current-voltage pair

measurements are averaged to calculate the sheet resistivity, ρ_s, then, four different current-voltage pair measurements each under forward and reverse **B** fields are averaged to calculate the Hall coefficient. The Hall mobility can be determined from

$$\mu_H = \frac{R_{Hs}}{\rho_s}. \tag{22}$$

Unless, steps are taken to account for multiple conducting layers or non-uniform carrier distributions, Hall effect measurements provide only the average carrier concentration and mobility values over the entire conducting layer thickness, i.e., the depth beneath the surface until a *pn*-junction or insulating layer is reached.

Temperature dependent Hall (TDH) measurements provide carrier concentration and mobility values as a functions of temperature. Because the carrier concentration is proportional to $\exp(-E/k_B T)$, the ionization energy, *E*, can be determined from the slope of an Arrhenius plot of TDH measurements. At sufficiently low temperatures, one would expect even the shallowest impurities to freeze out leaving the material highly resistive. However, if the material is highly degenerate, TDH measurements will reveal this degenerate layer at the lowest temperatures exhibiting a temperature-independent mobility and carrier concentration due to the effective ionization energy reducing to 0 meV. The samples are kept under a vacuum during TDH measurements to prevent condensation or oxidation which can adversely affect the sample and measurement accuracy. Figure 10 shows an automated TDH measurement system capable of measuring highly resistive semiconductor samples.

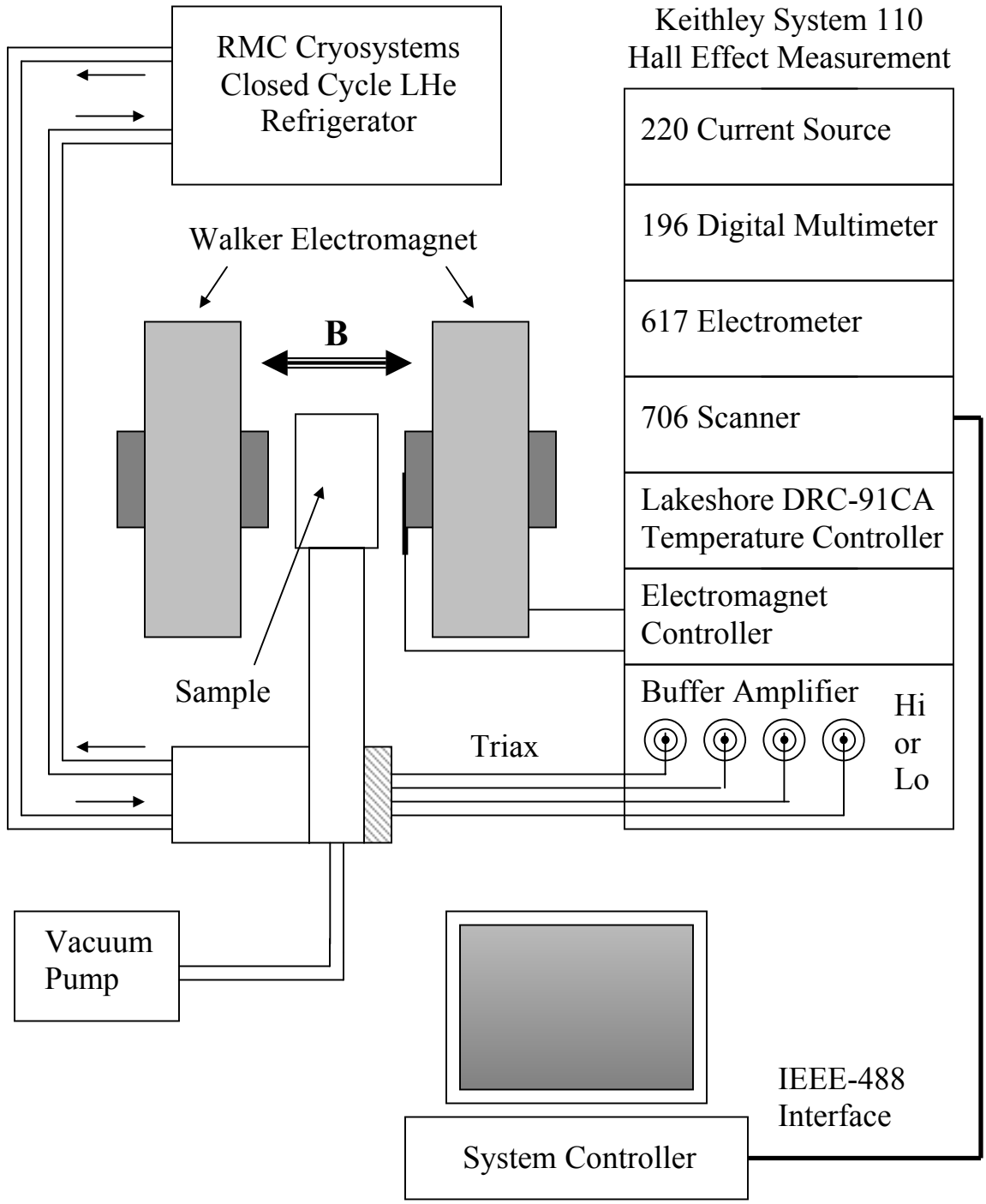

Figure 10. Schematic diagram of an automated Hall effect system used for high resistivity and temperature-dependent Hall effect measurements.

Photoluminescence

All luminescence spectroscopies probe the intrinsic and extrinsic radiative transitions of semiconductors when an electron from the valence band is excited into the conduction band leaving behind a hole. These spectroscopic methods are distinguished by their excitation source, which must be of greater energy than the semiconductor's bandgap. Photoluminescence (PL) uses a laser whose energy is typically 0.1-1eV greater than the typical bandgap, whereas cathodoluminescence (CL) uses an electron beam whose energy can be several thousand eV greater than the bandgap. For this reason, CL can be used when the material's bandgap is too wide to be excited by a laser, as for $Al_xGa_{1-x}N$ alloys with $x \geq 0.3$. Another advantage of CL is that the electron beam can penetrate, and therefore excite, the material more deeply than a laser. Thus CL spectra can be collected not only as a function of excitation intensity by varying the electron beam current, but also as a function of excitation depth by varying the electron beam energy. A disadvantage of CL compared to PL is that the material must be sufficiently conductive to prevent surface charge accumulation from severely degrading the spectra. A conductive path has to be established in the preparation of highly resistive samples. Figure 11 illustrates the components and connectivity of a PL system used to collect temperature- and power-dependent luminescence spectra.

Regardless of the particular excitation source, the non-equilibrium electron-hole pair will relax to its equilibrium lowest energy state by interacting with phonons and various impurity or defect energy levels within the bandgap until its eventual recombination occurs. A luminescence spectrum is collected for all pair recombinations that involve a radiative transition between two energy levels. Figure 12 shows a flatband

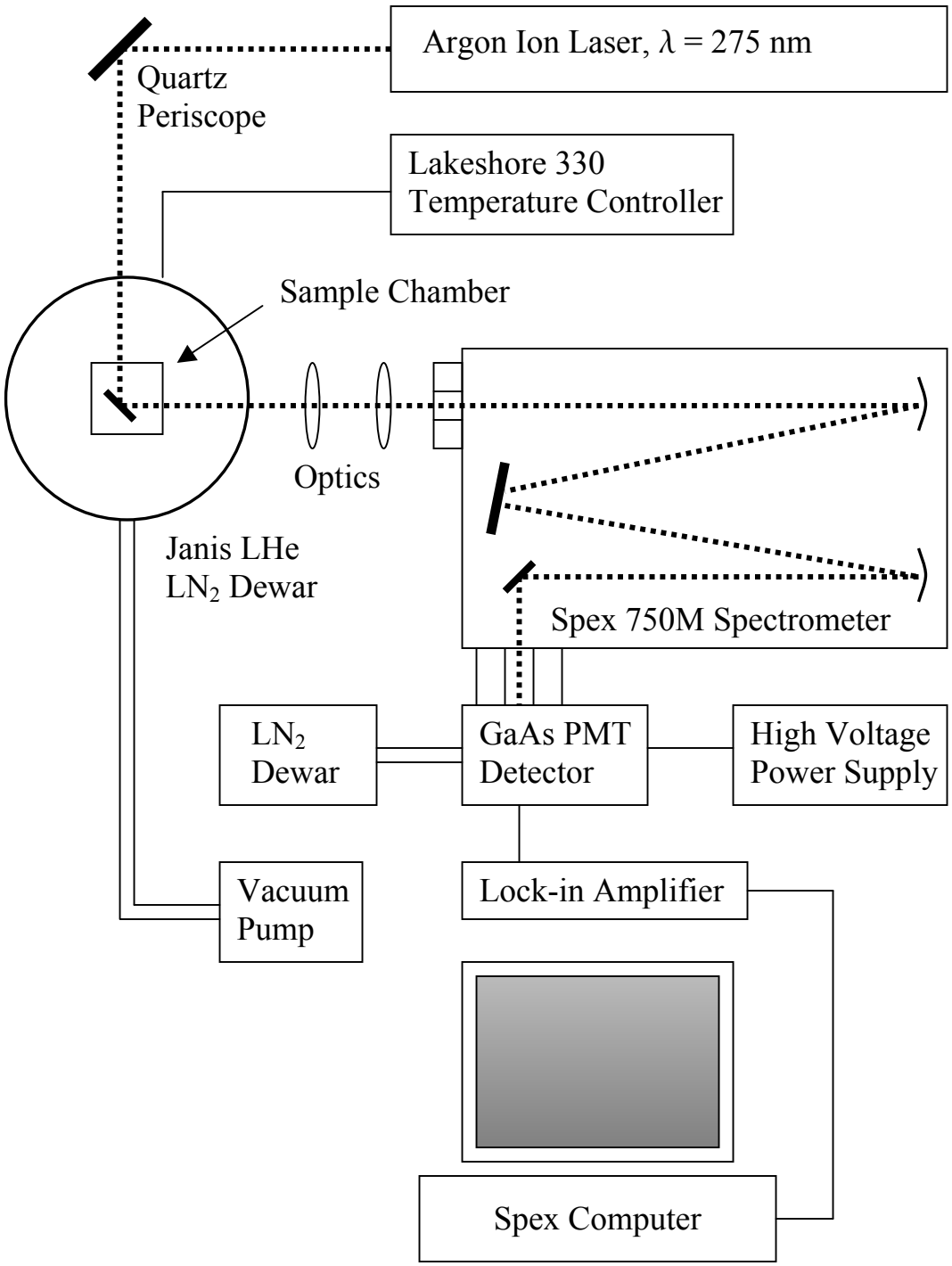

Figure 11. Schematic diagram of a photoluminescence system used to collect temperature- and power-dependent luminescence spectra.

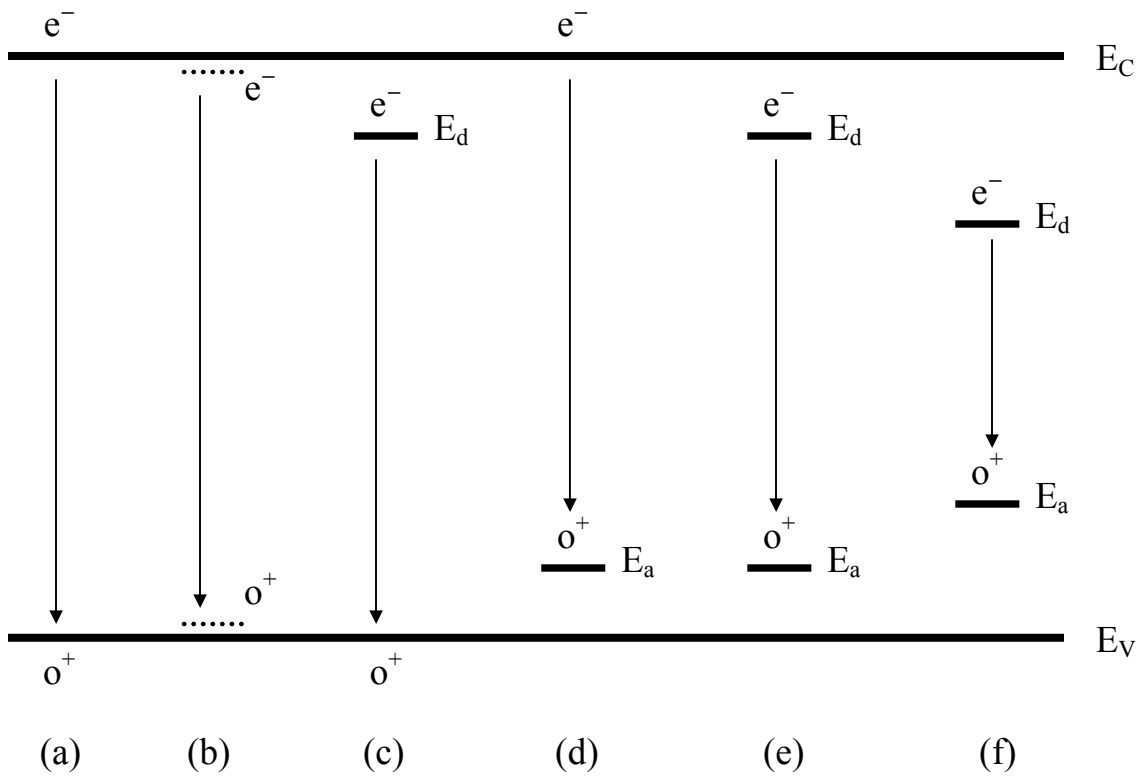

Figure 12. Radiative transitions observed in semiconductor luminescence spectra.

diagram annotated with several radiative transitions frequently observed in luminescence spectra.

Transition (a) is a band-to-band transition (eh) typically dominant in room temperature spectra, having a photon energy of $\hbar\omega = E_g + (k_B T)/2$. Transition (b) is a free exciton (FE): an electron (e^-) coulombically bound to a hole (o^+) acting as a single particle, analogous to a hydrogen atom. The photon energy of this transition is the bandgap energy, E_g, less the binding energy of the exciton as given by:

$$\hbar\omega = E_g - \frac{m_r * e^4}{2\kappa^2 \hbar^2}, \tag{23}$$

where m_r* is the reduced effective mass of the exciton. Luminescence spectra are typically collected on samples held at 10 K or less to ensure that nearly all impurity levels are in their lowest state, thus the spectra will show sharp transitions between the actual impurity levels rather than transitions broadened by a ½ $k_B T$ kinetic energy distribution. Perturbations in the periodic potential of the lattice enable excitons to become bound to impurities by coulombic interaction. The raditive energy from bound excitons such as a neutral-donor-bound exciton (D^o,X) is further reduced by the binding center. Transition (c) depicts an electron on a neutral donor recombining with a free hole (D^o,h), while transition (d) shows a free electron recombining with a hole on a neutral acceptor (e,A^o) with photon energies given by

$$\hbar\omega = E_g - E_{d,a} + \frac{1}{2}k_B T \,, \tag{24}$$

respectively. Transition (e) is a transition from an electron on a shallow neutral donor recombining with a hole on a shallow neutral acceptor (DAP), whereas (f) is a deep donor to deep acceptor pair transition (D_dA_dP). Shallow levels are usually substitutional effective mass dopants (e.g., Si_{Ga}, Mg_{Ga}) with extended wave functions. Deep levels can act as either donors or acceptors, have multiple charged states, and are often complexes comprised of shallow impurities bonded to various defects (e.g. V_{Ga}-Si_{Ga}, V_N-Mg_{Ga}). Deep levels can participate in generic DAP transitions with shallow levels, in free-to-bound transitions, and they can bind excitons like any other defect or impurity. The energy released in a DAP transition is given by

$$\hbar\omega = E_g - E_d - E_a + \frac{e^2}{\kappa r} \,, \tag{25}$$

where r is the spatial separation between the donor and the acceptor participating in the transition. The last term is the electrostatic energy gained when the neutral pair (D^oA^o) becomes a dipole (D^+A^-) after the transition has occurred. DAP peaks in a luminescence spectra can be rather broad due to the wide range of discrete values that r can assume. Knowing the bandgap energy, equations (24) and (25) are frequently used to calculate the ionization energies of donor and acceptors.

Theoretically, all of the radiative transitions shown in Figure 12 can involve phonons, though photon-phonon interactions are most readily seen in shallow DAP transitions. Phonons from the higher frequency longitudinal optical (LO) branch interact most frequently with DAP transitions. A portion of the transition energy is provided to the lattice via one or more phonons referred to as phonon replicas and designated as 1LO, 2LO, etc. The probability of interaction decreases as the number of phonons involved increases accounting for the reduction in intensity.

The relative intensity of each of the transition features in a luminescence spectrum supports general observations regarding the electrical and even structural properties of the semiconductor material. Because there are relatively few energy levels within the bandgap of high purity semiconductors, FE peaks generally dominate the low temperature ($T < 10$ K) PL spectra, whereas sharp bound exciton peaks typically dominate the spectra of high quality lightly doped or unintentionally doped semiconductors. The crystalline quality or impurity concentration has a significant effect on the intensity of excitonic transitions. Comparing the intensities of exciton peaks in unimplanted and implanted material is a qualitative measure of how much lattice damage remains after high temperature annealing to activate implanted ions and recover

crystalline order. Furthermore, as electrostatic lattice perturbations increase with doping concentration, exciton formation decreases. In addition to excitonic transitions, DAP recombinations offer valuable insights to understand the intrabandgap levels.

The relative intensity of shallow DAP peaks is a rough qualitative measure of the level of compensation within the material. Material that is highly compensated will likely have strong DAP activity and could be fairly resistive despite a high concentration of either shallow donors or acceptors. Deep DAP peaks indicate the presence of defects, or complexes in the material which may involve shallow impurities. If the concentration of shallow impurities participating in deep donor or acceptor complexes is much greater than the concentration of isolated shallow impurities, deep DAP peaks will dominate over shallow DAP peaks, and the material will likely be highly resistive. Occasionally, the low-temperature PL spectrum is rather weak and noisy with no dominant features. In this case, one would either suspect the sample to be highly degenerate or of very poor crystalline quality, perhaps resulting from many growth defects or unrecovered ion implantation damage. When a high concentration of defects exists, the majority of non-equilibrium carriers are trapped and recombine nonradiatively. However, in most cases, an even better understanding of the electrical and optical properties of a semiconductor can be gleaned by collecting variable-temperature PL spectra.

Temperature-dependent luminescence spectra often reveal the nature of unknown peaks and their associated energy levels. The spectral position of DAP transitions typically red-shift with increasing temperature according to the change in bandgap energy with temperature. More importantly however, shallow DAP peak intensities decrease rapidly with temperature. The rate at which the peak intensity is reduced provides a

qualitative measure of the individual donor and acceptor levels within the bandgap. The more shallow a level, the more readily it ionizes with temperature, thus quenching the corresponding DAP transitions. Deep levels are much less vulnerable to thermal ionization and thus strongly participate in DAP transitions at higher temperatures. Due to the wide bandgap of GaN, a deep DAP peak may be the result of a transition between a shallow level and a very deep level, or between two moderately deep levels. Temperature-dependent PL data can resolve this ambiguity by comparing the relative intensity variation of a shallow DAP and a deep DAP in the same spectra.

Power-dependent PL spectra can also often reveal the nature of unknown peaks. Considering all the transitions of Figure 12, only DAP transitions blue-shift with excitation power or intensity. At low excitation levels the most probable DAP transitions occur between distant pairs because there are many more distant impurities than there are nearer neighbors. As the excitation intensity is increased, more donor and acceptor pairs participate, thus reducing the average distance between transitioning pairs. As seen in equation (25), as r decreases, the peak photon energy increases. Naturally, the intensity of all luminescence goes as the excitation intensity; however, the spectral positions of exciton and free-to-bound transitions remain unaffected.

For sufficiently high carrier concentrations, the effects of band tailing and band filling may be seen in low-temperature PL spectra. As discussed in the background on semiconductor impurities, when $N \geq N_{crit}$, the interactions from such high impurity and free carrier concentrations alters the density of states near the band edge. The effect of band tailing and band filling on the near band edge PL spectra is a Gaussian-like broad peak centered around the bandgap.

Correlating the results of Hall effect measurements and luminescence spectra can generally provide synergistic insights, increasing an understanding of the electrical and optical centers, deep levels, and implantation damage recovery as functions of the implantation and annealing conditions. This understanding will then allow device fabrication procedures to be optimized fully exploiting GaN material properties.

V. Experimental Procedures

This chapter describes the experimental procedures including material growth, ion implantation, GaN surface protection, RTA and CFA annealing, contact preparation and deposition, and finally Hall effect and PL characterization. In this study, two sets of GaN material were examined. The principal differences between these two sets were the method of thermal encapsulation and the GaN epilayer thickness. Both sets were implanted with a variety of species, doses, and implant temperatures.

Sample Growth, Ion Implantation, and Annealing

The first set of samples was processed from undoped GaN layers grown on 2" sapphire substrates by SVT Associates via molecular beam epitaxy (MBE) using an RF atomic nitrogen plasma source. Substrate temperature, flux ratios, and growth rates were determined by a combination of pyrometry and reflectometry. Reflection high-energy electron diffraction (RHEED) was used to monitor the growth quality. First, a thin AlN nucleation layer was grown after thermal cleaning and nitridation of the sapphire. Next, a 1 μm thick GaN layer was grown at about 750 °C under slightly Ga-rich flux ratios.

These as-grown GaN wafers were cut into quadrants using a diamond wire saw in preparation for ion implantation. The wafer quadrants were implanted with Si, Si+Mg, Mg, or Mg+O ions at doses of $1x10^{13}$, $1x10^{14}$, and $1x10^{15}$ cm^{-2} at both room temperature and 500 ^{o}C. All Mg ions were implanted at twice these doses to overcome the *n*-type doping effects of the reactive donor coimplantation in hopes of realizing more efficient *p*-type GaN as the reactive codoping theory predicted. The implantation energy, chosen to

provide a peak concentration approximately 2000 Å into the GaN, was 220 keV for Si, 200 keV for Mg, and 160 keV for O.

Initial Annealing and AlN Encapsulation After Implantation.

Portions of the as-implanted wafer quadrants were cut into 5 mm x 5 mm samples and annealed in an AG Associates Heatpulse 610 RTA. In order to minimize GaN surface dissociation, the samples were placed face up on the Si thermocouple wafer then covered with a slightly larger piece of undoped GaN. Prior to annealing all samples and proximity caps were degreased sequentially in acetone, methanol, and blown dry with N_2. Annealing was performed in flowing N_2 at 1050-1150 ^{o}C with a dwell time of 15 sec at the anneal temperature. Initial attempts at characterizing both Si and Mg implanted samples under these anneal conditions resulted in high resistivity material, producing neither *n*-type nor *p*-type conductivity. Additionally, both the samples and proximity caps were showing signs of GaN pitting. Samples annealed at 1200 ^{o}C for 15 s with proximity caps in flowing N_2 were completely destroyed; surface morphology was visibly very poor and metallic Ga droplets could be seen in some regions. It appeared that successful activation of the implanted donors and acceptors called for either longer anneal times at 1050-1150 ^{o}C, or surviving a 1200 ^{o}C anneal for 15 s—both of which required more robust surface protection.

Other portions of the as-implanted wafer quadrants were cut and 1000 Å of AlN thermal encapsulant was grown by metal-organic chemical vapor deposition (MOCVD) at 450 ^{o}C. These samples were annealed open-face in flowing N_2 in a conventional tube furnace at 1100-1200 ^{o}C for 20 min. The quality of the AlN film decreased with annealing temperature. Generally, the AlN film on samples annealed at 1100 ^{o}C

remained fairly intact with only slight weakening and peeling on the sample periphery. The GaN underlying all AlN that had peeled or lifted was not adequately protected during the anneal and was unfit for any further processing or characterization. The region of degraded or destroyed AlN on the samples annealed at 1150 ^{o}C extended further towards the sample center though most samples survived well enough for electrical contact deposition. The samples annealed at 1200 ^{o}C were in most cases fully destroyed. The quartz tube and sample boat had been recently etch-cleaned in an HF acid solution, rinsed in deionized water (DI), test annealed to 1100 ^{o}C, and the furnace had been purged with flowing N_2 for several minutes prior to sample annealing. Despite these preparations and precautions, there was apparently enough O_2 present in the annealing environment to form an aluminum oxide on portions of the AlN cap surface. This oxide was very difficult to remove and often required over 40 min of ultrasonic cleaning at 50 ^{o}C in 0.3 M KOH solution to adequately remove. After considering sputtered AlN as more practical as well as potentially having a better thermal integrity, an alternative approach with a much greater chance of success was pursued.

The Search for a Better AlN Encapsulant.

Theoretically, the best AlN encapsulant should be grown on a clean GaN surface free of any contaminants or oxides. Other factors to consider include AlN thickness and growth temperature. The AlN thickness can influence the extent and onset of cracking due to differences in thermal expansion coefficient and lattice constant with the underlying GaN. The growth temperature can influence the degree of adherance to GaN, the nature of defects, crystallinity, and surface coverage. Four different test samples were examined in which the AlN was grown on the GaN without breaking the MBE chamber

vacuum at thicknesses of 500 and 1000 Å, and growth temperatures of 100 and 750 ^{o}C. The AlN grown at 100 ^{o}C under N-rich conditions was near-amorphous, with a small grain size, whereas the AlN grown at the normal MBE growth temperature of 750 ^{o}C was crystalline. These samples were annealed from 1200-1250 ^{o}C in minimally flowing high purity N_2 (O_2 content less than 1 ppm) in an Oxy-Gon chamber furnace using graphite heating elements. The samples were placed on top of a SiC-coated graphite pedastal in the following configurations: open-face, open-face wrapped in tantalum (Ta) foil, and face-to-face in Ta foil. To remove any residual O_2 that may have been trapped in the Ta foil envelopes, or elsewhere in the chamber, a mid 10^{-3} Torr vacuum was pulled on the chamber, backfilled with N_2, a vacuum pulled a second time, and the elements soft-baked to 200 ^{o}C at low 10^{-4} Torr before backfilling with N_2 again to perform the anneal. The cold-growth-AlN cap samples maintained much better surface morphology than the hot-growth-AlN cap samples, and the 500 Å thick cold-growth-AlN demonstrated greater integrity than the 1000 Å thick AlN. The Ta foil wrapping appeared to accelerate the degradation of the AlN film, while the open-face anneals had the least impact on the AlN morphology. Figure 13 compares the morphology of all four sample types under each of the three anneal configurations after annealing at 1250 ^{o}C for 3 min. All photographs shown in Figure 13 were taken at the same optical microscope magnification. Although all the samples show varying degrees of pitting, the samples with hot-growth-AlN cap wrapped in Ta foil show metallic Ga droplets indicative of significant GaN dissociation, whereas the sample with 500 Å thick cold-growth-AlN annealed open face is practically unaffected.

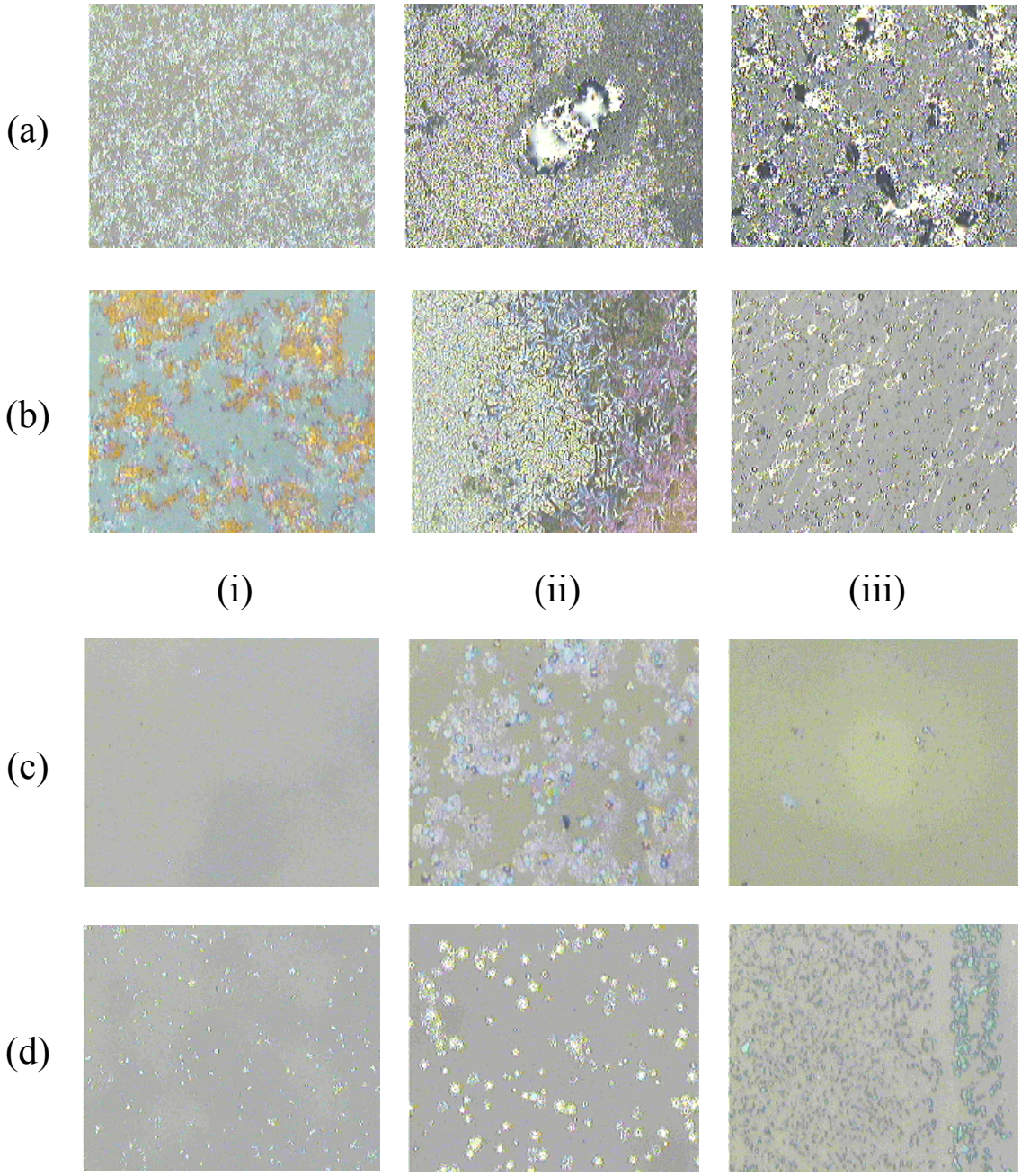

Figure 13. Morphology of AlN/GaN test samples annealed at 1250 ^{o}C for 3 min in minimally flowing N_2: (a) 500 Å and (b) 1000 Å thick hot-growth AlN (750 ^{o}C), (c) 500 Å and (d) 1000 Å thick cold-growth AlN (100 ^{o}C) arranged (i) open-face, (ii) open-face in Ta foil, and (iii) face-to-face in Ta foil.

AlN Encapsulation During GaN Growth.

The same basic growth procedures were followed on the second set of implanted material, except that after 2 μm growth of GaN, the samples were cooled to about 100 °C in the MBE chamber and a 500 Å thick AlN encapsulant was deposited under a N-rich condition, which gave the wafers a translucent brown color. A GaN thickness of 2 μm was chosen to minimize the effects of any dislocations originating in the defective epi/substrate interfacial layer, thus allowing for a better quality implanted layer. Because the MBE growth technique requires a good thermal path to the wafer, Ti was deposited on the backside of the sapphire substrate. Before cutting the AlN/GaN epiwafers into quadrants, the Ti was etched in a 40:1:1 solution of DI, HF, and HNO_3 for 3 min, rinsed in DI, ultrasonically cleaned in DI for 30 sec, swabbed in DI to fully remove the soot-like TiN residue from the sapphire, rinsed again in DI, and blown dry in N_2. The wafer quadrants were implanted with Mg, Mg+P, Mg+C, Mg+O, Li, Li+P, and C ions at doses of $5x10^{14}$ and $5x10^{15}$ cm^{-2} at 800 ^{o}C, as well as Mg and Mg+P ions implanted at room temperature at a dose of $5x10^{15}$ cm^{-2}. Silicon implantation was performed at six different doses ranging from $1x10^{13}$ to $5x10^{15}$ cm^{-2} at both room temperature and 800 ^{o}C. Similarly, Ar implantation was performed with doses of $1x10^{13}$, $1x10^{14}$, and $1x10^{15}$ cm^{-2} at both room temperature and 800 ^{o}C. The implantation energy was 200 keV for Si, Mg, and Ar, 260 keV for P, 125 keV for C, 160 keV for O, and 55 keV for Li. The energies for all coimplantations were chosen such that the peak of each profile occurred at the same depth. A significant amount of effort was spent understanding and optimizing the deposition parameters, anneal conditions, and etch procedures for AlN, because protecting the GaN surface from dissociation during annealing is such a critical step in

the implantation and activation process. The following optimized procedures were used in this study.

Optimized Annealing and AlN Removal.

Each time samples were cut from the AlN/GaN wafers (including the initial quadrant cut), photoresist was spun on and baked at 100 ^{o}C for 5 min as a protecting layer. After cutting, the samples were soaked for 5 min in acetone to dissolve all photoresist and crystal bond wafer adhesive. The cutting disks on which the samples were mounted tended to leave a ceramic residue that was best loosened and removed by ultrasonically cleaning the samples in a 3:1 solution of acetone and DI for 20 sec. Rinsing in acetone, methanol, DI, then blowing dry with N_2 completed the cleaning process. Prior to annealing, the samples were backside scribed with an identifying mark, cleaned again in acetone and methanol, and tightly wrapped face-to-face using 5 mil thick Ta wire. Unlike the Ta foil, the Ta-wire had no adverse effects on the AlN encapsulant. The 5 mil thickness was thick enough to hold a rigid shape when bent, yet thin enough to closely conform to the samples without applying undo stress.

Samples were annealed from 1250 to 1350 ^{o}C for 10 to 20 sec in minimally flowing high purity N_2 in the Oxy-Gon furnace. The Ta wire-wrapped samples were placed on top of a SiC-coated graphite pedastal. To remove any residual O_2 that may have been trapped between the samples, or elsewhere in the chamber, a mid 10^{-3} Torr vacuum was pulled on the chamber, backfilled with N_2, a vacuum pulled a second time, and the elements soft-baked to 200 ^{o}C for 12 min at low-mid 10^{-5} Torr before backfilling with N_2 again to perform the anneal under approximately 0.5 PSIG N_2. Although the AlN on these samples survived an open face anneal at 1250 ^{o}C for 20 sec with near

mirror-like morphology, the AlN was considerably pitted after an open face anneal at 1300 ^{o}C for 20 sec. Therefore, the tight Ta-wire wrapping and O_2 removal steps are critical to maintain AlN morphology and to ease AlN removal after annealing. Before deciding on the use of Ta wire, samples were annealed in two other configurations: 1) face up and capped with a piece of polished sapphire, and 2) capped face-to-face with another sample with both caps held in place by the weight of a small SiC-coated graphite block. Due to the likelihood of slippage while securing the furnace door or during the anneal itself as well as the obvious benefit of a tight homogeneous AlN-AlN proximity cap, the Ta wire wrapping gave results superior to the other proximity techniques. Because of the large thermal mass of the graphite heating elements, the sample cooling rate was rather slow as seen in Figure 14, which shows the temperature profiles for representative ~20 sec anneals at 1250 and 1350 ^{o}C in the Oxy-Gon furnace. Notice that due to the low ramp rates, the anneal at 1350 ^{o}C for 17 sec spent almost 4 min above 1200 ^{o}C. To prevent any oxidation on the AlN films, the samples were kept under a flowing N_2 atmosphere until the chamber's tungsten-rhenium type C thermocouple (TC) read less than 30 ^{o}C. The TC probe tip was suspended above the samples, which were on a large graphite puck. For this reason, the actual sample temperature upon exposure to room air was likely as high as 60 ^{o}C, though low enough to prevent AlN oxidation.

Ohmic Contact Deposition.

After removing the now brittle Ta wire, the two samples should readily slide apart with the same mirror-like finish with which they were wrapped. The AlN survival rate after annealing at 1350 ^{o}C for 20 sec was approximately 85%. The AlN was easily and

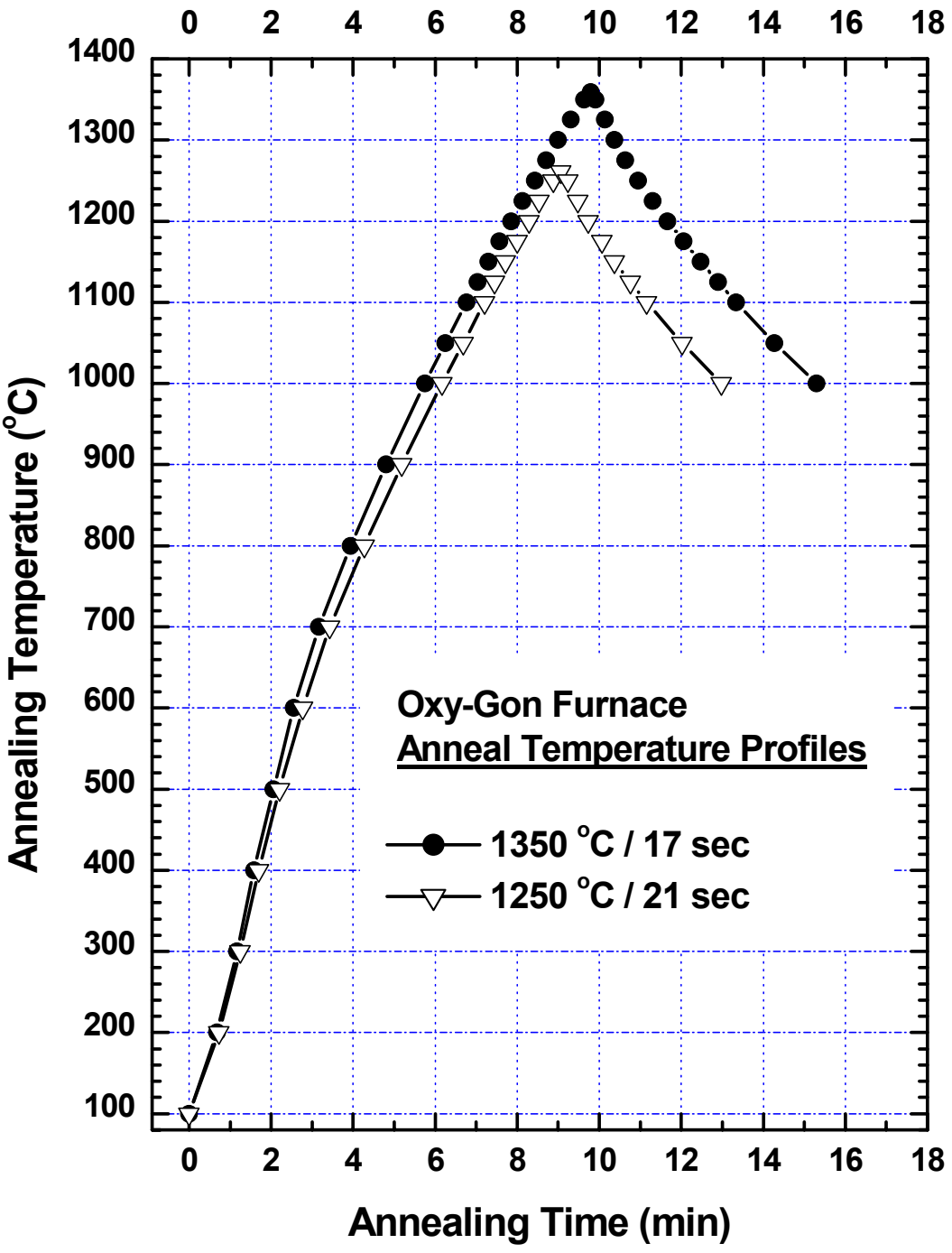

Figure 14. Anneal temperature profiles for representative 1350 °C for17 sec and 1250 °C for 21 sec anneals showing obtainable ramp rates in the Oxy-Gon furnace.

selectively etched by soaking for 5 min at 90 to 95 ^{o}C in a 0.5 M KOH solution prepared from solid KOH pellets, after which the samples were rinsed in DI and immediately placed in boiling aqua regia (3:1, HCl:HNO_3) for 2 min. The samples were then removed from the acid, rinsed in DI, blown dry with N_2, positioned and secured on a van der Pauw geometry contact shadow mask template, and loaded into a BOC Edwards 4-hearth 306 electron beam evaporator. Once a base pressure of $2x10^{-7}$ Torr was reached, 400 Å of Ti was evaporated at an average rate of 16 Å/sec, followed by 1200 Å of Al evaporated at an average rate of 22 Å/sec for *n*-type samples. For *p*-type samples, 500 Å of Ni was evaporated at an average rate of 18 Å/sec, followed by 1000 Å of Au evaporated at an average rate of 32 Å/sec. The shadow mask template was designed so that the contacts were approximately 500 μm in diameter. The ohmic contacts were annealed in an AG Associates Heatpulse 610 RTA face up on a Si wafer thermocouple at 900 ^{o}C for 30 sec in flowing N_2 for *n*-type, and 600 ^{o}C for 2 min for *p*-type. Prior to room-temperature Hall effect measurements, I-V curves were measured on a probe station with an HP 4155A Parameter Analyzer to determine the linearity of the contacts and relative conductivity of the samples. Detailed step-by-step procedures for sample cutting and cleaning, sample preparation for annealing, Oxy-Gon furnace annealing, post-anneal contact preparation, and electron beam metal evaporation can be found in Appendix B.

Hall Effect Measurements

All Hall effect data were taken under a 5 kG magnetic field using a semi-automated rack mounted Keithley 110 system suitable for high resistivity measurements. The forced current ranged from ~10 pA to 30 mA depending on the sample resistivity,

and each sample was placed in a closed dewar to eliminate any ambient light effects as well as for standardization. Three different room-temperature measurements over a decade of current were performed on each sample and the results for sheet resistivity, mobility, and sheet carrier concentration were averaged to increase confidence in data accuracy. The high temperature system, which used tungsten pressure contacts to the sample, collected data from 293-800 K, whereas the low-temperature system, which used Au wire soldered with indium to the van der Pauw contacts, collected data from 10 to 320 K. On both systems the high-impedance connections were used to collect data if the applied voltage safety limit of ±10 V was exceeded by attempting to force a current ≤ 1 mA on the low impedance connections. Temperature-dependent Hall effect measurements were typically run with the current that resulted in 100 to 200 mV during resistivity measurements.

Photoluminescence and Cathodoluminescence Measurements

PL spectra were collected at a nominal temperature of 3 K using the 275 nm line of a Spectra Physics argon-ion laser as the excitation source. After passing through a quartz periscope, laser power into the sample chamber was typically 150 to 200 mW. CL spectra were collected at a nominal temperature of 10 K using a Kimball electron gun with an electron beam energy between 1 and 10 keV, a beam diameter of ~1-2 mm, and a typical emission current of 25 or 50 μA. The PL and CL signals were dispersed with a ¾-m and ½-m spectrometer, respectively, using a 5000 Å blazed grating and a liquid nitrogen cooled GaAs PMT detector. Luminescence data on both systems were collected from 1.8 to 3.6 eV (6888 to 3444 Å) using a spectrometer step size of 2 Å, and an

integration time of 0.05 sec with spectrometer slits set between 100-400 μm depending on sample intensity and desired spectral resolution. On selected samples, temperature dependent PL spectra were collected from 3 to 300 K, and power-dependent spectra were collected from 2 to 200 mW using UV-rated neutral density filters. Detailed PL and CL experimental procedures can be found in Appendix B.

VI. Results and Discussion

Mg-Implanted and Mg-Coimplanted GaN

Luminescence studies are perhaps the simplest techniques to determine what defect and impurity levels exist within semiconductor bandgaps. A typical low-temperature acceptor-doped GaN PL spectrum contains a sharp neutral-donor-bound exciton (D^o,X) line near the band-edge from 3.46-3.48 eV and a dominant donor-to-acceptor pair (DAP) band peaking from 3.20-3.29 eV with associated phonon replicas. The (D^o,X) emission typically dominates as-grown unintentionally doped *n*-type GaN. Lightly acceptor-doped samples may also show neutral-acceptor-bound exciton (A^o,X) lines just below the (D^o,X) lines. The DAP band, which is due to transitions involving isolated acceptors and residual donors, is often referred to as ultraviolet (UV) luminescence because the visible cutoff occurs at 3.17 eV. When the acceptor concentration is increased to the mid 10^{19} cm^{-3} range, the UV DAP band is frequently quenched and a broader blue luminescence (BL) band peaking from 2.77-2.88 eV begins to dominate due to acceptor-related deep donor complexes. The probability of transitions between these deep donor complexes and isolated acceptors significantly increases as the acceptor concentration increases. When acceptors are incorporated, the Fermi level approaches the valence band maximum (VBM) enhancing the formation of deep donor defect complexes such as Mg_{Ga}-V_N or Mg_i-V_N.

Often a broad green luminescence (GL) band centered near 2.4 eV or a broad yellow luminescence (YL) band centered near 2.2 eV are observed due to a variety of native defects or impurity-related complexes. The GL and YL bands can either dominate

the PL spectrum or be quite weak depending on the concentration of impurities or material processing. Due to Mg's widespread use as the acceptor of choice, many reported PL spectra involve Mg-doped samples. Most of the reported GaN luminescence work has been done on *in-situ* doped material.

Hong *et. al.* reported on the room-temperature CL of Si- and Mg-doped GaN via MOCVD. The Si-doped sample had a line at 3.41 eV and a broad YL band centered at 2.25 eV. The Mg-doped sample had a band that peaked at 3.235 eV for Mg concentrations less than 1.5×10^{19} cm^{-3} but was quenched and replaced by a new band centered at 2.88 eV for Mg concentrations of 5×10^{19} cm^{-3} or greater (Hong *et. al.*, 1998). Obloh *et. al.* reported room-temperature PL for Mg-doped MOCVD-grown GaN. For Mg-concentrations less than 2×10^{19} cm^{-3}, the 3.2 eV band dominates, whereas for Mg-concentrations approaching 5×10^{19} cm^{-3} and beyond, the 2.8 eV band dominates. They attributed the 3.28 eV band to free electrons recombining with isolated Mg acceptors because the peak does not shift with the changing excitation intensity. Conversely, because the 2.8 eV band blue-shifts with increasing excitation intensity they attributed this luminescence to a recombination involving isolated Mg acceptors and deep donors. They asserted the deep donors are likely Mg_{Ga}-V_N complexes induced by self-compensation at higher Mg concentrations (Obloh *et. al.*, 1998).

Apparently, Mg-implanted GaN is not as likely to exhibit the DAP BL as is *in-situ* Mg-doped GaN. Chi *et. al.* implanted GaN with 150 keV Mg^+ at a dose of 5×10^{13} cm^{-2} and annealed at 1000 ^oC for 15 s in N_2. PL spectra from the as-grown GaN taken at 20 K reveal a 3.461 eV (D^o,X) line and an intense broad 2.2 eV YL band. After Mg-implantation and annealing, PL shows a 3.277 eV DAP peak with phonon replicas and a

broad GL band at 2.346 eV, which they attribute to Mg-induced defect clustering (Chi *et. al.*, 1998).

Kim *et. al.* measured the PL spectra taken at 100 K from Mg-doped and Mg+Si-codoped MOCVD-grown GaN as a function of Mg and Si incorporation, respectively. As the growth ratio of Mg to Ga increased in the Mg-doped sample, a dominant peak near 3.25 eV was quenched as peaks at 3.17 and 3.01 grew and were quenched, until a 2.77 peak was finally dominant. They attributed the 3.25 and 2.77 eV peaks to DAP and deep DAP transitions, respectively, but could not explain the 3.17 eV peak. The quenching of the 3.25 eV line and gradual rise of the 2.77 eV line was attributed to an increased transition probability from a deep-donor Mg-related complex to a shallow Mg-acceptor as the Mg concentration increased (Kim *et. al.*, 1999). The 3.17 eV peak was also seen in MBE-grown Mg-doped GaN. Grandjean *et. al.* reported PL taken at 9 K on Mg-doped MBE-grown GaN. Their spectrum for low hole concentrations ($< 10^{17}$ cm^{-3}) was dominated by a 3.26 eV DAP line, but also included a weak near-band-edge line at 3.465 eV. At a hole concentration of $3\text{x}10^{17}$ cm^{-3}, the band-edge line disappeared and the DAP peak shifted to 3.17 eV (Grandjean *et. al.*, 1998).

Skromme and Martinez (2000) implanted Mg and C separately at three different energy/dose combinations into GaN and annealed at 1300 ^{o}C for 8 s in N_2. Their PL spectra from Mg-implanted GaN taken at 1.8 K revealed a 3.476 eV (D^{o},X) peak (dominant in the as-grown material) that decreased with increasing Mg concentration, and a 3.470 eV (A^{o},X) peak that increased with increasing Mg concentration. A 3.27 eV DAP peak with phonon replicas became the dominant emission at the highest Mg concentration of $1\text{x}10^{17}$ cm^{-3}. Also present in the spectra of the samples with $1\text{x}10^{16}$ and

$1x10^{17}$ cm^{-3} Mg concentrations were a GL band peaking at 2.35 eV, and a weaker RL band peaking at 1.73 eV. They speculated that these two deeper bands might be due to Mg-related complexes or to defects whose formation is stimulated by the Fermi level moving closer to the VBM as Mg acceptors are activated. The C-implanted samples displayed no (A^o,X) peak and only a weak DAP peak at even the highest dose. In their C-implanted samples, the (D^o,X) peak remains dominant and a broad YL band peaked at 2.2 eV emerges nearly three times more intense than the weak DAP peak. They surmised that the lesser implantation damage produced by the lighter C ions provides fewer vacancies for substitution and is thus responsible for the much weaker PL spectra.

Ronning *et. al*. implanted Mg separately at 60 and 120 keV at doses from $1x10^{13}$ to $1x10^{15}$ cm^{-2} into GaN and annealed at 1200, 1250, and 1300 ^oC in vacuum for 11, 30, and 10 min, respectively. After removing the 300 Å AlN encapsulant, low-temperature PL spectra was collected on the implanted samples. The 3.467 eV (D^o,X) peak on the $1x10^{13}$ cm^{-2} sample was largely recovered after the 1300 ^oC anneal. A Mg-related DAP peak at 3.25 eV with phonon replicas were present on all annealed samples, but had the greatest intensity after the 1300 ^oC anneal. Also, present on each sample was a broad GL band peaking near 2.35 eV. All samples annealed less than 1250 ^oC for 30 min were highly resistive, whereas Hall effect measurements on other samples showed only *n*-type conductivity. They suggested annealing for longer periods at higher temperatures to obtain electrical activation of the acceptors, while cautioning that beyond 1300 ^oC the AlN cap could oxidize with residual O_2 in the vacuum (Ronning *et. al*., 2000). It is worth noting that no Mg-implanted GaN in the literature whose PL spectrum exhibits a GL band has shown *p*-type conductivity. This present study characterized Mg-implanted,

Mg-coimplanted, as well as C- and Li-implanted GaN to better understand the defect levels and centers unique to ion implantation doping so that ion implantation can be exploited in future device designs. The next few sections in this chapter will discuss the PL and Hall effect results obtained on these acceptor-implanted samples.

Low-temperature Photoluminescence.

The PL spectra obtained at 3 K from GaN implanted at 800 ^{o}C with Mg at 200 keV with a dose of $5x10^{15}$ cm^{-2} and annealed at various temperatures are shown in Figure 15. Fabry-Pérot interference fringes can be seen on most of the PL spectra in this study. For comparison, the spectra from as-grown GaN and unimplanted GaN annealed at 1250 ^{o}C for 18 s are also shown in this figure along with *in-situ* Mg-doped MOCVD-grown GaN. The PL spectra of the as-grown sample shows a typical neutral donor bound exciton (D^{o},X) peak at 3.48 eV, a shallow donor-to-shallow acceptor pair (DAP) peak at 3.28 eV, and its phonon replica. After annealing the as-grown GaN at 1250 ^{o}C for 18 s, its spectra remained about the same, and did not show any significant annealing related damage peak other than the weak broad peak centered at 2.64 eV. One interesting point could be that the intensities of both the (D^{o},X) and DAP peaks of the unimplanted and annealed sample rather increased significantly from those of the as-grown sample, which may indicate that both luminescence peaks are related to the same donor, possibly a nitrogen vacancy. For the Mg-implanted and annealed samples, the (D^{o},X) and DAP peaks are not observed even after annealing at 1300 ^{o}C, but all Mg-implanted samples show a broad GL peak centered at 2.37 eV. Furthermore, this GL peak intensity increases as the anneal temperature increases from 1100 to 1300 ^{o}C. The GL peak in

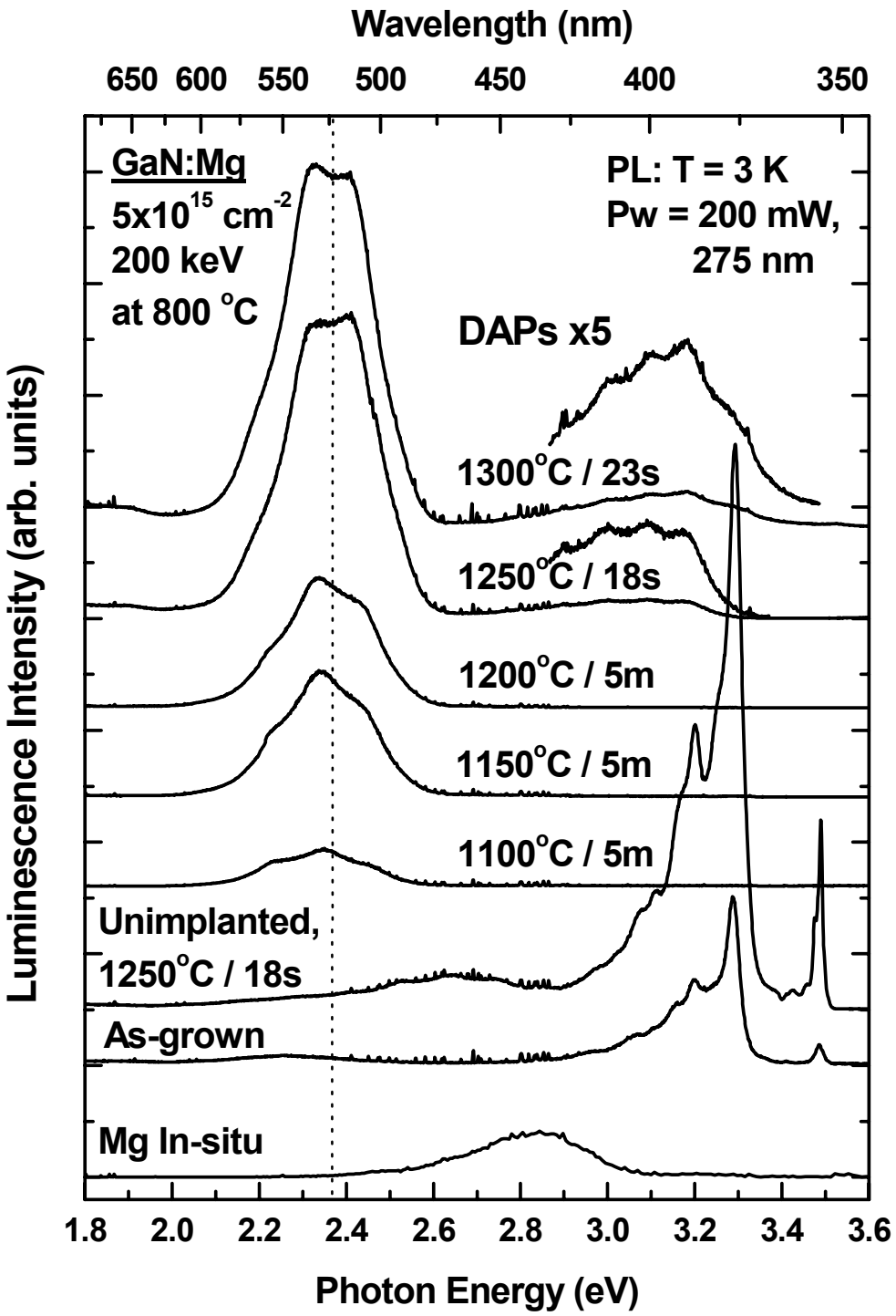

Figure 15. PL spectra taken at 3 K for GaN implanted with Mg and annealed at various temperatures from 1100-1300 °C. Also shown are the spectra from two unimplanted samples and an *in-situ* Mg-doped sample.

Mg-implanted GaN has been reported previously and attributed to Mg-induced defect clustering or to residual implantation defects (Chi *et. al.*, 1998; Skromme and Martinez, 2000; Ronning *et. al*., 2000). Also, the samples annealed at 1250 and 1300 ^{o}C show a fairly broad weak violet luminescence (VL) peak centered at 3.09 and 3.18 eV, respectively. The 3.09 eV peak has previously been reported for Mg-doped MOCVD GaN layers, and is attributed to a Mg-related deep DAP peak (Hess *et. al.*, 1998). The broad peak centered at 3.18 eV for the sample annealed at 1300 ^{o}C has been attributed to a deepening of the widely accepted DAP peak at 3.28 eV in GaN. This DAP red-shift has been observed in GaN doped with a Mg concentration greater than or equal to $1x10^{19}$ cm^{-3} (Grandjean *et. al*., 1998). TRIM simulation for 200 keV Mg at a dose of $5x10^{15}$ cm^{-2} implanted into GaN through a 500 Å cap produces a peak concentration of about $2x10^{20}$ cm^{-3}. At this high Mg concentration, the increased formation of Mg-related deep donors reportedly shifts the dominant DAP transition from 3.28 eV to as low as 2.85 eV. Thus, the 3.09 and 3.18 eV peaks are likely localized Mg-related DAP transitions with associated phonon replicas. The blue-shift and slight intensity increase of the shallow DAP peak as the anneal temperature increases from 1250 to 1300 ^{o}C may be due to more Mg being incorporated as a substitutional shallow acceptor as well as more crystalline lattice damage removal. The *in-situ* Mg-doped MOCVD-grown sample shows a broad BL band centered at 2.85 eV, whereas none of the Mg-implanted samples show this peak which has been attributed to a deep donor to effective mass Mg acceptor (Mg_{Ga}) transition (Kaufmann *et. al*., 1999).

Figure 16 shows the PL spectra taken at 3 K from GaN coimplanted at 800 ^{o}C with Mg and either P, C, or O, and annealed at 1250 ^{o}C for 18 s. The band edge

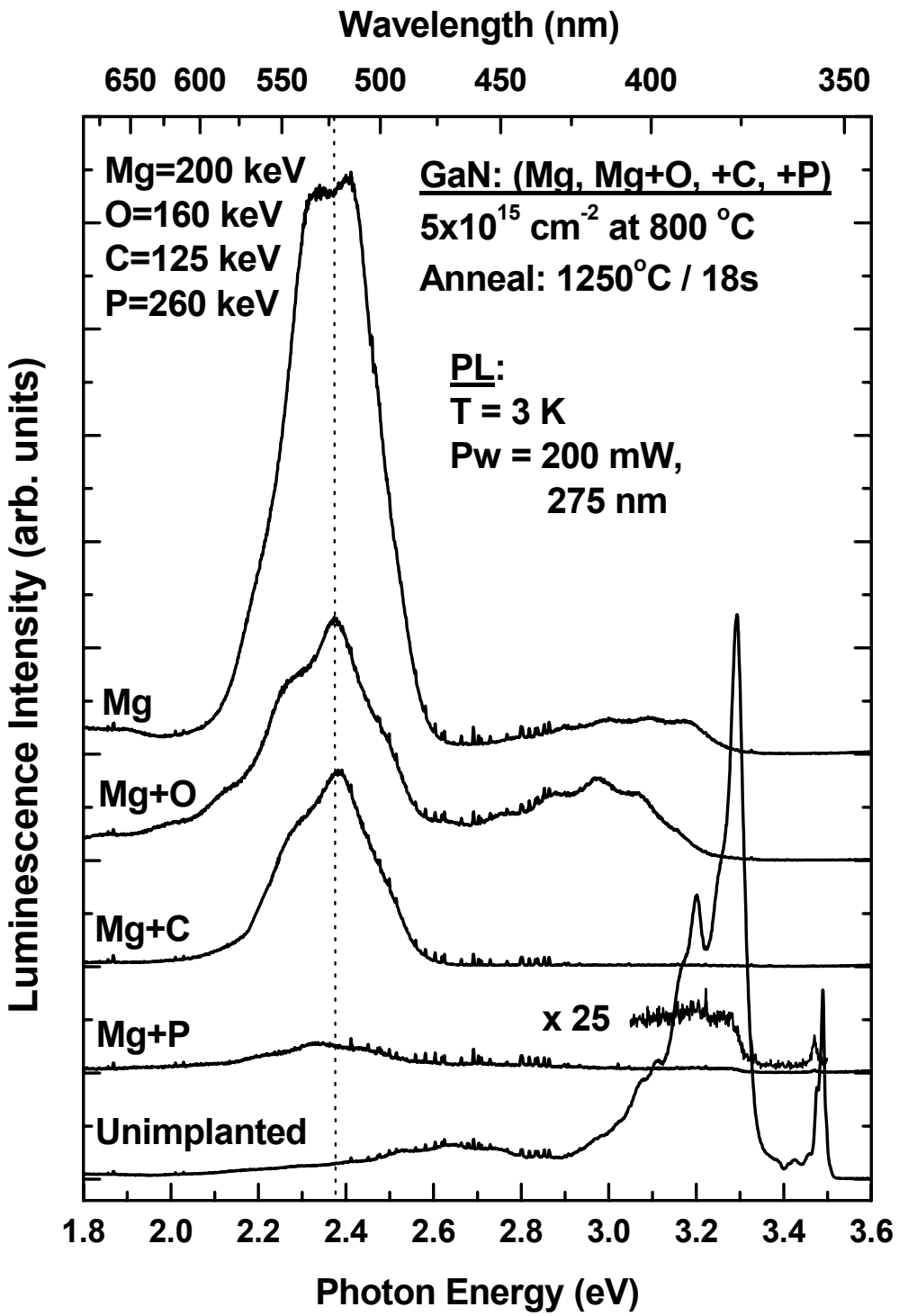

Figure 16. PL spectra taken at 3K for GaN implanted with Mg and various coimplants annealed at 1250 ^{o}C for 18 s.

luminescence peaks were not observed from these dual implanted samples, except the Mg+P sample. Each of these Mg-coimplanted samples shows a dominant GL peak occurring at 2.37 eV. The luminescence peak intensity is weakest for the Mg+P sample and strongest for the sample implanted with Mg-alone. Although the Mg+P spectrum is the weakest, it shows a discernible DAP peak at 3.28 eV with phonon replicas and a weak (A^o,X) peak at 3.470 eV, as previously reported (Skromme and Martinez, 2000). Also, the Mg+O sample shows a broad peak centered at 2.97 eV, which will be discussed further later in Figs. 17 and 23.

Figure 17 shows the PL spectra taken at 3 K from the dual implanted GaN with Mg+C, Mg+O, and Mg+P annealed at two different temperatures. The former two samples were annealed at 1300 and 1250 ^oC for 9 and 18 s, respectively, and the Mg+P sample was annealed at 1250 ^oC for 18 s. The Mg+P sample implanted with a lower dose of $5x10^{14}$ cm^{-2} shows a broad BL band centered at 2.75 eV nearly as intense as the GL peak. This 2.75 eV band may be closely related to the widely accepted 2.8 eV peak of the deep donor to Mg_{Ga} transition band. For the Mg+O samples, the intensity of the GL peak at 2.37 eV increased considerably when the anneal temperature is increased from 1250 to 1300 ^oC, whereas the intensity of the GL peak from the Mg+C samples rather reduced considerably when the anneal temperature is increased from 1250 to 1300 ^oC. Increasing the anneal temperature from 1250 to 1300 ^oC for the Mg+O samples seems to shift the weak broad BL band centered at 2.97 eV to another broad BL band centered at 3.13 eV, similar to the blue-shift observed for the Mg-alone samples as the anneal temperature is increased from 1250 to 1300 ^oC. However, the individual peaks of the Mg+O samples do not occur at the same positions as they do for the Mg-alone

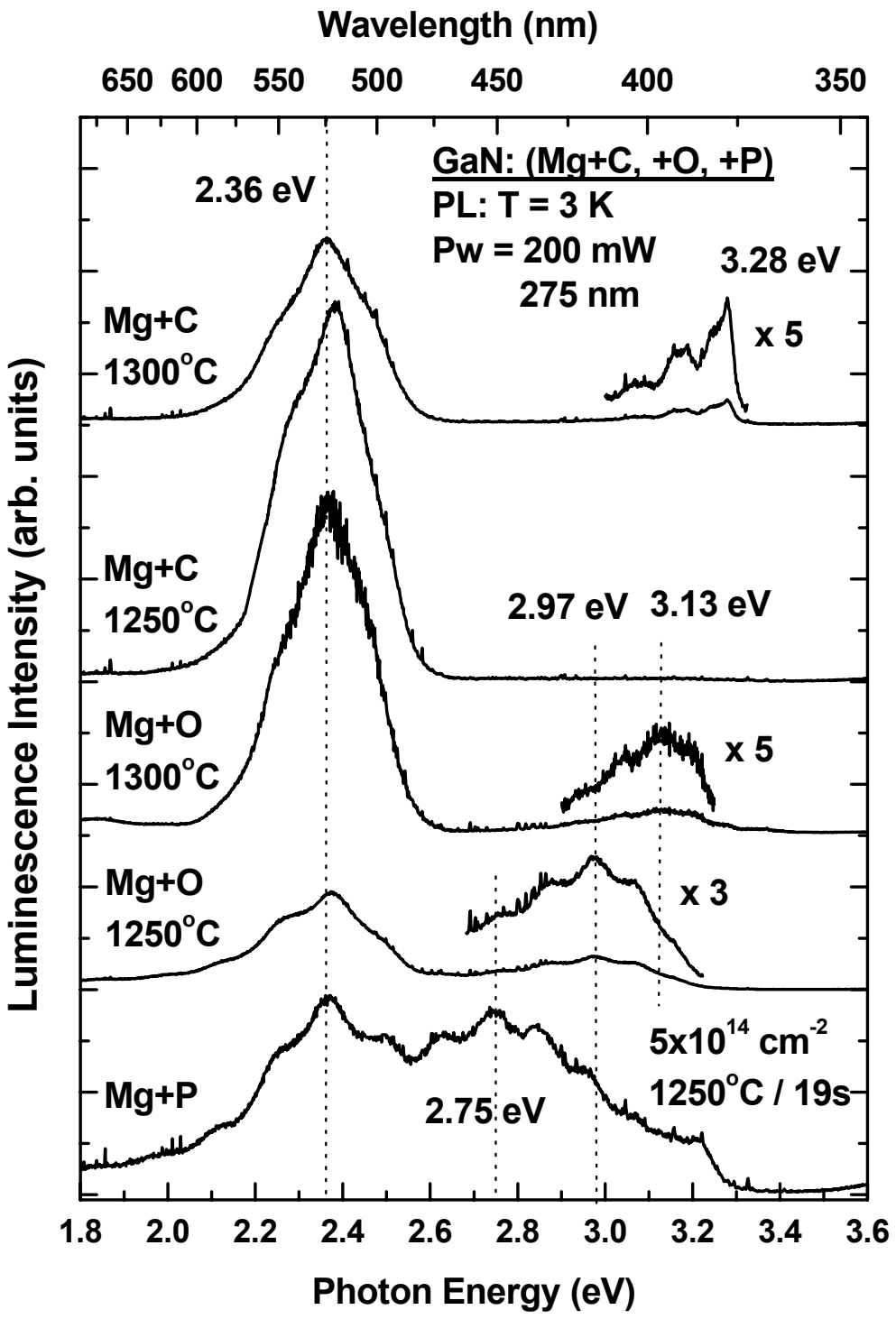

Figure 17. PL spectra taken at 3K for GaN implanted with Mg+C, Mg+O, and Mg+P at various doses and anneal temperatures.

samples. Although the GL peak intensity from the Mg+C sample annealed at 1300 ^{o}C decreased compared to that of the sample annealed at 1250 ^{o}C, the former shows a nicely shaped DAP peak at 3.28 eV, implying that a significant amount of the implantation damage has been recovered after annealing at this temperature.

The CL spectra obtained at 10 K from GaN implanted at either 25 or 500 ^{o}C with 200 keV Mg at a dose of $2x10^{15}$ cm^{-2} and annealed at various temperatures for 20 min are shown in Figure 18. These samples are from the set of 1 μm thick GaN capped with 1000 Å thick AlN after implantation. A 2.37 eV GL peak which increases with anneal temperature dominates each spectrum. The sample annealed at 1100 ^{o}C shows no band-edge or DAP luminescence indicating that an 1100 ^{o}C anneal is insufficient to adequately remove implantation damage. This damage tends to limit all luminescence by preventing exciton formation and providing non-radiative recombination paths. A weak 3.28 eV DAP peak with 1LO begins to emerge in the spectra of the two samples annealed at 1150 ^{o}C. Both samples annealed at 1150 ^{o}C show comparable intensities in both GL and DAP peaks. However, the intensity of both the GL and DAP increases in the sample annealed at 1200 ^{o}C indicating at least more implantation damage removal if not more shallow Mg_{Ga} activation.

The CL spectra for GaN implanted at 25 ^{o}C with Mg, Si, and Mg+Si at a dose of $2x10^{15}$ cm^{-2} for Mg and $1x10^{15}$ cm^{-2} for Si, and annealed at 1100 ^{o}C for 20 min are shown in Figure 19. The Si-implanted sample shows a 2.2 eV YL band and a weak 3.28 eV DAP peak, whereas the Mg-implanted sample shows only a 2.38 eV GL peak. The Mg+Si-implanted sample shows a dominant 2.35 eV GL peak and a strong 3.28 eV DAP peak. It appears that the shallow DAP activity in the sample implanted with Mg+Si is

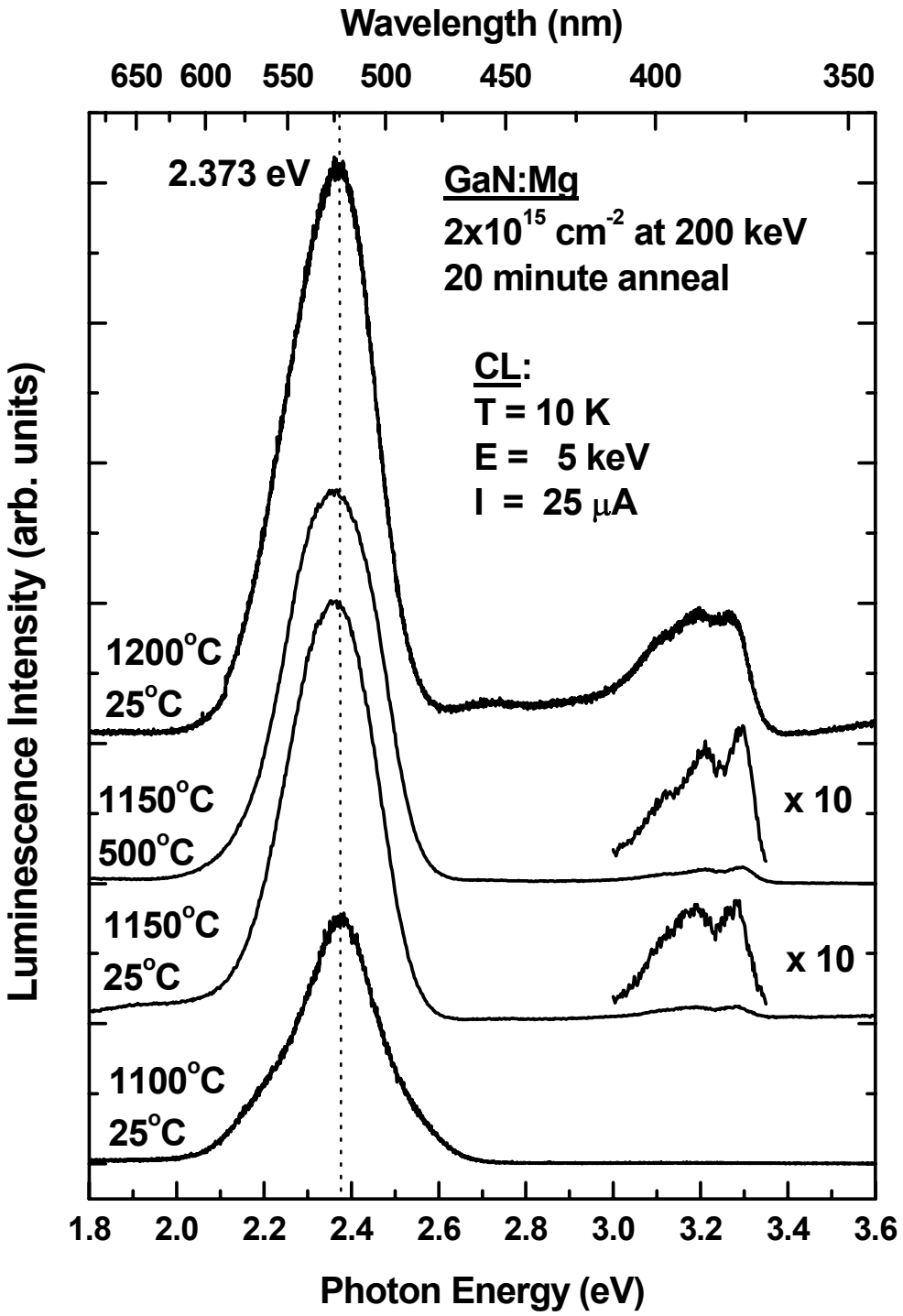

Figure 18. CL spectra taken at 10 K for GaN implanted with 200 keV Mg at either 25 or 500 ^{o}C and annealed at various temperatures from 1100-1200 ^{o}C for 20 minutes.

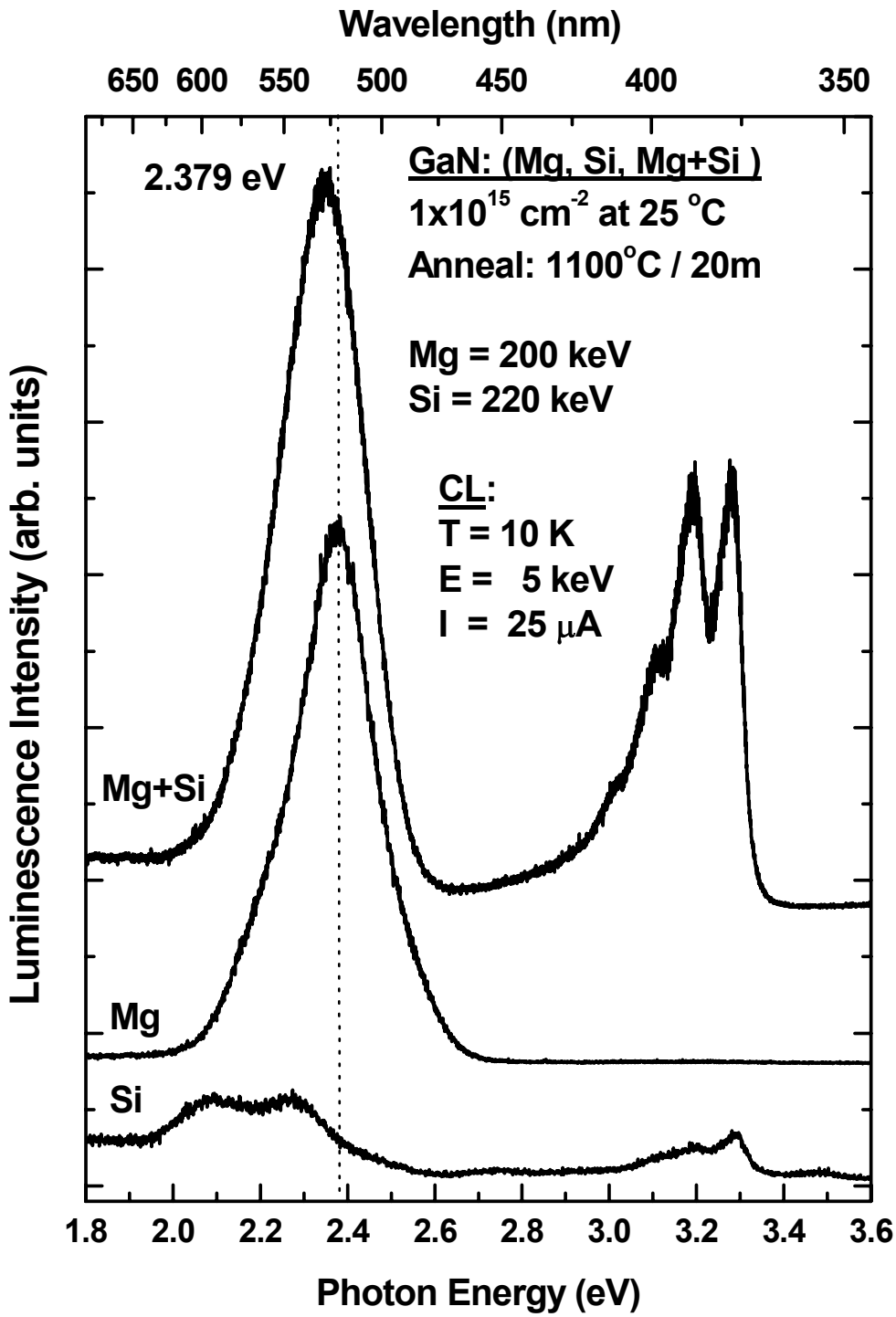

Figure 19. CL spectra taken at 10 K for GaN implanted at 25 °C with Mg, Si, and Mg+Si at a dose of $1x10^{15}$ cm^{-2} for Si and $2x10^{15}$ cm^{-2} for Mg, and annealed at 1100 °C for 20 minutes.

due to the presence of both Mg and Si since neither Mg-alone nor Si-alone have such a strong peak. This sample will be discussed further in Figure 20.

The CL spectra taken at 10 K from GaN coimplanted at either 25 or 500 ^{o}C with Mg+Si annealed at either 1100 or 1150 ^{o}C for 20 min are shown in Figure 20. All the spectra show two distinct peaks: a DAP peak at 3.28 eV and a GL peak at 2.35 eV. Interestingly, the intensity variations of these two peaks show an inverse relationship; that is, the higher the DAP peak intensity, the weaker the GL peak intensity. This may indicate that these two peaks are interrelated to the same ion species. Because the 3.28 eV DAP peak is due to a transition from a shallow donor, most likely Si, to a shallow acceptor, and the 2.35 eV GL peak is Mg-related, we may conclude that the acceptor involved in the 3.28 eV peak is Mg_{Ga}.

Figure 21 shows the PL spectra taken at 3 K from GaN coimplanted at either 25 or 500 ^{o}C with Mg+Si annealed from 1150 to 1300 ^{o}C. All Mg+Si coimplanted samples are from the set of 1 μm thick GaN and are not affected by Fabry-Pérot interference fringes, thus allowing greater accuracy in identifying asymmetries, shifts in peak positions, and individual peaks within the GL bands. Consistent with all of the Mg-implanted material in this study, a strong GL peak is seen in each spectra independent of the anneal time or temperature, which, unlike the GL peaks seen in Fig. 18, is asymmetric with sub-peaks ranging from 2.30-2.41 eV. This asymmetry is likely due to the Si coimplant producing another deep level from which to transition. At each anneal temperature, the GL from the sample implanted at 500 ^{o}C is more intense than from the sample implanted at room temperature. A more interesting observation is the effect of

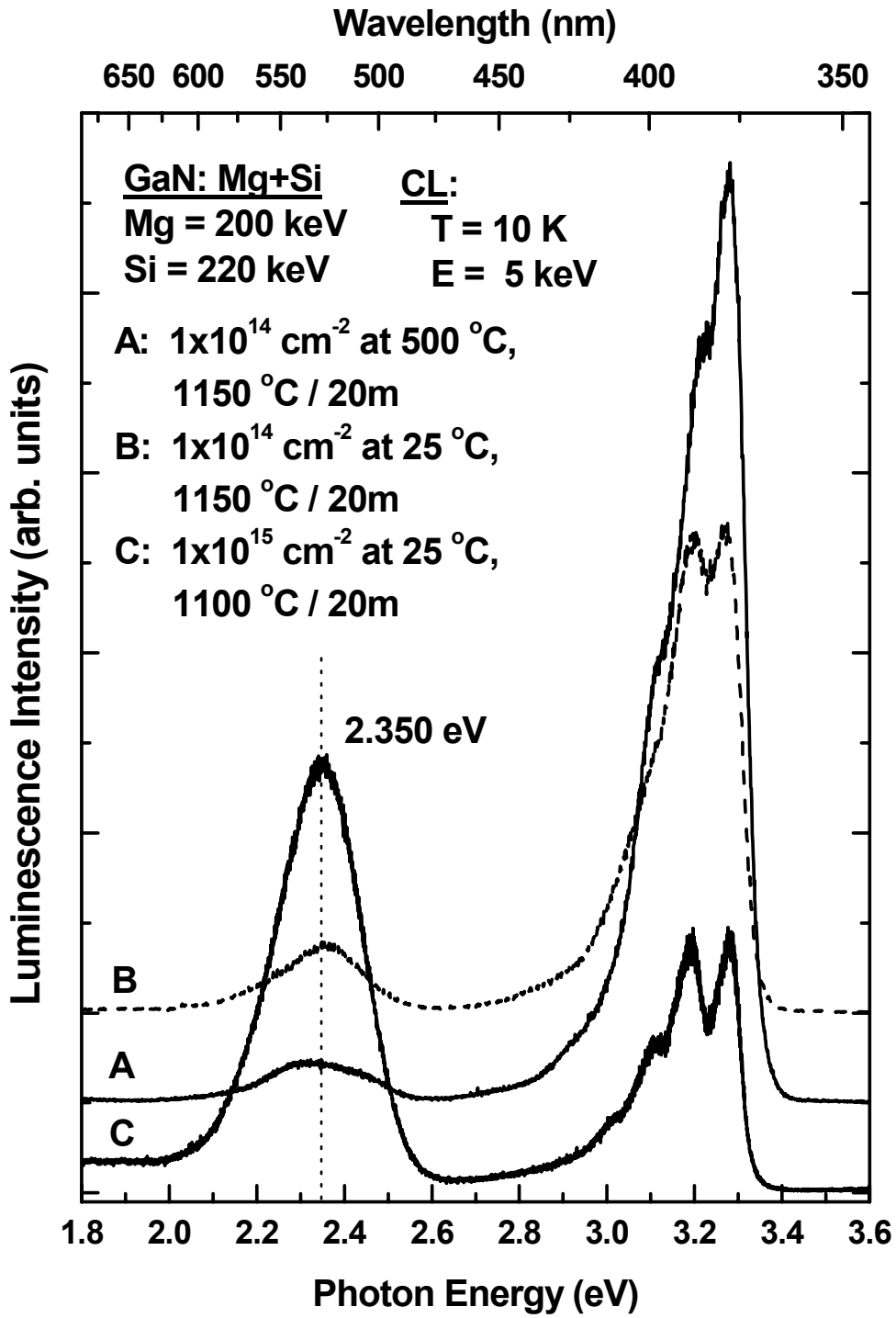

Figure 20. CL spectra taken at 10 K for GaN coimplanted at either 25 or 500 ^{o}C with Mg+Si at a dose of $2x10^{15}$ cm^{-2} for Mg and $1x10^{15}$ cm^{-2} for Si. Samples were annealed at either 1150 or 1100 ^{o}C for 20 min.

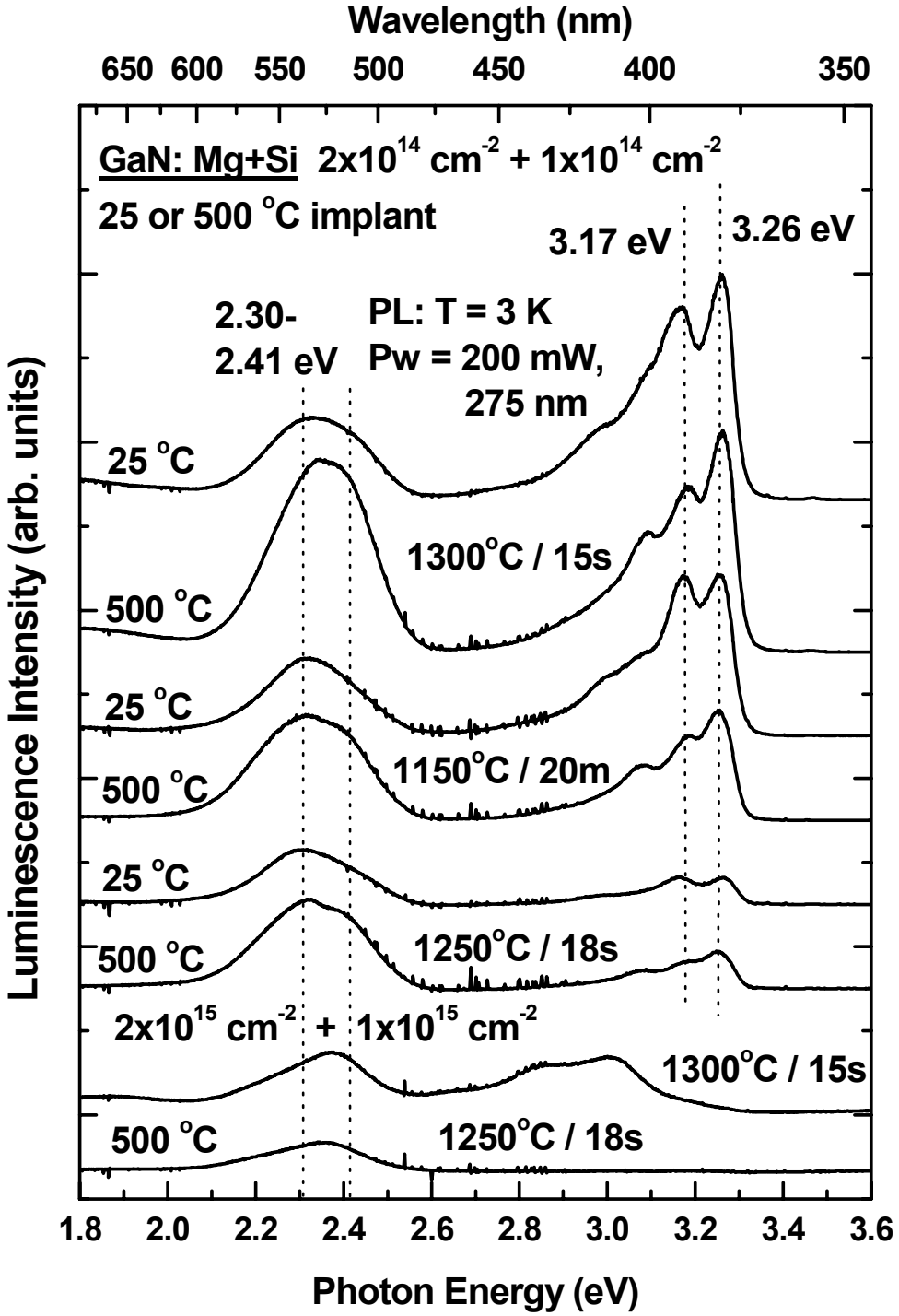

Figure 21. PL spectra for GaN coimplanted at either 25 or 500 °C with Mg+Si at doses of $2x10^{14}$ cm^{-2} for Mg and $1x10^{14}$ cm^{-2} for Si and annealed at various temperatures from 1150-1300 °C and times from 15 sec to 20 min.

anneal time on the spectra. A 20-min anneal at 1150 ^{o}C produces greater intensity in the DAP peaks than an 18-sec anneal at 1250 ^{o}C. The greatest intensity in both GL and DAP peaks is seen after annealing at 1300 ^{o}C for 15 sec independent of implant temperature. This suggests that annealing at lower temperatures requires longer anneal times to remove implantation damage and activate implanted ions as efficiently as annealing at somewhat higher temperatures for shorter times. Each of the samples implanted with a dose on the order of 10^{14} cm^{-2} shows a DAP peak at 3.26 eV with a 1LO peak at 3.17 eV, whereas the samples implanted with a dose on the order of 10^{15} cm^{-2} show no shallow DAP peak. The sample implanted with a dose on the order of 10^{15} cm^{-2} and annealed at 1250 ^{o}C shows only a GL peak, while the sample annealed at 1300 ^{o}C shows additional peaks at 2.87 and 3.00 eV. The greater implantation damage in the samples implanted with the higher dose at 500 ^{o}C appears to require a higher anneal temperature to realize DAP activity than do the samples implanted with the lower dose. Furthermore, such DAP transitions are likely to involve deeper levels, perhaps donor and acceptor related complexes. It is also likely that the 2.87 and 3.00 eV DAP transitions involve interim deep states and may be supplanted by the more typical shallow states of the 3.28 eV DAP transitions as seen from spectrum C in Fig. 20.

Temperature-dependent Photoluminescence.

Temperature-dependent PL spectra from GaN implanted at 800 ^{o}C with 200 keV Mg at a dose of $5x10^{15}$ cm^{-2} and annealed at 1300 ^{o}C for 23 s are shown in Figure 22. The two primary features of these spectra are a dominant GL band at 2.36 eV and a broad VL band centered around 3.15 eV. The intensity of the VL band has been increased by a

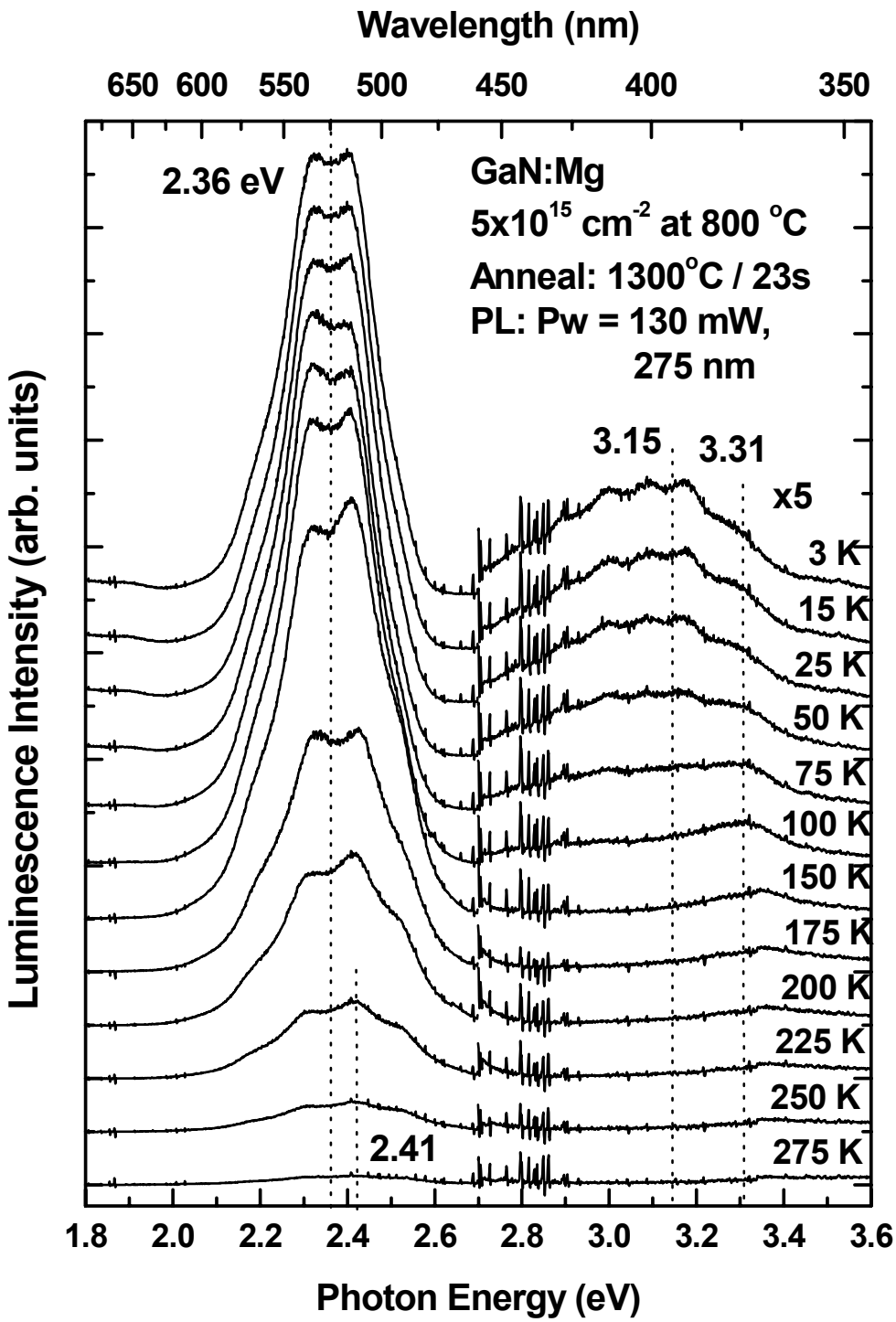

Figure 22. Temperature-dependent PL spectra for GaN implanted at 800 ^{o}C with 200 keV Mg at a dose of $5x10^{15}$ cm^{-2} and annealed at 1300 ^{o}C for 23 sec.

factor of 5 to better observe its thermal characteristics. The intensity of the GL band remains relatively constant as the temperature is increased from 3 to 150 K, above which the intensity drops rapidly. The GL intensity drops to approximately 50% of its low-temperature value at 175 K and to about 2% at 275 K. As the temperature is increased, the peak position of the GL peak blue-shifts 50 meV from 2.36 eV at 3 K to about 2.41 eV at 275 K. This temperature induced shift is opposite of the shift expected from the variation of the bandgap, which decreases about 54 meV over the same temperature range (3-275 K). However, the blue-shift observed in this GL is typical for defects with strong electron-phonon coupling and is predicted by the configuration coordinate model for DAP recombinations (Reshchikov *et. al.*, 2001; Zhang and Kuech, 1998). The GL band could be due to a transition from a deep donor-to-deep acceptor (D_dA_dP) with at least one of these levels caused by a Mg-related complex. Alternatively, the near 50 meV blue-shift observed in the GL band could be the result of the GL changing from a DAP to a (e,A^o) transition as temperature increased from 3 to 275 K. In this model, approximately 12 meV of the actual 104 meV shift (50 meV observed + 54 meV to overcome the bandgap decrease) is due to the kinetic energy of the thermally excited free electrons. By subtracting the expression for DAP luminescence from that for (e,A^o) luminescence given by eqs. (24) and (25), the donor level may be estimated:

$$\hbar\omega_{(e,A^o)} - \hbar\omega_{(DAP)} = E_g(275\text{K}) - E_g(3\text{K}) + \frac{k(275\text{K})}{2} + E_d - \frac{e^2}{\kappa r}. \qquad (26)$$

An empirical expression for the bandgap energy of GaN as a function of absolute temperature is found is Appendix C along with a graph of E_g versus T. Assuming a nominal coulombic energy of 10 meV, the donor level, E_d, associated with the DAP to

(e,A^o) GL model is about 102 meV, and the deep acceptor level, E_a, would be about 1.05 eV. This acceptor level is perhaps too deep to account for the nearly full quenching of the GL peak at a temperature of 275 K. Thus, the GL is more likely attributed to a Mg-related D_dA_dP.

The intensity of the VL band centered at about 3.15 eV quenches more rapidly than the GL band, reaching approximately 50% of its low-temperature value at 50 K. A new peak at 3.31 eV begins to dominate the UV features at 75 K and virtually all evidence of the 3.15 band that dominated at low-temperature is gone at 150 K. The weak 3.31 eV peak quenches slowly and blue-shifts 60 meV to about 3.37 eV at 225 K. Because of its wide bandgap, DAP transitions in GaN frequently involve donor and acceptor levels where one level is 200 meV or more deeper than the other. When the donor level is shallower than the acceptor level, the shallow donors will thermally ionize as temperature is increased quenching the DAP luminescence. However, this leaves the deeper neutral acceptor levels ready to accept the excited photoelectrons from the conduction band via a (e,A^o) transition. The 3.31 eV peak has been previously attributed to a (e,A^o) transition involving Mg (Kaufmann *et. al.*, 1999). Using equation (24) for free-to-bound luminescence at a temperature of 75 K, the 3.31 eV transition corresponds to a Mg level of 192 meV which is comparable to the 200 meV value commonly reported. If the band at 3.15 eV is due to DAP transitions involving shallow Mg acceptors, then the donor level is easily found. When 192 meV is used in equation (25) along with a nominal coulombic energy of 10 meV, a donor energy of 171 meV is obtained. Although this value is well below the range (280-430 meV) reported for the

Mg-related deep donor complex, Mg_{Ga}-V_N, it could account for the quenching of the 3.15 eV DAP band and subsequent revealing of the weak 3.31 eV (e,A^o) transition.

Temperature-dependent PL spectra from GaN implanted at 800 ^oC with Mg+O at a dose of $5x10^{15}$ cm^{-2} for Mg and $2x10^{15}$ cm^{-2} for O, and annealed at 1250 ^oC for 18 s are shown in Figure 23. The two features of these spectra are a dominant GL band at 2.35 eV and a broad VL band centered at 2.97 eV. It must be noted that although the GL band peaks at 2.373 eV, the band is not centered at 2.373 eV due to the etalon effect. If the etalon peaks were symmetric about the band as they are on the spectrum collected at 200 K, then the peak intensity would be an accurate measure of the band center. Due to the asymmetry in the etalon peaks, the true band center will be shifted toward the side with more luminescence, which in this case is lower in energy. The intensity of the GL peak centered at 2.352 eV remains about the same as the temperature increases up to 150 K, then slowly decreases as the temperature increases to 230 K, and finally decreases rapidly around 260 K. This temperature-dependent behavior may indicate that this GL peak could be due to a transition from an effective-mass acceptor to a deep donor complex. The GL band center blue-shifts about 48 meV from 2.352 eV at 3 K to about 2.40 eV at 260 K. The thermal characteristics of the GL band for the sample implanted with Mg+O are very similar to the GL band for the sample implanted with Mg-alone seen in Fig. 22. Because of these similarities, the DAP to (e,A^o) GL model will likewise result in an acceptor energy too deep to account for both the observed blue-shift and the rate of GL thermal quenching. Based upon the rate of GL quenching with temperature, the GL band may be attributed to a D_dA_dP transition involving complexes, where at least one of

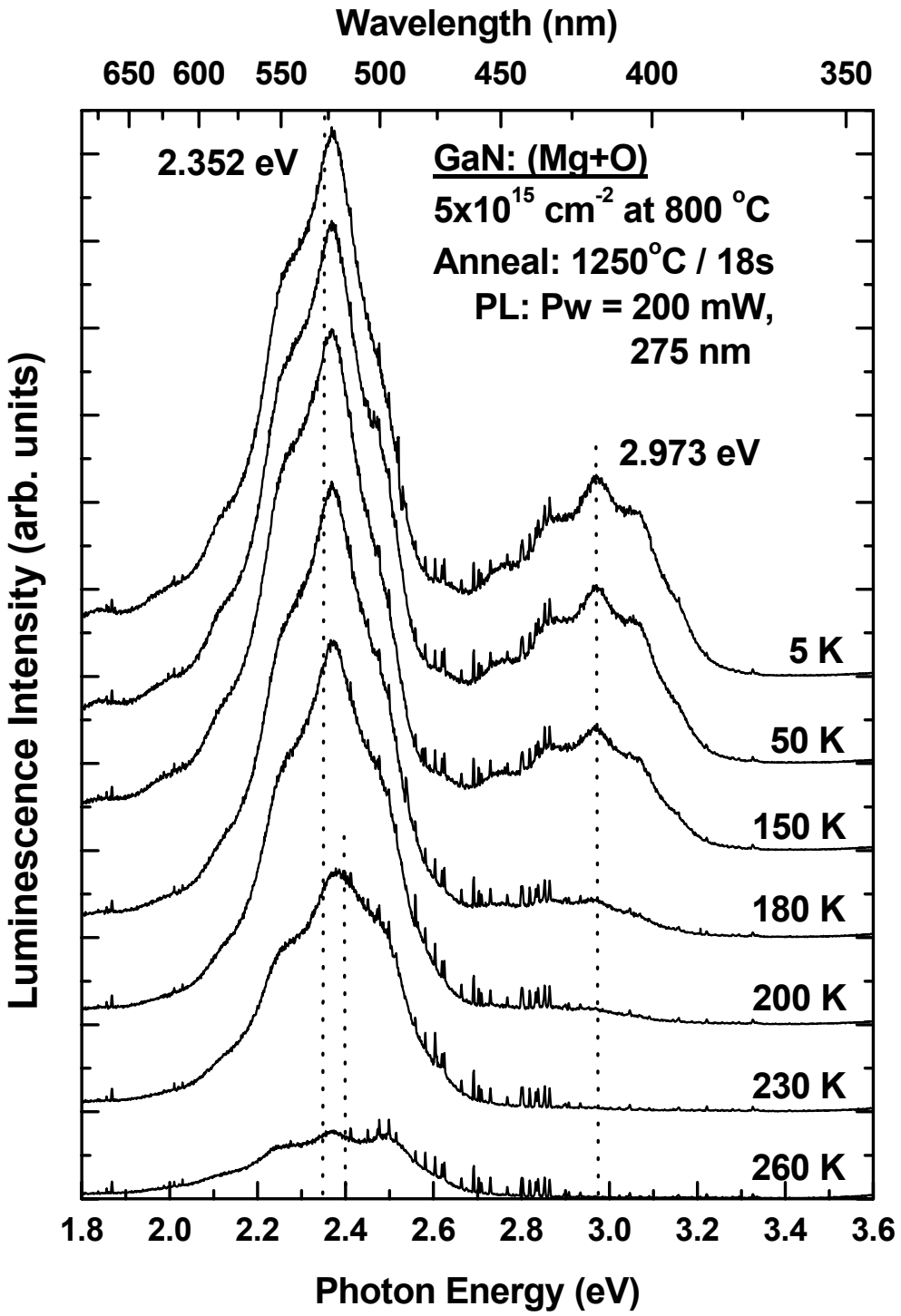

Figure 23. Temperature-dependent PL spectra for GaN implanted at 800 °C with Mg+O at doses of $5x10^{15}$ cm^{-2} for Mg and $2x10^{15}$ cm^{-2} for O and annealed at 1250 °C for 18 s.

the two participating levels is Mg-related. In the D_dA_dP model for GL, the observed blue-shift is explained by strong electron-phonon coupling.

The intensity of the broad BL peak centered at 2.973 eV decreases slowly as the temperature increases up to 150 K, then quickly quenches above ~150 K. This temperature-dependent behavior indicates that a level much shallower than either of the levels associated with the GL DAP peak is responsible for the 2.973 eV peak. Sheu *et. al.* grew Mg-doped GaN and attributed a 2.95 eV PL peak at 20 K to a DAP transition involving a Mg-related deep acceptor having an energy level of 510 meV above the valence band (Sheu *et. al.*, 1998). Because this sample was implanted with a high dose of O, it is reasonable to assume that the shallow donor participating in the transition is O, which is reported to have an optical binding energy similar to but slightly higher than that of Si (Niebuhr *et. al.*, 1997). Thus, taking O_N to be 40 meV and the coulombic energy to be 20 meV results in the observed DAP luminescence energy of 2.973 eV according to eqn. (25).

Figure 24 shows the temperature-dependent PL spectra from GaN implanted at 500 ^{o}C with Mg+Si at a dose of $2x10^{14}$ cm^{-2} for Mg and $1x10^{14}$ cm^{-2} for Si, and annealed at 1300 ^{o}C for 23 s. These spectra show a strong DAP peak with phonon replicas and a broad GL band nearly as intense. This sample was from the set of 1 μm-thick GaN, which was not affected by Fabry-Pérot interference fringes. The intensity of the GL band centered at 2.362 eV remains fairly constant as temperature is increased to 150 K, at which point it begins to drop quickly and at 250 K is less than 2% of its low-temperature value. The GL band blue-shifts 62 meV as temperature is increased to 250 K where the peak occurs at 2.424 eV. This temperature behavior is very similar to that of the GL

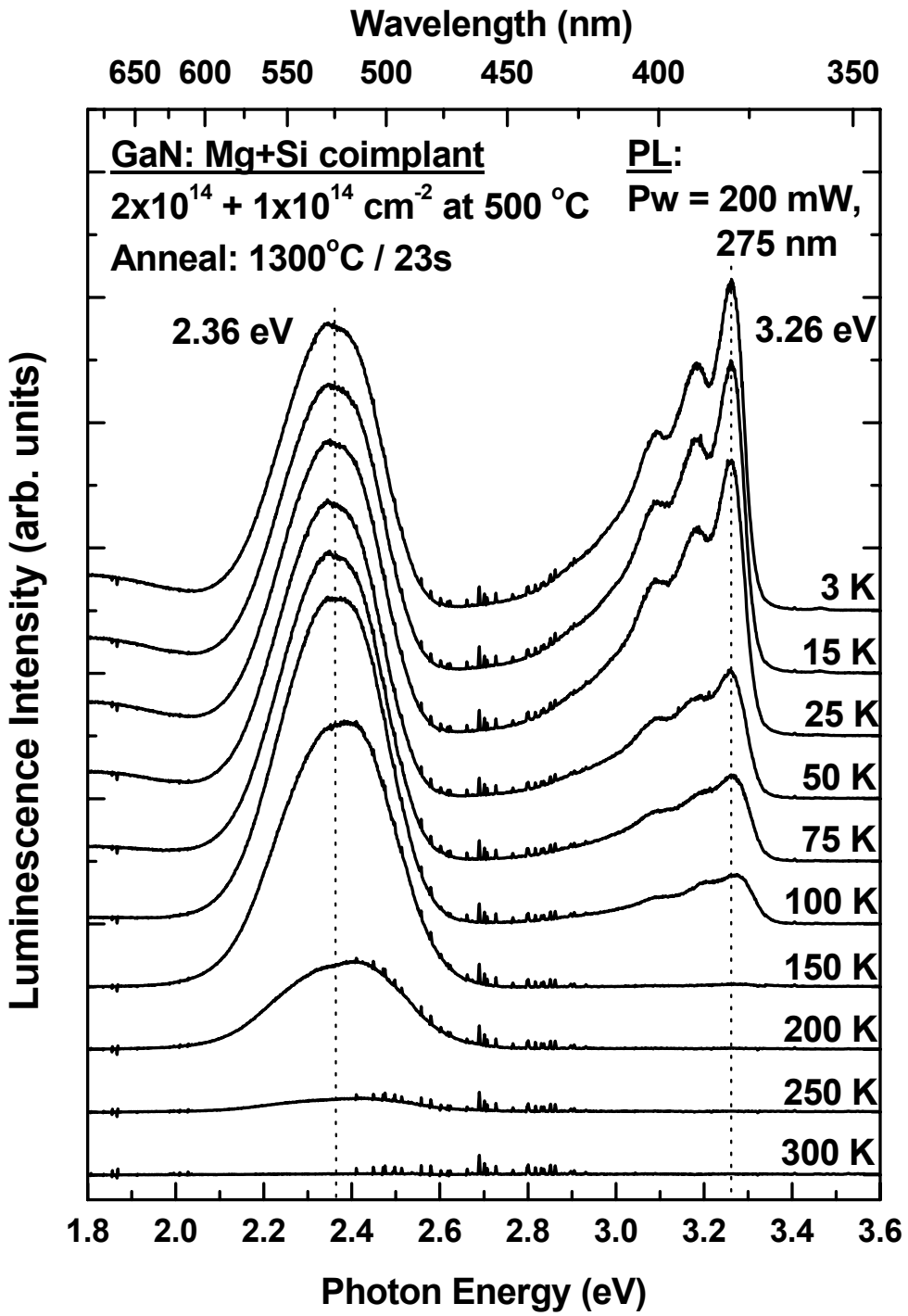

Figure 24. Temperature-dependent PL spectra for GaN coimplanted at 500 °C with Mg+Si at doses of $2x10^{14}$ cm^{-2} for Mg and $1x10^{14}$ cm^{-2} for Si and annealed at 1300 °C for 23 sec.

band in the Mg+O- and Mg-implanted samples and further supports the position that the GL band is the result of a Mg-related deep donor to deep acceptor transition. The PL intensity of the zero-phonon DAP peak at 3.262 eV drops slowly as temperature is increased from 3 K to 25 K, then more rapidly, and finally quenches almost completely by 150 K. The temperature behavior of this undisputed DAP peak is remarkably similar to the band attributed to the DAP peak from the Mg-implanted sample seen in Fig. 22. The behavior of the DAP bands in the spectra shown in Figs. 8-10 is very different from the GL bands observed in all three samples implanted or coimplanted with Mg. Both DAP bands from the Mg- and Mg+Si-implanted samples are fully quenched at 150 K, and the DAP band from the Mg+O-implanted sample is still 18% of its low-temperature intensity at 180 K. Although the GL bands don't fully quench until after 250 K or higher, Mg_{Ga} may still be the responsible acceptor level in the GL DAP transition. However, if this is the case then the corresponding donor level is very likely a Mg-related deep donor complex for two reasons. Firstly, a much deeper level than Mg (on the order of 0.9 eV) would be necessary to produce the observed luminescence energy and thermal quench rate. Secondly, due to the high intensity of the GL bands, the samples would not be extremely resistive were it not for a proportional concentration of self-compensating centers.

Li, Li+P, and C were implanted into GaN at 800 ^{o}C with doses of $5x10^{15}$ cm^{-2} and annealed at temperatures from 1200-1300 ^{o}C, because both Li and C were reported to act as acceptors potentially shallower than Mg. The corresponding PL spectra taken at 3 K are shown in Figure 25 along with the spectra from an unimplanted sample annealed at 1250 ^{o}C and the spectra of an *in-situ* Mg-doped sample. All samples implanted with

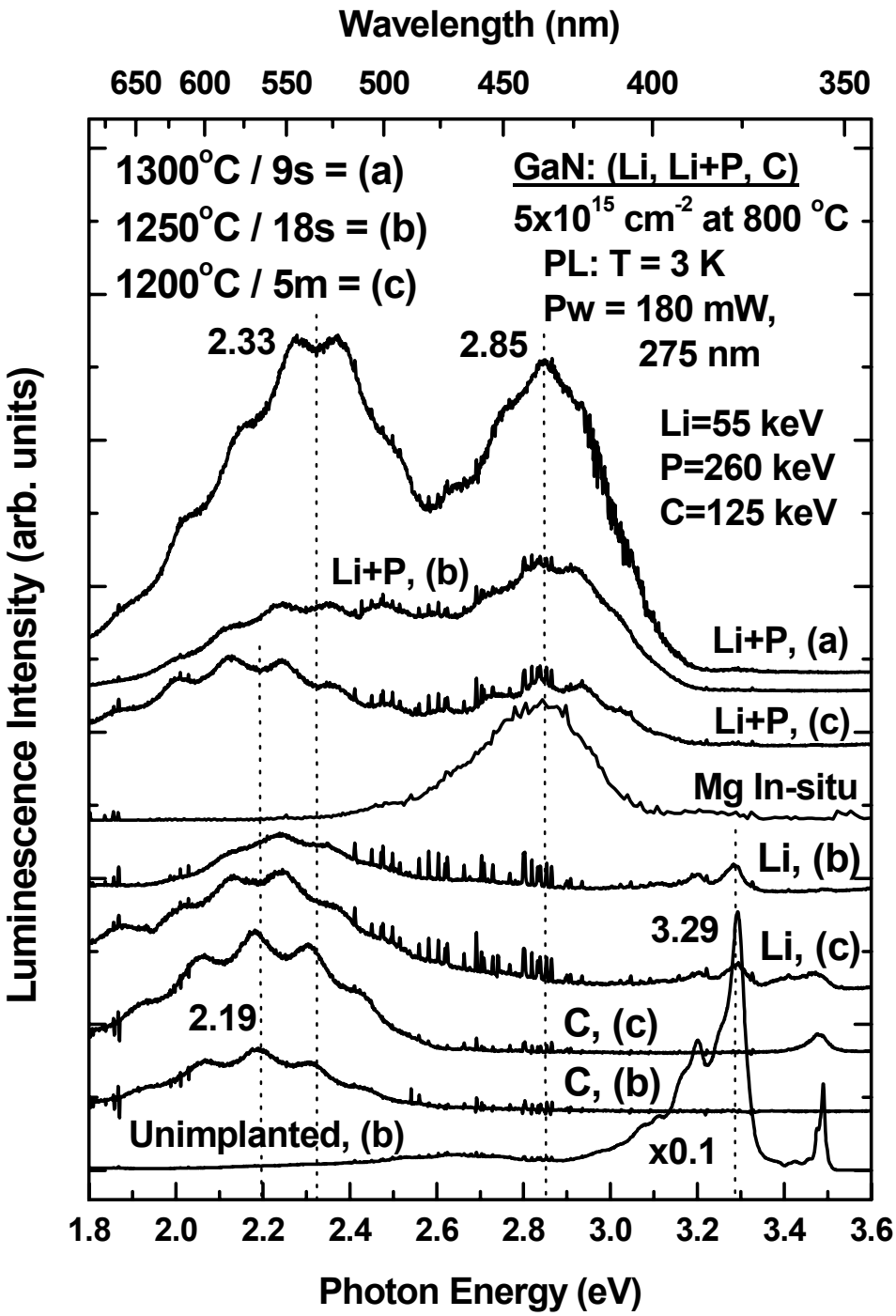

Figure 25. PL spectra taken at 3K for GaN implanted at 800 °C with Li, Li+P, and C annealed at various temperatures from 1200-1300 °C and times from 9 sec to 5 min. Also shown are the PL spectra for unimplanted GaN annealed at 1250 °C and *in-situ* Mg-doped GaN.

Li+P have a characteristic BL peak at 2.85 eV, which is rather similar to the only spectral feature of the *in-situ* Mg-doped sample. The samples implanted with Li+P also show a second peak that blue-shifts from YL to GL as the anneal temperature is increased from 1200 to 1300 ^{o}C. Both samples implanted with Li-alone show a broad YL-GL band and a weak 3.29 eV DAP peak with phonon replica. The sample implanted with Li and annealed at 1200 ^{o}C for 5 min also has a weak but broad band-edge peak which is most likely a (D^{o},X) peak. The two samples implanted with C are dominated by a broad YL band centered at 2.19 eV, which is common in unintentionally doped or moderately Si-doped GaN samples. Like the sample implanted with Li, the sample implanted with C and annealed at 1200 ^{o}C for 5 min also shows a (D^{o},X) peak. Of the spectra shown in this figure, recovery of the exciton peak is limited to single implant samples annealed at the lowest temperature, but for a longer time, providing further evidence that a longer anneal time may be necessary to more fully remove the implantation damage.

Electrical Characterization of Acceptor-implanted GaN.

In the recent years, a great many attempts have been made to produce highly conductive *p*-type GaN. Due to the relatively large ionization energy of acceptors in GaN and the tendency of many defects in GaN to behave as donors, the pursuit of high conductivity *p*-type GaN has been difficult, especially when doping via ion implantation. Although a significant amount of work has been done on acceptor ion-implanted GaN, only a limited amount of success has been reported in producing *p*-type conductive GaN via Mg (Rubin *et. al.*, 1994; Pearton *et. al.*, 1995), Ca (Zolper *et. al.*, 1996), or Be (Sun *et. al.*, 2000) implantation which is not easily reproducible by other laboratories. This study examined acceptor implanted GaN focusing on the potential advantages of a variety

of coimplants, high temperature implantation, novel AlN encapsulant techniques, and very high temperature annealing. Table 3 lists the implanted species, dose, energy, implantation temperature, and anneal conditions of the acceptor implanted samples that survived annealing and from which electrical and/or optical characterization data were collected. The two different sets of material distinguished by GaN epilayer thickness and encapsulation technique are differentiated in Table 3.

Table 3. Acceptor Implantation and Anneal Conditions

Ion Species	Dose (cm^{-2})	Energy (keV)	Temperature (^oC)	Anneal Temp (^oC) / Time
1000 Å AlN grown after implantation into 1 μm GaN				
Mg	$2x10^{14}$	200	25	950 / 60 min 1150 / 15 sec
Mg	$2x10^{15}$	200	25	1100 / 20 min 1150 / 5 min 1150 / 20 min 1200 / 20 min
Mg	$2x10^{14}$	200	500	1150 / 15 sec 1150 / 20 min
Mg	$2x10^{15}$	200	500	1150 / 20 min
Mg +Si	$2x10^{14}$ $1x10^{14}$	200 220	25 25	1150 / 20 min 1250 / 18 sec 1300 / 5 sec
Mg +Si	$2x10^{15}$ $1x10^{15}$	200 220	25 25	1100 / 20 min 1250 / 18 sec
Mg +Si	$2x10^{14}$ $1x10^{14}$	200 220	500 500	1150 / 20 min 1250 / 18 sec 1300 / 23 sec
Mg +Si	$2x10^{15}$ $1x10^{15}$	200 220	500 500	1250 / 18 sec 1300 / 23 sec

Ion Species	Dose (cm^{-2})	Energy (keV)	Temperature (^oC)	Anneal Temp (^oC) / Time
Implantation through 500 Å AlN into 2 μm GaN				
Mg	$5x10^{15}$	200	800	1100 / 5 min 1150 / 5 min 1200 / 5 min 1250 / 18 sec 1300 / 23 sec 1350 / 17 sec
Mg	$5x10^{14}$	200	800	1250 / 19 sec 1300 / 23 sec 1350 / 17 sec
Mg	$5x10^{15}$	200	25	1250 / 18 sec 1300 / 23 sec
Mg +P	$5x10^{15}$ $5x10^{15}$	200 260	800 800	1200 / 5 min 1250 / 18 sec 1300 / 23 sec 1350 / 17 sec
Mg +P	$5x10^{14}$ $5x10^{14}$	200 260	800 800	1250 / 19 sec 1300 / 23 sec 1350 / 17 sec
Mg +P	$5x10^{15}$ $5x10^{15}$	200 260	25 25	1250 / 18 sec 1300 / 23 sec
Mg +C	$5x10^{15}$ $5x10^{15}$	200 125	800 800	1200 / 5 min 1250 / 18 sec 1300 / 9 sec 1350 / 17 sec
Mg +C	$5x10^{14}$ $5x10^{14}$	200 125	800 800	1350 / 17 sec
Mg +O	$5x10^{15}$ $2x10^{15}$	200 160	800 800	1200 / 5 min 1250 / 18 sec 1300 / 9 sec 1350 / 17 sec
Mg +O	$5x10^{14}$ $2x10^{14}$	200 160	800 800	1250 / 19 sec 1350 / 17 sec
Li	$5x10^{15}$	55	800	1200 / 5 min 1250 / 18 sec 1300 / 9 sec
Li +P	$5x10^{15}$ $5x10^{15}$	55 260	800 800	1200 / 5 min 1250 / 18 sec 1300 / 9 sec
Li +P	$5x10^{14}$ $5x10^{14}$	55 260	800 800	1250 / 19 sec 1350 / 17 sec

Ion Species	Dose (cm^{-2})	Energy (keV)	Temperature (^oC)	Anneal Temp (^oC) / Time
C	$5x10^{15}$	125	800	1200 / 5 min 1250 / 18 sec 1300 / 9 sec
C	$5x10^{14}$	125	800	1250 / 19 sec

An important consideration in obtaining *p*-type GaN is the background electron concentration that must be overcome to convert the film to *p*-type. An additional factor when doping via ion implantation is the carrier contribution from residual implantation defects or defects thermally generated by the high-temperature anneal. These contributions can be accounted for by implanting the GaN with neutral Ar ions, and then annealing the Ar-implanted material and unimplanted material under identical conditions. The room-temperature background electron concentration of the GaN epitaxial layers in this study were less than 10^{15} cm^{-3} for as-grown, ~10^{15} cm^{-3} after annealing at 1200 ^oC for 5 min, and only $1.5x10^{15}$ cm^{-3} after annealing at 1350 ^oC for 17 sec.

The first step in performing electrical characterization of the Mg single and dual implanted GaN samples was ohmic contact deposition. Although the Ni/Au metallic bilayer thickness ratio was determined from a survey of the literature, determining the temperature and time of the optimum contact anneal was hindered by highly resistive samples. The detailed procedures outlined in the previous chapter produced ohmic contacts on *in-situ* Mg-doped *p*-type GaN and were used on all acceptor implanted material. I-V curves were measured on a probe station and used as a benchmark to provide a quick qualitative check on the resistivity of each sample. Empirically, Hall effect measurements reliably determined the conductivity type only on samples having ohmic contacts that passed at least 1 μA of current when 5 V was applied. In the absence

of reliable Hall effect data due to the extreme resistivity of most Mg single and dual implanted GaN samples, I-V curves offered the only insight on electrical activation of implanted acceptors. Table 4 summarizes the range of currents obtained with 5 V applied on the 2 μm-thick GaN samples implanted and annealed per Table 3.

Table 4. Range of currents on acceptor implanted and annealed samples

Implants	$5x10^{15}$ cm^{-2}, 800 ^oC	$5x10^{14}$ cm^{-2}, 800 ^oC	$5x10^{15}$ cm^{-2}, 25 ^oC
Mg	Noise (≤ 10 pA)	5 nA-0.8 μA	Noise
Mg+P	0.6-3 μA	1.7-4 μA	0.7 μA
Mg+C	Noise	32 nA	-
Mg+O	Noise	1.5-3.5 μA	-
Li	1.2-6 μA	-	-
Li+P	7-45 μA	14-260 μA	-
C	4-10 μA	2-3 μA	-

All of the Mg single and most of the Mg dual implanted GaN samples became extremely resistive, and did not show a definite *p*-type conductivity even after annealing at 1350 ^oC for 17 sec under a nitrogen environment. Furthermore, the samples did not show any *p*-type conductivity and remained highly resistive even at a sample temperature as high as 800 K. The samples implanted with Mg+P, Mg+Si, Li, Li+P, and C, showed *n*-type conductivity, but only the samples coimplanted with Li+P and annealed at 1250 ^oC or higher had electron concentrations larger than the correspondingly annealed unimplanted samples. The sheet resistivities, electron mobilities, and sheet electron concentrations for each of these samples are shown in Table 5.

For the samples implanted with Li+P and C, as well as the unimplanted samples, the sheet resistivity decreases with increasing anneal temperature, while the electron concentration increases. The opposite trend is observed for samples implanted with Mg+P at a dose of $5x10^{14}$ cm^{-2} perhaps indicating that more Mg has become electrically

Table 5. Hall Effect Data for Mg+P-, Mg+Si-, Li-, Li+P-, and C-implanted GaN at 300 K

Ion Species	Implant Dose (cm^{-2}) / Temp(^oC)	Anneal Temp (^oC) / Time	Sheet resistivity (KΩ/□)	Mobility (cm^{-2}/Vs)	Electron Concentration (cm^{-2})
Mg+P	$5x10^{15}$ / 800	1200 / 5 m	1,600	132	$2.94x10^{10}$
	$5x10^{14}$ / 800	1250 / 19 s	654	223	$4.29x10^{10}$
		1300 / 23 s	1,090	152	$3.75x10^{10}$
Mg+Si*	$1x10^{14}$ / 25	1300 / 5 s	5,640	31	$3.51x10^{10}$
	$1x10^{14}$ / 500	1150 / 20 m	4,840	10	$1.30x10^{11}$
Li	$5x10^{15}$ / 800	1250 / 18 s	1,330	64	$7.39x10^{10}$
Li+P	$5x10^{15}$ / 800	1200 / 5 m	384	182	$8.96x10^{10}$
		1250 / 18 s	20.9	147	$2.04x10^{12}$
		1300 / 9 s	1.98	154	$2.04x10^{13}$
C	$5x10^{15}$ / 800	1200 / 5 m	1,040	134	$4.48x10^{10}$
		1250 / 18 s	368.5	278	$6.10x10^{10}$
		1300 / 9 s	328	255	$7.45x10^{10}$
Unimplanted	-	1250 / 18 s	150	191	$2.20x10^{11}$
		1300 / 9 s	94	229	$2.93x10^{11}$

* Data from the sample annealed at 1150 / 20 m was collected at 400 K.

active and further compensates the electron concentration. The data shown in Table 5 do not contradict what has been reported in the literature on acceptor implanted GaN, but rather confirm earlier published conclusions and provide additional insights and understanding.

Pearton *et. al*. reported *p*-type GaN resulting from Mg coimplanted with P in late 1995. Mg and Mg+P were implanted at a dose of $5x10^{14}$ cm^{-2} into unintentionally doped *n*-type ($n \leq 4x10^{16}$ cm^{-3}) MOCVD-grown GaN epilayers on *c*-plane sapphire. Both samples were annealed for 10 s with a face-to-face proximity cap in a SiC coated graphite susceptor between 700 and 1100 ^oC. Only the coimplanted sample converted from the background *n*-type to *p*-type conductivity after annealing at 1050 ^oC. Though remaining *n*-type, the resistivity of the Mg singly implanted sample increased likely due to the compensating Mg-activation. Assuming an ionization energy for Mg of 150 meV, they

reported an activation percentage of Mg in the Mg+P coimplanted sample of 62% (Pearton *et. al*., 1995). The purpose of the equivalent dose P coimplant was to maintain stoichiometry by introducing Ga vacancies into which the Mg could more readily substitute, while simultaneously reducing the concentration of N vacancies, which are believed to complex with substitutional Mg_{Ga} forming deep donors.

Edwards *et. al.* also studied ion implantation into GaN by implanting multiple energy/dose Mg, and Mg+P coimplants from room temperature up to 800 ^{o}C into MOCVD-grown unintentionally doped *n*-type and semi-insulating GaN epilayers on *c*-plane sapphire. All samples were annealed in an N_2 ambient for 120 s face-up in a SiC coated graphite susceptor at 1150 ^{o}C. The unencapsulated samples showed evidence of dissociation when annealed above 1050 ^{o}C; therefore the SiC susceptor lid was placed in close contact with the samples which then maintained pre-anneal morphology. They expected the P coimplant to suppress the interstitial diffusion of Mg, which is known to occur in narrow gap III-V compounds; however, they noticed a significant redistribution of Mg under this anneal condition. This redistribution of Mg is surprising given a report by Wilson *et. al*., who detected no motion of Mg implanted at a dose of $5x10^{14}$ cm^{-2} into GaN and annealed at 1450 ^{o}C for 10 s (Wilson *et. al*., 1999). As shown in the PL spectra of this present study, perhaps anneal time has a greater effect on damage removal and implant redistribution than currently believed.

Most significant is Edwards' inability to obtain *p*-type conductivity in any of these samples, but rather only highly resistive material. Apparently, neither implantation temperature nor conductivity of the as-grown GaN epilayer (either *n*-type or semi-insulating) had any effects. Acceptor passivation can be ruled out because annealing at

1150 ^{o}C is more than adequate to fully remove the H-passivation of acceptors common to MOCVD-grown epilayers. Measuring carrier concentration at 300 ^{o}C likewise resulted in highly resistive material, which would indicate that either insufficient acceptors were activated (which is unlikely after an 1150 ^{o}C anneal), or that there is a much greater concentration of implantation- or anneal-induced compensating defects. They did not understand why they were unable to obtain *p*-type conductivity, nor did they report any luminescence characterization of their samples implanted with Mg and Mg+P (Edwards *et. al.*, 1997). In this present study, correlating PL or CL spectra with I-V curves and Hall effect measurements has provided valuable insights into why *p*-type conductivity was not obtained.

Ronning *et. al.* implanted Be alone and coimplanted Be and N into MOVPE-grown unintentionally doped *n*-type GaN epilayers on *c*-plane 6H-SiC. Implantation doses ranged from $1x10^{13}$ to $2.5x10^{14}$ cm^{-2} with an equal dose of N in the coimplanted samples to determine the effect of N on the activation of Be acceptors. All samples were sequentially annealed at 300, 600, and 900 ^{o}C for 10 min each in vacuum followed by 1 hour anneal under a flux of atomic N at 1100 ^{o}C. A comparison of the PL spectra indicated that N coimplantation did not enhance Be activation. X-ray diffraction (XRD) data indicates that after the 10 min 900 ^{o}C anneal, structural damage from the $2.5x10^{14}$ cm^{-2} dose Be implant is fully recovered. However, PL data shows that after annealing for 1 hour at 1100 ^{o}C, point defects are still present attributing to the low optical activation of Be. Due to residual point defects, the samples were too highly resistive for Hall measurements. The authors concluded that annealing up to 1300 ^{o}C is necessary to

fully recover the point defects and electrically activate the Be acceptors (Ronning *et. al.*, 1999).

These conclusions (Ronning *et. al.*, 1999) regarding activation of acceptors in GaN were also reported by Zolper *et. al.* (1997a) following the work of Pearton *et. al.* (1995). Zolper coimplanted Mg+P at equal doses from $2x10^{14}$ to $5x10^{15}$ cm^{-2} into MOCVD-grown GaN epilayers on *c*-plane sapphire. Samples were annealed in a SiC coated graphite susceptor in flowing N_2 for 15 s at 1100 ^{o}C. This RTA failed to obtain *p*-type conductivity for all Mg+P implant doses. In fact, the samples implanted with Mg+P at doses from $2x10^{14}$ to $1x10^{15}$ cm^{-2} resulted in a sheet electron concentration greater than the samples implanted with Si at the same doses. This is a very interesting occurrence which will discussed later. The authors concluded that the Mg acceptors are being compensated by either implant induced point defects or another impurity in the as-grown material. They further surmised that annealing above 1100 ^{o}C may be required to fully remove implant damage thereby optimizing carrier concentrations.

This present study confirms some of the conclusions of Zolper *et. al.* (1997a) and Pearton *et. al.* (1995), but provides further valuable insight. Not only is GaN implanted with Mg-alone compensated by residual lattice damage, but Mg is a participant in this self-compensation by forming deep complexes as evidenced by a dominant GL band in the PL spectra of all Mg implanted samples. Furthermore, these Mg-related deep complexes form independent of the 25, 500, or 800 ^{o}C implantation temperature and remain thermally stable even at anneal temperatures as high as 1350 ^{o}C, indicating a very high binding energy. The GL band was also present in samples implanted with Mg-alone after annealing at just 1050 ^{o}C for 15 s, indicating a very low formation energy.

Therefore, one may conclude the deep complex responsible for the GL band in the PL and CL spectra is much more energetically favorable than isolated Mg_{Ga} under ion implantation and annealing conditions. It is important to note that the only feature in the PL of the *in-situ* Mg-doped sample from Fig. 15 is a BL band at 2.85 eV. This sample had a room-temperature hole concentration and mobility of 1.25×10^{17} cm^{-3} and 16 $cm^2/V \cdot s$, respectively. In almost no circumstances has the PL spectrum of a *p*-type *in-situ* Mg-doped sample been reported to show a GL band. The GL band is predominantly seen in acceptor-implanted GaN, and can therefore be attributed to deep complexes formed between the acceptor ion and implantation defects. Another key observation is that the deep complexes responsible for the GL form independent of and despite various coimplants designed to control stoichiometry (P and C coimplantation) or enhance *p*-type conductivity by forming reactive donor-acceptor dipole pairs (Si or O coimplantation). The intensity of the deep donor-deep acceptor pair (D_dA_dP) GL band relative to the 3.28 eV DAP is reduced only in samples implanted with Mg+Si (Fig. 20). However, in the latter case, in addition to forming deep complexes, Mg is also compensated by shallow Si donors. Despite its lower dose, at sufficiently long (1150 ^oC for 20 min) or high (1300 ^oC for 23 sec) anneal times, Si prevails over the highly compensated Mg and the samples become *n*-type. Considering all the Mg- implanted samples in this study, the Mg+P samples were uniquely *n*-type. The PL spectra of each Mg+P sample reveals the same dominant GL band but also UV DAP activity and a broad BL band centered near 2.75 eV that tends to increase with increasing electron concentration. Although the samples implanted with Mg+P in this study were *n*-type, the sheet electron concentrations were over an order of magnitude less than the electron concentrations obtained by Zolper *et. al.*

(1997a), who implanted Mg+P at the same doses. Also, the Mg+P samples in this study had nearly an order of magnitude less electron concentration than the unimplanted samples under the same anneal conditions. Therefore, although the P coimplants in this study did not enhance Mg activation as they did for Pearton *et. al.* (1995), they certainly did not produce a greater electron concentration than an equivalent dose of Si implants would as they did for Zolper *et. al.* (1997a). Nonetheless, the exact nature of the P coimplants contributing to electron concentration is unknown. In this study, P coimplants were also used with Li.

The investigation of Li as an acceptor in GaN was in part motivated by some work in SiC. Ramungul *et. al.* implanted Be as an alternative acceptor into SiC to form P^+N junctions and achieved nearly a factor of 5 increase in diode forward current over similarly implanted and annealed B-implanted SiC (Ramungul *et. al.*, 1999). Be in SiC has one less electron than the typical group III acceptor. Similarly, the alkalis (Li and Na) in GaN have one less electron than the typical group II acceptor. Neugebauer and Van de Walle stated that Li_i is a donor, but Li_{Ga} is a double acceptor in GaN although Li suffers from poor solubility (Neugebauer and Van de Walle, 1999). The latter characteristic is not an ion implantation concern since implantation is a non-equilibrium process where acceptor activation is not limited by the same thermodynamic considerations. Li has a covalent radius of 1.23 Å, which is much closer to Ga's covalent radius of 1.26 Å than is Be's. Dalmer *et. al*. reported that for implantation temperatures of 700 K (427 ^oC), Li_i^+ starts to diffuse and presumably interacts with vacancies created in the implantation process leading to the formation of substitutional Li (Dalmer *et. al*., 1998). Ronning *et. al.* used emission channeling to determine that more than 60% of the

Li ions implanted at 300 K are substitutional when annealed at 770 K or when implanted at 700 K. They state that due to Li's low stability on the N-sublattice, Li will substitute for Ga (Ronning *et. al.*, 2000). Li_{Ga} behaves as a double acceptor in GaN with 1st and 2nd thermal ionization energies of 0.16 and 0.63 eV, respectively, which is comparable to Mg as a shallow acceptor. Interstitial Li, Li_i, is highly favored over Li_{Ga} unless there are sufficient V_{Ga} available, which should be true after ion implantation. Researchers have estimated that isolated or distant Li_i and V_{Ga} pairs will recombine to the energetically favorable Li_{Ga} above 600 K (Bernardini and Fiorentini, 2000).

Based on this, one could hypothesize that implanting Li into GaN at implantation temperatures greater than 500 ^{o}C should provide near 100% electrical activation of the Li atoms. Because there are likely many more vacancies produced during implantation than the number of implanted ions, there should be a large concentration of donor-like interstitial Ga, Ga_i, as well as other implantation-induced defects. Annealing the implanted GaN will be required to recombine the Ga_i with the V_{Ga}; however, the remaining Ga_i will likely compensate the activated Li_{Ga}. Removal of the residual Ga_i displaced by the implanted ions could be accomplished by codoping with an equal dose of P or N ions to maintain stoichiometry. Apparently, the problem with implanting Li to obtain *p*-GaN is not the activation of Li, but the elimination of compensating defects.

Although the potential behavior of Li as an acceptor in GaN has been theoretically investigated, this study may be the first to discuss the electrical and optical characteristics of Li and Li+P implanted into GaN. The Li-implanted sample had the lowest mobility of all the acceptor implanted samples in Table 5, and a sheet electron concentration 3 times less than that of the unimplanted sample annealed under the same

conditions. Based on the PL spectra of Fig. 25, the Li-implanted samples' DAP peak and weak exciton peak indicate reasonably good damage recovery. The YL suggests the presence of slightly different deep donor and/or deep acceptor compensating levels than those responsible for the GL in Mg-implanted GaN. It is likely that after annealing the implanted Li ions are acting as shallow acceptors, remaining as interstitial donors, and participating in self-compensating complexes. As experienced with the samples coimplanted with Mg+P, the P coimplant, intended to enhance the activation of Li acceptors, appears to have had an opposite effect in the samples implanted with Li+P. The electron concentration in these samples increases rapidly with anneal temperature from 1200-1300 ^{o}C. The net effect at 1300 ^{o}C is equivalent to about 0.4% activation of Li donors. Although P is isoelectronic on the N-sublattice, the significant increase in electron concentration over that of Li-alone seems to suggest that P may be doing more than just filling N vacancies. Optically, P clearly causes deeper levels in the bandgap as the 3.29 eV DAP peaks in the single Li-implanted samples are replaced by a rather intense 2.85 eV peak in the Li+P implanted samples. This 2.85 eV peak, albeit 100 meV higher in energy, may be similar in nature to the 2.75 eV peak observed in the Mg+P implanted samples.

Carbon is widely used as an acceptor in GaAs and has been favored as an acceptor in GaN primarily because of its theoretically lower ionization energy; however, carbon is only reported to have produced *p*-type GaN when doped *in-situ* via MOMBE. All other attempts to dope GaN with C, including ion implantation, have resulted in *n*-type GaN (Wilson *et. al.*, 1999), or at best heavily compensated, highly resistive material. Although C may prefer the N-sublattice, self-compensation is expected to dominate

beyond a certain concentration as amphoteric C also substitutes on the Ga-sublattice (Boguslawski and Bernholc, 1997). For this reason, coimplantation of Mg+C was investigated in an attempt to produce *p*-type GaN by increasing the probability of C_N vice C_{Ga}. The fact that C-alone implantation produces only *n*-type GaN was expected. It is reasonable to assume however, that more of the implanted C ions were activated as shallow acceptors (C_N) than as self-compensating donors (C_{Ga}) because the sheet electron concentration of a sample implanted with C and annealed at 1300 ^{o}C for 9 sec was 4 times less than an unimplanted sample after the same anneal. Based on the dominant GL band in the PL spectra of samples coimplanted with Mg+C (Fig. 17), there was most likely still a significant amount of implanted Mg forming deep complexes and only enough shallow Mg_{Ga} activated to compensate the residual donors resulting in highly resistive material. On the other hand, the PL spectra from the samples implanted with C-alone are dominated by a YL band, which has been widely reported for *n*-type GaN doped with Si or unintentionally doped, as well as for C-doped GaN (Zhang and Kuech, 1998). It is interesting to note that this YL band is not uniquely caused by implantation damage because it does not appear on samples implanted with Mg, nor is it unique to samples containing shallow Si donors (Si_{Ga}) for it dominates the spectra of GaN implanted with C. Thus, the YL appears to be generic to *n*-type GaN, which is known to favor the formation of Ga vacancies over N vacancies. Nonetheless, *n*-type GaN may be a necessary, but by itself an insufficient condition for YL, because the unimplanted and annealed material used in this study is more *n*-type than the samples implanted with C, yet it shows no YL. If more C ions were substitutional on the N-sublattice after annealing, then an increased concentration of Ga vacancies would likely occur and help

account for the YL. It is also worth noting that of all the acceptor implanted samples, the only three that showed any exciton peaks had *n*-type conductivity.

Surprisingly, the most conductive sample implanted with Mg alone was implanted at 25 ^{o}C with a dose of $2x10^{14}$ cm^{-2} and annealed at 1150 ^{o}C for 15 sec. As discussed later in the section on Si-implanted GaN, the higher conductivity of this sample is possibly due to a combination of the moderate Mg dose and 25 ^{o}C implantation temperature. Although Hall measurements were unable to determine conductivity type, temperature-dependent reistivity data fit very well as shown in Figure 26. An activation energy of 204 meV was extracted from the slope of the Arrhenius plot. Even though this value is within 15 meV of the measured thermal ionization energy for Mg reported by (Kozodoy *et. al.*, 2000), the observed decrease in resistivity cannot be reliably attributed to Mg, because the conductivity type could not be reliably determined.

The conductivity type of the sample coimplanted at 500 ^{o}C with Mg+Si at a dose of $2x10^{14}$ cm^{-2} for Mg and $1x10^{14}$ cm^{-2} for Si and annealed at 1100 ^{o}C for 20 min could not be determined at 300 K. However, this sample had an electron concentration of ~10^{15} cm^{-3} at 400 K and remained weakly *n*-type up through 800 K. Assuming only one donor was responsible for the increase in carrier concentration with temperature, an ionization energy of about 150 meV was extracted from the slope of the line best fit to carrier concentration. Because the temperature-dependent concentration of this sample closely matches that of an unimplanted sample, it is more likely that this carrier concentration is due to residual implantation defects or thermally activated intrinsic defects than from Si.

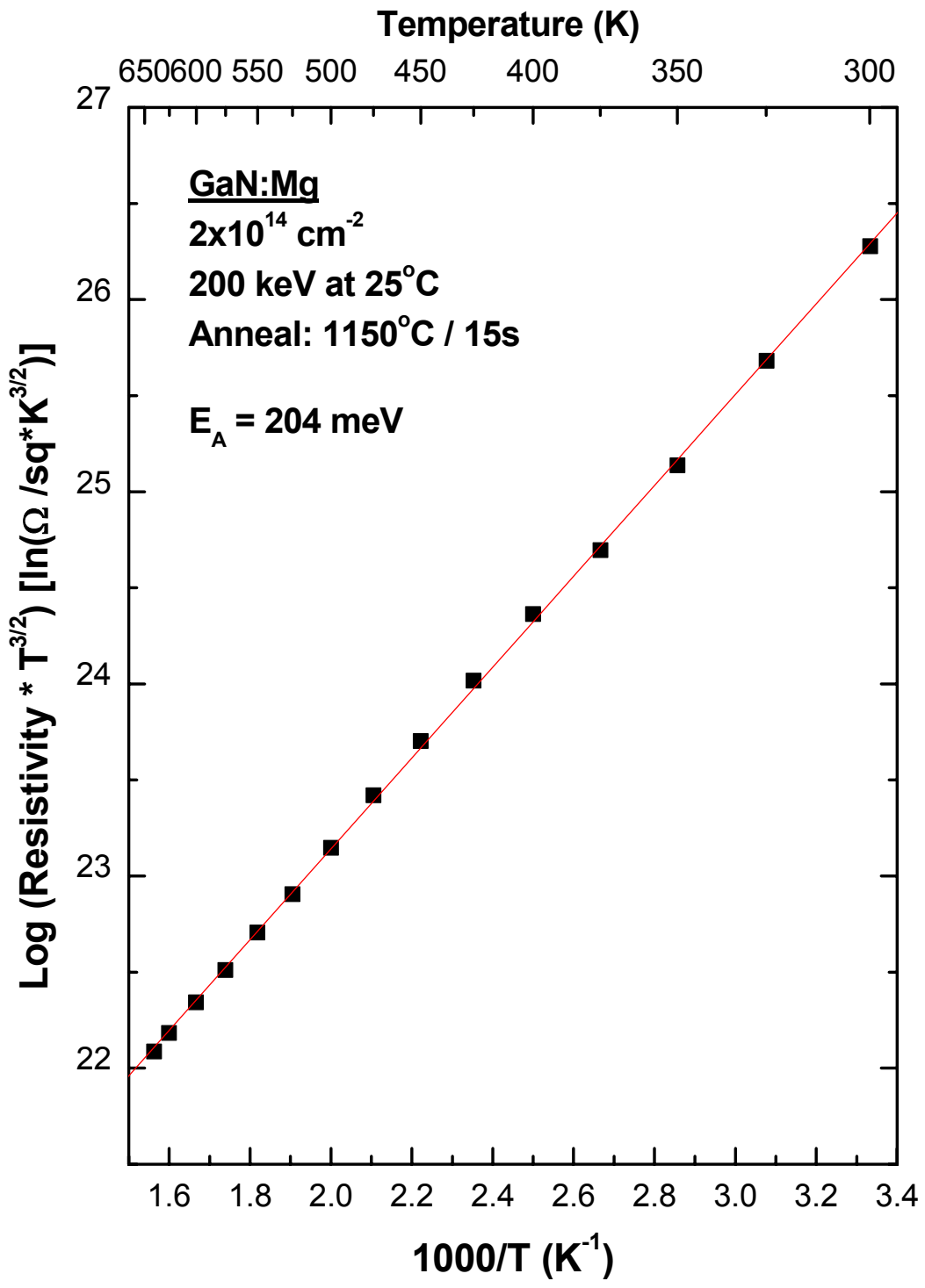

Figure 26. Arrhenius plot of resistivity data from GaN implanted at 25 ^{o}C with Mg at a dose of $2x10^{14}$ cm^{-2} and annealed at 1150 ^{o}C for 15 sec.

The effects of single Si implantation on the electrical and optical properties of GaN are much more pronounced and will be discussed in the next two sections of this chapter.

Silicon Implanted into GaN at Room Temperature

Although ion implantation as a tool for doping semiconductors has become a mature technology in Si- and GaAs-based devices, the technique is less well developed for GaN. The two key applications for ion implantation in semiconductor device technology are high conductivity ohmic contact layer regions using high dose implantation and field effect transistor channel layer doping using low dose implantation. Silicon is the primary donor species for producing *n*-type III-V semiconductors because of its low mass, shallow ionization energy, and the ease of forming a Si ion beam. The activation efficiency of Si implanted into GaAs decreases with implantation dose. This is likely due to less implantation damage in the lower doses as well as an increase in the amphoteric tendency of Si, which increasingly occupies both Ga and As sublattices as the dose is increased. Pearton reported an electron concentration of $\sim 2\text{x}10^{18}$ cm^{-3} as the practical limit in high dose Si-implanted GaAs due to self-compensation (Pearton, 1988).

It should be noted that electrical activation refers to the percentage of implanted Si ions that contribute an electron to the conduction band, whereas donor activation represents the percentage of substitutional donors. The difference between the two activations is due to the donor ionization energy. Electrical activation is calculated simply by dividing the room-temperature sheet carrier concentration, n_s, by the implanted dose, ϕ. If one implants through an encapsulant, the implanted dose must be reduced to the actual dose, ϕ_{act}, that came to rest in the GaN epilayer. Furthermore, the background

carrier concentration measured on unimplanted or Ar-implanted and annealed samples, $n_{s,bg}$, must be subtracted from the carrier concentration measured on the Si-implanted samples, as necessary. Assuming the percentage of ionized donors is proportional to the factor $\exp\left(-E_d / k_B T\right)$, the donor activation efficiency is calculated by

$$\eta = \frac{n_s - n_{s,bg}}{\phi_{act} \exp\left[\frac{-E_d}{k_B T}\right]}. \tag{27}$$

Recent studies indicate that Si-implanted GaN may not suffer from self-compensation; however, the lower doses have experienced problematic activation. Zolper *et. al*. implanted GaN with 100 keV Si ions at doses from $5\text{x}10^{13}$ to $1\text{x}10^{16}$ cm^{-2} and annealed samples at 1100 ^{o}C for 15 s in a SiC-coated graphite susceptor. They reported negligible activation for doses below $5\text{x}10^{15}$ cm^{-2}, but electrical activation as high as 50% for an implant dose of $1\text{x}10^{16}$ cm^{-2} (Zolper *et. al*., 1997b). Dupius *et. al*. reported only 19% electrical activation for GaN implanted at room temperature through a 500 Å AlN cap with 100 keV Si ions at a dose of $5\text{x}10^{14}$ cm^{-2} and annealed at 1150 ^{o}C for 5 min in flowing nitrogen (Dupius *et. al*., 1999). Molnar *et. al*. implanted a total dose of $4.4\text{x}10^{14}$ cm^{-2} Si ions with multiple energies at room temperature and annealed at 1150 ^{o}C for 2 min. Assuming a donor ionization energy of 26 meV, they calculated a donor activation of only 1% (Molnar *et. al*., 1996). Higher activation efficiencies have been reported for higher doses of Si implantations annealed at higher temperatures. Cao *et. al*. reported electrical activation efficiency as high as 90% for 100 keV Si ions implanted into GaN at room temperature with a dose of $5\text{x}10^{15}$ cm^{-2} and annealed at 1400 ^{o}C for 10 s. Their samples were capped with 1000 Å AlN after implantation and

sealed in a quartz ampoule under 15 psi of N_2 for annealing (Cao *et. al*., 1998). Many activation studies of Si-implanted GaN report the results of only a single implantation dose annealed at a single temperature, while some others discuss Si activation dependence on implantation dose or anneal temperature, but not both. The understanding they provide is range-limited, lacking the comprehensive details regarding activation efficiencies as a function of dose and anneal temperature. A detailed study of this type is valuable for optimizing or engineering advanced electronic and optoelectronic GaN device applications requiring low- to high-dose implantations.

This study provides a systematic, comprehensive investigation of Si-implanted MBE-grown GaN as a function of implantation temperature, anneal temperature, and to a lesser extent, anneal time to optimize the ion implantation conditions for low- to high-dose implants. The remainder of this chapter will discuss the room-temperature and temperature-dependent Hall effect measurements as well as the low-temperature and temperature-dependent PL spectra for Si implanted at both 25 and 800 ^{o}C. The PL and Hall effect results from both Si- and Ar-implanted GaN will be correlated to provide a synergistic understanding of Si activation.

Room-Temperature Hall Effect Measurements.

GaN wafers capped with 500 Å AlN were implanted at room temperature with 200 keV Si ions with doses ranging from $1x10^{13}$ to $5x10^{15}$ cm^{-2} and annealed at 1050 to 1350 ^{o}C from 5 min to 17 sec in a flowing nitrogen environment. The sheet carrier concentrations as determined from room-temperature Hall effect measurements on this set of samples are shown in Figure 27. Data from a representative sample implanted at 25 ^{o}C with 200 keV Ar ions at a dose of $1x10^{13}$ cm^{-2} shows the effect of the residual

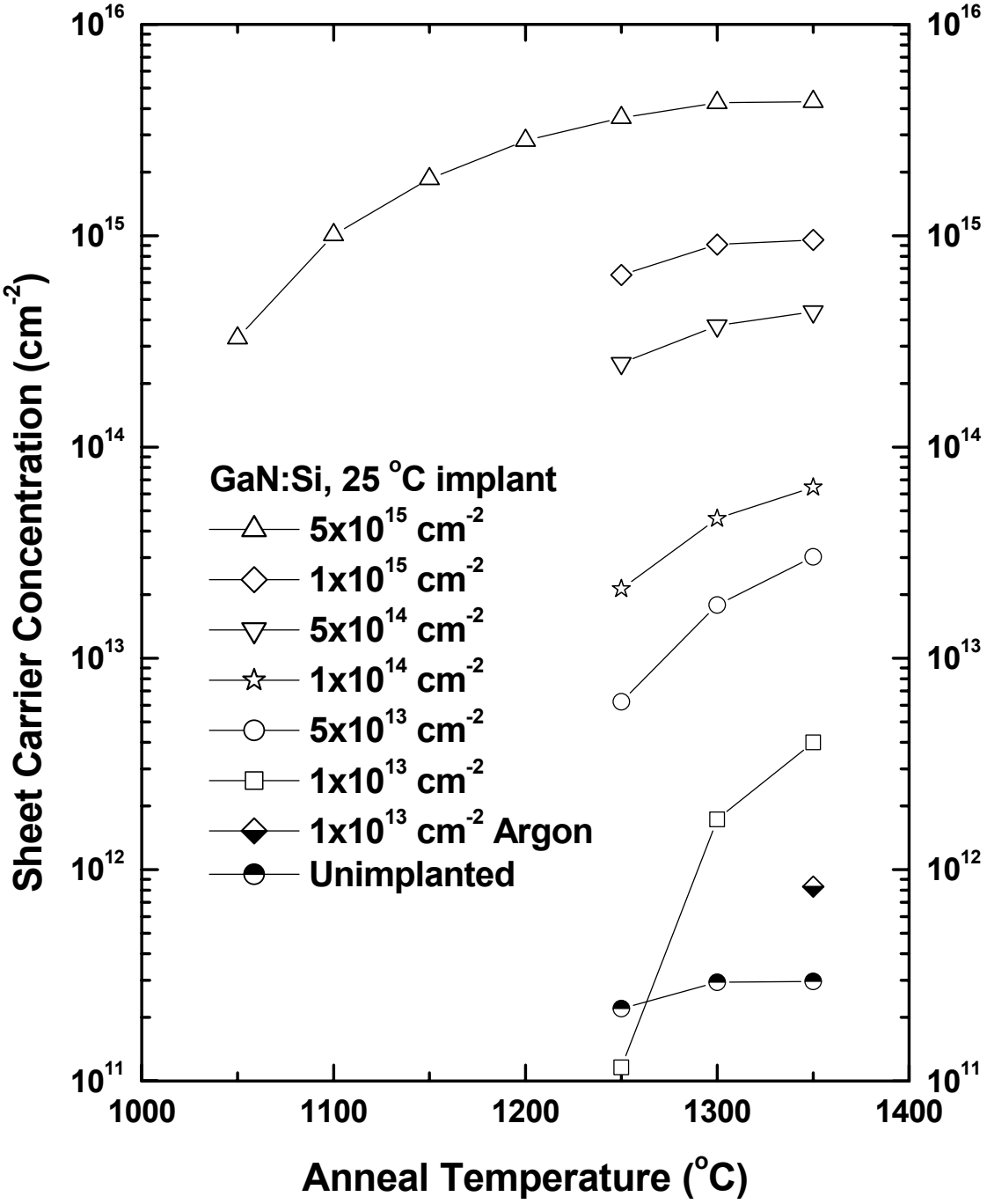

Figure 27. Room-temperature sheet electron concentrations for GaN implanted at room temperature with 200 keV Si ions at doses ranging from $1x10^{13}$ to $5x10^{15}$ cm^{-2} and annealed at 1050 to 1350 ^{o}C from 5 min to 17 sec in a flowing nitrogen environment.

implantation damage on the GaN background carrier concentration. Data from unimplanted samples annealed from 1250 to 1350 ^{o}C are also included for comparison to show the effects of high temperature annealing on the GaN background carrier concentration. The set of curves shown in this figure provides a complete picture of sheet carrier concentration as a function of anneal temperature and ion dose. An open-tube furnace was used to anneal the samples at temperatures from 1050-1200 ^{o}C for 5 min, while an Oxy-Gon furnace was used to anneal the samples from 1250-1350 ^{o}C for an average of 15 sec. Recall from Fig. 14 in Chapter 5 that the slow ramp rates on the Oxy-Gon furnace cause the samples to remain above 1100 ^{o}C for up to several minutes despite a dwell time at the quoted anneal temperature of only 15 sec. The electron concentration is highly dependent upon implantation dose and annealing temperature, and increases steadily up through 1350 ^{o}C for each of the six doses.

Figure 28 shows the electrical activation efficiency for all Si-implanted samples using an effective dose because of the AlN cap. For example, a nominal dose of $1x10^{14}$ or $5x10^{14}$ cm^{-2} produces an effective dose of $9.51x10^{13}$ or $4.75x10^{14}$ cm^{-2} within the GaN, respectively. Thus, for each implanted dose, only 95% of the implanted ions come to rest within the GaN. Generally, the higher the dose, the greater the activation efficiency at any given anneal temperature. The highest dose of $5x10^{15}$ cm^{-2} displays significant activation (> 20%) even after annealing for only 1100 ^{o}C for 5 min and an excellent activation (~ 90%) after annealing at just 1300 ^{o}C for 23 sec. This is one of the highest reported activation efficiencies for Si implanted at a dose of $5x10^{15}$ cm^{-2}, and is about 7% greater than the activation reported by Cao *et. al*. (1998) for the same dose at the same anneal temperature. The 100% electrical activation obtained for the sample

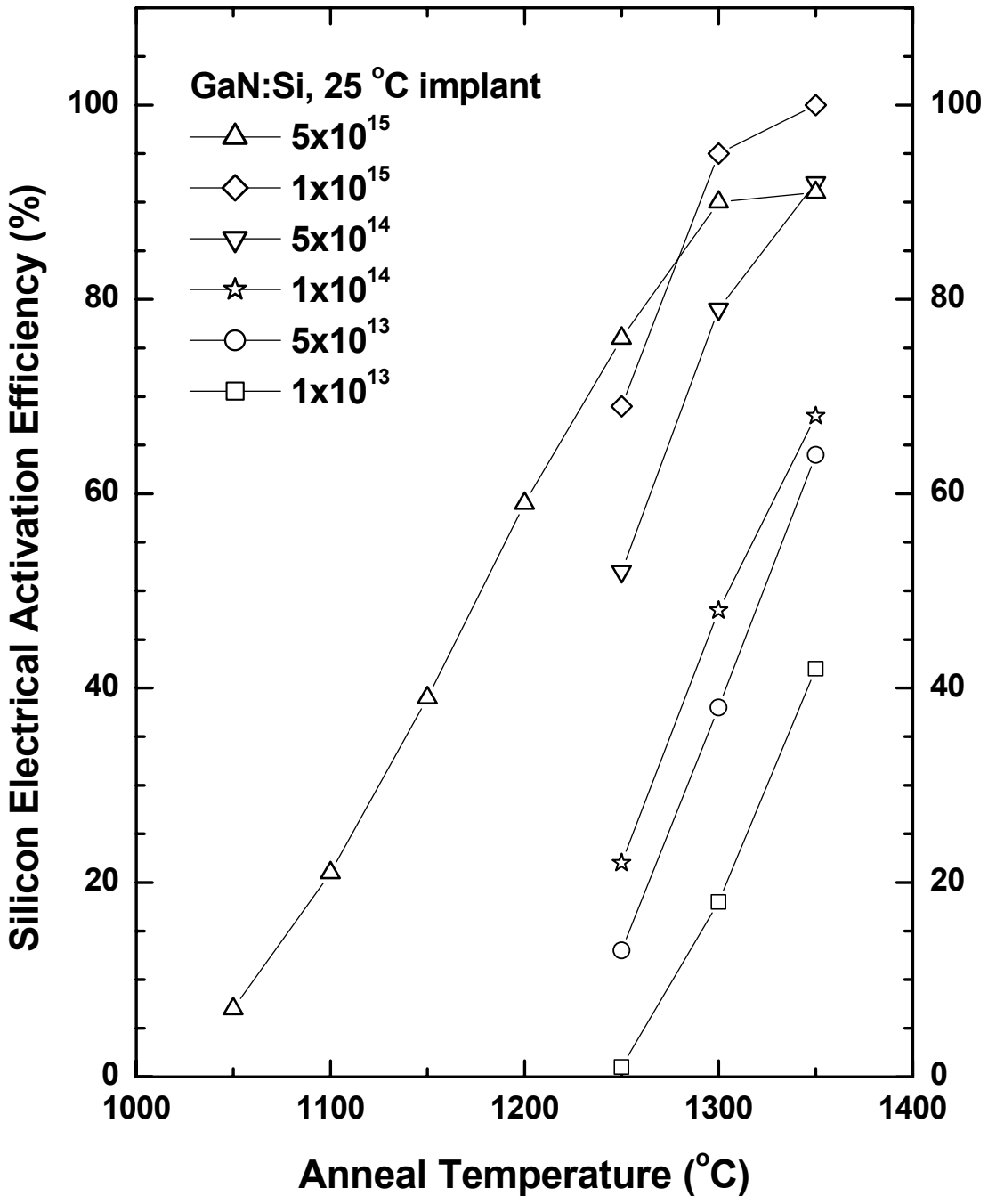

Figure 28. Electrical activation efficiency for GaN implanted at room temperature with 200 keV Si ions at doses ranging from $1x10^{13}$ to $5x10^{15}$ cm^{-2} and annealed at 1050 to 1350 ^{o}C from 5 min to 17 sec in a flowing nitrogen environment.

implanted with a dose of $1x10^{15}$ cm^{-2} and annealed at 1350 ^{o}C for 17 sec is the highest known to be reported for that dose. Even the sample implanted with the lowest dose of $1x10^{13}$ cm^{-2} and annealed at 1350 ^{o}C for 17 sec shows an unprecedented electrical activation of 40%. The electrical activation efficiencies for all six doses increase fairly linearly with annealing temperature. The highest two doses show 90% or better activation efficiency after annealing at 1300 ^{o}C, reaching near maximum efficiency after annealing at 1350 ^{o}C. The lower four doses show rapid increases in activation efficiency with increasing annealing temperature from 1250 to 1350 ^{o}C. This indicates that the optimum anneal temperature for these doses may be higher than 1350 ^{o}C. The data reveal that the optimum anneal temperature for Si-implanted GaN is dose dependent with lower doses requiring higher anneal temperatures to maximize electrical activation efficiency. The lowest dose of $1x10^{13}$ cm^{-2} displays measurable activation (1%) only after annealing at 1250 ^{o}C. Figure 29 shows sheet carrier concentration versus effective implantation dose. The 100% electrical activation line clearly shows concentration very nicely approaching 100% activation as the dose is increased.

In addition to carrier concentration, mobility is also a key parameter for characterizing the suitability of semiconductor layers for device applications. Many researchers have shown that although the electrical activation of high-dose Si-implanted GaN begins at anneal temperatures as low as 1050 ^{o}C, there still remains a considerable amount of radiation damage at this anneal temperature. This damage is often structurally characterized using techniques such as Rutherford Back-scattering (RBS), X-ray diffraction (XRD), or X-ray transmission electron microscopy (XTEM), though PL spectra can reveal the optical nature of radiation damage as we shall see later in this

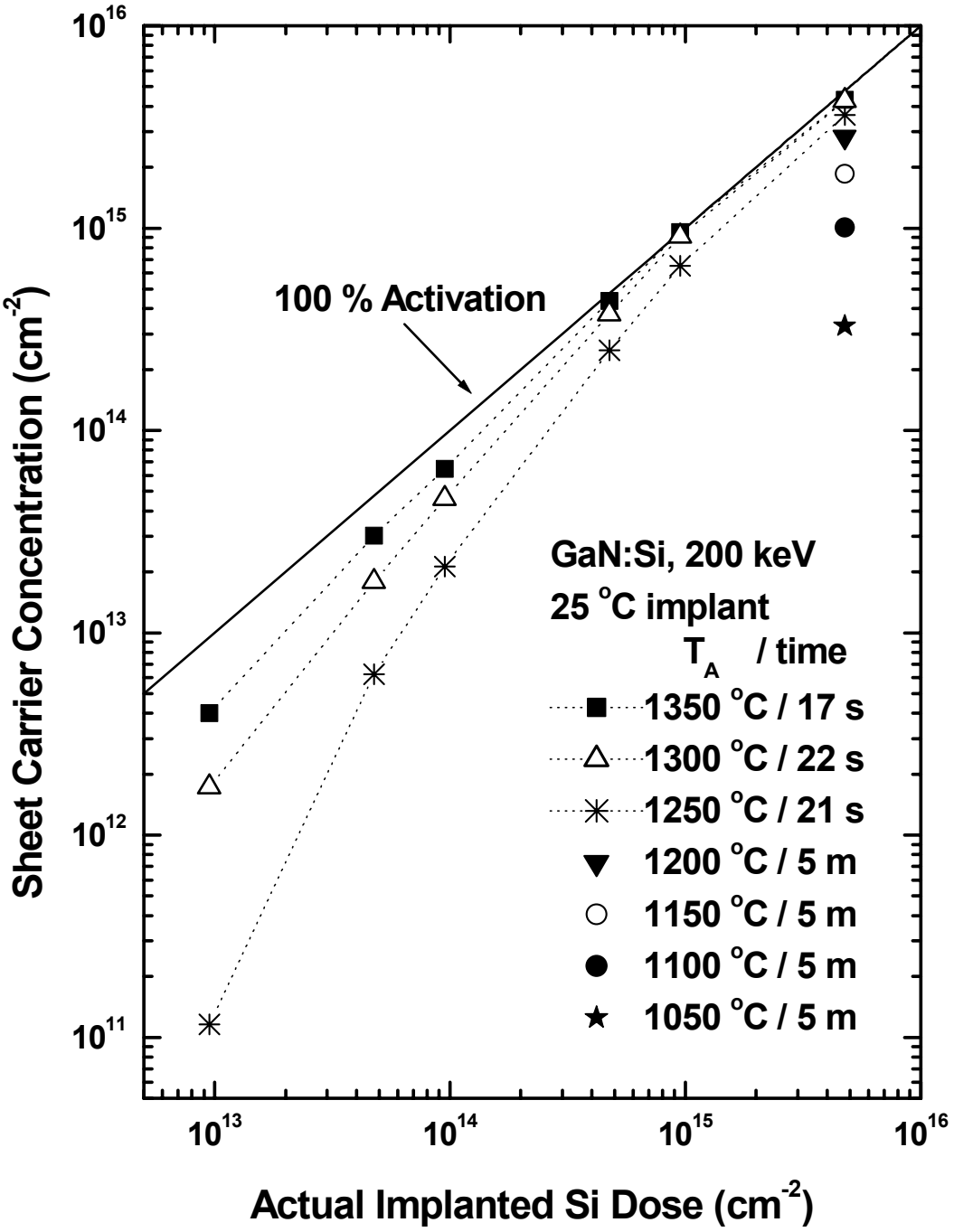

Figure 29. Sheet carrier concentration versus actual implanted dose for GaN implanted at 25 °C with 200 keV Si ions at doses ranging from $1x10^{13}$ to $5x10^{15}$ cm^{-2} and annealed at 1050 to 1350 °C from 5 min to 17 sec in a flowing nitrogen environment.

chapter. Clearly, poor electrical activation causes low carrier concentration and low mobility as the inactive Si and residual damage serve as scattering centers degrading electron mobility. However, electrical activation of implanted Si on the order of 50% can occur despite mobility limiting residual implantation damage. This seems to imply that some of the residual defects are electrically inactive, acting primarily to limit mobility and quench band-edge luminescence (Zolper *et. al.*, 1997a). Figure 30 shows the electron Hall mobility for all six doses as well as for unimplanted GaN as a function of anneal temperature. The mobilities increase considerably as anneal temperature is increased up to 1350 ^{o}C for all doses. After annealing at 1350 ^{o}C, the mobility values are higher for the lower doses. The highest mobility obtained at room temperature is about 250 $cm^2/V{\cdot}s$ on the sample with the lowest dose of $1x10^{13}$ cm^{-2}, while the lowest mobility of almost 100 $cm^2/V{\cdot}s$ was found on the sample with the highest dose of $5x10^{15}$ cm^{-2}. These values of mobility are much higher than reported values of mobility on samples implanted at the same dose. Zolper *et. al*. implanted 100 keV Si^+ into GaN with a dose of $5x10^{15}$ cm^{-2}, annealed at 1100 ^{o}C for 15 s in a SiC-coated graphite susceptor, and reported a mobility of less than 10 $cm^2/V{\cdot}s$ (Zolper *et. al.*, 1997b). The mobility obtained in this study for the same dose and anneal temperature is at least twice as large. This is likely due to further damage removal from the 5 min anneal duration at 1100 ^{o}C versus only 15 s. Cao *et. al*. reported a constant mobility of 43 $cm^2/V{\cdot}s$ for Si-implanted GaN with a dose of $5x10^{15}$ cm^{-2} after annealing at 1300 and 1400 ^{o}C for 10 s (Cao *et. al*., 1998). The mobility of the samples implanted with a dose of $5x10^{15}$ cm^{-2} in this study increased from 84 to 96 $cm^2/V{\cdot}s$ as anneal temperature increased from 1300 to 1350 ^{o}C. These values demonstrate not only a mobility twice as large but also further improvement

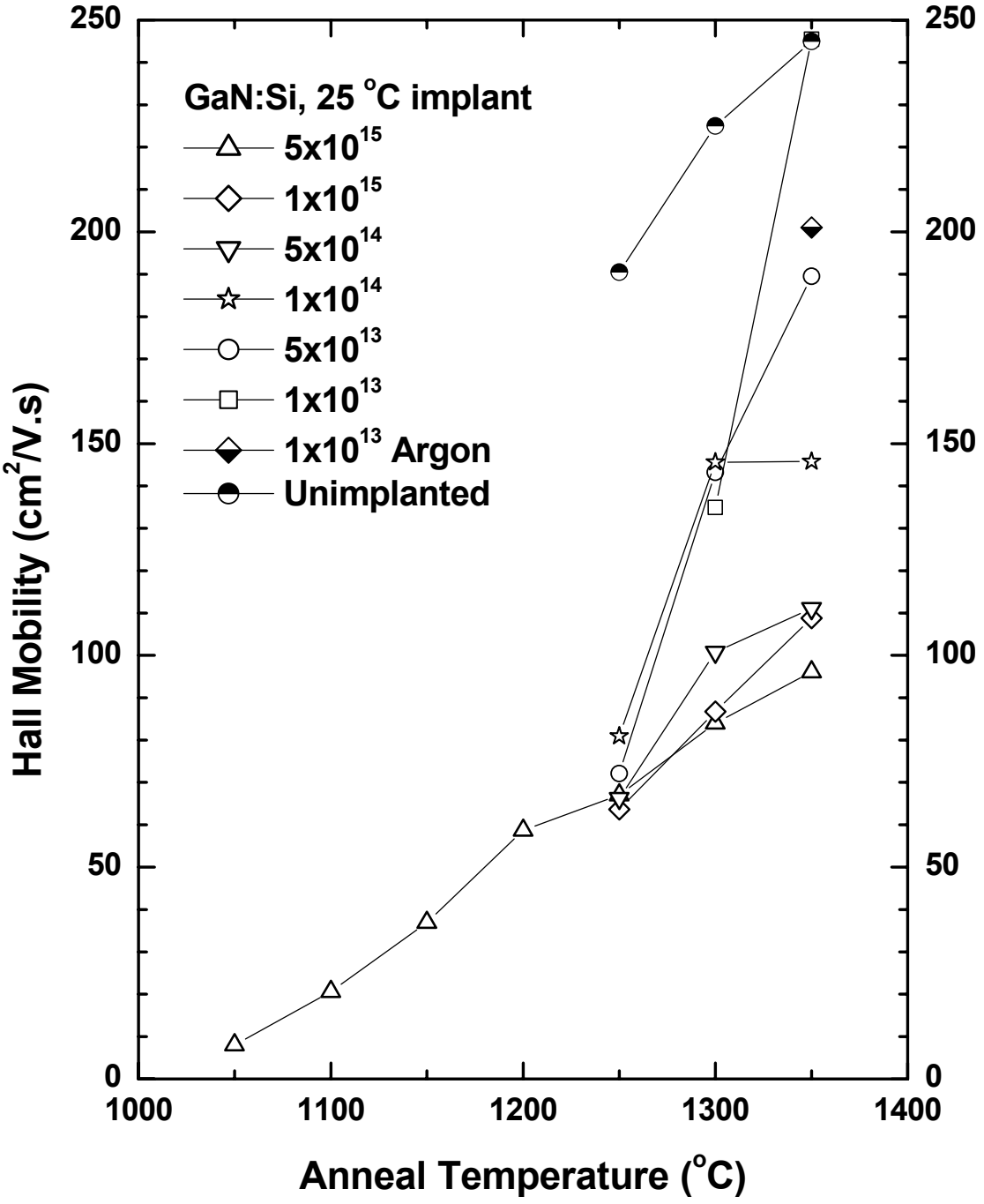

Figure 30. Room-temperature Hall mobility for GaN implanted at room temperature with 200 keV Si ions at doses ranging from $1x10^{13}$ to $5x10^{15}$ cm^{-2} and annealed at 1050 to 1350 ^{o}C from 5 min to 17 sec in a flowing nitrogen environment.

even after annealing at 1350 ^{o}C. Furthermore, unlike Cao's samples that were sealed in a quartz ampoule under 15 psi of N_2 for annealing, the samples in this study were merely held tightly face-to-face. The only report of mobilities of ~100 $cm^2/V{\cdot}s$ for Si-implanted GaN was achieved under extreme annealing conditions. Zolper *et. al*. implanted 100 keV Si^+ into GaN at a dose of $5x10^{15}$ cm^{-2} and annealed from 1250 to 1500 ^{o}C for 15 min under N_2 pressures from 10 to 15.3 kbar. The samples were uncapped as the high N-overpressure suppressed GaN decomposition. Despite evidence from RBS spectra indicating the implantation damage was completely removed only after annealing at 1500 ^{o}C for 15 min in 15.3 kbar N_2, the mobility values for all samples were ~100 $cm^2/V{\cdot}s$. This saturated value illustrates that their mobility had already peaked as a result of the anneal at 1250 ^{o}C. Furthermore, even with the extreme anneal conditions, the electrical activations of the implanted Si were only 46 and 88% for the anneals at 1250 and 1500 ^{o}C, respectively (Zolper *et. al.*, 1998). Data presented in Figs 27-30 show that higher carrier concentrations, greater electrical activation, and potentially higher mobility have been achieved in the present study for Si-implanted GaN under more practical annealing conditions.

Table 6 compiles the data from Figs. 27-30 and also adds sample sheet resistivity. The most interesting point to make on Table 6 is that the mobilities and carrier concentrations increase with anneal temperature for every dose in spite of the increased ionized impurity scattering from an increased number of active donors. This trend suggests that although substantial damage has been removed at each successive anneal up to 1350 ^{o}C, even further damage recovery and electrical activation are possible for anneals beyond 1350 ^{o}C.

Table 6. Room-Temperature Hall Effect Data for Si implanted into GaN at 25°C

Implant Dose (cm^{-2})	Implant Temp. (°C)	Anneal Condition (°C / time)	Sheet Resistivity (Ω/□)	Mobility ($cm^2/V\cdot s$)	Sheet Conc. (cm^{-2})	Activation Efficiency (%)
-	-	1250 / 18s	150,000	190.5	2.20×10^{11}	-
-	-	1300 / 9s	93,500	225	2.93×10^{11}	-
-	-	1350 / 17s	86,440	245	2.96×10^{11}	-
1×10^{13}	25	1350 / 21s	37,410	201.4	8.30×10^{11}	Argon
1×10^{13}	25	1250 / 21s	186,300	290.2	1.16×10^{11}	1
1×10^{13}	25	1300 / 22s	26,810	134.9	1.73×10^{12}	18
1×10^{13}	25	1350 / 17s	6,358	245.5	4.00×10^{12}	42
5×10^{13}	25	1250 / 21s	13,910	72.1	6.23×10^{12}	13
5×10^{13}	25	1300 / 22s	2,440	143.2	1.79×10^{13}	38
5×10^{13}	25	1350 / 17s	1,092.8	189.5	3.02×10^{13}	64
1×10^{14}	25	1250 / 21s	3,620	81.0	2.13×10^{13}	22
1×10^{14}	25	1300 / 22s	934.7	145.6	4.59×10^{13}	48
1×10^{14}	25	1350 / 17s	701.7	145.8	6.46×10^{13}	68
5×10^{14}	25	1250 / 21s	379.0	66.3	2.49×10^{14}	52
5×10^{14}	25	1300 / 22s	165.3	100.8	3.75×10^{14}	79
5×10^{14}	25	1350 / 17s	128.7	111.1	4.37×10^{14}	92
1×10^{15}	25	1250 / 21s	150.5	63.7	6.52×10^{14}	69
1×10^{15}	25	1300 / 22s	79.4	86.7	9.08×10^{14}	95
1×10^{15}	25	1350 / 17s	60.1	108.8	9.56×10^{14}	100
5×10^{15}	25	1050 / 5m	2380.5	8.0	3.28×10^{14}	7
5×10^{15}	25	1100 / 5m	299.6	20.6	1.01×10^{15}	21
5×10^{15}	25	1150 / 5m	90.8	36.9	1.86×10^{15}	39
5×10^{15}	25	1200 / 5m	37.8	58.7	2.82×10^{15}	59
5×10^{15}	25	1250 / 21s	25.8	67.0	3.62×10^{15}	76
5×10^{15}	25	1300 / 23s	17.5	84.0	4.26×10^{15}	90
5×10^{15}	25	1350 / 7s	15.1	96.1	4.31×10^{15}	91

Temperature-Dependent Hall Effect Measurements.

The sheet carrier concentrations determined from temperature-dependent Hall measurements taken from 10 to 800 K for a sample from each of the six doses annealed at 1350 ^{o}C for 17 sec are shown in Figure 31. The carrier concentration of the unimplanted sample annealed at 1300 ^{o}C for 9 sec is also shown in the figure. The scale of the 1000/T axis is split at 20 K^{-1} (50 K), and an expanded 1000/T scale is used for greater clarity in the regime where sheet carrier concentration is most sensitive to temperature. The carrier concentrations for each of the six doses kept increasing as temperature increased above about 200 K and showed no signs of saturation even at a sample temperature of 800 K, except perhaps on the lowest dose sample of $1x10^{13}$ cm^{-2}. The sheet concentration of the unimplanted sample begins to saturate at 500 K, which will be discussed more fully later in Figure 34. The flat temperature-independent carrier concentration seen on all but the lowest dose sample of $1x10^{13}$ cm^{-2} indicates the formation of a degenerate impurity band. The critical doping density for GaN at which the Mott transition occurs and all donors are ionized independent of temperature is calculated from eqn. (16) to be $8.84x10^{17}$ cm^{-3}. The TRIM calculated implantation profiles for 200 keV Si ions through a 500 Å AlN cap into GaN at doses of $5x10^{13}$ and $1x10^{14}$ cm^{-2} are shown in Figure 32. The peak volume concentrations of Si donors for the two doses are $2.81x10^{18}$ and $5.62x10^{18}$ cm^{-3}, respectively. Thus, the peak concentration of the sample implanted with a dose of $1x10^{13}$ cm^{-2} is still below the Mott transition, whereas the peak concentrations of all other doses exceed the critical Mott concentration. Furthermore, most of the implanted region for the higher doses contains a

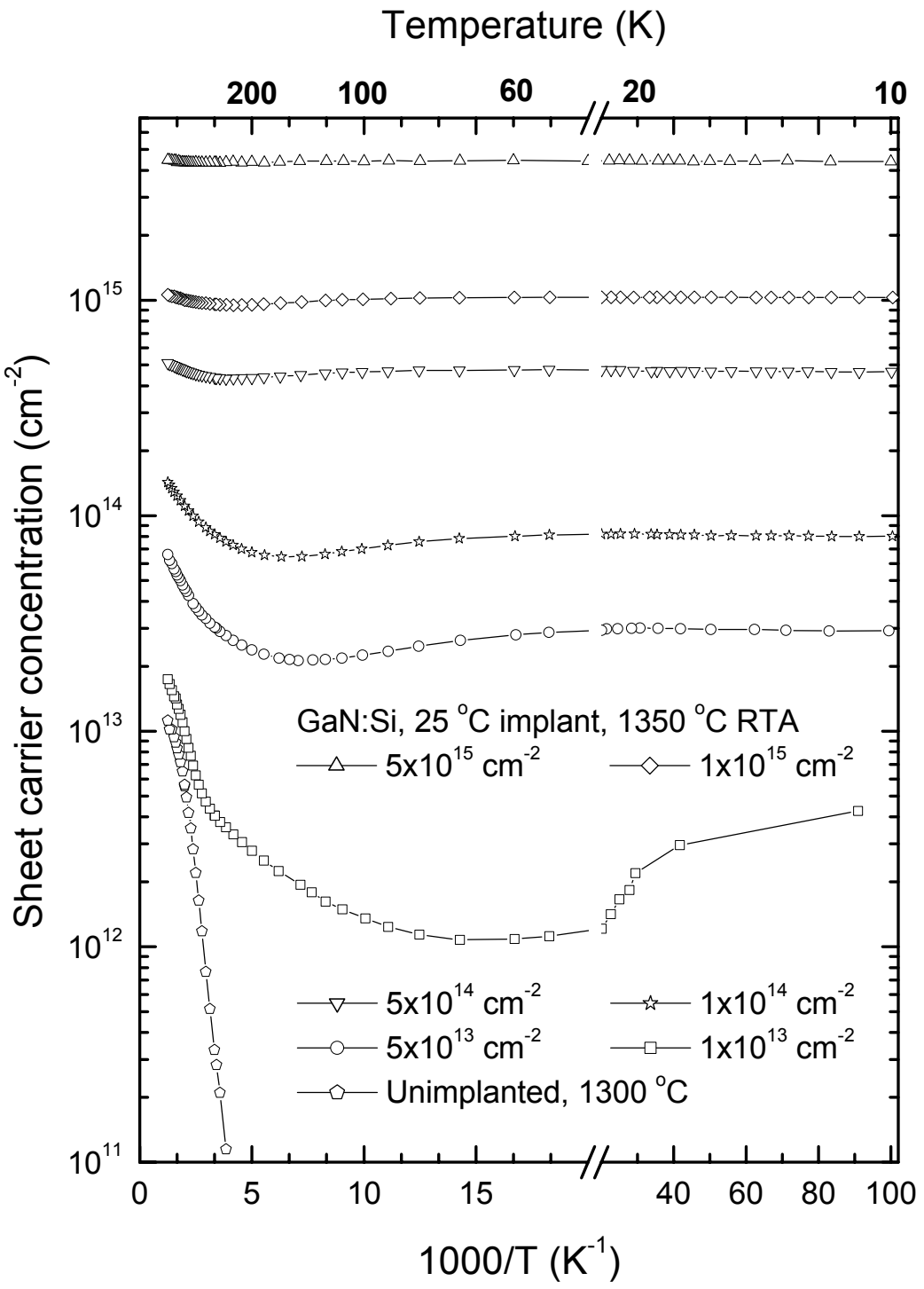

Figure 31. Temperature-dependent sheet electron concentrations taken from 10-800 K for GaN implanted at room temperature with 200 keV Si ions at doses ranging from $1x10^{13}$ to $5x10^{15}$ cm^{-2} and annealed at 1350 °C for 17 sec in a flowing nitrogen environment.

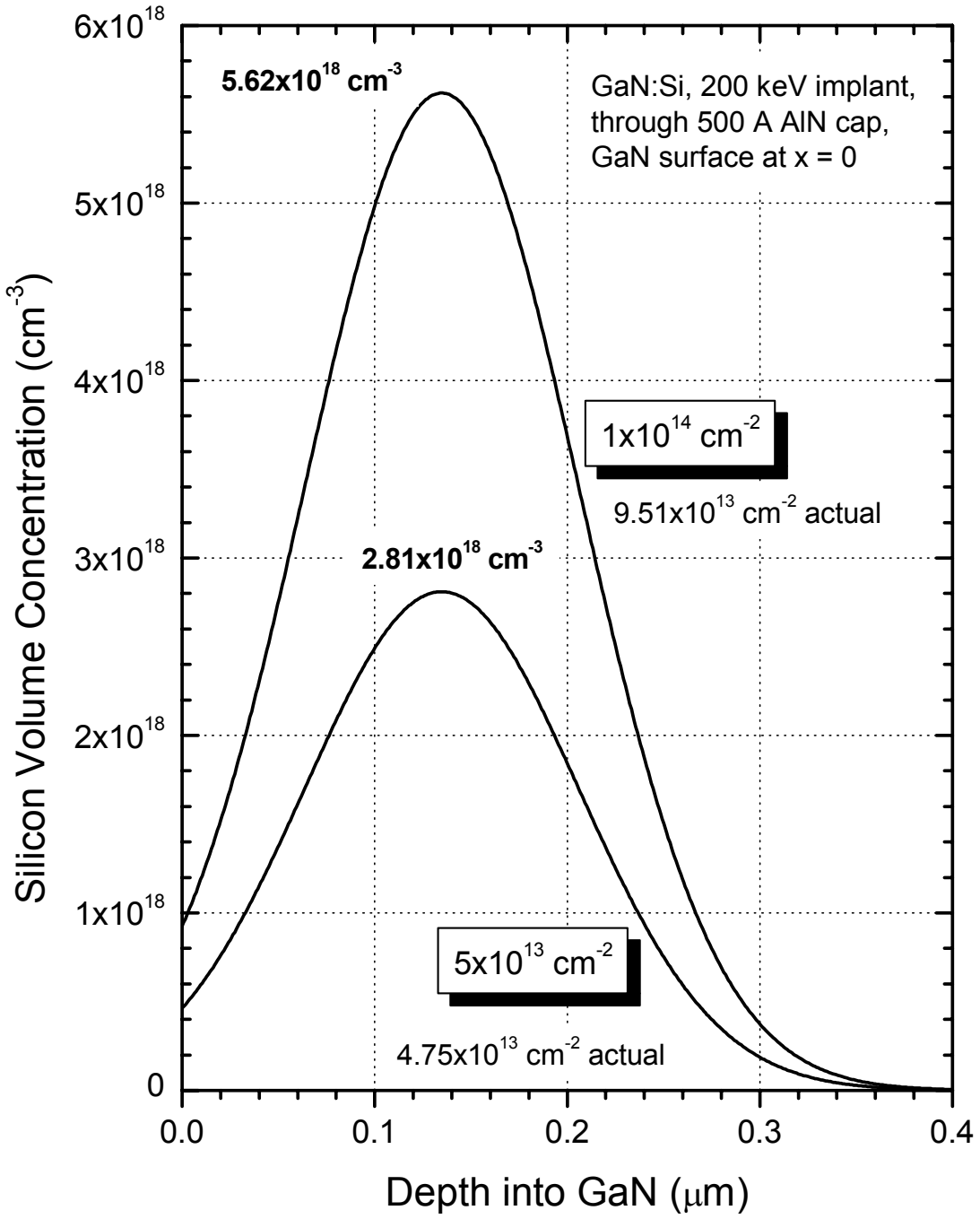

Figure 32. Calculated implantation profiles for 200 keV Si ions through a 500 Å AlN cap into GaN at doses of $5x10^{13}$ and $1x10^{14}$ cm^{-2}.

Si concentration higher than the Mott transition. The dip in the carrier concentration curves seen in Figure 31 may indicate multi-layer conduction (Look and Molnar, 1997). Because of the Gaussian implantation profile, the carrier concentration of the degenerate layer is non-uniform. Additionally, most of the implanted layer is degenerate; the remainder is non-degenerate. The carrier concentration of the sample implanted with a dose of $5\text{x}10^{15}$ cm^{-2} is almost entirely temperature-independent from 10-800 K, as expected for a case of extreme degeneracy due to a peak Si concentration of almost $3\text{x}10^{20}$ cm^{-3}.

As electrical activation and therefore the concentration of ionized donors increases, impurity screening will effectively reduce the donor ionization energy as described in equation (17). There are basically two different techniques for determining the effective ionization energy from Hall effect measurements, both of which require either sheet carrier concentration or sheet resistivity as a function of temperature. The first technique is the simplest and assumes that the carrier concentration is proportional to $T^{3/2}\exp(-E_d/k_BT)$. Temperature dependence of this form was seen in equation (8), though the actual expression for the free carrier concentration in an extrinsic semiconductor is derived from equation (13). Resistivity has a temperature dependence reciprocal to that of carrier concentration. Whether resistivity or carrier concentration is used, the ionization energy is extracted from the slope of the least-squares fit on an Arrhenius plot. There is no standardized approach for this graphical technique in the literature, and the data are routinely plotted as either $\ln(n_s)$, $\ln(n_sT^{-3/2})$, $\ln(\rho_s)$, or $\ln(\rho_sT^{3/2})$. The second technique involves fitting measured sheet carrier concentrations converted to volume carrier concentrations as a function of temperature to the charge

balance equation, eqn. (13). The parameters varied in the fit are the ionization energy, the dopant volume concentration, and the volume concentration of compensating acceptors. Multiple donor levels can be easily incorporated in the curve-fitting technique; however, one must exercise caution to ensure realistic fit values when the measured data is from a non-uniform implanted layer. Using these two techniques to determine ionization energy, the reported values for Si in GaN range from 17 to 29 meV. One report stated an ionization energy as high as 62 meV; however this value was calculated from zincblende β–GaN and should not be used for wurtzite α–GaN. Götz *et. al*. reported ionization energies for in-situ Si-doped MOCVD GaN that ranged from 15-12 meV for Si concentrations of 2-9x10^{17} cm^{-3}, respectively (Götz *et. al*., 1996). Dupius *et. al*. measured an ionization energy of 15 meV for a Si-implanted sample with a room-temperature sheet carrier concentration of 9x10^{13} cm^{-2} (Dupius *et. al*., 1999). Zolper *et. al*. measured a much lower value of 3.4 meV for a Si-implanted sample with a room-temperature sheet carrier concentration of 1.75x10^{15} cm^{-2} as expected from a degenerate concentration (Zolper *et. al*., 1997a).

The graphical technique was used to determine the Si ionization energy in this study, and the results for each of the six Si-implantation doses annealed at 1350 ^{o}C for 17 sec are shown in Figure 33. The data used in the least squares fit were taken at sample temperatures from 120-800 K. The extracted apparent ionization energies vary significantly from 2.5 to 74 meV, and the actual ionization energy of isolated Si could only be estimated from the sample implanted at 1x10^{13} cm^{-2}. The relatively low apparent ionization energies measured on the samples with the highest three doses is attributed to

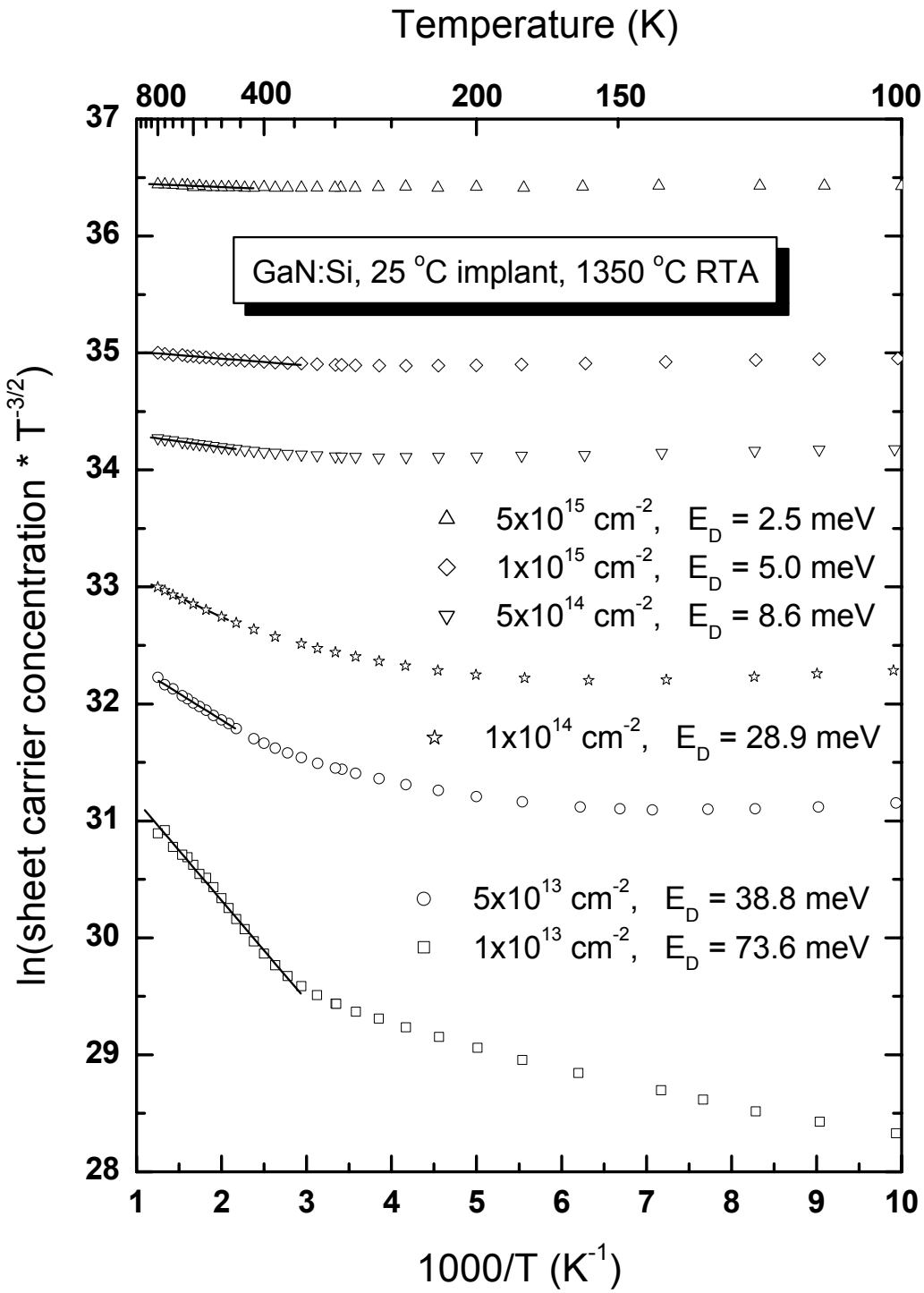

Figure 33. Measured ionization energies for GaN implanted at room temperature with 200 keV Si ions at doses ranging from $1x10^{13}$ to $5x10^{15}$ cm^{-2} and annealed at 1350 °C for 17 sec in a flowing nitrogen environment.

the formation of a degenerate impurity band from the Si-implanted region. The relatively high apparent ionization energies measured on the samples with the lowest three doses are attributed to the effect of a deeper level donor activation that becomes dominant at higher sample temperatures once the lower concentration of shallow Si donors is all ionized. This effect is clearly seen in Figure 34 as the slope of the Arrhenius plot for the sample implanted at $1x10^{13}$ cm^{-2} sharply increased from 15 to 74 meV above 300 K. In the figure, the carrier concentration of the sample implanted at $1x10^{13}$ cm^{-2} is influenced when the carrier concentration of the unimplanted sample becomes comparable. Only the sample implanted at $1x10^{13}$ cm^{-2} distinctly shows two donor levels. The lower ionization energy of 15 meV can be attributed to the shallow Si donors, whose peak volume concentration at this dose is about $6x10^{17}$ cm^{-3}. However, due to the Gaussian implant profile and because the Hall effect measures an average sheet concentration, less than half this peak value is a better estimate for the Si volume concentration in the implanted layer. Thus, 15 meV corresponds to the ionization energy of Si at a concentration of about $2x10^{17}$ cm^{-3}, which agrees very well with the 14 meV ionization energy reported for a $2.3x10^{17}$ cm^{-3} Si concentration in *in-situ* doped GaN (Götz *et. al*., 1996). Interestingly, the *n*-type background of all unimplanted samples, whether they are annealed or not, is not due to a shallow donor but rather a deep donor whose ionization energy is about 190 meV.

Figure 35 shows the temperature-dependent Hall mobility for the same set of samples discussed in Figs. 31 and 33. The peak mobilities decrease from 258 to 108 $cm^2/V{\cdot}s$ as the implantation dose is increased from $1x10^{13}$ to $5x10^{15}$ cm^{-2}. This is due to

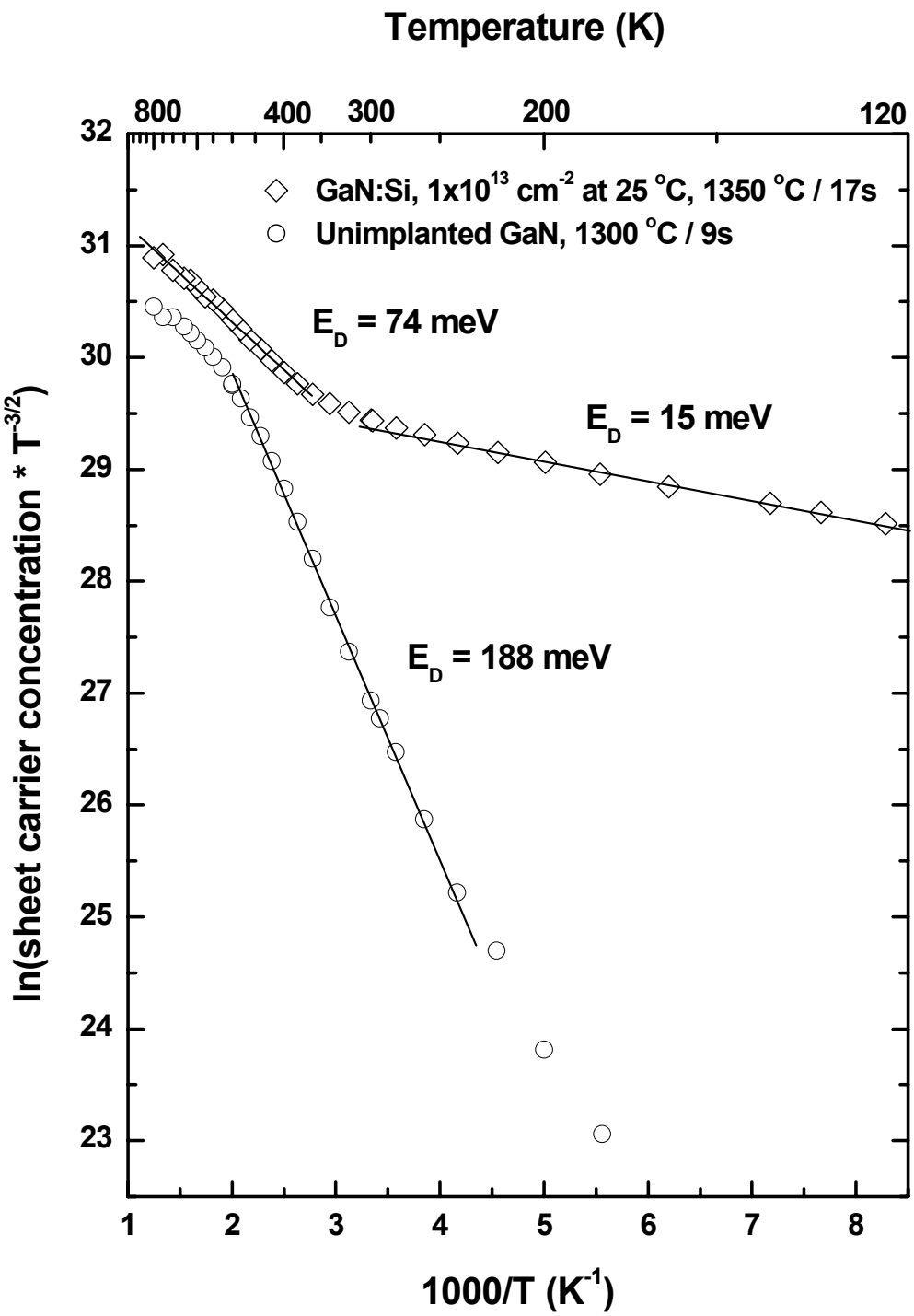

Figure 34. Measured ionization energies for GaN implanted at room temperature with 200 keV Si ions at a dose of $1x10^{13}$ cm^{-2} and annealed at 1350 ^oC for 17 sec along with unimplanted GaN annealed at 1300 ^oC for 9 sec in a flowing nitrogen environment.

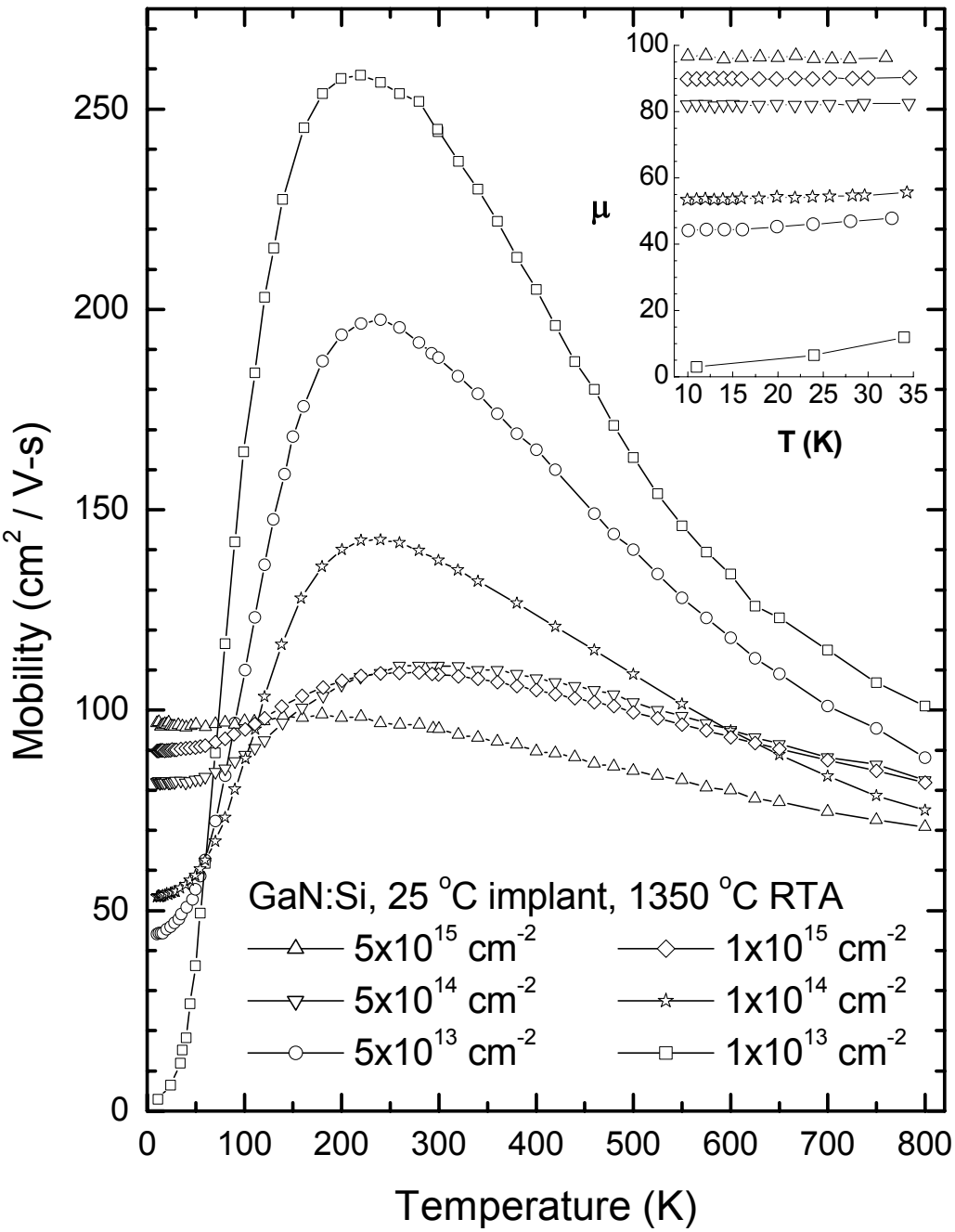

Figure 35. Temperature-dependent Hall mobility taken from 10-800 K for GaN implanted at room temperature with 200 keV Si ions at doses ranging from $1x10^{13}$ to $5x10^{15}$ cm^{-2} and annealed at 1350 ^oC for 17 sec in a flowing nitrogen environment.

increased ionized impurity and polar optical phonon lattice scattering. The most interesting feature of these mobility curves is their low-temperature behavior shown with greater resolution in the inset. As the implantation dose increases from $1x10^{13}$ to $5x10^{15}$ cm^{-2}, the mobilities at 10 K increase from 3 to 97 $cm^2/V{\cdot}s$. As theoretically predicted, the mobility of the non-degenerate sample implanted with a dose of $1x10^{13}$ cm^{-2} approaches zero at 0 K and increases rapidly with temperature where ionized impurity scattering is dominant. As the implantation dose is increased, the degenerate impurity band causes the low-temperature mobility to become more temperature independent and to increase with doping concentration because the Fermi velocity of the electrons is greater than their thermal velocity. The increasing influence of the degenerate impurity band in the three highest dose samples is further shown by a general flattening of the mobility curve.

The temperature-dependent sheet resistivity from 10-800 K for the same set of samples annealed at 1350 ^{o}C for 17 sec is shown in Figure 36. As the implantation dose is increased from $1x10^{13}$ to $5x10^{15}$ cm^{-2}, the room-temperature resistivity decreases proportionally from 6,350 to 15 Ω/□. Only the samples implanted with the three lowest doses, which are least affected by the degenerate impurity band, show any appreciable decrease in resistivity with increasing temperature. A slight knee on the curve from the sample implanted with a dose of $1x10^{13}$ cm^{-2} occurs slightly above 300 K. This is due to the effect of a deeper donor level that becomes dominant once the lower concentration of shallow Si donors are all ionized as seen previously in Figs. 33 and 34. The samples implanted with the three highest doses, whose carrier concentration and mobility vary little with temperature, have resistivities that are relatively temperature independent. The

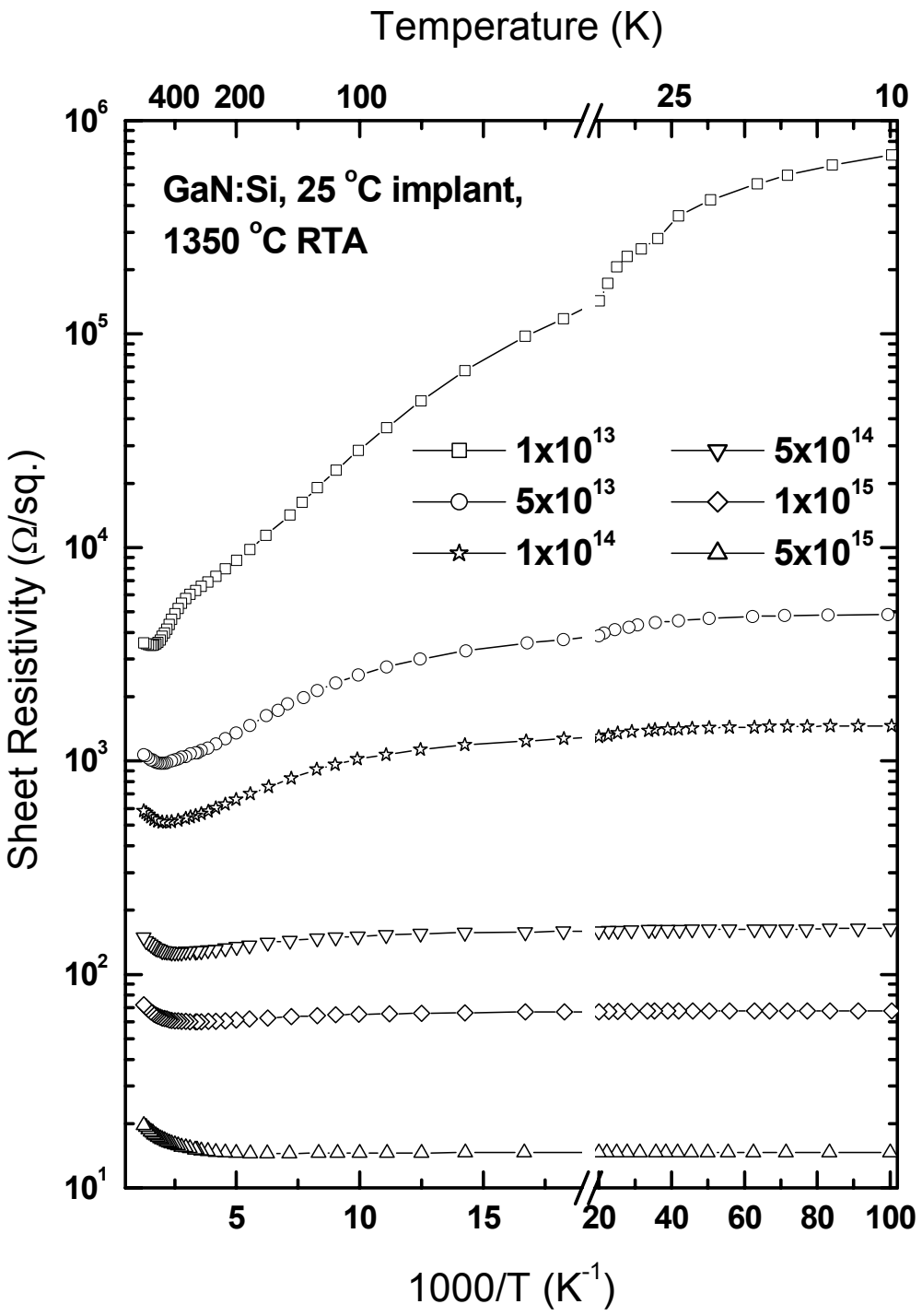

Figure 36. Temperature-dependent sheet resistivity taken from 10-800 K for GaN implanted at room temperature with 200 keV Si ions at doses ranging from $1x10^{13}$ to $5x10^{15}$ cm^{-2} and annealed at 1350 ^{o}C for 17 sec in a flowing nitrogen environment.

resistivity for all implantation doses increases in the high-temperature region as the carrier concentration·mobility product decreases. Recall from equation (11) that resistivity may be expressed as $\rho = \left[e\left(n\mu_n + p\mu_p \right) \right]^{-1}$ where e is the elementary charge, and n (p) and μ_n (μ_p) are the concentration and mobility of electrons (holes), respectively.

The anneal temperature dependence of the temperature-dependent Hall effect measurements were investigated on GaN implanted with Si at a dose of 5×10^{14} cm^{-2}, and the results are shown in Figs. 37 and 38. Figure 37 shows the extracted ionization energies from the slope of the least-squares fit on an Arrhenius for samples annealed from 1250 to 1350 ^{o}C for an average of 20 sec. The energies vary moderately from 8.6 to 18.4 meV. As anneal temperature is increased, the ionization energies decrease due to increased screening effects and widening of the impurity band as a greater percentage of Si donors are activated. The relative changes in the three ionization energies as anneal temperature is increased are proportional to the corresponding changes in sheet carrier concentration. Figure 38 shows the mobility curves for the same set of samples implanted with Si at a dose of 5×10^{14} cm^{-2} and annealed from 1250 to 1350 ^{o}C for an average of 20 sec. As anneal temperature is increased, the peak mobility increases from about 72 to 112 cm^2/V·s and the temperature at which the peak value occurs decreases from about 480 K to 300 K.

Low-Temperature Photoluminescence.

Before presenting the spectra for the Si-implanted GaN, is it important to examine the features and anneal temperature behavior of the spectra for the unimplanted material. The PL spectra taken at 3 K for the as-grown and unimplanted GaN annealed from 1250

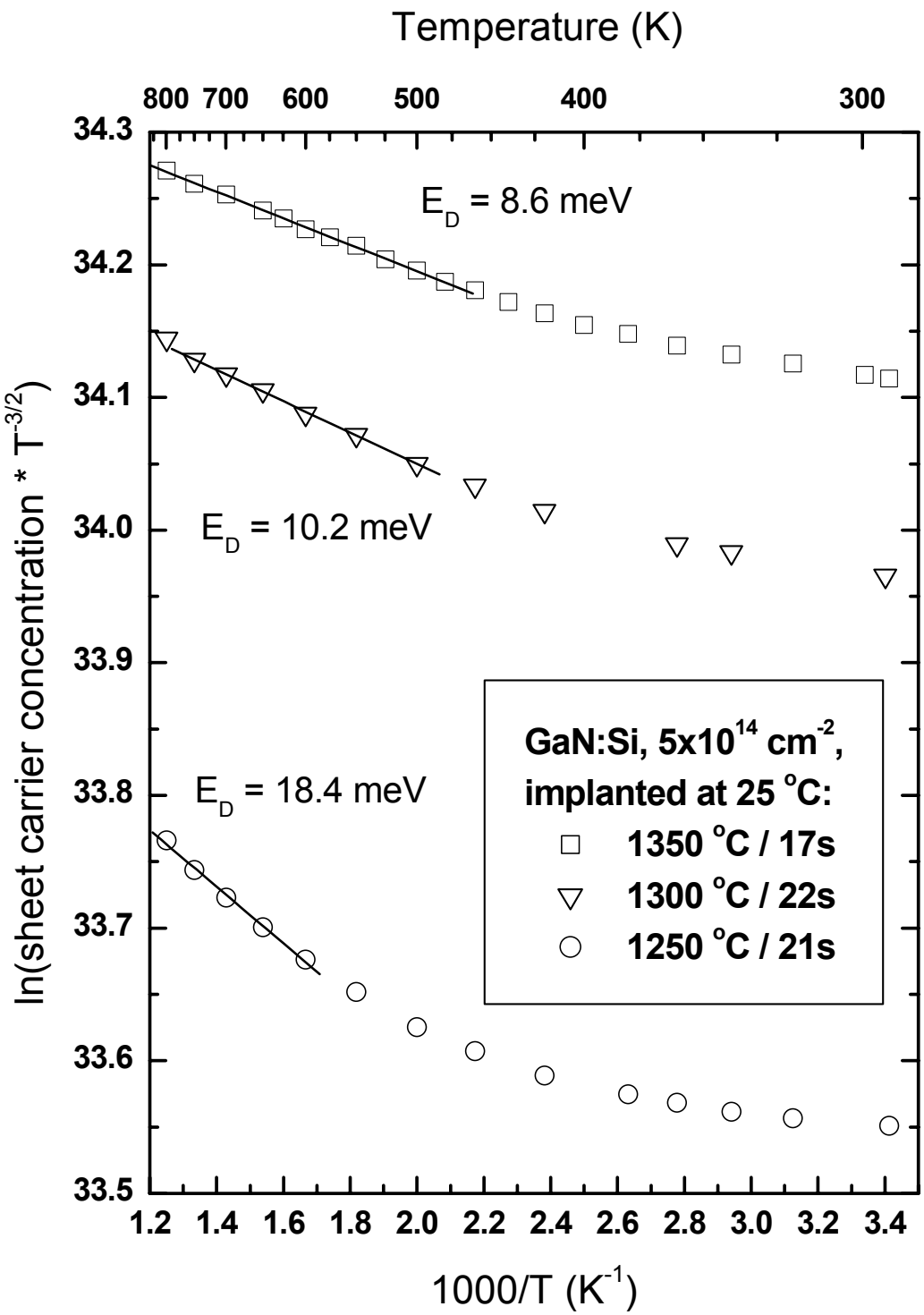

Figure 37. Measured ionization energies for GaN implanted at room temperature with 200 keV Si ions at a dose of $5x10^{14}$ cm^{-2} and annealed from 1100 to1350 ^{o}C for 5 min to 17 sec in a flowing nitrogen environment.

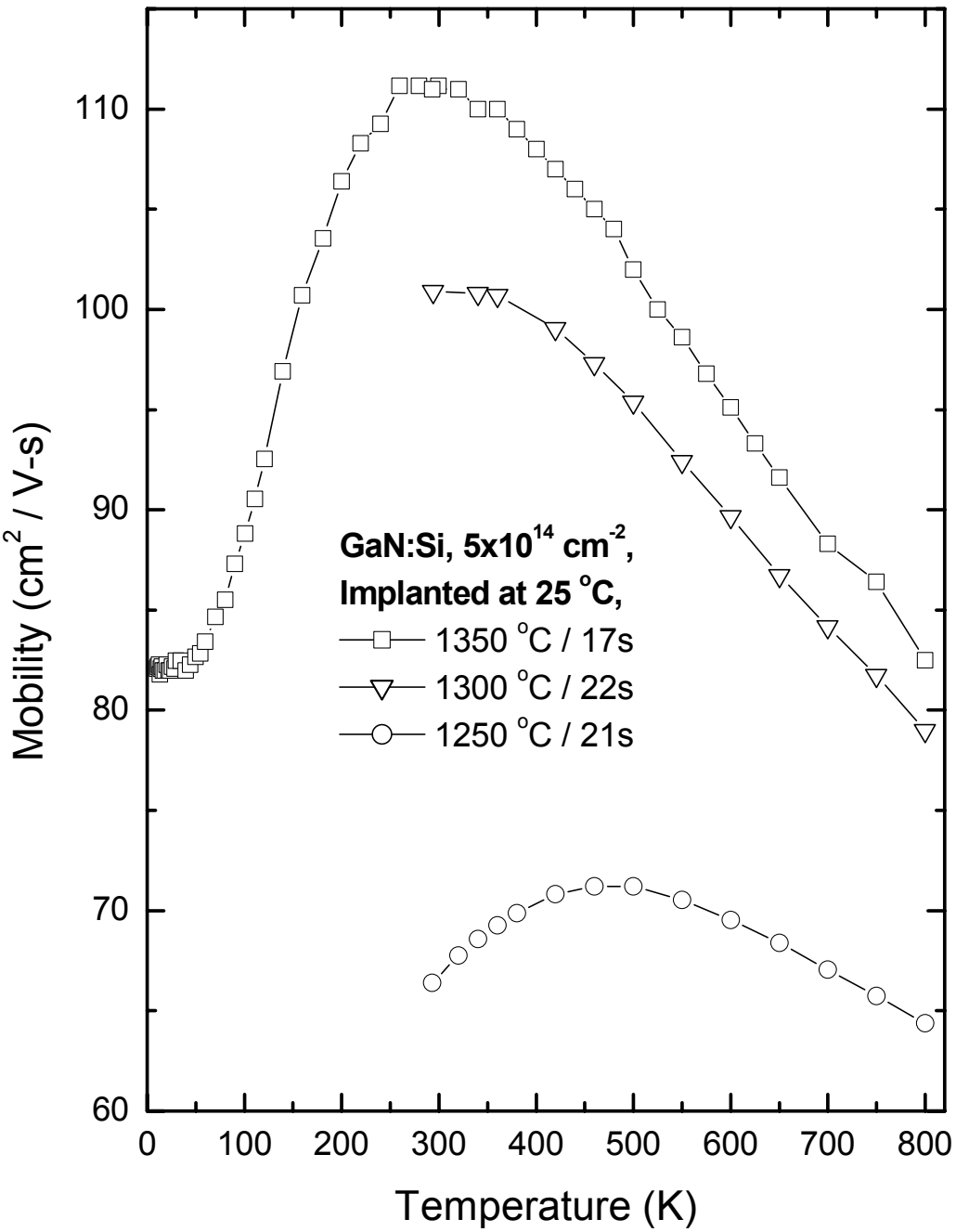

Figure 38. Temperature-dependent Hall mobility taken from 10-800 K for GaN implanted at room temperature with 200 keV Si ions at a dose of $5x10^{14}$ cm^{-2} and annealed from 1100 to1350 ^{o}C for 5 min to 17 sec in a flowing nitrogen environment.

to 1350 ^{o}C are shown in Figure 39. Each of these spectra show a typical (D^{o},X) peak at 3.49 eV and a dominant DAP peak at 3.29 eV with phonon replicas. The as-grown spectrum, whose intensity has been increased by a factor of 5, reveals a weak YL band at 2.26 eV typical for unintentially-doped *n*-type GaN. The as-grown YL band is supplanted by a BL band centered at 2.65 eV, whose peak becomes ⅓ as intense at the (D^{o},X) peak after annealing at 1350 ^{o}C for 17 s. The intensities of the (D^{o},X) and DAP peaks in the unimplanted GaN remain largely unaffected when anneal temperature is increased from 1250 to 1350 ^{o}C.

The PL spectra taken at 3 K for GaN implanted at room temperature with 200 keV Si ions with doses ranging from $1x10^{13}$ to $5x10^{15}$ cm^{-2} and annealed at 1350 ^{o}C for 17 sec in a flowing nitrogen environment are shown in Figure 40. In general, these spectra show a (D^{o},X) peak at 3.487 eV, a DAP peak at 3.28 eV with phonon replicas, and a broad YL band centered at 2.2 eV. Also shown in Fig. 40 is the spectrum for the unimplanted sample annealed at 1350 ^{o}C for 17 sec, whose intensity has been reduced by a factor of 5. The intensity of the (D^{o},X) peaks from each Si-implanted spectrum except for the highest dose has also been reduced by a factor of 5 for easier viewing and comparison. All spectra reveal a (D^{o},X) peak that decreases in intensity and broadens with increasing dose. The near band-edge broadening begins on the low energy side of the (D^{o},X) peak in the sample implanted with a dose of $5x10^{13}$ cm^{-2} and is due to band tailing. Recall that at a dose of $5x10^{13}$ cm^{-2}, the peak of the implant profile exceeds the Mott concentration causing random band-edge fluctuations and band tailing. At a dose of $5x10^{14}$ cm^{-2}, the free carrier concentration is high enough to initiate noticeable band filling. This is seen as a broadening on the high energy side of the (D^{o},X) peak above the

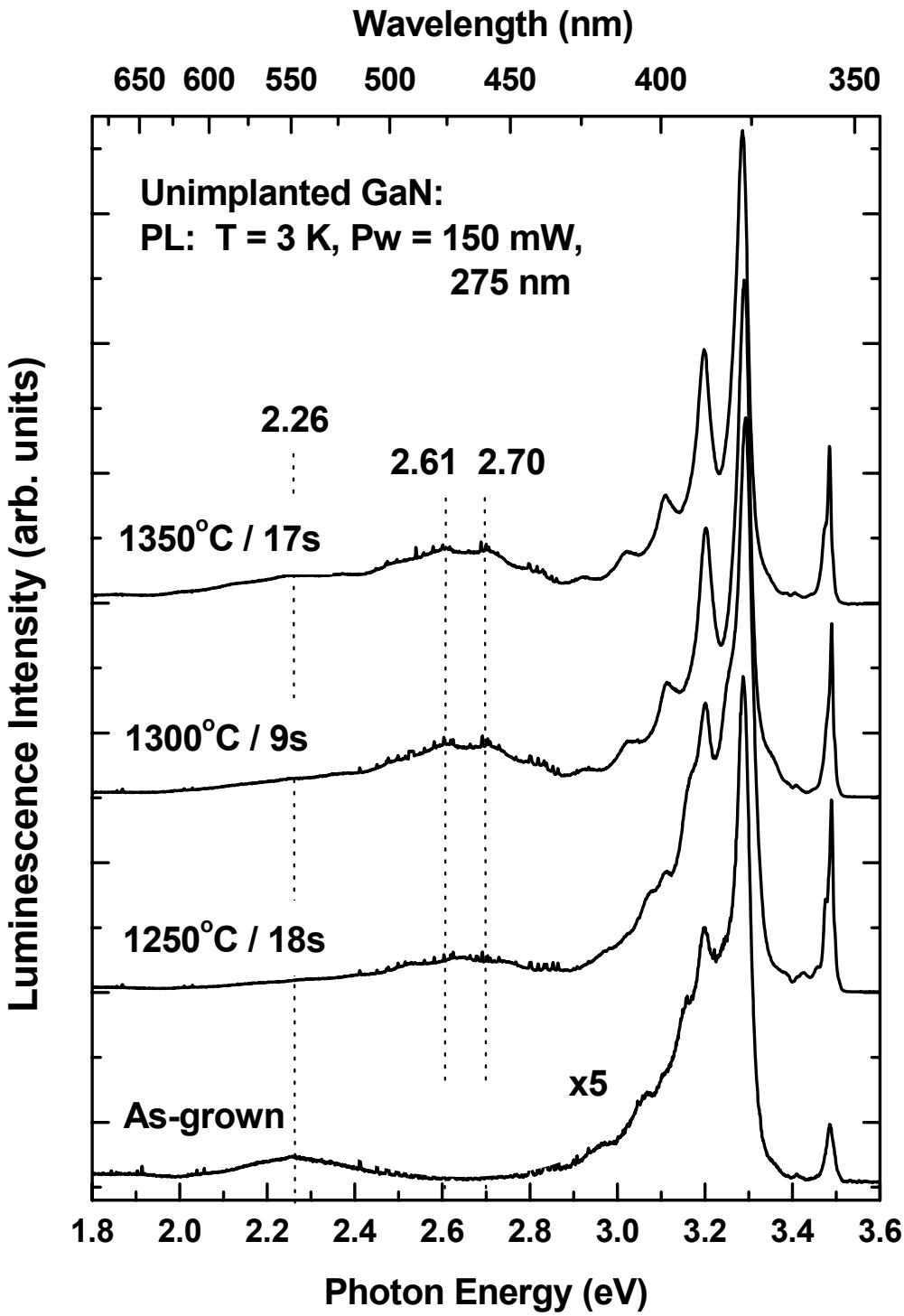

Figure 39. PL spectra taken at 3 K for unimplanted GaN as-grown and annealed at 1250, 1300, and 1350 ^{o}C from 9 to 17 sec in a flowing nitrogen environment.

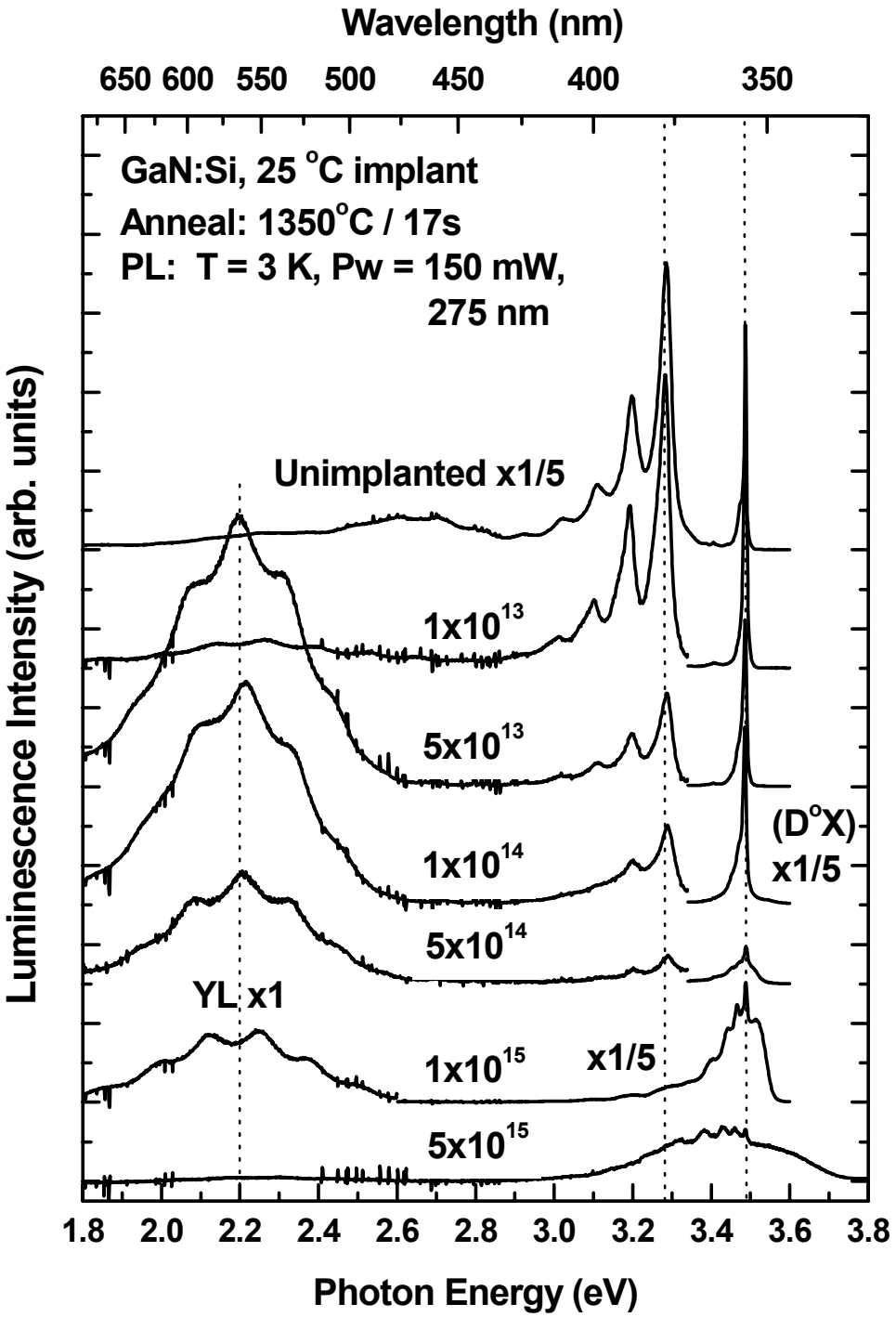

Figure 40. PL spectra taken at 3 K for GaN implanted at room temperature with 200 keV Si ions at doses ranging from $1x10^{13}$ to $5x10^{15}$ cm^{-2} and annealed at 1350 °C for 17 sec in a flowing nitrogen environment.

bandgap. Luminescence from the band tailing and filling is most intense on the sample implanted with a dose of $1x10^{15}$ cm^{-2}. Though weaker in intensity, the band tailing and filling on the sample implanted with the highest dose produces a very broad band-to-band transition extending from 3.1 to 3.7 eV. The interference patterns shown as lower energy shoulders of the (D^o,X) peak on the two highest dose samples are spaced too closely to be LO replicas or to be caused by the etalon effect.

The (D^o,X) and DAP peaks are the most intense on the sample with the lowest dose. As the dose increases from $1x10^{13}$ to $1x10^{14}$ cm^{-2}, the zero-phonon DAP peak blue-shifts 6 meV and its FWHM broadens by about 25 meV. This is because at higher doses there are many more closer donor-acceptor pairs as well as a wider donor impurity band. All evidence of DAP transitions have disappeared on the spectra from the two highest doses because the donor band has merged with the conduction band. After annealing at 1350 ^oC, the unimplanted GaN has nearly 5 times the DAP intensity that the sample implanted with a dose of $1x10^{13}$ cm^{-2} has. However, the sample implanted with a dose of $1x10^{13}$ cm^{-2} has nearly 4 times the (D^o,X) intensity and over 10 times the sheet carrier concentration that the unimplanted sample has.

The intensity of the YL band is fairly weak on the lowest-dose spectrum but increases by almost an order of magnitude and becomes the strongest for the next highest dose, $5x10^{13}$ cm^{-2}. The intensity of the YL band decreases as the dose further increases, and no YL is observed for the highest dose of $5x10^{15}$ cm^{-2}. This YL has not been observed in any of the Mg-implanted GaN in this study and appeared when Si-alone was implanted. This may indicate that this YL is closely related to a Si-related complex or a complex or defect that has a low formation energy in *n*-type GaN. Despite a small

ambiguity introduced by the Fabry-Pérot oscillations, the YL appears to peak at 2.2 eV independent of implantation dose. Overall, the features of the low-temperature PL spectra are well correlated with the Hall effect measurements as a function of implantation dose for samples annealed at 1350 ^{o}C for 17 sec.

The sharpness (FWHM of about 16 meV) and intensity of the (D^{o},X) peak from the lowest dose sample correlate well with the high mobility obtained on this sample. Both the exciton peak and the high mobility observed from low-dose Si-implanted GaN indicate excellent implantation damage recovery after annealing at 1350 ^{o}C for 17 sec. Clearly, the sample implanted with the lowest dose has suffered the least implantation damage and exhibited the most complete damage recovery after annealing according to PL data. However, unlike Si-implanted GaAs, which shows higher Si activation at lower implantation doses, Si-implanted GaN experiences lower Si activation for lower implantation doses. Tan *et. al*. implanted 90 keV Si into GaAs and GaN at 77 K with doses from $1x10^{12}$ to $9x10^{17}$ cm^{-2} and characterized the damage with ion channeling. They reported that a dose of $4x10^{13}$ cm^{-2} completely amorphized the GaAs, whereas the same dose in GaN produced a channeling yield comparable to the unimplanted GaN (Tan *et. al*., 1996). Clearly, GaN is a robust material that suffers much less implantation damage than GaAs does for a given ion mass at nominal doses. Chan and Chen implanted C and C+Ar into GaAs with doses from $5x10^{12}$ to $1x10^{14}$ cm^{-2} and characterized the samples with Hall effect measurements. They reported that C+Ar coimplantation produced 100% C activation compared to only 25% with C-alone implantation. Additionally, they reported that C activation increased by as much as 70% as the coimplantation dose increased from $5x10^{12}$ to $5x10^{13}$ cm^{-2} at a single anneal

temperature. In all cases the increased activation was attributed to increased implantation damage, which increased vacancies, crucial for enhancing activation (Chan and Chen, 1993). The activation of Si-implanted GaN in this present study also increased significantly as the implantation dose was increased. It may be that although low-dose Si activates well in GaAs, it does not activate well in the more structurally robust GaN. A possible explanation is that Si activation in GaN, like C activation in GaAs, is enhanced by implantation damage.

The PL spectra taken at 3 K for GaN implanted at room temperature with 200 keV Ar ions with doses ranging from $1x10^{13}$ to $1x10^{15}$ cm^{-2} and annealed at 1350 ^{o}C for 22 sec in a flowing nitrogen environment are shown in Figure 41. In general, these spectra show a (D^{o},X) peak at 3.487 eV, a DAP peak at 3.28 eV with phonon replicas, and a broad YL band centered near 2.2 eV. Also shown in Fig. 41 is the spectrum for the unimplanted sample annealed at 1350 ^{o}C for 17 sec, whose intensity has been reduced by a factor of 10. The intensities of all three luminescence features from the Ar-implanted samples are the strongest on the sample implanted with the lowest dose. As the dose increases, the intensity of the (D^{o},X) peak, the DAP peak, and the broad YL band all decrease.

The PL spectra taken at 3 K for GaN implanted with Si at a dose of $1x10^{13}$ cm^{-2} and annealed from 1250 to 1350 ^{o}C for 22-17 sec in a flowing nitrogen environment are shown in Figure 42. As in the previous figure, the intensity of the (D^{o},X) peak on the spectrum from the sample annealed at 1350 ^{o}C has been reduced by a factor of 5 for easier viewing. The spectrum from the sample annealed at 1250 ^{o}C shows only a weak

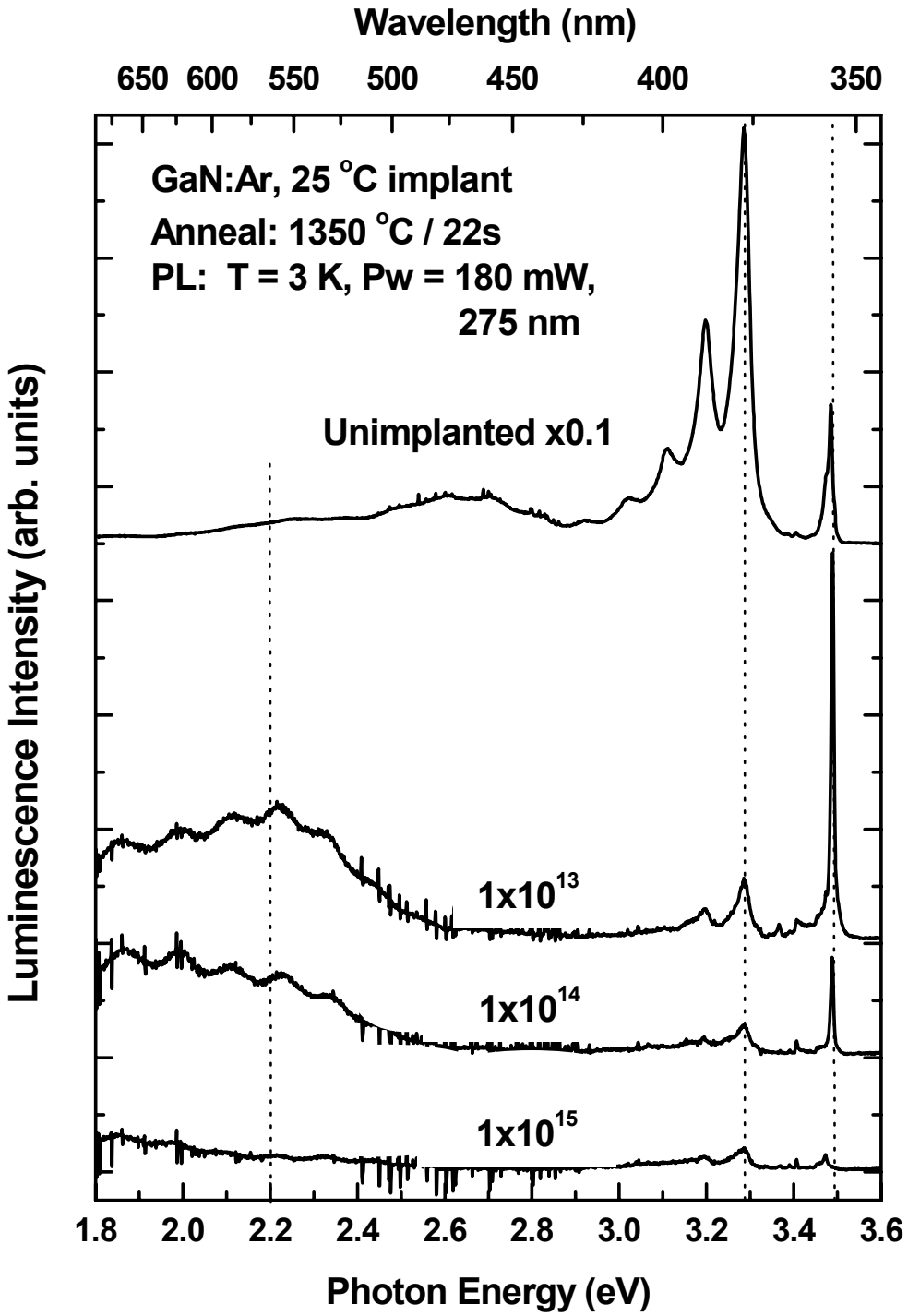

Figure 41. PL spectra taken at 3 K for GaN implanted at room temperature with 200 keV Ar ions at doses ranging from $1x10^{13}$ to $5x10^{15}$ cm^{-2} and annealed at 1350 °C for 22 sec in a flowing nitrogen environment.

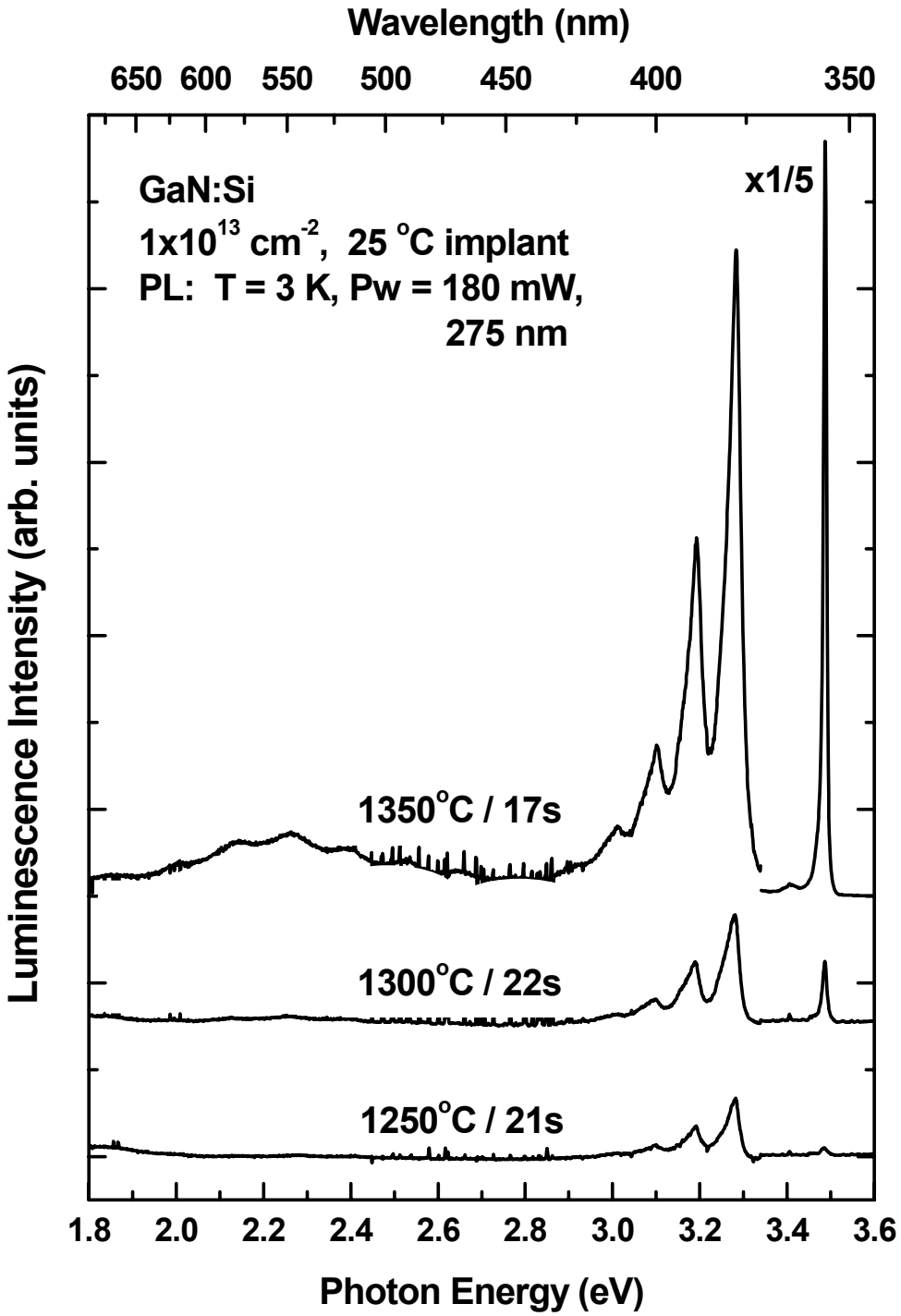

Figure 42. PL spectra taken at 3 K for GaN implanted at room temperature with 200 keV Si ions at a dose of $1x10^{13}$ cm^{-2} and annealed at 1250, 1300, and 1350 ^{o}C for approximately 20 sec in a flowing nitrogen environment.

concentration increased by factors of about 18 and 2, as anneal temperature was increased to 1300 and 1350 ^{o}C, respectively. Thus, the improvements in PL spectral intensity after annealing at 1300 and 1350 ^{o}C are attributed to both more Si activation and further lattice damage recovery.

Temperature-Dependent Photoluminescence.

Temperature-dependent PL spectra from GaN implanted at room temperature with 200 keV Si at a dose of $5x10^{13}$ cm^{-2} and annealed at 1350 ^{o}C for 17 sec in a flowing nitrogen environment are shown in Figure 43. The three features shown in the spectra are a (D^{o},X) peak, a DAP peak with phonon replicas, and a YL band with Fabry-Pérot interference reflections. The sharp and intense (D^{o},X) peak at 3.487 eV decreases monotonically, broadens, and red-shifts by about 63 meV as temperature increases from 3 to 300 K. This red-shift is due to the thermal characteristics of the GaN bandgap which decreases by about 66 meV over the same temperature range. The intensity of the DAP peak at 3.289 eV and its phonon replicas also decrease monotonically as temperature increases, maintaining 50% and 1% of its original intensity at 100 and 200 K, respectively, but totally disappearing above 200 K. This temperature dependence, similar to that seen on the 3.28 eV DAP peak in the Mg+Si coimplanted sample (Fig. 24), is attributed to the ionization of the shallow Si donor. The intensity of the broad YL band behaves very differently than that of the (D^{o},X) and DAP peaks dropping to only about 50% of its low-temperature value at 300 K. As the temperature is increased from 3 to 300 K, the peak position of the YL band red-shifts about 13 meV from 2.212 to 2.199 eV. Although this red-shift is not as large as the bandgap reduction with temperature, it is noticeably different from the 50 meV blue-shift seen on the GL band in the spectra from

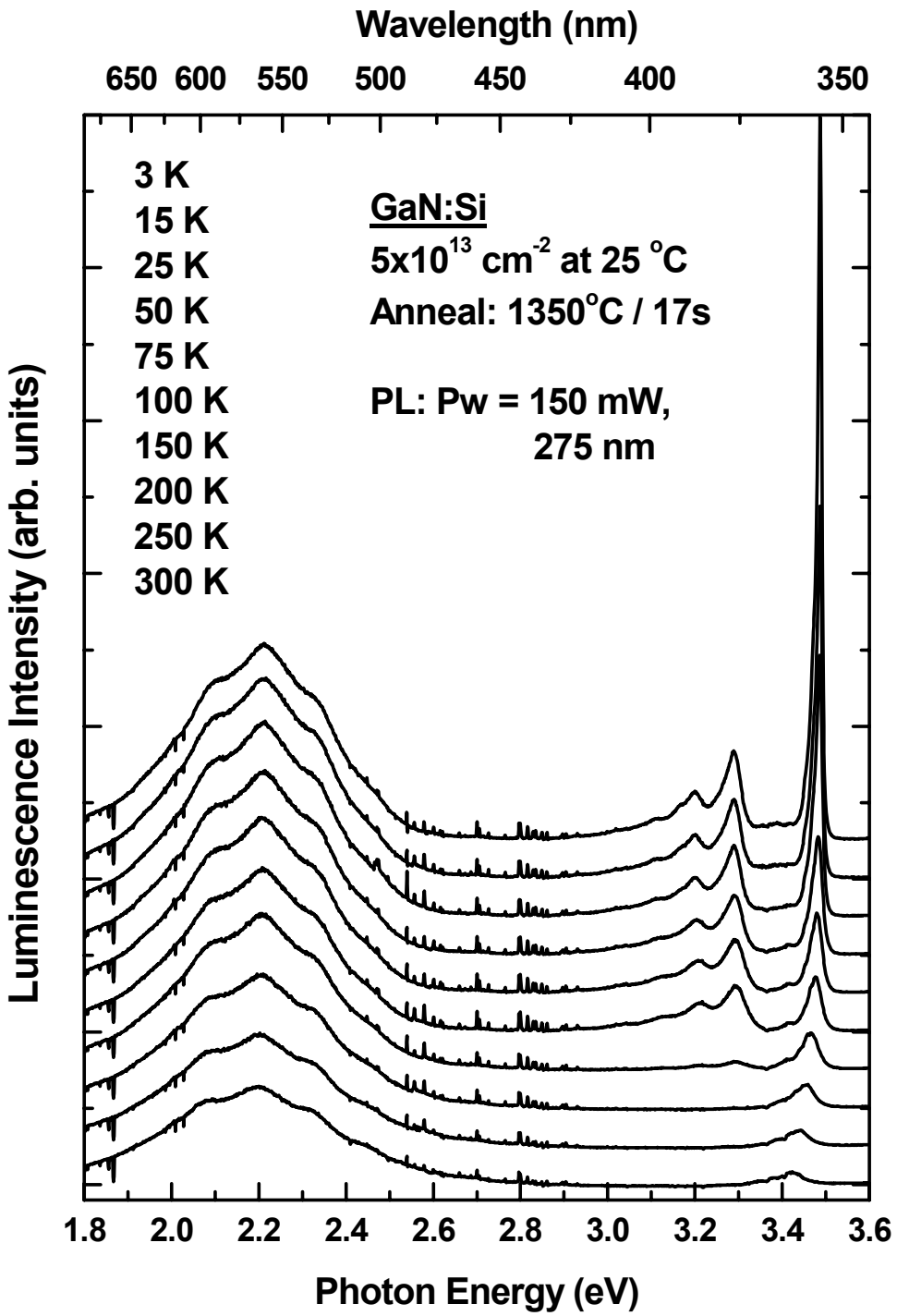

Figure 43. Temperature-dependent PL spectra (3-300 K) from GaN implanted at room temperature with 200 keV Si ions at a dose of $5x10^{13}$ cm^{-2} and annealed at 1350 ^{o}C for 17 sec in a flowing nitrogen environment.

the Mg-implanted samples. This YL also quenches less rapidly with temperature than does the GL band. This behavior indicates a deeper level, less susceptible to thermal ionization, is responsible for the YL band.

There is still much debate in the literature concerning the nature of the YL in *n*-type GaN. Several of the most likely explanations are described below. The nature of the YL in GaN can be explained by one of two models: 1) an electron either in the conduction band or at a shallow donor transitions to a deep acceptor, (e-A^o) or DA_dP, respectively, 2) an electron occupying a deep donor level transitions to either the valence band or an acceptor, (D^o-h) or (D_dAP), respectively (Shalish *et. al.*, 1999). As early as 1980, the YL in GaN was attributed to a transition between a shallow donor and a deep acceptor (Ogino and Aoki, 1980). In 1996, Neugebauer and Van de Walle theoretically determined that the Ga vacancy or its related complexes formed the deep acceptor responsible for the YL in GaN. Complexes typically form due to the energy gained when a negatively-charged acceptor is attracted to a positively-charged donor. Because the dominant native defect in *n*-type GaN is the triple acceptor, V_{Ga}, the most likely complexes to form should be the double acceptors, V_{Ga}-Si_{Ga} and V_{Ga}-O_N (Neugebauer and Van de Walle, 1996). Yang *et. al*. doped GaN with Si concentrations from 4.5×10^{17} to 5.2×10^{18} cm^{-3} and collected room-temperature PL spectra. Finding that the YL intensity decreased with increasing Si concentration, they attributed the YL to Ga vacancies, whose concentration should decrease as more Si substitutes on the Ga sublattice (Yang *et. al*., 1999). Schubert *et. al*. doped GaN with Si concentrations from 5×10^{16} to 7×10^{18} cm^{-3} and also collected room-temperature PL spectra. However, contrary to Yang *et. al*., they found the intensity of the YL to increase linearly as the Si

concentration increased and attributed the YL to acceptor impurities or compensating native defects (Schubert *et. al*., 1997). Kwon *et. al*. doped GaN with Si concentrations from 2.0×10^{18} to 1.3×10^{19} cm^{-3} and collected PL spectra at 10 K. They found the PL decay time to decrease with increasing Si concentration attributing a shallow Si donor to the YL DAP transition (Kwon *et. al*., 2000). Xu *et. al*. grew unintentionally-doped *n*-type GaN and performed temperature-dependent PL from 8 to 300 K and excitation intensity dependent PL over three orders-of-magnitude. They concluded that the YL is caused by a DA_dP transition at low temperatures and changes to a $(e\text{-}A^o)$ transition as temperature is increased (Xu *et. al*., 2001).

To summarize, a transition from a shallow donor to a V_{Ga} or V_{Ga}-related deep acceptor is commonly reported to cause the YL in GaN. Many reports that have arrived at this conclusion concerning the nature of the YL in GaN considered the ratio of YL to UV (D^o,X) peak intensities but not the typical DAP peak. However, in the present study the 3.29 eV DAP peak, which is widely accepted to involve a shallow donor, quenches much more rapidly than the 2.2 eV YL band. If the YL involved a shallow donor, its thermal characteristics would be similar to that of the 3.29 eV DAP peak. One may therefore conclude that the YL band does not involve a shallow donor, but only deep energy levels.

Having examined the electrical and optical properties of GaN implanted with Si at room temperature, the next few sections in this chapter will discuss the electrical and optical properties of GaN implanted with Si at a high temperature of 800 ^oC.

Silicon Implanted into GaN at 800 ^{o}C

The primary motivation for implanting GaN above room temperature is to minimize implantation damage during ion implantation. Fully removing implantation damage and activating implanted species in GaN are difficult because GaN begins to dissociate well below optimum anneal temperatures. As the implantation temperature is increased, one would expect dynamic annealing during the implantation process to simultaneously recover a portion of the damage as well as activate some implants. Therefore, lower post-implantation anneal temperatures may be required to obtain the same level of damage recovery and implant activation compared with room-temperature implantation if hot-implantation is used. To the best of our knowledge, no one has performed a comprehensive study examining the effects of hot implantation on the electrical activation of Si-implanted GaN. Furthermore, preliminary reports on structural characterization of high-temperature implants in GaN are sometimes contradictory and often incomplete.

In an attempt to better understand implantation damage, Liu *et. al.* found using RBS, XRD, and XTEM found that for a given ion species, amorphization of the implanted region occurs at lower doses as implantation temperature is reduced. They recommended that improved dopant activation may be obtained by implanting at higher temperatures, which they showed reduced lattice distortion (Liu *et. al.*, 1999). However, electrical measurements are needed to confirm the effects of both low- and high-temperature implantation induced defects on dopant activation.

In a related report, possibly on the same samples as Liu, Wenzel *et. al.* used RBS spectroscopy to characterize implanted GaN but reported no electrical measurements. Ca

and Mg were implanted from 25 to 550 ^{o}C into MBE-grown GaN at doses from $1x10^{14}$ to $5x10^{15}$ cm^{-2}, and annealed at 1150 ^{o}C for 15 s in flowing N_2. Contrary to Liu's conclusion, Wenzel contends that damage (specifically point defects) was proportional to the mass of the ion species, implant dose, and implant temperature; and was independent of ion current. Therefore, to avoid certain point defects, they oppugn that implantation should be completed at room temperature rather than higher temperatures (Wenzel *et. al.*, 1999).

Parikh *et. al.* implanted 160 keV Si^{+} with doses from $1x10^{14}$ to $1x10^{15}$ cm^{-2} at room temperature and 550 ^{o}C into GaN, and annealed with a face-to-face proximity cap in Ar ambient at 1000 ^{o}C for 60 s. As-grown and implanted samples were characterized by RBS, PL, and XTEM. Reportedly, even the highest dose produced little damage when implanted at 550 ^{o}C according to RBS spectra. As expected from dynamic annealing, hot-implantation produced less damage than the corresponding room-temperature implantation. Although damage was partially recovered on all annealed samples, on even the lowest dose, the characteristic band-edge PL emission at 3.46 eV was lost (Parikh *et. al.*, 1997). As already seen from the PL spectra in this current study, this was likely due to their 1000 ^{o}C anneal being too low to adequately recover from the implantation damage.

Room-Temperature Hall Effect Measurements.

GaN wafers capped with 500 Å AlN were implanted at 800 ^{o}C with 200 keV Si ions with doses ranging from $1x10^{13}$ to $5x10^{15}$ cm^{-2} and annealed at 1050 to 1350 ^{o}C from 5 min to 17 sec in a flowing nitrogen environment. The sheet carrier concentrations as determined from room-temperature Hall effect measurements on this set of samples

are shown in Figure 44. Data from a representative sample implanted at 800 ^{o}C with 200 keV Ar ions at a dose of $1x10^{15}$ cm^{-2} shows the effect of the hot implantation on the GaN background carrier concentration. Data from unimplanted samples annealed from 1250 to 1350 ^{o}C are also included for comparison to show the effects of high-temperature annealing on the GaN background carrier concentration. The electron concentration is dependent upon implantation dose and annealing temperature, and increases steadily up through 1350 ^{o}C for each of the six doses. Compared to the samples implanted at 25 ^{o}C (see Fig. 27), the carrier concentrations of the three lowest dose samples implanted at 800 ^{o}C are much greater and much less dependent on anneal temperature. Sheet electron concentrations on these samples annealed from 1250 to 1350 ^{o}C fall within a relatively narrow range of $4x10^{13}$ to $1x10^{14}$ cm^{-2}. An interesting observation is that if a fixed background concentration of $3.98x10^{13}$ cm^{-2} were subtracted from each of these measurements, the resulting carrier concentrations would be remarkably similar to those of the corresponding samples implanted at room temperature. For this reason, it was suspected that this high background electron concentration was somehow caused by the hot implantation process itself. However, samples implanted at 800 ^{o}C with Argon and annealed at 1350 ^{o}C for 17 sec exhibited an electron concentration of only $8.98x10^{11}$ cm^{-2}—over 40 times less than expected to account for the high concentrations on the Si-implanted samples. The simplest explanation is that the Ar was not actually implanted at 800 ^{o}C, but perhaps only room temperature. Thus, without further study it remains unclear why the three lowest dose samples implanted with Si at 800 ^{o}C have such high carrier concentrations.

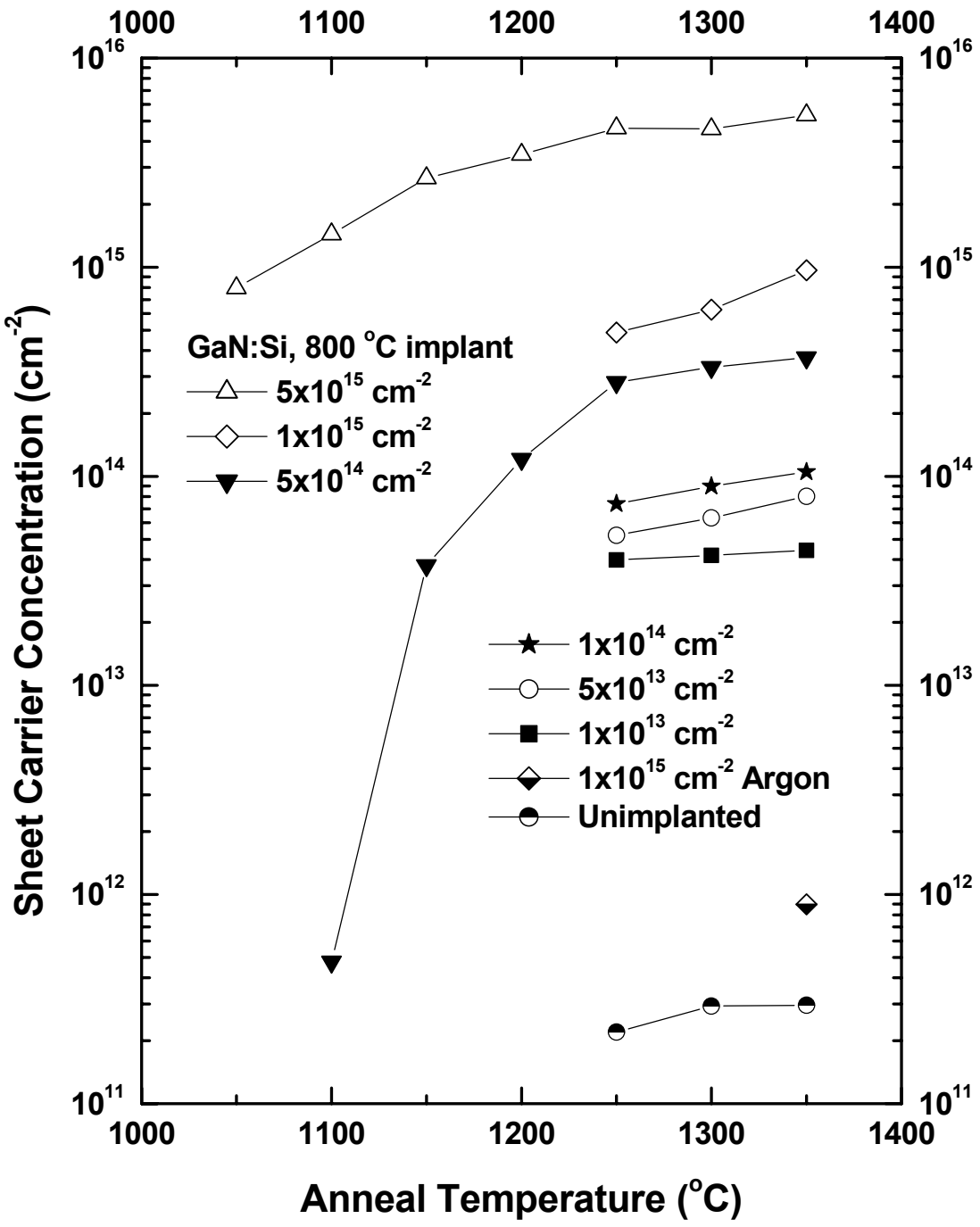

Figure 44. Room-temperature sheet electron concentrations for GaN implanted at 800 ^{o}C with 200 keV Si ions at doses ranging from $1x10^{13}$ to $5x10^{15}$ cm^{-2} and annealed at 1050 to 1350 ^{o}C from 5 min to 17 sec in a flowing nitrogen environment.

Figure 45 shows the electrical activation efficiency for all Si-implanted samples using a corrected dose after accounting for the AlN cap. Generally, for the three highest doses, the higher the dose, the greater the activation efficiency at any given anneal temperature. The highest dose of $5x10^{15}$ cm^{-2} displays fair activation (17%) even after annealing at only 1050 ^{o}C for 5 min and excellent activation (~ 97%) after annealing at just 1250 ^{o}C for 18 sec. This is one of the highest reported activation efficiencies for Si implanted at a dose of $5x10^{15}$ cm^{-2}. This exceeds the activation of the room-temperature implanted sample in this study for the same dose and anneal conditions by over 20%. Most interesting are the activation efficiencies greater than 100% for the lowest two doses. After annealing from 1250-1350 ^{o}C, the samples implanted with doses of $1x10^{13}$ and $5x10^{13}$ cm^{-2} have average activation efficiencies of 442% and 137%, respectively. Table 7 compares the carrier concentrations and electrical activation efficiencies at these two lowest doses if a fixed background concentration of $3.98x10^{13}$ cm^{-2} were subtracted from the measurements on samples implanted at 800 ^{o}C. The corrected 800 ^{o}C activation efficiency is remarkably similar to the room-temperature implantation electrical activation efficiency. Despite the fact that the data from the samples implanted with Ar at 800 ^{o}C do not provide evidence that such a large background electron concentration results from the 800 ^{o}C implantation, the implantation process is still suspect. Figure 46 shows sheet carrier concentration versus actual implantation dose. The 100% electrical activation line clearly shows the lower doses exceeding 100% activation, then falling below 100% as dose is increased only to approach 100% at the higher doses. Such behavior strongly suggests a nearly constant background concentration whose effect becomes less significant as the dose is increased.

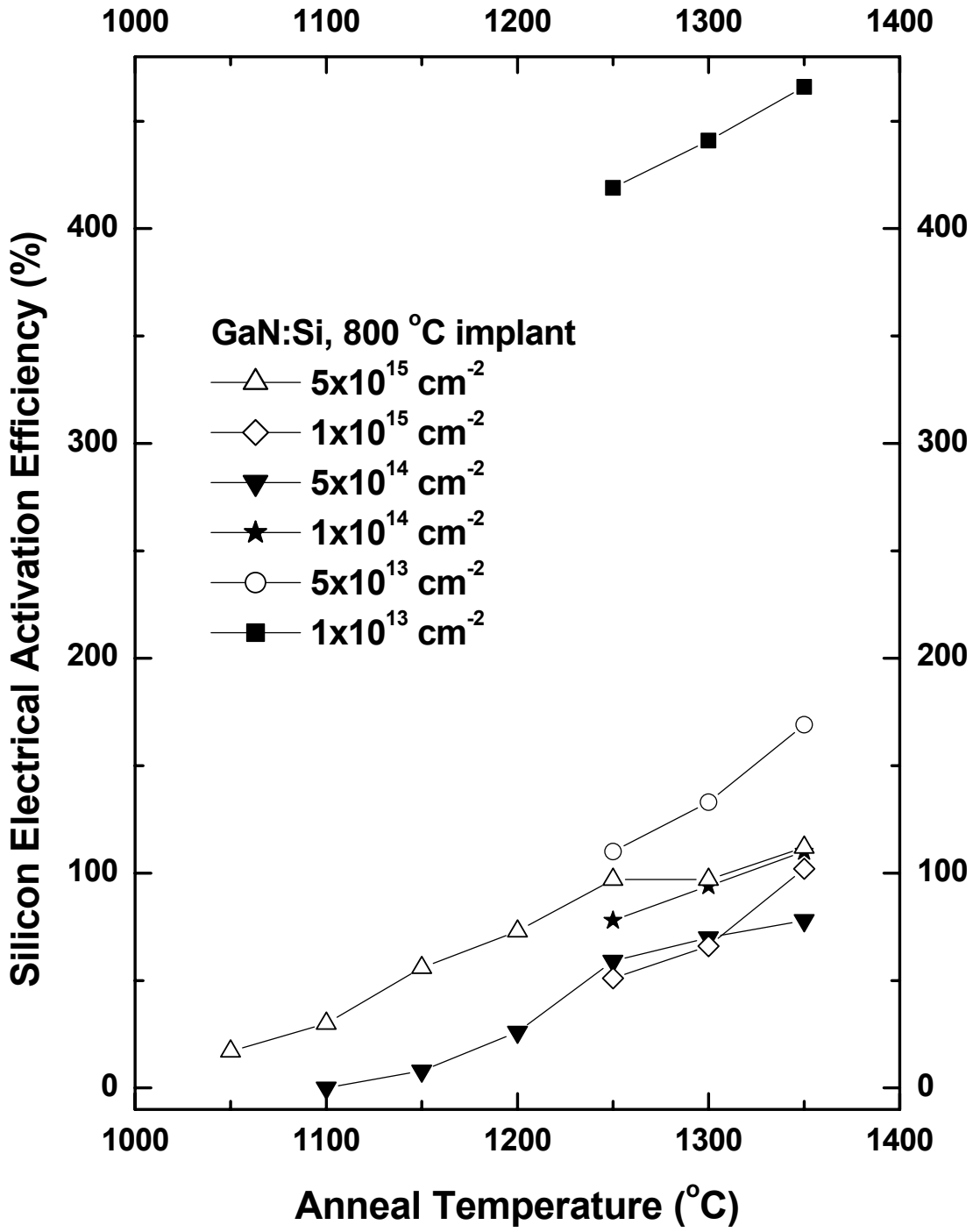

Figure 45. Electrical activation efficiency for GaN implanted at 800 °C with 200 keV Si ions at doses ranging from $1x10^{13}$ to $5x10^{15}$ cm^{-2} and annealed from 1050 to 1350 °C for 5 min to 17 sec in a flowing nitrogen environment.

Table 7. Hall Effect Data for Si-implanted GaN at 25, 800, and 800 ^{o}C Corrected

Anneal Condition (^{o}C/ time)	RT Sheet Conc. (cm^{-2})	Hot Sheet Conc. (cm^{-2})	Corrected Hot Sheet Conc. (cm^{-2})	RT Act. Eff. (%)	Hot Act. Eff. (%)	Corr. Hot Act. Eff. (%)
Nominal dose of 1 x 10^{13} cm^{-2}, Actual dose of 9.51 x 10^{12} cm^{-2} into GaN						
1250/ 21s	1.16 x 10^{11}	3.99 x 10^{13}	1.00 x 10^{11}	1	419	1
1300/ 22s	1.73 x 10^{12}	4.19 x 10^{13}	2.10 x 10^{12}	18	441	22
1350/ 17s	4.00 x 10^{12}	4.43 x 10^{13}	4.50 x 10^{12}	42	466	47
Nominal dose of 5 x 10^{13} cm^{-2}, Actual dose of 4.75 x 10^{13} cm^{-2} into GaN						
1250/ 21s	6.23 x 10^{12}	5.22 x 10^{13}	1.24 x 10^{13}	13	110	26
1300/ 22s	1.79 x 10^{13}	6.32 x 10^{13}	2.34 x 10^{13}	38	133	49
1350/ 17s	3.02 x 10^{13}	8.02 x 10^{13}	4.04 x 10^{13}	64	169	85

Figure 47 shows the electron Hall mobility for all six doses as well as for unimplanted GaN as a function of anneal temperature. The mobilities increase considerably with anneal temperature up to 1350 ^{o}C for all doses. After annealing at 1350 ^{o}C, the mobility values are higher for the lower doses. The highest mobility obtained at room temperature is greater than 180 $cm^2/V{\cdot}s$ on the sample with the lowest dose of 1x10^{13} cm^{-2}, while the lowest mobility of 100 $cm^2/V{\cdot}s$ was found on the sample with the highest dose of 5x10^{15} cm^{-2}.

Edwards *et. al.* implanted semi-insulating GaN at 300 ^{o}C with Si at a total dose of 4.4x10^{14} cm^{-2} and annealed at 1150 ^{o}C for 2 min in a SiC-coated graphite susceptor in an N_2 ambient. Dividing the measured room-temperature sheet carrier concentration by the implantation dose resulted in 27% electrical activation and a mobility of 55 $cm^2/V{\cdot}s$. By comparison, the sample implanted at 800 ^{o}C with Si at a dose of 5x10^{14} cm^{-2} and annealed at 1150 ^{o}C for 5 min in this study had only 8% electrical activation and a mobility of 20 $cm^2/V{\cdot}s$ (Edwards *et. al.*, 1997). However, many reports such as Edwards'

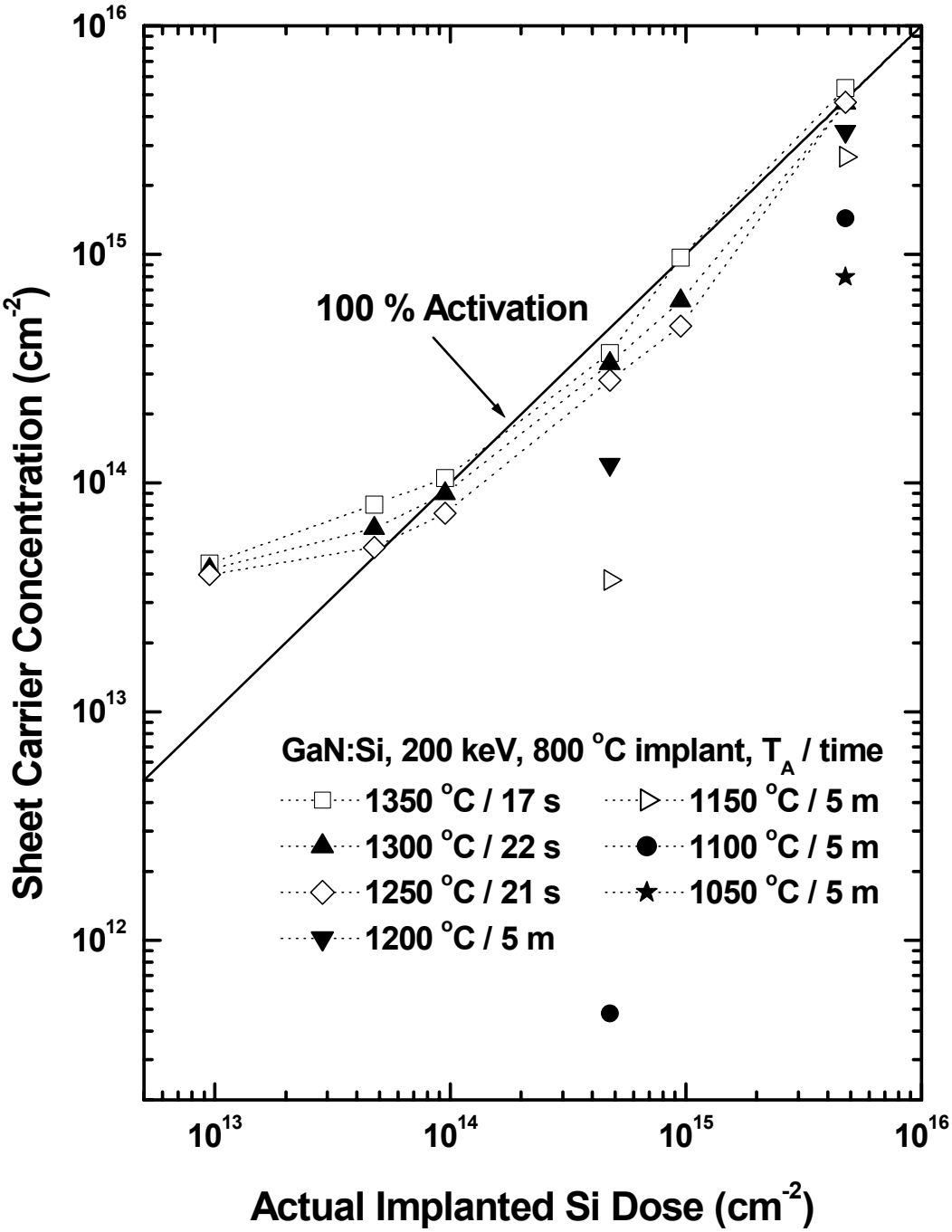

Figure 46. Sheet carrier concentration versus actual implanted dose for GaN implanted at 800 °C with 200 keV Si ions at doses ranging from $1x10^{13}$ to $5x10^{15}$ cm^{-2} and annealed at 1050 to 1350 °C from 5 min to 17 sec in a flowing nitrogen environment.

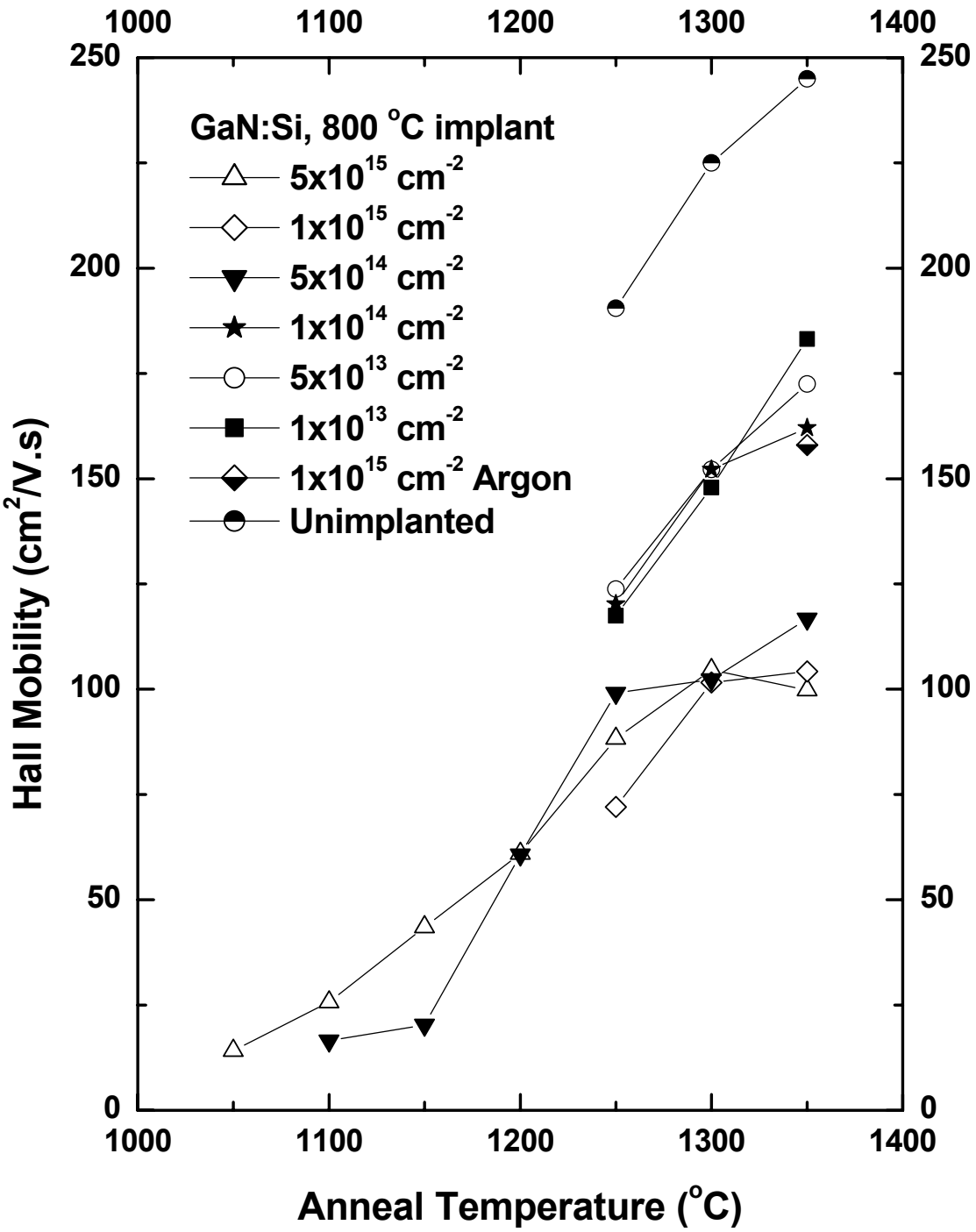

Figure 47. Room-temperature Hall mobility for GaN implanted at 800 ^{o}C with 200 keV Si ions at doses ranging from $1x10^{13}$ to $5x10^{15}$ cm^{-2} and annealed at 1050 to 1350 ^{o}C from 5 min to 17 sec in a flowing nitrogen environment.

lack sufficient depth to report optimization trends. A complete picture can only be realized by systematic investigation. In this study, annealing a sample with the same implantation conditions ($5x10^{14}$ cm^{-2}, 800 ^oC) at 1350 ^oC for 7 sec resulted in 78% electrical activation and a mobility of nearly 120 $cm^2/V{\cdot}s$.

Table 8 compiles the data from Figs. 44-47, and adds sample sheet resistivity. Just like the samples implanted at room temperature, the mobilities and carrier concentrations increase with anneal temperature for every dose in spite of the increased ionized impurity scattering from an increased number of active donors. Similarly, this trend suggests that substantial damage is being removed at each successive anneal up to 1350 ^oC and that even further damage recovery and electrical activation are possible for anneals beyond 1350 ^oC.

Temperature-Dependent Hall Effect Measurements.

The sheet carrier concentrations determined from temperature-dependent Hall measurements from 10 to 800 K for a sample at each of the six doses annealed at 1350 ^oC for 17 sec are shown in Figure 48. The carrier concentration of the unimplanted sample annealed at 1300 ^oC for 9 sec is also shown in the figure. The scale of the 1000/T axis is split at 20 K^{-1} (50 K), and an expanded 1000/T scale is used for greater clarity in the regime where sheet carrier concentration is most sensitive to temperature. The carrier concentrations for each dose kept increasing as temperature increased above about 200 K and showed no signs of saturation even at a sample temperature of 800 K, exhibiting the same behavior as the samples implanted at 25 ^oC. A temperature-independent carrier concentration due to the degenerate impurity band is seen on all samples for $T < 50$ K. The concentration of this degenerate band on the lowest two doses is significantly higher

Table 8. Room-Temperature Hall Effect Data for Si implanted into GaN at 800 ^{o}C

Implant Dose (cm^{-2})	Implant Temp. (^{o}C)	Anneal Condition (^{o}C/ time)	Sheet Resistivity (Ω/□)	Mobility (cm^2/V·s)	Sheet Conc. (cm^{-2})	Activation Efficiency (%)
1×10^{15}	800	1350/ 21s	43,920	158.4	8.98×10^{11}	Argon
1×10^{13}	800	1250/ 21s	1,334	117.5	3.99×10^{13}	419
1×10^{13}	800	1300/ 22s	1,009	147.9	4.19×10^{13}	441
1×10^{13}	800	1350/ 17s	768.6	183.2	4.43×10^{13}	466
5×10^{13}	800	1250/ 21s	966.8	123.8	5.22×10^{13}	110
5×10^{13}	800	1300/ 22s	649	152.2	6.32×10^{13}	133
5×10^{13}	800	1350/ 17s	451.6	172.5	8.02×10^{13}	169
1×10^{14}	800	1250/ 21s	703.5	120.3	7.39×10^{13}	78
1×10^{14}	800	1300/ 22s	457.4	152.2	8.97×10^{13}	94
1×10^{14}	800	1350/ 17s	366.9	162.1	1.05×10^{14}	110
5×10^{14}	800	1100/ 5m	833,000	16.5	4.77×10^{11}	0.1
5×10^{14}	800	1150/ 5m	8,190	20.3	3.75×10^{13}	8
5×10^{14}	800	1200/ 5m	850.1	60.7	1.21×10^{14}	26
5×10^{14}	800	1250/ 19s	223.9	99.1	2.82×10^{14}	59
5×10^{14}	800	1300/ 22s	183.7	102.3	3.33×10^{14}	70
5×10^{14}	800	1350/ 7s	144.9	116.7	3.70×10^{14}	78
1×10^{15}	800	1250/ 21s	178.2	72.0	4.87×10^{14}	51
1×10^{15}	800	1300/ 22s	98.1	101.6	6.27×10^{14}	66
1×10^{15}	800	1350/ 17s	62	104.2	9.68×10^{14}	102
5×10^{15}	800	1050/ 5m	552.4	14.2	7.95×10^{14}	17
5×10^{15}	800	1100/ 5m	168.8	25.7	1.44×10^{15}	30
5×10^{15}	800	1150/ 5m	53.7	43.5	2.67×10^{15}	56
5×10^{15}	800	1200/ 5m	29.6	61.0	3.46×10^{15}	73
5×10^{15}	800	1250/ 18s	15.27	88.3	4.63×10^{15}	97
5×10^{15}	800	1300/ 9s	13.04	104.6	4.58×10^{15}	97
5×10^{15}	800	1350/ 17s	11.73	99.8	5.34×10^{15}	112

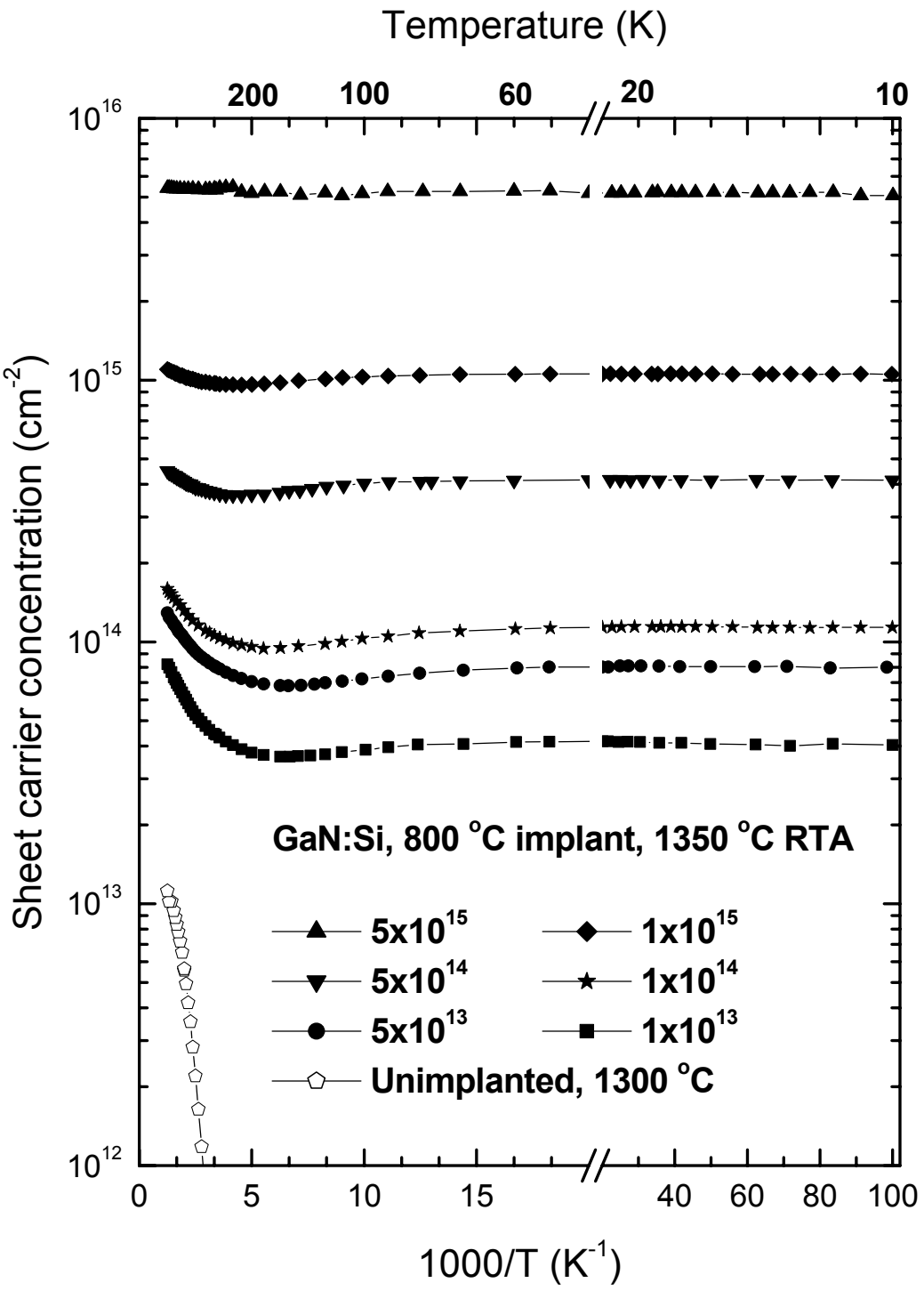

Figure 48. Temperature-dependent sheet electron concentrations from 10-800 K for GaN implanted at 800 °C with 200 keV Si ions at doses ranging from $1x10^{13}$ to $5x10^{15}$ cm^{-2} and annealed at 1350 °C for 17 sec in a flowing nitrogen environment.

than on the corresponding samples implanted at 25 ^{o}C. It was suspected that this is due to the hot implantation inducing a donor-like defect sheet concentration of about $4x10^{13}$ cm^{-2}. However, data from samples implanted with Ar at 800 ^{o}C show a room-temperature sheet electron concentration of only $8.98x10^{11}$ cm^{-2}, which is comparable to the sheet concentration from the sample implanted with Ar at room temperature.

Using the same graphical technique to determine the Si ionization energy as used for the 25 ^{o}C-implanted samples, the results for each of the 800 ^{o}C-implanted samples annealed at 1350 ^{o}C for 17 sec are shown in Figure 49. The data used in the least squares fit were taken at sample temperatures from 360-800 K. The extracted apparent ionization energies vary significantly from 0.6 to 32 meV, but consistently decrease as the implantation dose is increased. The relatively low apparent ionization energies measured on the samples with the highest three doses are attributed to the formation of a degenerate impurity band from the bulk of the Si-implanted region. The relatively high apparent ionization energies measured on the samples with the lowest two doses is attributed to the effect of a deeper level donor activation that becomes dominant at higher sample temperatures once the shallow Si donors are all ionized.

Figure 50 shows the temperature-dependent Hall mobility for the same set of samples discussed in Figures 48 and 49. The peak mobilities decrease from 192 to 108 $cm^2/V{\cdot}s$ as the implantation dose is increased from $1x10^{13}$ to $5x10^{15}$ cm^{-2}. This is mainly due to increased ionized impurity scattering. The peak mobilities of the two lowest doses are lower than those from the corresponding 25 ^{o}C implanted samples due to greater ionized impurity scattering. The peak mobilities, carrier concentrations, and extracted

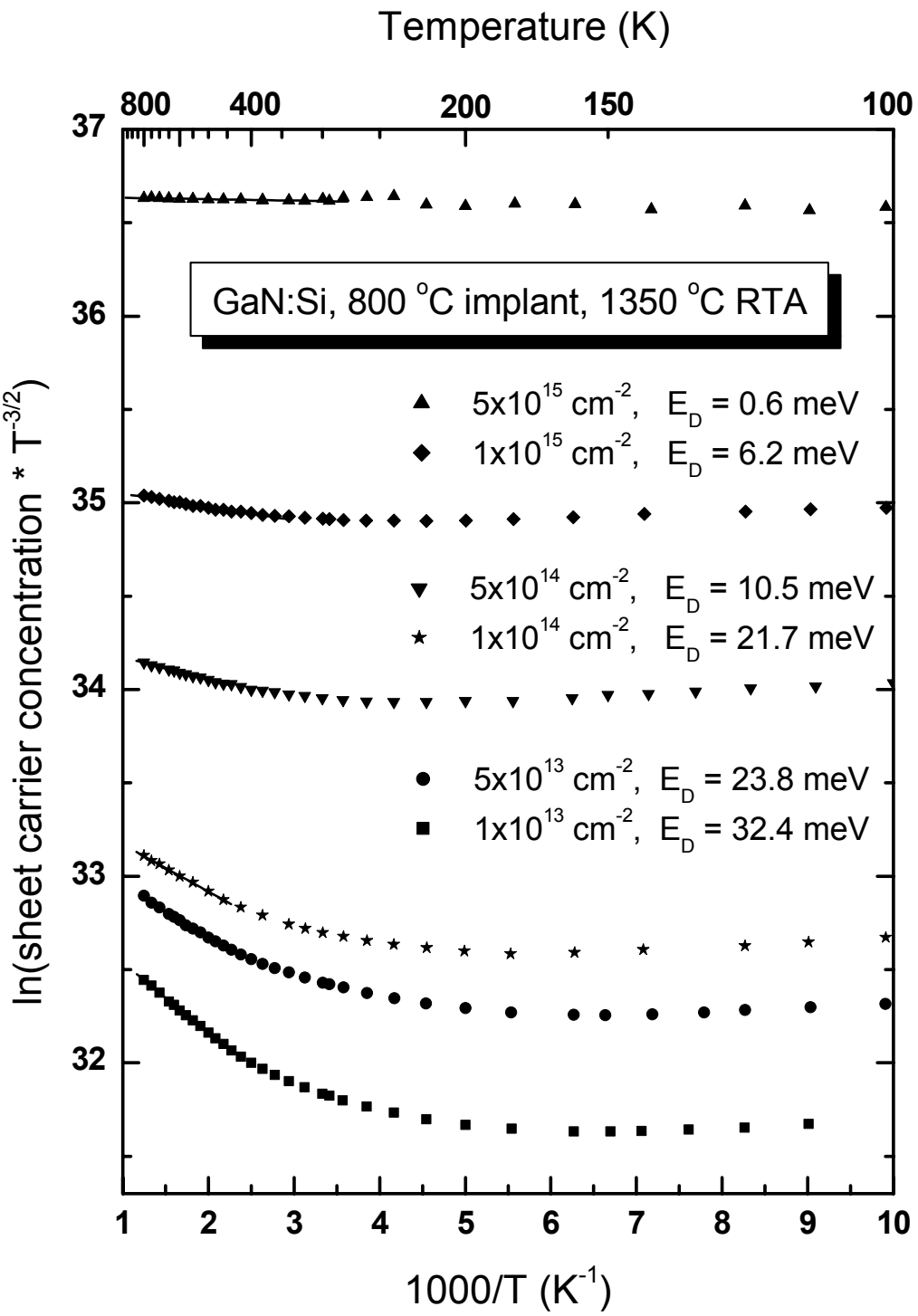

Figure 49. Measured ionization energies for GaN implanted at 800 °C with 200 keV Si ions at doses ranging from $1x10^{13}$ to $5x10^{15}$ cm^{-2} and annealed at 1350 °C for 17 sec in a flowing nitrogen environment.

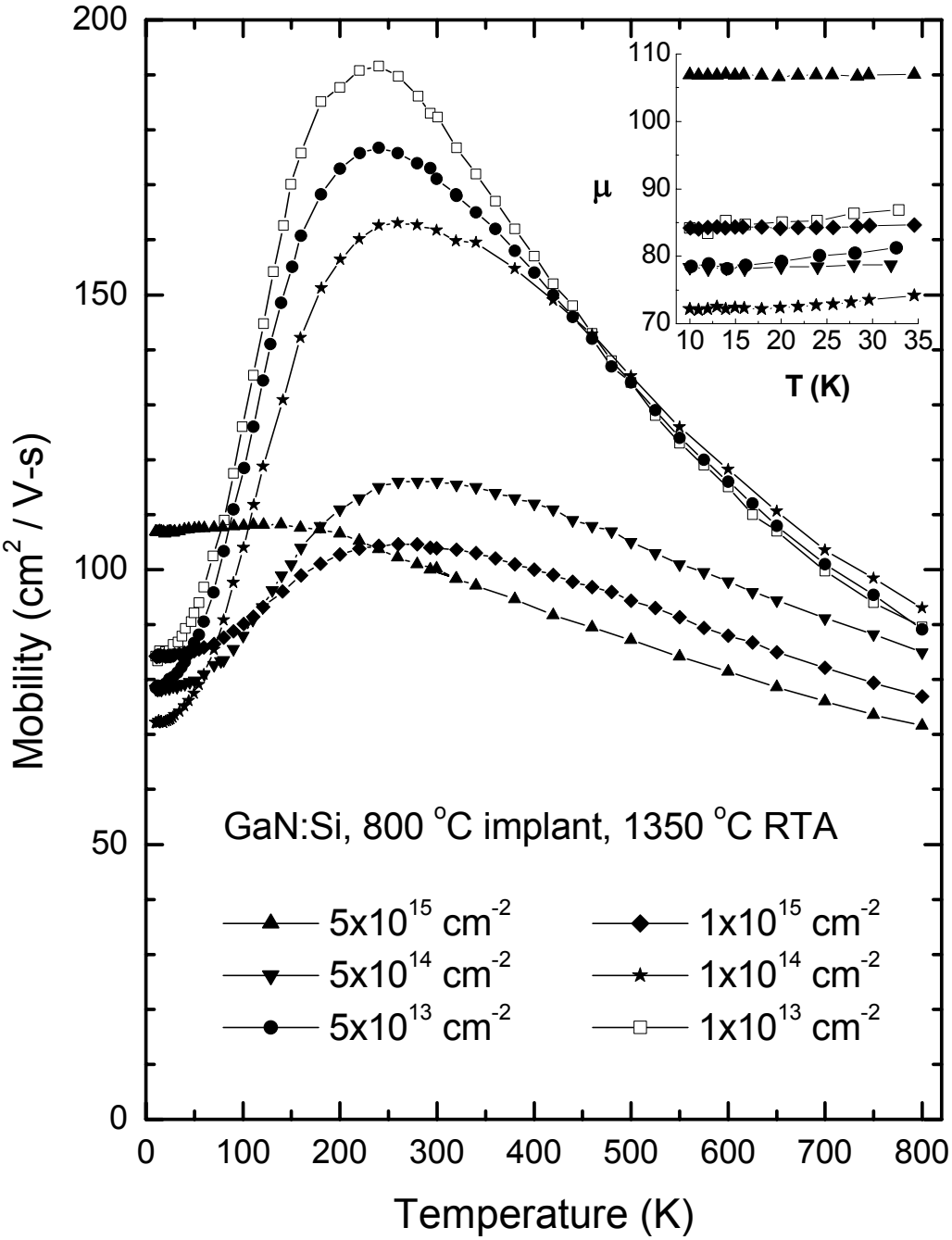

Figure 50. Temperature-dependent Hall mobility from 10-800 K for GaN implanted at 800 ^{o}C with 200 keV Si ions at doses ranging from $1x10^{13}$ to $5x10^{15}$ cm^{-2} and annealed at 1350 ^{o}C for 17 sec in a flowing nitrogen environment.

ionization energies for the other four doses are comparable to those implanted at room temperature. Unlike the samples implanted at 25 ^{o}C, the low-temperature mobility (shown in the inset), does not vary as nicely with implantation dose, although it is still temperature independent. The mobilities at 10 K range from 72 to 108 cm^2/V·s. As the dose is increased from 1x10^{13} to 1x10^{14} cm^{-2}, the low-temperature mobility decreases from 84 to 72 cm^2/V·s, then as the dose is further increased to 5x10^{15} cm^{-2}, the mobility values monotonically increase to 108 cm^2/V·s. This reversal in the trend of mobility with dose may be related to the exceptionally high carrier concentration seen on the samples implanted with the three lowest doses. Because all of the samples are degenerate, they all exhibit a temperature-independent carrier concentration and mobility at low temperature.

The temperature-dependent sheet resistivity from 10-800 K for the same set of samples annealed at 1350 ^{o}C for 17 sec is shown in Figure 51. As the implantation dose is increased from 1x10^{13} to 5x10^{15} cm^{-2}, the room-temperature resistivity decreases proportionally from 770 to 12 Ω/□. As the dose is increased and the samples become increasingly more degenerate, the resistivity curves become more temperature-independent. Unlike its room-temperature counterpart, the sample implanted with a dose of 1x10^{13} cm^{-2} shows no evidence of a deeper donor level that becomes dominant above 300 K. This is most likely due to the relatively large carrier concentration on this sample drowning out any such effect. The samples implanted with the three highest doses, whose carrier concentration and mobility vary little with temperature, have resistivities that are relatively temperature independent. The resistivity for all implantation doses increases in the high-temperature region as the carrier concentration·mobility product decreases as seen and discussed on the samples implanted at room temperature.

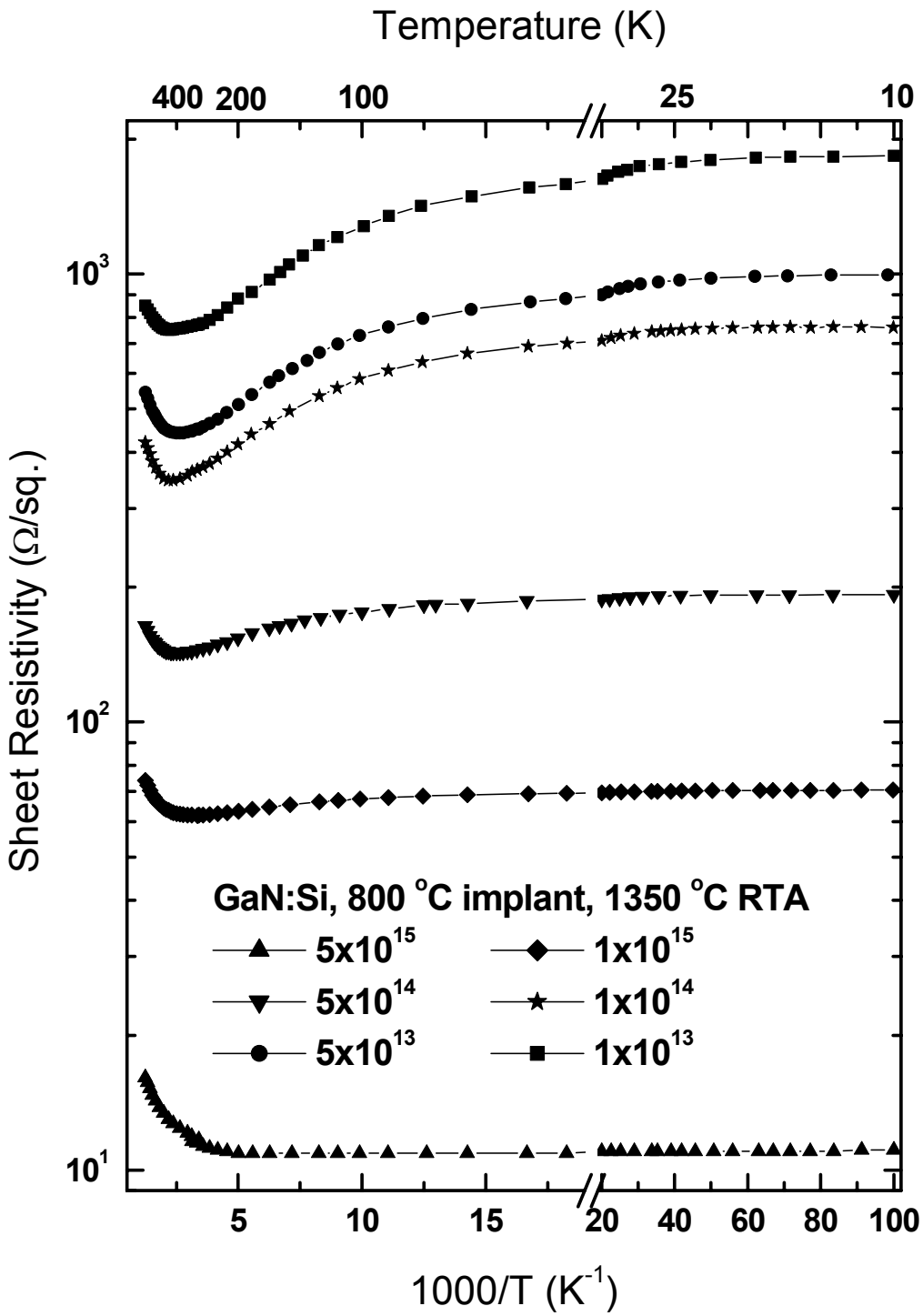

Figure 51. Temperature-dependent sheet resistivity from 10-800 K for GaN implanted at 800 °C with 200 keV Si ions at doses ranging from $1x10^{13}$ to $5x10^{15}$ cm^{-2} and annealed at 1350 °C for 17 sec in a flowing nitrogen environment.

Low-Temperature Photoluminescence.

The reader is referred to Fig. 39 and the associated discussion for the PL spectra taken at 3 K for the as-grown and unimplanted GaN annealed from 1250 to 1350 ^{o}C. The PL spectra taken at 3 K for GaN implanted at 800 ^{o}C with 200 keV Si ions at doses ranging from $1x10^{13}$ to $5x10^{15}$ cm^{-2} and annealed at 1350 ^{o}C for 17 sec in a flowing nitrogen environment are shown in Figure 52. In general, these spectra show a (D^{o},X) peak at 3.485 eV, a DAP peak at 3.28 eV with phonon replicas, and a broad YL band centered at 2.2 eV. Also shown in Fig. 52 is the spectrum for the unimplanted sample annealed at 1350 ^{o}C for 17 sec, whose intensity has been reduced by a factor of 5. The intensity of the (D^{o},X) peaks from each Si-implanted spectrum except for the highest dose has also been reduced by a factor of 5 for easier viewing and comparison. All spectra reveal a (D^{o},X) peak that decreases in intensity and broadens with increasing dose. The near band-edge broadening begins on the low energy side of the (D^{o},X) peak in the sample implanted with a dose of $1x10^{13}$ cm^{-2} and is due to band tailing. Band tailing is observed from the lowest dose sample implanted at 800 ^{o}C, because even this sample is degenerate. However, both 25 ^{o}C- and 800 ^{o}C-implanted samples exhibit the onset of band filling at a dose of $5x10^{14}$ cm^{-2}, where the free carrier concentrations of both samples are approximately equal. Luminescence from the band tailing and filling is most intense on the sample implanted with a dose of $5x10^{15}$ cm^{-2}, and produces a very broad band-to-band transition extending from 3.1 to 3.7 eV, as seen in the 25 ^{o}C-implanted sample.

The (D^{o},X) and DAP peaks are the most intense on the sample with the lowest dose. As the dose increases from $1x10^{13}$ to $1x10^{14}$ cm^{-2}, the zero-phonon DAP peak blue

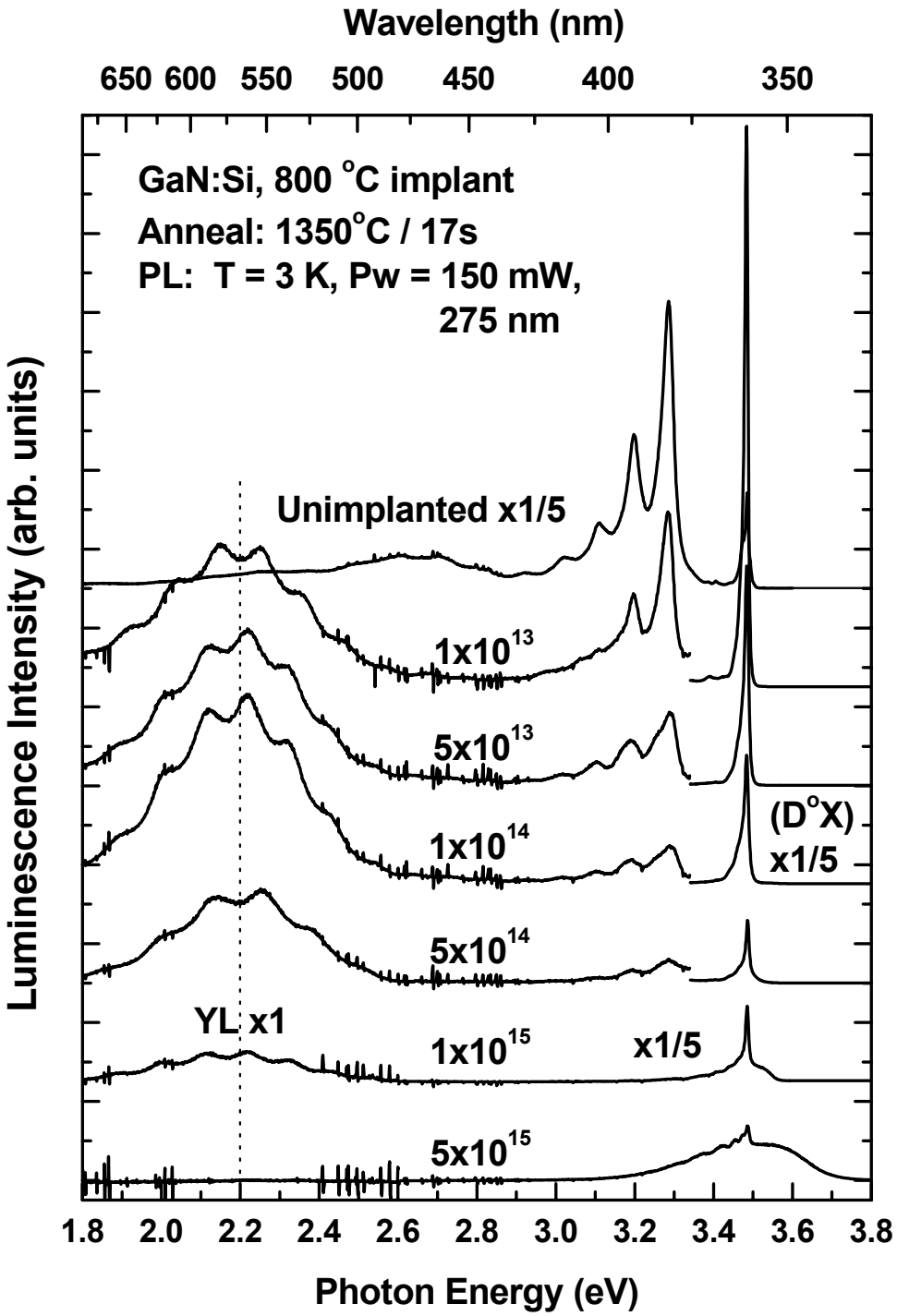

Figure 52. PL spectra taken at 3 K for GaN implanted at 800 ^{o}C with 200 keV Si ions at doses ranging from $1x10^{13}$ to $5x10^{15}$ cm^{-2} and annealed at 1350 ^{o}C for 17 sec in a flowing nitrogen environment.

shifts 4 meV. This shift is less than that seen in the 25 ^{o}C-implanted samples because the increase in carrier concentration over the same dose range is less. Identical to the spectra from the 25 ^{o}C-implanted samples, all evidence of DAP transitions have disappeared on the spectra from the two highest doses because the donor band has merged with the conduction band. After annealing at 1350 ^{o}C, the unimplanted GaN has nearly 8 times the DAP intensity that the sample implanted with a dose of $1x10^{13}$ cm^{-2} has. However, the sample implanted with a dose of $1x10^{13}$ cm^{-2} has nearly 7 times the (D^{o},X) intensity and over 150 times the sheet carrier concentration that the unimplanted sample has.

Except for the lowest dose spectrum, the intensity of the YL band is weaker on the 800 ^{o}C-implant samples compared to the corresponding 25 ^{o}C-implanted samples. The YL intensity increases as the dose is increased from $1x10^{13}$ to $1x10^{14}$ cm^{-2} then decreases more rapidly as the dose is increased further. Although the Hall effect measurement data were examined in an attempt to find a correlation between the observed intensities of the YL, it is unclear what factors determine the various intensities of the YL. Despite a small ambiguity introduced by the Fabry-Pérot oscillations, the YL appears to peak at 2.2 eV independent of implantation dose.

The sharpness (FWHM of about 11 meV) and intensity of the exciton peak from lowest dose sample correlate well with the peak mobility of nearly 200 $cm^{2}/V{\cdot}s$ obtained on this sample. Both the exciton peak and the high mobility indicate excellent implantation damage recovery resulting from annealing low-dose Si-implanted GaN at 1350 ^{o}C for 17 sec. Overall, the features of the low-temperature PL spectra are well correlated with the Hall effect measurements as a function of implantation dose for samples implanted at 800 ^{o}C and annealed at 1350 ^{o}C for 17 sec.

The PL spectra taken at 3 K for GaN implanted at 800 ^{o}C with 200 keV Ar ions with doses ranging from $1x10^{13}$ to $1x10^{15}$ cm^{-2} and annealed at 1350 ^{o}C for 22 sec in a flowing nitrogen environment are shown in Figure 53. In general, these spectra show a (D^{o},X) peak at 3.487 eV, a DAP peak at 3.28 eV with phonon replicas, and a broad YL band centered near 2.2 eV. Also shown in Fig. 53 is the spectrum for the unimplanted sample annealed at 1350 ^{o}C for 17 sec, whose intensity has been reduced by a factor of 10. The intensities of all three luminescence features from the Ar-implanted samples are the strongest on the sample implanted with the lowest dose. As the dose increases, the intensity of the (D^{o},X) peak, the DAP peak, and the broad YL band all decrease.

Temperature-Dependent Photoluminescence.

Temperature-dependent PL spectra from GaN implanted at 800 ^{o}C with 200 keV Si at a dose of $1x10^{13}$ cm^{-2} and annealed at 1350 ^{o}C for 17 sec in a flowing nitrogen environment are shown in Figure 54. The three features shown in the spectra are a (D^{o},X) peak, a DAP peak with phonon replicas, and a YL band with Fabry-Pérot interference reflections. The sharp and intense (D^{o},X) peak at 3.485 eV decreases monotonically, broadens, and red-shifts by about 56 meV as temperature increases from 3 to 300 K. This red-shift is due to the thermal characteristics of the GaN bandgap which decreases by about 66 meV over the same temperature range. The intensity of the DAP peak at 3.287 eV and its phonon replicas also decrease monotonically as temperature increases, maintaining 43% and less than 1% of its original intensity at 100 and 200 K, respectively, but totally disappearing above 200 K. This temperature dependence, similar to that seen on the 3.29 eV DAP peak in the sample implanted with Si at room temperature (Fig. 43), is attributed to the ionization of the shallow Si donor. The

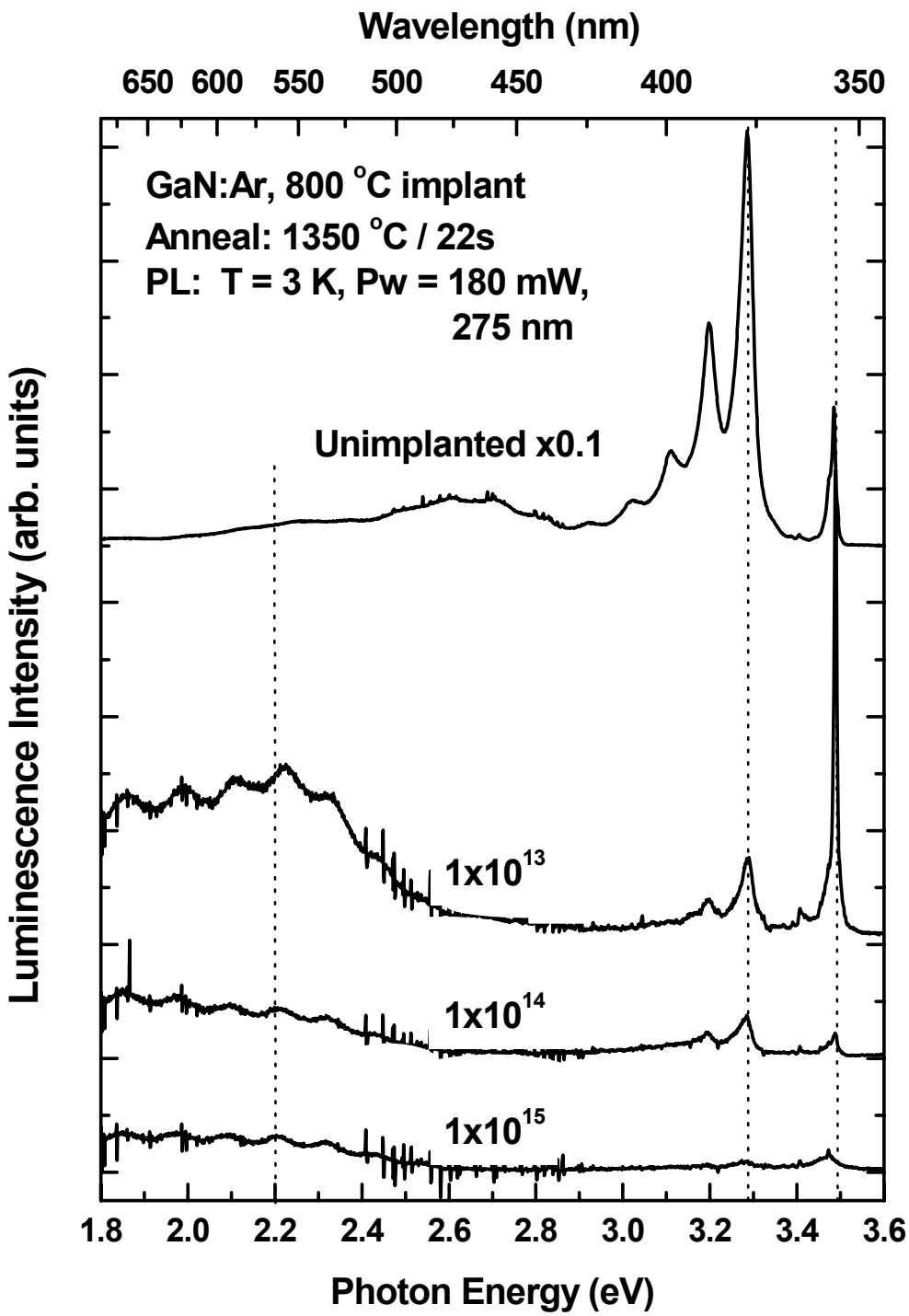

Figure 53. PL spectra taken at 3 K for GaN implanted at 800 °C with 200 keV Ar ions at doses ranging from $1x10^{13}$ to $5x10^{15}$ cm^{-2} and annealed at 1350 °C for 22 sec in a flowing nitrogen environment.

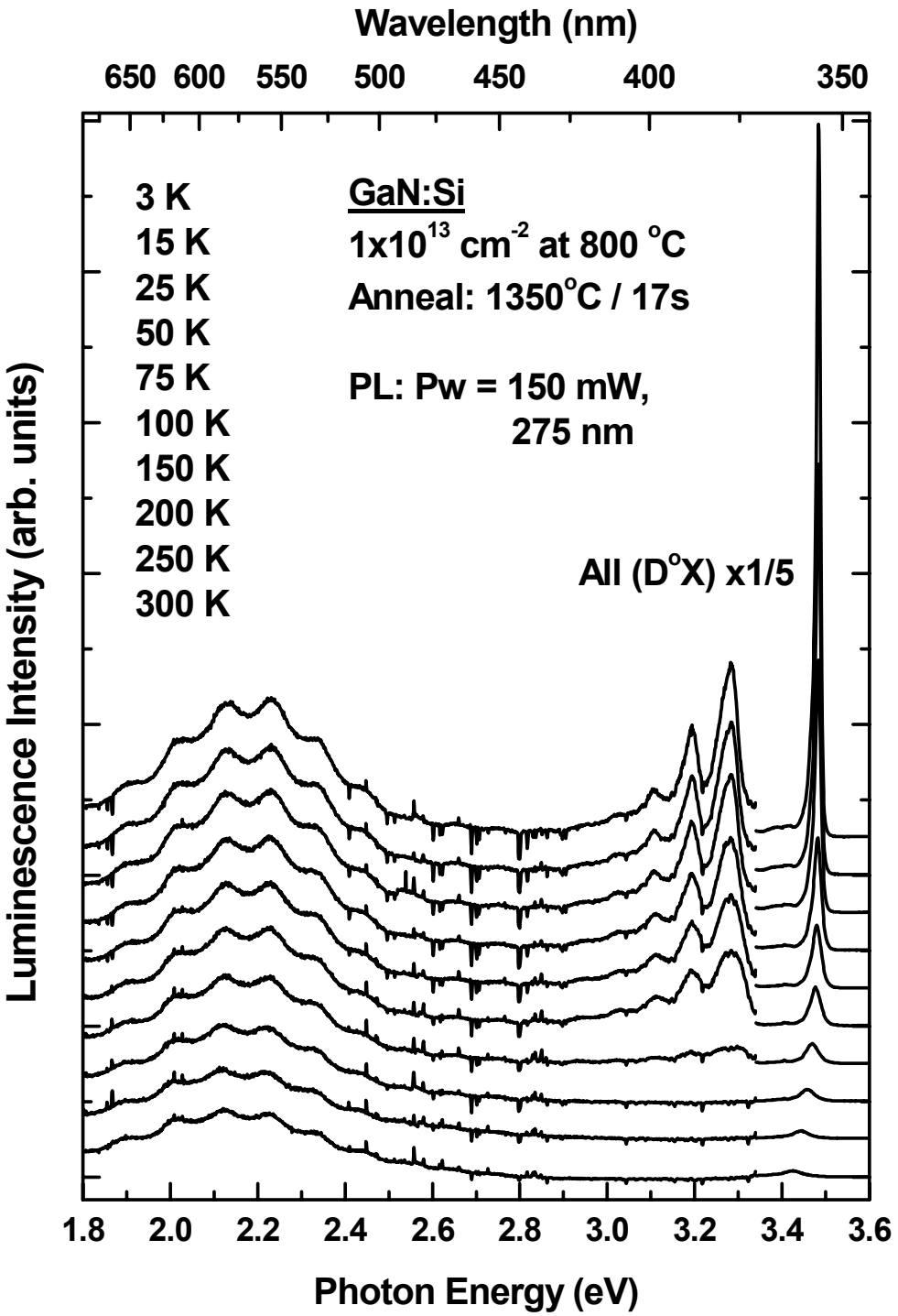

Figure 54. Temperature-dependent PL spectra (3-300 K) from GaN implanted at 800 ^{o}C with 200 keV Si at a dose of $5x10^{13}$ cm^{-2} and annealed at 1350 ^{o}C for 17 sec in a flowing nitrogen environment.

intensity of the broad YL band behaves very differently than that of the (D^o,X) and DAP peaks dropping to only about 50% of its low-temperature value at 300 K. As the temperature is increased from 3 to 300 K, the peak position of the YL band red-shifts about 12 meV from 2.218 to 2.206 eV, similar to the 13 meV red-shift observed on the RT-implanted sample. Although this red-shift is not as large as the bandgap reduction with temperature, it is noticeably different from the 50 meV blue-shift seen on the GL band in the spectra from the Mg-implanted samples. This YL also quenches less rapidly with temperature than does the GL band. This behavior indicates a deeper level, less susceptible to thermal ionization, is responsible for the YL band. A more detailed discussion of the nature of the YL band in Si-doped GaN was found in the section on temperature-dependent PL of GaN implanted at room temperature. To summarize, the 3.29 eV DAP peak, which is widely accepted to involve a shallow donor, quenches much more rapidly than the 2.2 eV YL band. If the YL involved a shallow donor, its thermal characteristics would be similar to that of the 3.29 eV DAP peak. One may therefore conclude that the YL band does not involve a shallow donor, but only deep energy levels.

Comparison of GaN Implanted with Si at Room Temperature and 800 ^oC

The room-temperature sheet electron concentrations for GaN implanted at 25 and 800 ^oC with 200 keV Si ions at doses ranging from $5x10^{14}$ to $5x10^{15}$ cm^{-2} and annealed at 1050 to 1350 ^oC from 5 min to 17 sec in a flowing nitrogen environment are shown in Figure 55. The concentrations of the sample implanted at 800 ^oC with a dose of $5x10^{15}$ cm^{-2} is an average of 44% greater than the concentrations of the corresponding sample implanted at room-temperature over all anneal temperatures. Although this difference

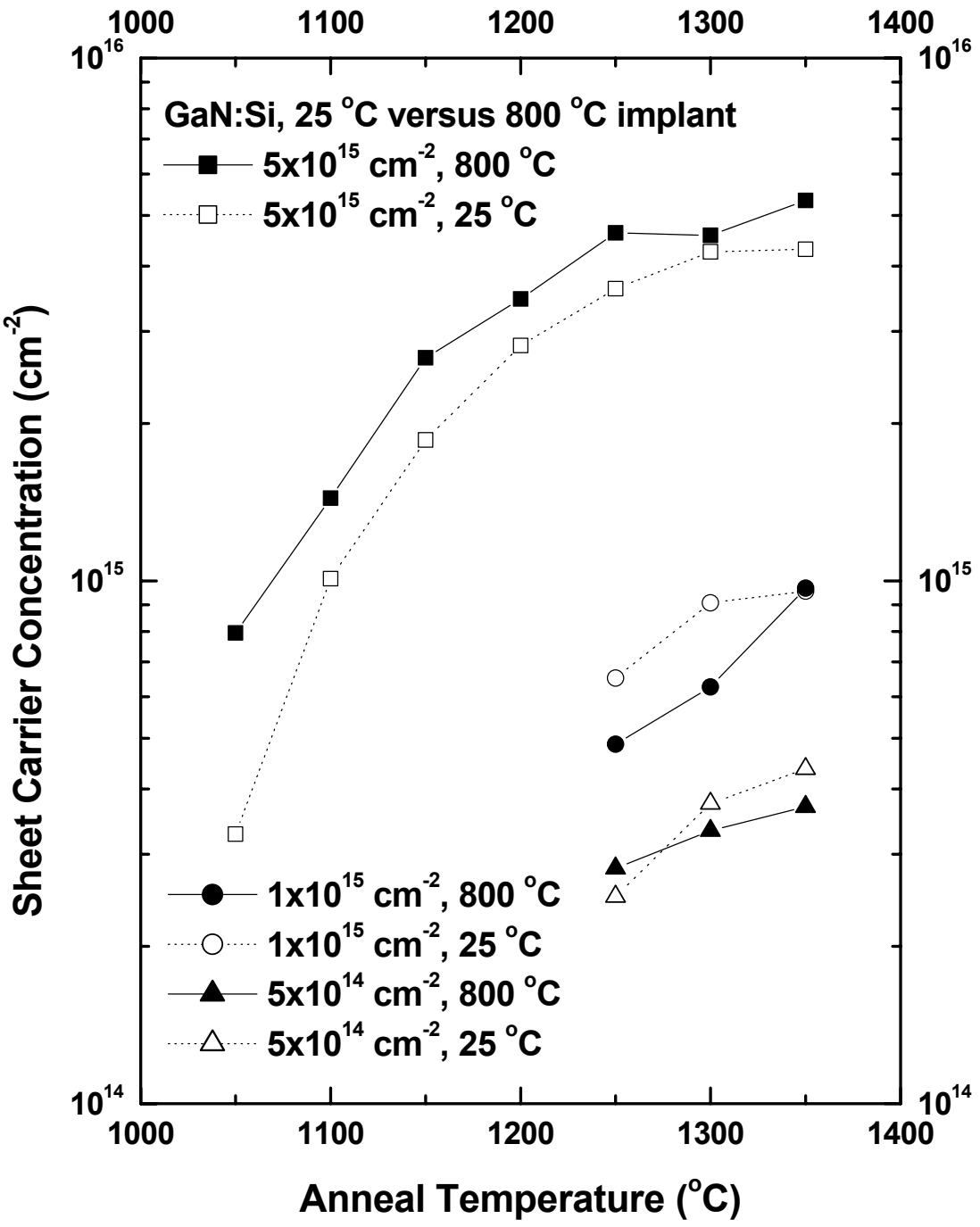

Figure 55. Room-temperature sheet electron concentrations for GaN implanted at 25 and 800 °C with 200 keV Si ions at doses ranging from $5x10^{14}$ to $5x10^{15}$ cm^{-2} and annealed at 1050 to 1350 °C from 5 min to 17 sec in a flowing nitrogen environment.

seems significant, it is not repeated for the next two lower doses. At doses of $5x10^{14}$ and $1x10^{15}$ cm^{-2}, the concentrations of the samples implanted at room temperature are on average 6 and 26% larger, respectively, than the samples implanted at 800 ^{o}C. The concentrations of the other samples were not compared because of the inexplicably large concentrations on the samples implanted at 800 ^{o}C for these lower doses. Overall, the concentration versus anneal temperature trend over all doses for the samples implanted at room temperature appears more well-behaved than that at 800 ^{o}C.

Figure 56 shows the room-temperature Hall mobility for the same set of samples examined in the previous figure. For nearly every dose and anneal temperature the mobility values of the samples implanted at 800 ^{o}C are larger than those implanted at room temperature. At a dose of $5x10^{15}$ cm^{-2}, the trend is consistent and averages to 26% larger. Figure 57 compares the PL spectra taken at 3 K for samples implanted with the lower doses ranging from $1x10^{13}$ to $1x10^{14}$ cm^{-2} and annealed at 1350 ^{o}C for 17 sec. As seen previously, the primary features of these spectra are a (D^{o},X) peak, a DAP peak with phonon replicas and a broad YL band. In each case, samples implanted at room temperature show lower (D^{o},X) intensity (except for the $1x10^{14}$ cm^{-2} dose), higher DAP intensity, and higher YL intensity (except for the $1x10^{13}$ cm^{-2} dose). Thus, for certain applications Si implantation into GaN at 800 ^{o}C may be worthwhile for the higher carrier concentrations and mobility values, though the improvement is not decisive and somewhat inconsistent.

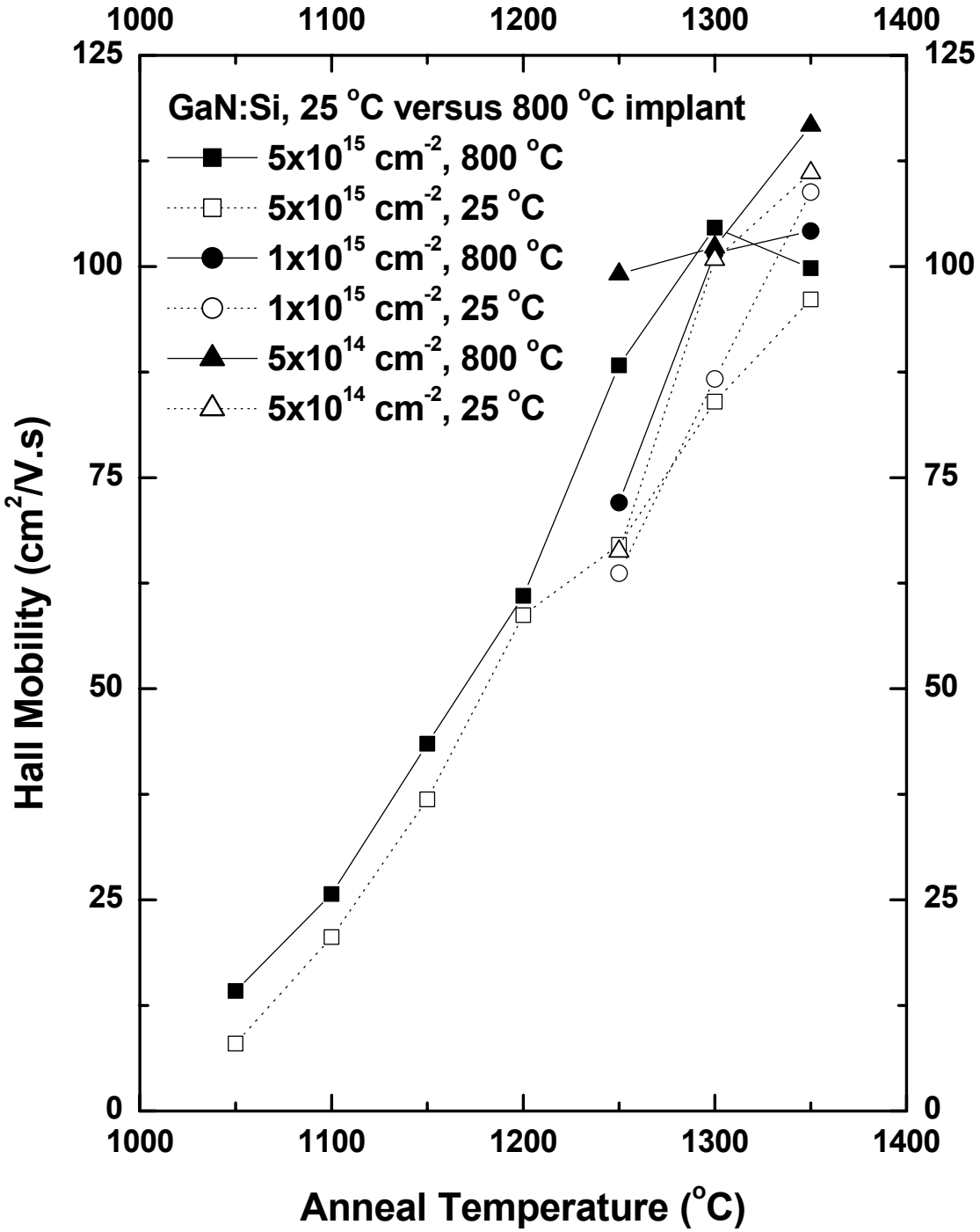

Figure 56. Room-temperature Hall mobility for GaN implanted at 25 and 800 ^{o}C with 200 keV Si ions at doses ranging from $5x10^{14}$ to $5x10^{15}$ cm^{-2} and annealed at 1050 to 1350 ^{o}C from 5 min to 17 sec in a flowing nitrogen environment.

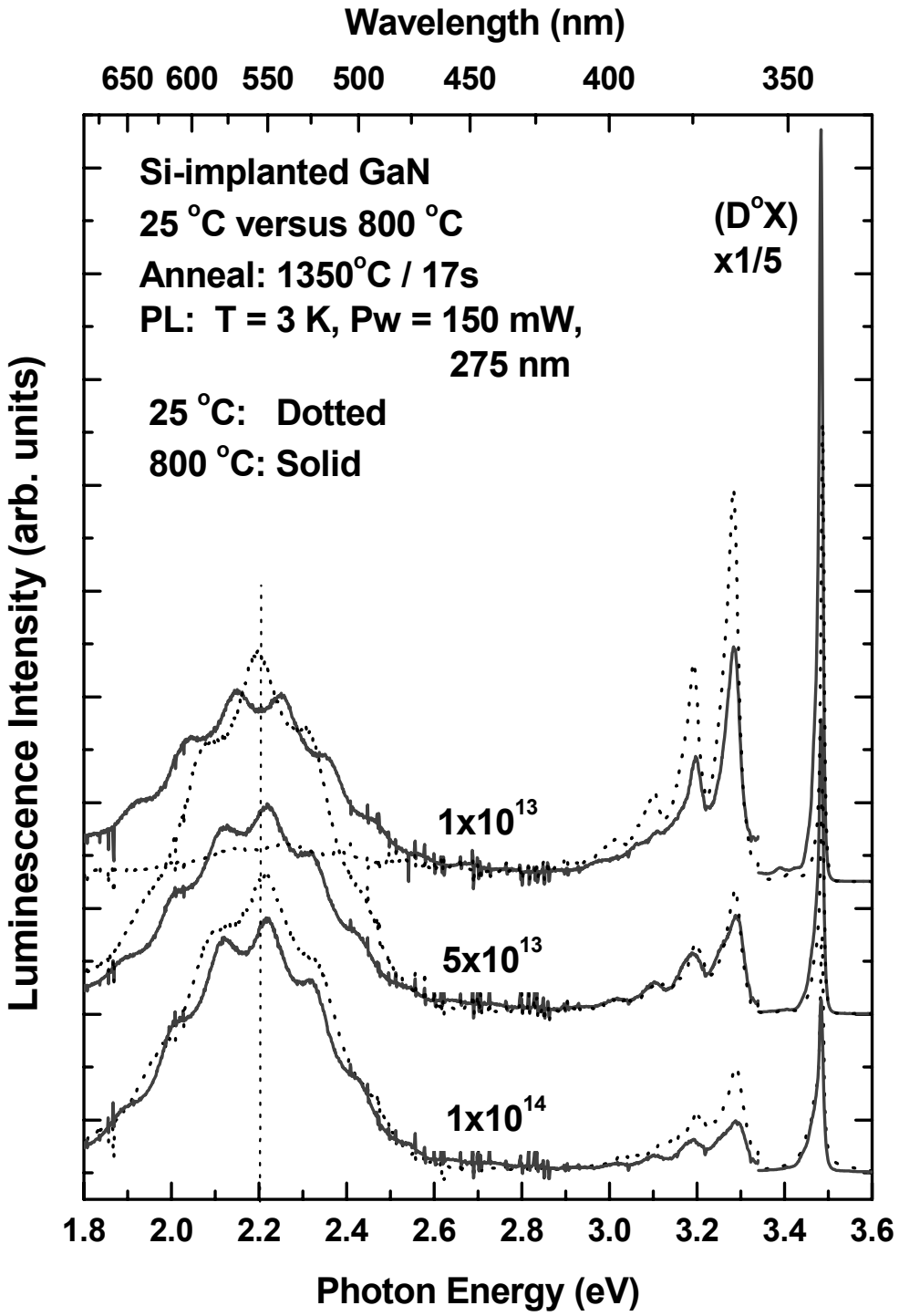

Figure 57. PL spectra taken at 3 K for GaN implanted at 25 and 800 °C with 200 keV Si ions at doses ranging from $1x10^{13}$ to $1x10^{14}$ cm^{-2} and annealed at 1350 °C for 17 sec in a flowing nitrogen environment.

VII. Conclusions and Recommendations

The primary objective of this research was to perform a comprehensive and systematic electrical activation study of Si-implanted GaN as a function of ion implantation dose, anneal temperature, and implantation temperature. A secondary objective was to investigate acceptor-implanted GaN. Both objectives were pursued with a goal to increase understanding of the implant activation process, and the defect levels associated with this process so that ion-implanted GaN can be exploited in advanced electrical and optical device applications. Each of these goals and objectives were accomplished.

GaN wafers capped with 500 Å AlN were implanted at room temperature and at 800 ^{o}C with 200 keV Si ions at doses ranging from $1x10^{13}$ to $5x10^{15}$ cm^{-2} and annealed from 1050 to 1350 ^{o}C for 5 min to 17 sec in a flowing nitrogen environment. Room-temperature Hall effect measurements were performed to determine sheet resistivity, Hall mobility, sheet carrier concentration, and electrical activation efficiency. Variable temperature Hall effect measurements were taken from 10 to 800 K to determine the Si ionization energy and to further assess the resistivity, mobility and carrier concentration. Photoluminescence (PL) spectra were collected at 3 K and also as a function of temperature from 3 to 300 K to identify various implant and defect energy levels, to assess crystal lattice recovery, and to determine the nature of observed luminescence bands. The carrier contribution from residual implantation defects and/or defects thermally generated by the high-temperature annealing were evaluated by characterizing Ar-implanted and unimplanted GaN. The PL spectra and Hall effect results from both Si-

and Ar-implanted GaN as well as unimplanted GaN were correlated to provide a synergistic understanding of Si activation. Additionally, GaN wafers capped with 500 Å AlN were implanted at 25, 500, and at 800 ^{o}C with Mg, Mg+Si, Mg+C, Mg+P, Mg+O, C, Li, and Li+P at doses ranging from $1x10^{14}$ to $5x10^{15}$ cm^{-2} and annealed from 1100 to 1350 ^{o}C for 20 min to 17 sec in a flowing nitrogen environment. Similarly, variable temperature Hall effect measurements and PL spectra were collected to electrically and optically characterize the implanted and annealed samples. The results of these efforts follow.

1) Exceptionally good electrical activation efficiencies of Si-implanted GaN were obtained. Generally, the higher the dose, the greater the activation efficiency at any given anneal temperature. A 100% electrical activation was obtained for the sample implanted with a dose of $1x10^{15}$ cm^{-2} and annealed at 1350 ^{o}C for 17 sec, which is the highest electrical activation to be reported for this dose. The sample implanted with the highest dose of $5x10^{15}$ cm^{-2} displays significant activation (> 20%) even after annealing for only 1100 ^{o}C for 5 min and an excellent activation (~ 90%) after annealing at both 1300 ^{o}C for 23 sec and 1350 ^{o}C for 17 sec. This is also one of the highest reported activation efficiencies for Si implanted at this dose. Even the sample implanted with the lowest dose of $1x10^{13}$ cm^{-2} and annealed at 1350 ^{o}C for 17 sec shows an unprecedented electrical activation of 40%.

2) Outstanding mobility values were obtained from Si-implanted GaN. The mobility generally increased with increasing anneal temperature and with decreasing dose. The highest room-temperature mobility obtained is 250 $cm^2/V{\cdot}s$ on the sample implanted at room temperature with the lowest dose of $1x10^{13}$ cm^{-2} after annealing at

1350 ^{o}C for 17 sec. Even the sample implanted at 800 ^{o}C with the highest dose of $5x10^{15}$ cm^{-2} had a remarkable room-temperature mobility of 105 $cm^2/V{\cdot}s$ after annealing at 1300 ^{o}C for 9 sec. These mobility values are much higher than those reported elsewhere on samples implanted at the same dose. Except for the lowest two doses at an anneal temperature of 1350 ^{o}C, the samples implanted at 800 ^{o}C typically had slightly higher mobilities than those implanted at room temperature.

3) Optimum annealing conditions were identified for Si-implanted GaN as a function of implantation dose. Based on electrical activation efficiency, the optimum anneal temperature appears to be around 1350 ^{o}C for the samples implanted with the two highest doses of $1x10^{15}$ and $5x10^{15}$ cm^{-2}. For the samples implanted with a dose of $5x10^{14}$ cm^{-2} or lower, the electrical activation efficiencies show no signs of saturating even after annealing at 1350 ^{o}C. Also, the mobilities continue to increase with anneal temperature for these doses in spite of the increased ionized impurity scattering from an increased number of active donors. This trend suggests that although substantial damage has been removed at each successive anneal up to 1350 ^{o}C, even further damage recovery and electrical activation may be possible for anneals beyond 1350 ^{o}C. This is especially true for the three lowest doses from $1x10^{13}$ to $1x10^{14}$ cm^{-2}.

4) An improved annealing technique was developed to minimize dissociation of the GaN surface and maximize sample survival even for anneal temperatures as high as 1350 ^{o}C and durations of several minutes above 1200 ^{o}C. After experiencing the onset of GaN decomposition at anneal temperatures as low as 1100 ^{o}C with a GaN proximity cap, an AlN thermal encapsulant was deposited post-implantation. When the survival rate of this AlN encapsulant was less than 50% after annealing at 1200 ^{o}C for 20 min, an AlN

cap grown *in-situ* with the GaN was adopted. Tests results showed that AlN grown 500 Å thick at 100 ^{o}C had greater thermal integrity than either AlN grown 1000 Å thick or AlN grown at 750 ^{o}C. The thinner cold-growth AlN survived open face anneals at 1250 ^{o}C for 20 sec but was destroyed at 1300 ^{o}C. The method finally adopted was holding these cold-growth AlN-capped samples tightly face-to-face with 5 mil Ta wire, by which they consistently survived anneals up to 1350 ^{o}C for 22 sec. Aside from the implantation itself, it is crucial to keep the AlN surface as free from contamination as possible.

5) Hall effect data were correlated with PL spectra to show the anneal temperature dependence on the relationships between carrier concentration, mobility, damage recovery, and impurity band formation. The PL spectrum from the sample implanted with Si at room temperature with a dose of $1x10^{13}$ cm^{-2} annealed at 1250 ^{o}C shows only a weak DAP peak and almost no (D^{o},X) or YL activity. However, after annealing at 1300 ^{o}C, the (D^{o},X) peak increases by almost a factor of 8, and the DAP and YL peaks increase by around a factor of 2. As the anneal temperature is increased further to 1350 ^{o}C, the (D^{o},X) peak increases by almost a factor of 60, while the DAP and YL peaks increase by factors of almost 6 and 5, respectively. As anneal temperature was increased to 1300 and then to 1350 ^{o}C, the carrier concentration increased by factors of about 18 and 2, respectively. Also, as anneal temperature was increased to 1350 ^{o}C the mobility increased by more than 80%. This confirms that the improvements in PL spectral intensity after annealing at 1300 and 1350 ^{o}C are attributed to both more Si activation and further lattice damage recovery.

6) Data showed that Si implantation at 800 ^{o}C offers no decisive advantages over implantation at room temperature. Although Si implantation at 800 ^{o}C generally resulted

in slightly higher electrical activation efficiencies and mobilities, these data were not consistent across all doses and anneal temperatures.

7) Temperature-dependent PL spectra provided evidence that the YL plaguing nearly all Si-doped GaN is not caused by a shallow Si donor, but rather a much deeper level. In samples implanted with Si at both room temperature and 800 ^{o}C, the 3.29 eV DAP peak, which is widely accepted to involve a shallow donor, quenches much more rapidly than the 2.2 eV YL band. If the YL involved the same or a similar shallow donor, its thermal characteristics would be similar to that of the 3.29 eV DAP peak. One may therefore conclude that the YL band does not involve a shallow donor, but only deep energy levels.

8) A study of PL spectra showed that the formation of Mg-related deep complexes are mainly responsible for the inefficient activation of Mg acceptors implanted into GaN. All of the Mg-implanted and most of the Mg-coimplanted GaN samples became extremely resistive, and did not show definite *p*-type conductivity even after annealing at 1350 ^{o}C for 17 sec. Furthermore, the samples did not show any *p*-type conductivity and remained highly resistive even at a sample temperature as high as 800 K. Because of the excellent mobility and band-edge luminescence of the Si-implanted samples after annealing at 1350 ^{o}C, it is unlikely that the Mg-implanted samples are significantly compensated by residual lattice damage. Instead, Mg probably formed deep complexes as evidenced by a dominant green luminescence (GL) band in the PL spectra of all Mg implanted samples. The GL band could be due to a transition from a deep donor-to-deep acceptor (D_dA_dP) with at least one of these levels caused by a Mg-related complex. These Mg-related deep complexes form independent of the 25, 500, or 800 ^{o}C

implantation temperature and remain thermally stable even at anneal temperatures as high as 1350 ^{o}C, indicating a very high binding energy. The GL band was also present in samples implanted with Mg-alone after annealing at just 1050 ^{o}C for 15 s, indicating a very low formation energy. Furthermore, these complexes form independent of and despite various coimplants designed to control stoichiometry (P and C coimplantation) or enhance *p*-type conductivity by forming reactive donor-acceptor dipole pairs (Si or O coimplantation). The GL band is predominantly seen in acceptor implanted GaN; in almost no circumstances has the PL spectrum of a *p*-type *in-situ* Mg-doped sample been reported to show a GL band, but typically only a BL band. Therefore, the Mg-related deep complex responsible for the GL is much more energetically favorable than isolated Mg_{Ga}, and can be attributed to deep complexes formed between Mg and implantation and/or other defects. The intensity of the deep donor-deep acceptor pair (D_dA_dP) GL band relative to the 3.28 eV DAP is reduced only in samples implanted with Mg+Si. However, in this case Mg can also be compensated by shallow Si donors, in addition to forming deep complexes.

9) Temperature-dependent Hall (TDH) measurements identified a Si ionization energy of 15 meV on the sample implanted with a dose of $1x10^{13}$ cm^{-2}, very similar to that reported for *in-situ* Si-doped GaN at about the same volume concentration. TDH measurements also revealed a deep donor in the unimplanted MBE-grown GaN samples having an ionization energy of about 190 meV.

Through this study to understand ion implanted GaN, some areas of further research have been identified. Unlike Si-implanted GaAs, which shows higher Si activation at lower implantation doses, Si-implanted GaN experiences lower Si activation

for lower implantation doses. Because the mobility and carrier concentrations of the lower dose Si-implanted GaN in this study had not yet peaked after annealing at 1350 ^{o}C for 17 sec, annealing at 1400 ^{o}C or at longer times for lower anneal temperatures should identify the optimum annealing conditions for the lower dose implantations. Although initial data indicate that the 800 ^{o}C implantation is not responsible for the apparent 400% electrical activation in the samples implanted with Si at a dose of $1x10^{13}$ cm^{-2}, hot Ar implantation should be repeated as the implantation is still suspected. Additional studies on Mg-implanted GaN are needed to find the optimum ion implantation and annealing conditions for successful *p*-type doping. Implanting Mg and Ar at various doses into *in-situ* Mg-doped GaN epilayers having various background hole concentrations is recommended. Any changes in the hole concentration after annealing these samples can be correlated with the intensity of the GL band and attributed to the implantation process. This should identify the Mg dose or concentration at which the GL begins to appear and help isolate the cause of the GL, thus preventing Mg–related complexes from forming and optimizing Mg electrical activation efficiency. Furthermore, implanting Mg at various doses into GaN epilayers grown under different conditions or techniques (e.g., MBE, MOCVD, HVPE, ELOG) should help determine the best GaN layers to optimize *p*-type conductivity. There is also much understanding to be gained from performing similar studies on donor- and acceptor-implanted $Al_xGa_{1-x}N$.

Appendix A

Publication Summary

The following is a complete list of publications resulting from this doctoral research. The list is divided into three sections: journal articles, refereed conference proceedings, and presentations. Papers labeled as "to be submitted" have already been prepared in draft form.

Journal Articles:

"Electrical activation studies of GaN implanted with Si from low to high dose," Fellows J., Yeo Y.K., Hengehold R., and Johnstone D., submitted to *Appl. Phys. Lett.*, 2001.

Refereed Conference Proceedings:

"Optical Characterization of Mg- and Si-Implanted GaN," Fellows J., Yeo Y.K., Hengehold R., and Krasnobaev L., *Mat. Res. Soc. Symp. Proc.*, Vol 680E, E7.1.1-E7.1.6, San Francisco, CA (2001).

"Electrical and Optical Studies of Si-implanted GaN," Fellows J., Yeo Y.K., Hengehold R., and Krasnobaev L., to be submitted, *Mat. Res. Soc. Symp I*, November 26-30, Boston, MA (2001).

Presentations:

"Optical Characterization of Mg- and Si-Implanted GaN," Fellows J., Yeo Y.K., Hengehold R., and Krasnobaev L., *Mat. Res. Soc. Symp. E*, April 16-20, San Francisco, CA (2001).

"Electrical and Optical Studies of Si-implanted GaN," Fellows J., Yeo Y.K., Hengehold R., and Krasnobaev L., to be presented, *Mat. Res. Soc. Symp I*, November 26-30, Boston, MA (2001).

Appendix B

Sample Cutting and Cleaning Procedures

Cleanroom:

1. Turn solvent hood hotplate ON and set to 100 ^{o}C.
2. Place clean 3" Si wafer face-up on hotplate.
3. Place as many 1¼" ceramic cutting disks face-down on hotplate as you have source wafers to cut.
4. Label a glassine envelope for each 5 mm x 5mm sample you expect to cut.
5. Place source wafer on appropriate-sized spinner vacuum chuck, spin wafer and clean with acetone, methanol, blow dry w/N_2.
6. Cover entire surface of source wafer with 1813 photoresist using dropper and spin on at 4000 rpm for 30 sec.
7. Place PR covered wafer face up on Si wafer for 4 min.
8. At 4 min mark, flip source wafer over and melt crystal bond onto backside ensuring edge from which samples will be cut has full coverage. Note: avoid getting crystal bond on Si wafer—this will make the mounting process go much smoother.
9. Immediately touch the face of a 1¼" ceramic cutting disk to the crystal bond coated wafer surface and lift. If wafer is stuck to Si wafer, carefully loosen with tweezers and reattempt bonding. If wafer bonds to disk, set aside to cool. Uniquely identify each ceramic disk. *** **Write down which disk has which source wafer!!!** ***
10. Repeat steps 5-9 for each source wafer to be cut.
11. Place all mounted wafers in transport box along with tweezers, crystal bond, and the brass mounting ring.
12. Turn OFF hotplate and remove Si wafer.
13. Place Si wafer on appropriate-sized spinner vacuum chuck, spin wafer and clean with acetone, methanol, blow dry w/N_2.

Wiresaw:

14. Carry box to wire saw room and turn on hotplate in fume hood on very lowest temperature.
15. Ensure there is adequate distilled drip water for wire saw.
16. Securely mount a disk on the wire saw pedestal.
17. Align wire parallel to sample edge to be cut so that wire is just barely not touching sample.
18. Once wire and sample are properly aligned, activate and zero the sliding micrometer.
19. Lower saw swing arm and slide sample tray until micrometer reads ± 5.18 mm.
20. Set appropriate drip rate; position drip spot over sample and wire.
21. Turn ON saw motor, and set to 50%.
22. Cut sample slice. When wire is almost through sample minimize pressure between sample and wire to prevent uneven cutting or chipping of sapphire substrate.
23. Lower swing arm, turn saw to 0%.
24. Secure swing arm, remove ceramic disk and place face-up on hotplate until the next wafer has been cut.

25. Repeat steps 16-24 for next source wafer to be cut.
26. Once crystal bond has been sufficiently softened on previously cut wafer, carefully remove the portion of source wafer that will not be cut into samples, remembering its ID.
27. Repeat steps 16-23 for each strip that will be cut into square samples; make initial wire alignment with the end of the strip that is closest to the center of the grown wafer—in some cases this requires remembering the location of the wafer flat.
28. After each square sample is cut, zero the micrometer and slide the sample tray ± 5.18 mm until end of strip is reached; continue until all samples are cut, keeping careful track of which pieces belong to which wafer.
29. Lower and secure saw swing arm, turn OFF saw; turn OFF hotplate.

Cleanroom:

30. Return to cleanroom and turn solvent hood hotplate ON and set to 100 ^{o}C; Place all cutting disks face-up on hotplate
31. Set out as many 2" diameter pitri dishes with covers as you have source wafers and fill each ~⅓ full w/ acetone.
32. Once crystal bond has been sufficiently softened, carefully remove each sample and place all pieces from each source wafer in their own pitri dish ***** Organization is crucial to keeping track of which samples are which! *****
33. Once all the pieces are soaking in covered dishes of acetone, turn OFF the hotplate.
34. Add DI water to each dish with a ratio of acetone:DI of about 3:1 to aid in removing the ceramic disk residue.
35. Fill the ultrasonic cleaner with DI water to the level of fluid in each pitri dish.
36. Place each dish in the ultrasonic cleaner simultaneously <u>ONLY</u> if you can tell them apart, and ultra for 20 seconds.
37. Remove dishes from the cleaner; carefully flush each dish with clean acetone and cover.
38. Clean each piece one at a time—holding with tweezers, rinse with acetone, methanol, and DI water, blowing dry w/N2 and immediately placing in the appropriate glassine envelop prepared beforehand.
39. Once all the samples and remaining source wafers (and remnants) have been cleaned and packaged, clean all quartzware with acetone and methanol--wiping will likely be necessary due to the PR, crystal bond and ceramic residue.

Oxy-Gon Sample Preparation Procedures

1. Select all the 5 mm x 5mm samples (which were previously cut & cleaned) you'll anneal.
2. On the cleanroom table, place a clean 3" Si wafer on a cloth wipe.
3. While holding them face down on the Si wafer, uniquely scribe the Al_2O_3 backside of each sample type (e.g., " / ", " < ", " | ", "O", "L", etc.)
4. Logically (e.g. hot and cold of same dose) and physically (e.g., best size match) pair up the samples.
5. After scribing, place all samples to be annealed in a 2" pitri dish for temporary storage and transport.
6. Measure out ~ 1¾" of Ta-wire for each sample pair to be annealed, cutting one long piece.
7. Place this single piece of Ta-wire in a 2" pitri dish, submerge the wire in TCE, and cover the dish.

8. Clean all samples again (front and back) with acetone and methanol rinses (and, as necessary to fully remove ceramic disk residue and make each surface mirror-like, DI H_2O), blow dry with N_2.
9. Rinse and flush the Ta-wire in the dish with acetone, then methanol. While still wet, pull the wire between a clean cloth wipe to dry.
10. Cut the wire into 1¾" sections.
11. Identify which samples will be wrapped face-to-face noting which sample will be on top.
12. Note: Practicing this process several times on a pair of junk samples is recommended.
13. Place a piece of Ta-wire on a cloth wipe and center the face-to-face samples in the middle of the wire.
14. Using two sets of tweezers, press the center of the samples together while wrapping the ends of the wire up and back across the top of the samples.
15. Bend first one end of the wire 90° at the center of the samples across the other wire, then bend the other end 90° so they interlock (like string on a Christmas package, or twine on a bail of hay).
16. Flip the sample pair over and repeat steps 14-15.
17. Flip the sample pair over and repeat steps 14-15 again, at which point you should have just enough wire to complete the final bends (step 15), only here interlock the ends and bend 180° vice 90°.
18. Keep the samples fully face-to-face throughout the process and wrap them securely. Any uncovered regions along the edge will be destroyed by the anneal—the samples must overlap perfectly!
19. Place the sample pair in the glassine envelope of the sample that started (and finished) on top.
20. Repeat steps 13-19 for each sample pair.
21. Place all the glassine envelopes in a plastic box and double bag for transport to anneal furnace.
22. Be sure to bring tweezers, gloves, wipes, and a metal dish for transport to/from the furnace.

Oxy-Gon AlN/GaN Anneal Procedures

System Start-Up (process selection switch should be in **STANDBY**):

1. Turn **ON** 80 psig house air (vent and vacuum valves are air pressure activated)
2. Turn **ON** Main Power switch (handle on lower front panel)
3. Turn Roughing pump **ON** (green button); Roughing pulls on Turbo to 10^{-3} Torr
4. Turn Turbomolecular pump **ON** (green button); Turbo pulls on itself
5. If chamber is still under a vacuum, turn process selection switch to **VENT GAS**, else GOTO 8
6. Turn **ON** low-O_2 N_2 at tank and regulator; ensure ball valve on furnace works
7. When chamber reaches atmospheric pressure, Turn **OFF** low-O_2 N_2 or Ar at tank and regulator
8. **Open** chamber, propping door open with ruler as necessary
9. **Inspect** graphite elements and electrodes for discoloration/wear; carefully **wipe** off any condensation or residue from walls
10. **Remove** previous samples as necessary and **insert** new samples evenly spaced in center of puck, then **secure** chamber door

Soft Bake (to remove impurities from hot zone):

11. Turn process selection switch to **STANDBY**, then **ROUGH**
12. Turn **ON** Ion Gauge Controller to read TCs
13. Rough pump until chamber is mid 10^{-2} Torr (read TC2); this will take a few minutes; Turbo still pulls on itself, and pressure increases slightly at TC1
14. Turn process selection switch to **HI VACUUM** (Turbo pulls on chamber, Rough pulls on Turbo—TC2 drops quickly; TC1 increases then drops more slowly)
15. To remove trapped O_2 between GaN samples, **Repeat** steps 5 through 7 only, and begin again at step 11
16. Turn **ON** Ion Gauge Filament when TC2 is in the10^{-3} Torr range, & pump until mid-high 10^{-5} Torr
17. After ~10 min into 2nd Hi-vac pull, **Open** H_2O inlet and outlet hand valves (only when chamber under vac. or filled with N_2)
18. Ensure yellow H_2O handles are open: 2, 4 & Chamber Main at 45°, 1 & 3 at full open, and H_2O safety light is ON.
19. **RESET** Over Temperature Controller to start pre-anneal soft bake of elements and chamber
20. Ensure Vacuum Interlock Bypass is OFF, Turn Heat Zone **ON**
21. Approx. 5 min after H_2O on, ion gauge should be mid-hi 10^{-5} Torr; **Ramp Up** AUTO/MAN power controls to 20%
22. Soft Bake chamber at 20% for 12 min (expect T to be approx. 230 °C; if significantly less, TC may be bad—abort run ***)
23. **Ramp Down** AUTO/MAN power controls to 8% and continue softbake for another 5 min
24. **Ramp Down** AUTO/MAN power controls to 0%
25. Turn **OFF** Ion Gauge Filament (Heat Zone may go off simultaneously) ensuring P ~mid-hi 10^{-5} Torr

Set-Up Anneal Environment:

26. Turn **ON** low-O_2 N_2 or Ar at tank and regulator
27. Turn process selection switch to **VENT GAS** to backfill chamber to ~1 PSIG
28. Adjust vent floating ball valve so that chamber gas is just barely flowing

Anneal Process:

29. Turn **ON** Vacuum Interlock Bypass (and turn **ON** Heat Zone as necessary)
30. **Ramp Up** AUTO/MAN power controls for desired temperature profile (55% initially for graphite to minimize excessive current, then gradually up to 69% max at T ≥ 1150 °C to maximize ramp rate). *Carefully* control power to not overshoot.
31. ANNEAL GaN samples
32. At appropriate time, **Ramp Down** AUTO/MAN power controls to 0%
33. Using floating ball valve, gently increase vent gas flow rate to the 10-15 lpm range
34. Turn **OFF** Heat Zone 10 min into cool-down (after power supply has cooled) on last run
35. Turn **OFF** Turbo during last run of the day
36. **Close** H_2O inlet and outlet hand valves, respectively, when T<100 °C
37. When chamber reads T<30 °C (for AlN/GaN), **Close** floating ball valve, Turn **OFF** low-O_2 N_2 at tank and regulator
38. If annealing more samples, GOTO 8
39. **Open** chamber, propping door open with ruler as necessary, carefully **remove** samples, then **secure** chamber door

System Shut Down:

40. Turn process selection switch to **STANDBY**, then **ROUGH**
41. Rough pump until TC2 ~ mid 10^{-2} Torr, if Turbo is still on, Turn process selection switch to **HI VACUUM** until TC2 ~10^{-3}
42. If short term shut down (< 1 day), Turn process selection switch to **STANDBY**, Turn **OFF** Turbo, GOTO 45
43. Turn process selection switch to **VENT GAS**, and **Open** floating ball valve to backfill chamber to ~1 PSIG
44. **Close** floating ball valve; Turn process selection switch to **STANDBY**
45. Turn **OFF** vent gas at tank and regulator
46. Turn **OFF** Vacuum Interlock Bypass
47. Turn **OFF** Roughing pump
48. Turn **OFF** Ion Gauge Controller
49. Turn **OFF** Main Power switch
50. Turn **OFF** 80 psi house air

Post-Anneal Contact Preparation Procedures

1. Obtain HCl and HNO_3 acids and place within the acid fume hood.
2. Turn ON one solvent fume hood hotplate and set to 140 ^{o}C.
3. Turn ON the second solvent fume hood hotplate and set to 90 ^{o}C.
4. On the cleanroom table, place an annealed Ta-wire-wrapped sample pair on a clean cloth wipe.
5. Using two sets of tweezers, carefully break off the brittle Ta wire-wrap, keeping track of which sample is which throughout the process.
6. Visually examine the AlN surface for signs of Ga droplets, cracking/peeling etc. (A good AlN surface post anneal will be as mirror-like as when it was wrapped.)
7. If the identifying scribe markings on the backside are no longer clearly distinguishable (at any angle or over a reflective Si wafer) place the sample on a clean 3" Si wafer and re-scribe.
8. Place the samples in a 2" pitri dish for temporary storage and transport.
9. Fill a clean 250 ml quartz beaker with 50 ml of DI H_2O; cover and place on the 140 ^{o}C hotplate.
10. Repeat steps 4-8 for each sample pair you have annealed.
11. Weigh out 1.63 g of KOH pellets (86% KOH) and tightly close the double bag.
12. Quickly place all pellets into the beaker of hot DI H_2O as the pellets will begin to melt in air.
13. Stir with tweezers until all pellets are fully dissolved and cover the beaker. (Although the hotplate is set at 140 ^{o}C, the DI H_2O will not boil, typically reaching at most 95 ^{o}C.)
14. *** Note: ensure the evaporator is not in use before proceeding with any acid processing.
15. Measure out 30 ml of HCl and place in a clean 250 ml quartz beaker.
16. Measure out 10 ml of HNO_3 and add to the HCl; gently circulate and cover the aqua regia.
17. Process ONLY the good morphology samples as the first batch (< 5-10% total metallic Ga surface area is good). Process all other samples in the second batch.
18. Place each sample in the 0.5M hot KOH solution; starting a 5 min timer on the first sample.

19. Continue placing samples one at a time at the same rate in the KOH sequentially along the circumference of the beaker and cover when finished.
20. When the samples have only 1 min left in the KOH, bring the covered beaker of aqua regia to the solvent fume hood and place on the 90 ^{o}C hotplate.
21. At 5 min, remove the samples at the same rate and in the same order in which you inserted them.
22. As each sample is removed, place it into a large (600 ml) beaker of clean DI H_2O.
23. Carefully rinse the samples in the beaker by dumping most of the DI/adding clean DI, dumping/adding—taking care to not even come close to loosing any samples. Leave at most 1" of DI in beaker.
24. When the aqua regia just begins to boil, place the samples into the acid solution directly from the DI beaker; starting a 2 min timer on the first sample.
25. Continue placing samples one at a time at the same rate in the aqua regia sequentially along the circumference of the beaker and cover when finished.
26. At 2 min, remove the samples at the same rate and in the same order in which you inserted them.
27. As each sample is removed, place it into a large beaker of clean DI H_2O.
28. When all the samples are in the DI, cover the aqua regia and turn off the 90 ^{o}C hotplate.
29. At this point, you may need to rinse a green residue off the metal tweezers, wipe, rinse and blow dry with N_2
30. Carefully rinse the samples in the beaker by dumping most of the DI/adding clean DI, dumping/adding—taking care to not even come close to loosing any samples. Leave at most 1" of DI in beaker.
31. Holding with tweezers, agitate each sample in the DI, remove, blow dry with N_2 and place in a clean 2" pitri dish.
32. Repeat steps 18-31 for the second batch as necessary using the same acid and base solutions.
33. On the cleanroom table, carefully mount all samples face down on the van der Pauw shadow mask on a clean cloth wipe.
34. Adjust and secure each sample by gently tightening mounting screws until all samples are positioned for contacts as much in the corners as possible.
35. Note: Each row on the mask is a different sized square; generally the largest two square rows are best.
36. *** Note: This is an iterative and tedious process as tightening one sample may loosen another. ***
37. When all samples are securely squared, vent the evaporator and carefully insert the mask.
38. Remember to change the microscope window slides, check metal levels, secure door and "process".
39. Turn off both hotplates, clean up all acids, bases, DI, Ta-wire-pieces, etc.

Edwards Auto 306 Evaporator Procedures

Sample preparation:
1. Degrease sample with solvents (acetone, methanol) DI rinse and N_2 blow dry.
2. Remove any oxides with 2 min of boiling aqua regia (HNO_3:HCl, 1:3), DI rinse and N_2 blow dry.

Vent chamber, Mount/Remove sample & Create vacuum:

1. Ensure chamber is not in use and has been cooled for at least ½ an hour after the last evaporation.
2. Press "**Seal/Vent**" and lift chamber clip—door will open *easily* at 7.6E2 Torr—not until!
3. When vented, **open** chamber door and remove sample jig—if removing, do so & go to Step 7.
4. **Mount** cleaned sample(s) properly on jig
5. Physically **verify** the metals in each carousel positions and note for assigning layer parameters.
6. Check amount of metal in hearths to be used and **fill only as necessary**—half full is OK.
7. **Insert jig** into chamber, and secure door.
8. Press "**Process**" to start vacuum.
9. **Fill** liquid N_2 reservoir to improve pump-down time.
10. Confirm metal **parameters** on each layer to be used (density, tooling, z-factor, etc.).
11. Program the **thickness** for each layer in nm.

Evaporation:
1. Wait until vacuum ≤ $2x10^{-7}$ Torr is obtained.
2. Turn electron **Gun Power Supply ON**.
3. Turn **gun** and **on/off ON**, and wait for lights (Power, Vac, H_2O, Rot, Gun, Local, and Beam).
4. **Check** ~4.85 kV high voltage setting and 15-17 ^oC water chiller.
5. Using **Data** button, select appropriate layer and confirm settings changing as necessary.

	Ti	Al	Au	Ni
Layer	1	3	2	4
Density	4.5	2.7	19.3	8.91
Z-factor	14.1	8.2	23.2	26.6
Tooling	0.85	0.85	0.85	0.85
Beam for evap	120 mA	45 mA	100 mA	120 mA

6. Ensure shutter is **closed** and **no** shutter control buttons are pushed.
7. Activate **Beam Sweeping** by setting control knob to "1".
8. Turn **Beam Current** control knob to 1st notch (~ 20 mA).
9. Slowly ramp **Beam Current** up in 20 mA steps every several seconds, monitoring vacuum pressure—don't let pressure exceed $1x10^{-5}$ Torr.
10. If metal has not been used recently, **evaporate off impurities** by getting metal liquid hot (i.e., at the onset of evaporation—watch for solid to liquid phase change) otherwise go to step 12.
11. As necessary, allow chamber to return to $2x10^{-7}$ Torr, then repeat starting at step 9.
12. Stop ramping **Beam Current** when desired beam current is achieved, or turn down if $9x10^{-6}$ Torr is exceeded.
13. Arm shutter by depressing **Remote** button
14. Press "**Run**" to open shutter and start evaporation, noting start time.
15. Watch deposition rate and pressure; modify **Beam Current** to keep both within proper limits.
16. **Log** time when deposition completes.
17. Turn **Beam Current** down slowly (2-3 seconds) to zero.
18. Activate **Carousel** and move to position of next metal, else go to step 21 if done evaporating.
19. Using **Data** button, select appropriate layer and confirm settings changing as necessary.
20. Go to Evaporation step 8 when chamber returns to $2x10^{-7}$ Torr
21. Deactivate **Beam Sweeping**, **Carousel**, and disarm shutter **Remote**.
22. Turn **gun** and **on/off OFF**, turn **Gun Power Supply OFF**.

23. Log evaporation results into the Evaporation log book.
24. Wait at least ½ hour and follow vent procedures.

Photoluminescence Procedures

Mounting and Inserting Samples:
1. Mount up to three 5 mm x 5 mm samples on each side of copper block using dot of rubber cement on top back.
2. Carefully slide rod into chamber, reconnect TC gauge wire; secure w/clamp.
3. When sample chamber is already under a vacuum:
    Close valve on top Cu pipe to sample chamber.
    Connect pressurized He line to small red lever and **open valve**.
    Undo clamp on sample rod. When chamber is pressurized w/He, cap will pop.
    Complete steps 1 & 2 above.
    Close small red lever; **open** valve on top Cu pipe, turn **off He tank** & disconnect line.

Initial Start-up (everything at 760 Torr and room temperature):
1. **Turn on roughing** pump to rough out vacuum jacket through dormant turbo, ensuring valve to jacket is open.
2. When jacket < 100 μm Hg, **turn on turbo** pump on top shelf (after ~ x hours of roughing).
3. When jacket < 2 μm Hg, **turn on big roughing** pump at wall to rough sample chamber (~ x hrs of turbo).
4. Ensure vacuum release valve is closed (black knob by chamber gauge) and **open valve** on top Cu pipe.
5. **Purge LHe reservoir** w/pressurized He:
    Connect He gas tank to inlet of LHe reservoir;
    Open black knob at top of chamber & put "+" pressure into resvr;
    Close black knob & open valve on bottom Cu pipe (rough pump pulls on LHe resvr & pump gurgles); **Close bottom pipe valve**.
6. Perform step 5 three times to **fully purge** LHe resvr.
7. **Open black knob** at top of chamber & put "+" pressure into resvr again.
8. **Open needle valve** to pull pressurized He through sample chamber (pump will gurgle); **close needle valve**.
9. **Close vacuum jacket valve** to turbo just before adding LN_2 to avoid cryo-pumping through turbo into jacket
10. **Dump LN_2** into LN_2 resvr maintaining "+" pressure on LHe resvr.
11. **Test needle valve** to ensure free LHe flow to chamber (pump gurgles).
12. When LN_2 resvr is full and stops bubbling over, **close black knob** to LHe resvr & **disconnect He gas** tank
13. **Wait** at least 3 hours and **top off LN_2** resvr before adding LHe to resvr.

Adding LHe: (everything under a vacuum and LN_2 reservoir full for > 3 hours)
1. Position LHe dewar and **Connect He gas** tank to dewar; turn on **LHe meter**.
2. Open top dewar valve and **insert transfer tube** to LHe level (watch dewar pressure and add as necessary).
3. When LHe begins to "puff" from transfer tube, **insert** into LHe resvr inlet; **remove rubber stop** on exhaust.

4. Dewar pressure determines transfer rate. **Test needle valve** to ensure free LHe flow to chamber (pump gurgles).
5. When meter reads appropriate LHe level, quickly **raise dewar tube** above LHe level.
6. Quickly pull LHe resvr **tube fully out** and **cap** with valve fixture.
7. **Store** transfer tube, **close** dewar valve, **disconnect** He tank; **replace** rubber stop on LHe resvr exhaust.
8. **Adjust needle valve** so that sample chamber pressure ~ 23 mm Hg to begin cooling samples, monitor T_A, T_B.

System Start-up (everything under a vacuum and LN_2 & LHe reservoirs full):
1. **Start N2 purge**: open N2 tank & set flow to ~5 on GF-1 unit.
2. Turn yellow **H_2O lever on**; turn **chiller power on**, press **green start** button.
3. Put on appropriate **safety goggles**; turn on laser **warning light**.
4. **Turn key** on argon ion laser controller, **ramp up current** to ~50 A, wait until laser is visible.
5. Set laser **output power** to appropriate wattage.
6. Ensure **LN_2 dewar is full** and pressurized (5-8 psi)
7. Turn on **PMT cooling** system; set to –40 ^oC.
8. After PMT is cooled, **set HV** to 1700 V from within SPEX PC program.
9. Run **test spectra** to check noise level in PMT.

Collect Spectra (when laser power, sample temp, and PMT temp are at appropriate levels):
1. T = 3K spectra requires T_A ~5.7 K and T_B ~ 1.8 K (chamber pressure will be ~18-23 mm Hg)
2. **Set slits** appropriately (100-400 μm) depending on sample intensity & resolution desired.
3. **Illuminate sample** & send reflected beam into corner of sample dewar ***before*** window to spectrometer.
4. Select a spectral feature & **optimize** luminescence intensity into spectrometer by laterally adjusting 2nd lens.
5. **Run scan** using SPEX program (3.6-1.8 eV, 2 Å step, 0.05 s integration).

Varible Temperature Spectra:
1. Run lowest temp spectra first, then collect spectra as T increases.
2. Adjust needle valve to stablize at T < 100 K.
3. Adjust needle valve and sample heater to stablize at T > 100 K.

Varible Power Spectra:
1. Set laser for highest power spectra into sample dewar; measure w/meter; collect spectra.
2. Set up neutral density filters just before sample dewar; use UV ND filters to collect lower power spectra.

System Shut-down:
1. **Close needle valve** to LHe resvr.
2. Turn laser **power down** to zero; turn **key off**; wait 10 min & turn **chiller off** and **H_20 off**.
3. Turn N2 purge gas **tank off**.
4. Turn **off PMT HV** from within SPEX PC program.
5. Turn **off PMT cooling** system.
6. Ensure **pressure release** valve on LN_2 dewar is closed.
7. **Close shutter** to spectrometer entrance to keep dust out.
8. **Top off LN_2** resvr if you want to keep vacuum jacket at usable vacuum level.

Cathodoluminescence Procedures

1. Ensure both Spectrometer computers are turned **ON**
2. Check chamber pressure with ion guage (nominally 1.6×10^{-6} Torr), then turn **OFF** ion gauge so filament light doesn't corrupt CL signal.

CAUTION: Should have $P \sim 10^{-6}$ Torr prior to turning on gun or cooling samples to maintain cathode life and prevent condensation on samples. Chamber can get to 10^{-7} Torr range after pumping overnight, can get to 1.2×10^{-7} Torr after weeks of pumping.

<u>PMT and electron gun start-up</u>:

3. Turn **ON** PMT cooler (set for -40 to –35 ^{o}C)
4. Turn **ON** Stanford high voltage for PMT (trip ON)
5. Turn **ON** Gamma box with single toggle
6. Turn **ON** Kimball unit (turn key and light 4 buttons)
7. Set Beam Energy to 5 keV
8. Close Faraday cup to monitor Beam Current
9. Slowly ramp source current UP in 0.5 A increments every several seconds until cup current reaches desired level. Note: Kimball Source Current = 2.43 A at E=10 keV, T=10 K for 50 μA.
10. Wait for spectrometer scan to stabilize at noise level (10^{-5} μA) before collecting spectra

<u>Low-temperature set-up</u> (do this in parallel with PMT and electron gun start-up):

11. Plug in heater to prevent icing at tip exhaust
12. Slowly lower transfer tube down into He tank ensuring pressure 5-8 psi
13. Open shield and tip flow valves two full turns (Note: T may go up beginning to drop ~ 20 min later)
14. Insert transfer tube into the He tank as necessary and adjust flow valves to maintain 10-12 K temperature (nominal flow meter readings of 3)

<u>Shut down</u>:

1. Pull transfer tube above liquid level in He tank. Caution: Do not break seal and lose pressure.
2. Close flow meter valves finger tight
3. Turn **OFF** PMT cooler
4. Turn **OFF** Stanford high voltage for PMT (trip **OFF**)
5. Slowly ramp source current Down to 0 A in 0.5 A increments every several seconds
6. Set Beam Energy to 0 keV
7. Turn **OFF** Kimball unit (4 buttons ending with "power" and turn key OFF)
8. Turn **OFF** Gamma box with single toggle
9. Leave spectrometer computers **ON**
10. Turn monitor **OFF**
11. Unplug heater after chamber T=100 K

<u>Vent chamber, change samples and reload</u>:

CAUTION: Ensure chamber is at room temperature and electron gun is fully **OFF** for at least 1 hour.

1. Toggle stop switch on 450 Turbo pump
2. If green lights on vent valve controller don't come on after 2 minutes, cycle power to vent valve controller
3. Place magnet on fitting and open valve (Turbo pump winds down, keep magnet there so N_2 can vent chamber)
4. Disconnect Temperature gauge and Tip exhaust from heater/sample holder
5. Pull cold finger out holding heater down while waiting for vacuum to break
6. Place finger on top of chamber depressing the end of transfer tube
7. Once vacuum breaks, close vent valve using magnet and return magnet to holder
8. Carefully pull sample holder straight out of chamber
9. Change out samples using sharp stick to apply rubber cement to back of samples
10. Replace sample holder carefully, lowering without pinching the two O-rings
11. Manually switch roughing pump **ON** (it will beep and chug)
12. Replace cold finger carefully into chamber top all the way and tighten a couple of threads
13. Wait for TCs to read in the low 10^{-3} Torr range, then turn roughing pump switch **OFF**
14. Turn **ON** Turbo pump at front panel (yellow light on)
15. Turn **ON** ion gauge to confirm vacuum is building ($P<10^{-3}$ Torr)
16. Turn **OFF** ion gauge and TC should read $1x10^{-3}$ Torr

<u>Increase pressure in He tank then change when empty</u>:

1. Change fitting on vent valve to accept small tube on standing He tank
2. Add He until pressure on main He tank reads 6-8 psi
3. Close vent valve, close standing tank valve, and remove flex tube
4. Repeat steps 2 and 3 once more when pressure and flow become too low
5. Replace standard fitting on vent valve
6. Vent main He tank when T begins rising and main tank pressure is < 1 psi,
7. Remove transfer tube
8. Close both tank valves, and label as residue
9. Clean frost off transfer tube, close vent valves, open top valve and insert transfer tube maintaining < 10 psi
10. Secure transfer tube with brass fittings and clamp at proper height

<u>Collect spectra</u>:

1. Ensure PMT T ~ –38 to –40 ^{o}C and spectrometer noise level has stabilized in 10^{-5} μA range
2. Ensure sample T is stable at desired measurement T
3. Ensure Beam Energy, all slits, and Beam Current are at desired levels at measurement T
4. Position E beam on sample center using X & Y controls; adjust Focus as necessary to control beam size/shape
5. If not already known, set scan parameters (F4) and run a quick spectrum (20 Å steps) to identify largest peaks
6. Set spectrometer to look at the most intense energy/wavelength (F9)
7. Optimize signal at the peak E/λ by adjusting lenses and X & Y controls; record max luminescence current
8. Set nominal scan parameters (3.6—1.8 eV at 2 Å step for GaN samples) and collect data

9. Output all *.spt files to *.txt ASCII files and copy to A:\

Appendix C

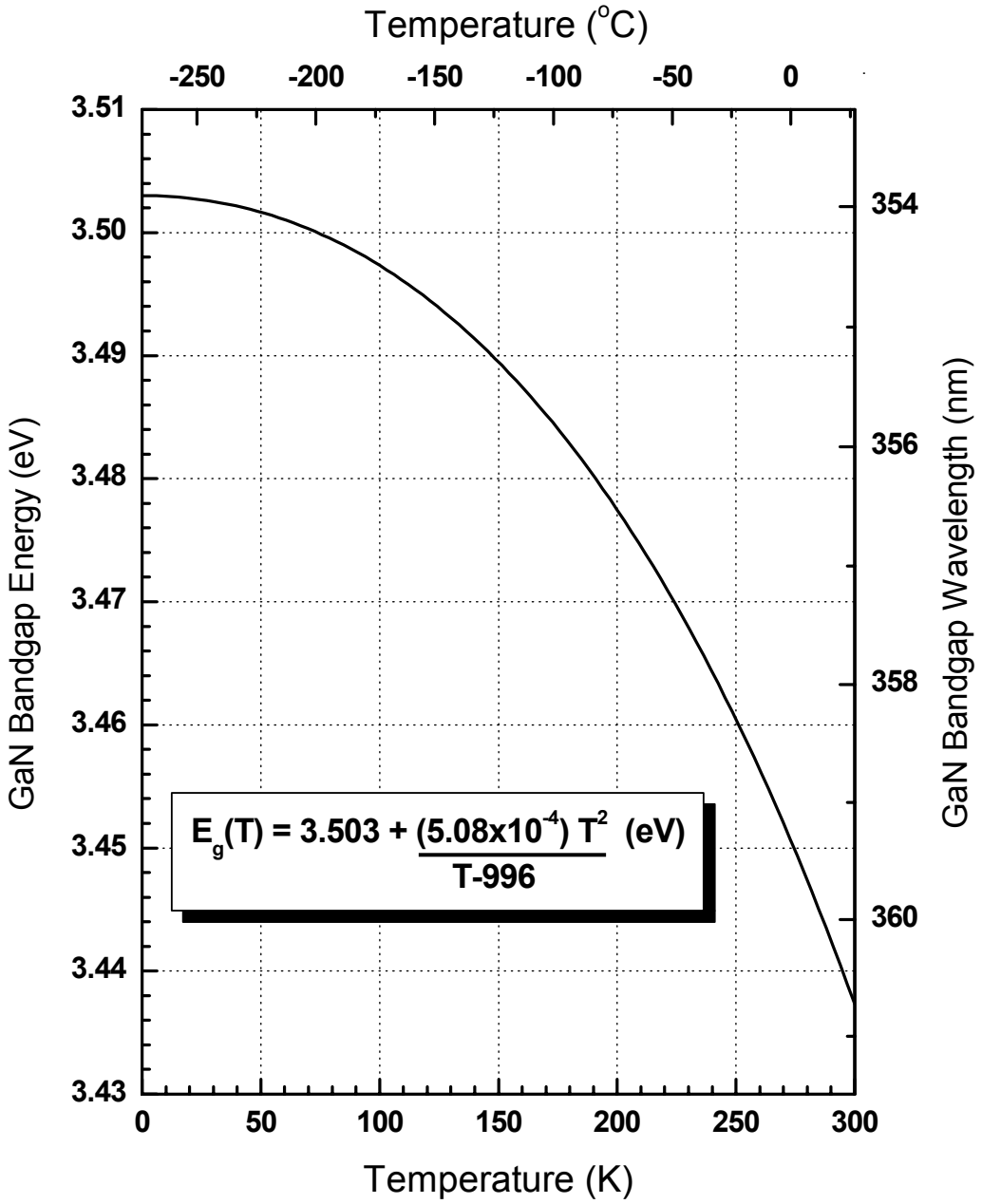

Figure 58. An empirical expression for the bandgap energy of GaN as a function of absolute temperature along with the associated graph of E_g versus T (Monemar, 1974).

Bibliography

Amano, H., M. Kito, K. Hiramatsu, and I. Akasaki "p-type conduction in Mg-doped GaN treated with low-energy electron beam irradiation," *Jap. J Appl Phys*, Part 2, 28, L2112 (1989).

Ashcroft N. W. and N. D. Mermin. *Solid State Physics*. Fort Worth: Saunders College Publishing, 1976.

Barbour, E. "How a Vacuum Tube Works," from http://www.svetlana.com/docs/tubeworks.html.

Bernardini, F. and V. Fiorentini "Incorporation, diffusion, and electrical activity of Li in GaN," *Phys Rev B*, 61 (19), 12,598-12,601 (15 May 2000).

Bhattacharya, P. *Semiconductor Optoelectronic Devices*. Englewood Cliffs NJ: Prentice Hall, 1994.

Boguslawski, P. and J. Bernholc, "Doping properties of C, Si, and Ge impurities in GaN and AlN," *Phys Rev B*, 56 (15), 9496-9505 (15 October 1997).

Brandt, O. *et. al.* "High p-type conductivity in cubic GaN/GaAs(113)A by using Be as the acceptor and O as the codopant," *Appl Phys Lett*, 69 (18), 2707-2709 (28 October 1996).

Brinkman, W. F. *et. al.* "A History of the Invention of the Transistor and Where It Will Lead Us," *IEEE J Sol-St Ckts*, 32 (12), 1858-1864 (December 1997).

Cao, X. A., *et. al.* "Ultrahigh Si^+ implant activation efficiency in GaN using a high-temperature rapid thermal process system," *Appl Phys Lett*, 73 (2), 229-231 (13 July 1998).

Chan, Y-J. and C-H. Chen "Carbon + argon co-implantation for GaAs p-channel metal-semiconductor field-effect transistors," *Appl Phys Lett*, 63 (8), 1092-1094 (23 August 1993).

Chi, G. *et. al.* "Characterizations of Mg implanted GaN," *Mat Res Soc Symp Proc*, 482, 1027-1031 (1998).

Chow, T. P. and R. Tyagi, "Wide Bandgap Compound Semiconductors for Superior High-Voltage Unipolar Power Devices," *IEEE TED*, 41 (8), 1481-1483 (August 1994).

"CREE unveils new 3 inch 4H-SiC wafers," *Compound Semiconductor*, 7 (4), 8 (May 2001).

Dalmer, M. *et. al.* "Lattice site location studies of ion implanted ^{8}Li in GaN," *J Appl Phys*, 84 (6), 3085-3089 (15 September 1998).

Dixon, R. "Major Push Needed for US Nitride Effort," *Compound Semiconductor*, 7 (1), 39-41 (February 2001).

Dreike, P. L. *et. al.* "An Overview of High-Temperature Electronic Device Technologies and Potential Applications," *IEEE TCPMT Part A*, 17 (4), 594-608 (December 1994).

Dupuis, R. D. *et. al.* "Activation of Silicon Ion-Implanted Gallium Nitride by Furnace Annealing," *J Elect Mat*, 28 (3) 319-324 (March 1999).

Eastman, L. F. *et. al.* "Undoped AlGaN/GaN HEMTs for Microwave Power Amplification," *IEEE TED*, 48 (3), 479-483 (March 2001).

Edwards, A. *et. al.* "Ion Implantation Doping of OMCVD Grown GaN," *J Elect Mat*, 26 (3) 334-339 (March 1997).

Götz, W. *et. al.* "Activation energies of Si donors in GaN," *Appl Phys Lett*, 68 (22), 3144-3146 (27 May 1996).

Grandjean, N. *et. al.* "Si and Mg doped GaN layers grown by gas source MBE using ammonia," *Mat Res Soc Symp Proc*, 482, 211-216 (1998).

Hall, E. H. "On a New Action of the Magnet on Electric Currents," *Amer. J. Math*. 2, 287-292, (1897).

Heckingbottom R. and T. Ambridge, "Ion implantation in compound semiconductors – an approach based on solid state theory," *Radiat. Eff.*, 17, 31-36 (1973).

Hess, S. *et. al.* "Photoluminescence Studies of Mg-doped and Si-doped Gallium Nitride Epilayers," *Phys. Stat. Sol. (b)* 210, 465-470 (1998).

Hong, C. *et. al.*"Cathodoluminescence investigations of Si- and Mg-doped GaN films on sapphire," *2nd Inter Blue Laser & Light Emit Diodes Symp*, 262-265 (1998).

Jain, S. C. *et. al.* "III-nitrides: Growth, characterization, and properties," *J Appl Phys*, 87 (3), 965-1006 (1 February 2000).

Kaufmann, U. *et. al.* "Origin of defect-related photoluminescence band in doped and nominally undoped GaN," *Phys. Rev. B*, 59 (8), 5561-5567 (15 February 1999).

Kim, K. S. *et. al.* "The study on the growth and properties of Mg doped and Mg-Si codoped p-type GaN," *Solid-state Electronics*, 43, 1807-1812 (1999).

Kozodoy, P. *et. al.* "Heavy doping effects in Mg-doped GaN," *J Appl Phys*, 87 (4), 1832-1835 (15 February 2000).

Kwon, Y-H. *et. al.* "Time-resolved study of yellow and blue luminescence in Si- and Mg-doped GaN," *Appl Phys Lett*, 76 (7), 840-842 (14 February 2000).

Lindhard, J., M. Scharff, and H. E. Schiøtt, *Kgl. Danske Videnskab. Selskab., Mat.-Fys. Medd*. 33, 14 (1963).

Liu, C. *et. al.* "Influence of substrate temperature on damage buildup in removal of ion implanted gallium nitride," *Nuc Instr & Meth in Phys Res B*, 148, 396-400 (1999).

Look, D. C. and R. J. Molnar "Degenerate layer at GaN/sapphire interface: Influence on Hall-effect measurements," *Appl Phys Lett*, 70 (25), 3377-3379 (23 June 1997).

Madelung, O. (Ed.) *Semiconductors – Basic Data* (2nd Edition). Berlin: Springer, 1996.

McCarthy, L. S. *et. al.* "GaN HBT: Toward and RF Device," *IEEE TED*, 48 (3), 543-549 (March 2001).

McKelvey, J. P. *Solid State and Semiconductor Physics*. Malabar FL: Robert E. Krieger Publishing Co., 1966.

Molnar, B. *et. al.* "Si Implantation and Annealing of GaN for n-type Layer Formation," *Mat. Res. Soc. Symp. Proc*. 423, 183-187 (1996).

Monemar, B. "Fundamental energy gap of GaN from photoluminescence excitation spectra," *Phys Rev B*, 10, 676 (1974).

-----. "Basic III-V nitride research—past, present and future," *J Cryst Growth*, 189/190, 1-7 (1998).

-----. "III-V nitrides—important future electronic materials," *J Mat Sci: Matls in Elect*, 10, 227-254 (1999).

Morton, R. *et. al.* "Carbon and group II acceptor coimplantation in GaAs," *J Appl Phys*, 84 (9), 4929-4934 (1 November 1998).

Neugebauer, J. and C. G. Van de Walle "Gallium vacancies and the yellow luminescence in GaN," *Appl Phys Lett*, 69 (4), 503-505 (22 July 1996).

-----. "Chemical trends for acceptor impurities in GaN," *J Appl Phys*, 85 (5), 3003-3005 (1 March 1999).

Niebuhr, R. *et. al.* "Electrical and Optical Properties of Oxygen Doped GaN Grown by MOCVD Using N_2O," *J Elect Mat*, 26 (10) 1127-1130 (October 1997).

Obloh, H. *et. al.* "Self-compensation in Mg doped p-type GaN grown by MOCVD," *J Cryst Growth*, 195, 270-273 (1998).

Ogino, T., and M. Aoki "Mechanism of yellow luminescence in GaN," *Jap. J Appl Phys*, 19, 2395 (1980).

Ohno, Y. and M. Kuzuhara, "Application of GaN-Based Heterojunction FETs for Advanced Wireless Communication," *IEEE TED*, 48 (3), 517-523 (March 2001).

Parikh, N. *et. al.* "Ion implantation of epitaxial GaN films: damage, doping and activation," *Nuc Instr & Meth in Phys Res B*, 127/128, 463-466 (1997).

Pearton, S. J. "Ion Implantation in GaAs," *Solid State Phenomena*, 1&2, 247-280 (1988).

-----. *et. al.* "GaN: Processing, defects, and devices," *J Appl Phys*, 86 (1), 1-78 (1 July 1999).

-----. *et. al.* "Ion implantation doping and isolation of GaN," *Appl Phys Lett*, 67 (10), 1435-1437 (4 September 1995).

Ploog, K. H. and O. Brandt, "Doping of group III nitrides," *J Vac Sci Technol A*, 16 (3) 1609-1614 (May/Jun 1998).

Ramungul. N. *et. al.* "6H-SiC P+N Junctions Fabricated by Beryllium Implantation," *IEEE TED*, 46 (3), 465-469 (March 1999).

Reshchikov, M. A. *et. al.* "Photoluminescence Study of Defects in GaN Grown by Molecular Beam Epitaxy," *Mat. Res. Soc. Symp. Proc*. 639, G6.7.1-G6.7.6 (2001).

Ronning, C. *et. al.* "Characterization of Be-implanted GaN annealed at high temperatures," *MRS Inter. J NSR*, 4S1, G3.17 (1999).

-----. *et. al.* "Photoluminescence characterization of Mg implanted GaN," *MRS Inter. J NSR*, 5S1, W11.44 (2000a).

-----. *et. al.* "Ion implanted dopants in GaN and AlN: Lattice sites, annealing behavior, and defect recovery," *J Appl Phys*, 87 (5), 2149-2157 (1 March 2000b).

Rubin, M. *et. al.* "p-type gallium nitride by reactive ion-beam molecular beam epitaxy with ion implantation, diffusion, or coevaporation of Mg," *Appl Phys Lett*, 64 (1), 64-66 (3 January 1994).

Ryssel, H. and I. Ruge. *Ion Implantation*. Chichester: John Wiley & Sons, 1986.

Schubert, E. F. *Doping in III-V Semiconductors*. Cambridge: Cambridge University Press, 1993.

-----. *et. al.* "Evidence of compensating centers as origin of yellow luminescence in GaN," *Appl Phys Lett*, 71 (22), 3224-3226 (1 December 1997).

Shalish, I. *et. al.* "Yellow luminescence and related deep levels in unintentionally doped GaN films," *Phys Rev B*, 59 (15), 9748-9751 (15 April 1999).

Sheu, J. K *et. al.* "Photoluminescence spectroscopy of Mg-doped GaN," *J Appl Phys*, 84 (8), 4590-4594 (15 October 1998).

Skromme, B. J. and G. L. Martinez "Optical activation behavior of ion implanted acceptor species in GaN," *MRS Inter. J NSR*, 5S1, W9.8 (2000).

Sun, Y. *et. al.* "Activation of beryllium-implanted GaN by two-step annealing," *MRS Inter. J NSR*, 5S1, W3.82 (2000).

Sze, S. M. *Physics of Semiconductor Devices* (2nd Edition). New York: John Wiley & Sons, 1981.

-----. *Semiconductor Devices Physics and Technology*. New York: John Wiley & Sons, 1985.

Tan, H. H. *et. al.* "Damage to epitaxial GaN layers by silicon implantation," *Appl Phys Lett*, 69 (16), 2364-2366 (14 October 1996).

Van der Pauw, L. J. "A Method of Measuring the Resistivity and Hall Coefficient on Lamellae of Arbitrary Shape," *Phil. Tech. Rev*., 20, 220-224, (August 1958).

Wenzel, A. *et. al.* "Effect of implantation-parameters on the structural properties of Mg-ion implanted GaN," *Mat Sci & Eng B*, 59, 191-194 (1999).

Wilson, R. G. *et. al.* "Redistribution and activation of implanted S, Se, Te, Be, Mg, and C in GaN," *J Vac Sci Technol A*, 17 (4) 1226-1229 (July/August 1999).

Wu, Y.-F. *et. al.* "Very-High Power Density AlGaN/GaN HEMTs," *IEEE TED*, 48 (3), 586-592 (March 2001).

Xu, H. Z *et. al.* "Competition between band gap and yellow luminescence in undoped GaN grown by MOVPE on sapphire substrate," *J Cryst Growth*, 222, 96-103 (2001).

Yamamoto, T. and H. Katayama-Yoshida. "Materials design for the fabrication of low-resistivity p-type GaN using a codoping method," *Jpn J Appl Phys*, 36, part2 (2B), L180-L183 (1997).

Yang, H. C. *et. al.* "Optical properties of Si-doped GaN films," *J Appl Phys*, 86 (11), 6124-6127 (1 December 1999).

Yoshida, S., S. Misawa, and S. Gonda "Improvements on the electrical and luminescent properties of reactive molecular beam epitaxially grown GaN films by using AlN-coated sapphire substrates," *Appl Phys Lett*, 42 (5), 427-429 (1 March 1983).

Zhang, R. and T. F. Kuech "Photoluminescence of carbon in situ doped GaN grown by halide vapor phase epitaxy," *Appl Phys Lett*, 72 (13), 1611-1613 (30 March 1998).

Zolper, J. C. "Ion Implantation Doping and Isolation of III-Nitride Materials," in *GaN and Related Materials* (edited by S. J. Pearton). Gordon and Breach Science Publishers, 1997.

-----. *et. al.* "Ca and O ion implantation doping of GaN," *Appl Phys Lett*, 68 (14), 1945-1947 (1 April 1996).

-----. *et. al.* "High dose Si- and Mg-implantation in GaN: Electrical and structural analysis," *Nuc Instr & Meth in Phys Res B*, 127/128, 467-470 (1997a).

-----. *et. al.* "Electrical and structural analysis of high-dose Si implantation in GaN," *Appl Phys Lett*, 70 (20), 2729-2731 (19 May 1997b).

-----. *et. al.* "Recent Progress in Implantation and Annealing of GaN and AlGaN," *Mat. Res. Soc. Symp. Proc*. 482, 979-983 (1998).

REPORT DOCUMENTATION PAGE

Form Approved
OMB No. 074-0188

The public reporting burden for this collection of information is estimated to average 1 hour per response, including the time for reviewing instructions, searching existing data sources, gathering and maintaining the data needed, and completing and reviewing the collection of information. Send comments regarding this burden estimate or any other aspect of the collection of information, including suggestions for reducing this burden to Department of Defense, Washington Headquarters Services, Directorate for Information Operations and Reports (0704-0188), 1215 Jefferson Davis Highway, Suite 1204, Arlington, VA 22202-4302. Respondents should be aware that notwithstanding any other provision of law, no person shall be subject to an penalty for failing to comply with a collection of information if it does not display a currently valid OMB control number.
PLEASE DO NOT RETURN YOUR FORM TO THE ABOVE ADDRESS.

1. REPORT DATE *(DD-MM-YYYY)*	2. REPORT TYPE	3. DATES COVERED *(From – To)*
05-11-2001	**Doctoral Dissertation**	Aug 1998 – Nov 2001

4. TITLE AND SUBTITLE

ELECTRICAL ACTIVATION STUDIES OF ION IMPLANTED GALLIUM NITRIDE

5a. CONTRACT NUMBER

5b. GRANT NUMBER

5c. PROGRAM ELEMENT NUMBER

6. AUTHOR(S)

Fellows, James A., Major, USAF

5d. PROJECT NUMBER

5e. TASK NUMBER

5f. WORK UNIT NUMBER

7. PERFORMING ORGANIZATION NAMES(S) AND ADDRESS(S)
Air Force Institute of Technology
Graduate School of Engineering and Management (AFIT/EN)
2950 P Street, Building 640
WPAFB OH 45433-7765

8. PERFORMING ORGANIZATION REPORT NUMBER

AFIT/DS/ENP/02-2

9. SPONSORING/MONITORING AGENCY NAME(S) AND ADDRESS(ES)

Major Daniel K. Johnstone
AFOSR/NE
801 North Randolph St.
Arlington, VA 22203-1977
(703) 696-7545

Dr. William C. Mitchel
AFRL/MLPS
3005 P St., Ste 6
WPAFB, OH 45433-7707
(937) 255-4474 x3214

10. SPONSOR/MONITOR'S ACRONYM(S)

11. SPONSOR/MONITOR'S REPORT NUMBER(S)

12. DISTRIBUTION/AVAILABILITY STATEMENT

APPROVED FOR PUBLIC RELEASE; DISTRIBUTION UNLIMITED.

13. SUPPLEMENTARY NOTES

14. ABSTRACT

A comprehensive and systematic electrical activation study of Si-implanted gallium nitride (GaN) was performed as a function of ion implantation dose, anneal temperature, and implantation temperature. Additionally, Mg-implanted GaN was also investigated. Temperature-dependent Hall effect measurements and photoluminescence (PL) spectra were used to characterize the samples. GaN wafers capped with AlN were implanted Si ions at doses ranging from 1×10^{13} to 5×10^{15} cm^{-2} and annealed from 1050 to 1350 ^{o}C. The optimum anneal temperature for samples implanted with the higher Si doses is around 1350 ^{o}C, exhibiting nearly 100% electrical activation efficiency. Exceptional mobilities and carrier concentrations were obtained on all Si-implanted samples. PL spectra revealed nearly complete implantation damage recovery as well as the nature of the yellow luminescence plaguing nearly all Si-doped GaN. Additionally, GaN wafers were implanted with Mg and various coimplants and annealed from 1100 to 1350 ^{o}C. All of the Mg-implanted and most of the Mg-coimplanted GaN samples became extremely resistive, and did not show definite *p*-type conductivity even after annealing at 1350 ^{o}C, remaining highly resistive even at an 800 K sample temperature. A dominant 2.36 eV green luminescence band in the PL spectra of all Mg implanted samples is attributed to a Mg-related deep complex DAP transition. The inefficient electrical activation of Mg acceptors implanted into GaN is attributed to these Mg-related deep complexes.

15. SUBJECT TERMS

Wide Bandgap Semiconductor, Gallium Nitride (GaN), Ion Implantation, Silicon, Activation Efficiency, Hall Effect, Photoluminescence

16. SECURITY CLASSIFICATION OF:			17. LIMITATION OF ABSTRACT	18. NUMBER OF PAGES	19a. NAME OF RESPONSIBLE PERSON
a. REPORT	b. ABSTRACT	c. THIS PAGE			Dr. Yung Kee Yeo, AFIT/ENP
U	U	U	UU	221	**19b. TELEPHONE NUMBER** *(Include area code)* (937) 255-3636, ext 4532; e-mail: Yung.Yeo@afit.edu

Standard Form 298 (Rev. 8-98)
Prescribed by ANSI Std. Z39-18